# Lift and Drag of Kayak Rudders

by

Simon Willmann

***THESIS***

*for the degree of*

***MASTER OF SCIENCE***

*(Master i Anvendt matematikk og mekanikk)*

*Faculty of Mathematics and Natural Sciences*
*University of Oslo*

*Dezember 2011*

*Det matematisk- naturvitenskapelige fakultet*
*Universitetet i Oslo*

# LIFT AND DRAG OF KAYAK RUDDERS

BY

SIMON WILLMANN

# Abstract

This master's thesis studies the kayak rudder flow phenomena and uses analytic, numerical and experimental methods to describe the force coefficients of kayak rudders. Also an analysis of the sport of flatwater kayaking is conducted – amongst others with regard to the motion of the kayak hull and with regard to the propulsion. The former is based on measurement data of a K1 kayak. Further the focus is put on the rudder, and the gained knowledge finds e.g. utilization in modeling of the dynamic angle of attack.

Simulations based on CAD-data of a kayak rudder type are conducted (mostly RANS models) and discussed. Assumptions in this framework are that the boundary layer of the kayak hull is not accounted for and that possible effects of a transitional flow are not incorporated. Naturally, also the process and the solutions used to face the challenges of the grid development are described. Furthermore, a comparative analysis of different simulations (meshes, turbulence models and two sizes of the rudder) is undertaken. The main outcome are force coefficients and lift-to-drag ratios. They are based on angles of attack: $0° \leq \alpha \leq 7.5°$ and found for three different Reynolds numbers.

These force coefficients are compared to analytical methods and discussed in the context of general flow phenomena and its modeling. The mainly discussed and derived analytical methods are slender body and lifting line theory (SBT & LLT). If the known error of LLT at small aspect ratios is empirically taken into account, the simulation results are in excellent agreement with the LLT. However, all of the studied sizes of the kayak rudder exceed the slenderness approximation of SBT. The simulation results are combined with the study of the kayak-hull motion, and the approximate dynamic power loss caused by the rudder is deduced. For the smallest rudder that is approximately 1.2 W.

In addition, an experiment is designed and build up to measure lift and drag of kayak rudders. First runs are conducted. They deliver a reasonable preliminary result for the drag force at zero angle of attack (compared with the simulations), but could unfortunately not be pursued further.

This master's thesis was not part of any ongoing project, and one can conclude that a further study in the field of kayak rudders most certainly could benefit from the achievements of this work.

# Contents

# List of Figures

# List of Tables

# 1. Introduction

This master's thesis opens with presenting its objectives in *what, why and how*. Then the structure of the work is introduced in the section *outline*. The introduction chapter further contains basic information on fluid flow properties in terms of *dimensional analysis*. This also acts as a foundation for the final introduction-section discussing the *sport of kayaking*.

## 1.1. Objectives: what, why and how

The starting point of this thesis is the question, what can be done to improve a flatwater kayaker's performance from the perspective of fluid mechanics.

First a screening of the technology of kayaking is conducted. It includes an analysis of a kayak's motion and its energy losses as well as a description of the state of the art paddling propulsion. Consequently the decision to analyze the *fluid flow around kayak rudders* is made. Three different approaches to gain knowledge about the drag and lift forces acting on such rudders are worked on:

- *Analytical* methods in the field of potential flow, but also (semi-analytically) on dimensional grounds are studied. The lifting line and slender body theory are described in detail. Both are applied to kayak rudders and its validity is discussed.

- The *numerical* approach using turbulence modeling first tackles the hurdles of meshing and then investigates different RANS models in steady flow conditions. Also transient calculations are touched upon inter alia with help of large eddy simulation. Finally a comparison of the resulting force coefficients at different angles of attack for different Reynolds numbers completes the simulation results.

- Ultimately *experiments* pulling rudders through a wave tank are partly accomplished. Drag and lift can be measured at different velocities and angles of attack with the help of a strain gauge force sensor.

The outcomes of all three methods are comparable with one another and build the foundation for arguments about the validity of the different strategies to predict lift and drag forces on the considered kayak rudders.

## 1.2. Structure of the Thesis

The structure of the thesis is build upon seven chapters. The introduction chapter gives an overview of the thesis's structure and it introduces basic arguments on dimensional grounds that are applied throughout the thesis, as well as it discussed the sport of kayaking.

The second chapter (2) is the first theory chapter. It compactly introduces the basic equations and assumptions used to describe fluid flow behavior. These are then applied to both, the slender body theory and lifting surface, in particular the lifting line theory. Chapter three (3) is the second theory chapter describing the principles of turbulence modeling. Its knowledge is applied in the following chapter (4) presenting the simulations. Here, not only the methods used to compute the simulations are described, but also the employed solutions used to face the challenges of the grid generation are elaborated in detail. The experiment is introduced and discussed in chapter five (5).

The results of the simulation, the analytical methods and analysis, as well as parts of the experiment are finally presented in chapter six (6). Here the most relevant information is combined, interesting outcomes are illustrated and limitations discussed.

The thesis is completed with chapter seven (7). The conclusion briefly summarizes the main achievements, gives further suggestions on possible improvements and concludes with ideas that evolved while working on this master's thesis.

The following note concerns the citing in the master's thesis. The author is endeavored to in all conscience denote where information is taken from. Therefore, all direct quotations are marked by either quotation marks or environments. In the event of particular information being taken from a specific source, the citation is found *within* the sentence. Yet, if the context of a whole paragraph is meant, and if not stated differently, the citation is found at the *end* of the paragraph.

## 1.3. Dimensional Analysis

Many physical phenomena can be understood on the basis of relatively simple dimensional arguments. This section describes fundamental relations that are used throughout the rest of the thesis.

Starting with an illustrating example: a problem is assumed to be characterized by a physical length $l$ [m], velocity $U$ [m/s], fluid density $\rho$ [kg/m$^3$], gravitational acceleration $g$ [m/s$^2$] and a dynamic viscosity $\mu$ [kg/(m s)]. The squared brackets indicate commonly used units, known from the International System of Units (SI), but the physical relations do not depend up on them.

Using just this information to construct expressions for the order of magnitude of inertial, gravitational and viscous forces yields:

$$\text{inertial} \propto \rho U^2 l^2, \qquad \text{gravitational} \propto \rho g l^3, \qquad \text{viscous} \propto \mu U l. \tag{1.1}$$

Their units here are [kg m/s$^2$]. The forces are estimates and valid in the sense that changes in the magnitudes of any of the physical parameters $l$, $U$, $\rho$, $g$ and $\mu$ will affect them as indicated. Thus supposing that only one scale is changed, say the length scale is doubled, then the inertial force increases by $2^2$, the gravitational force by $2^3$ and the viscous force by 2. Hence their importance in comparison to each other changes fundamentally. [New77, p.2]

Such comparison leads directly onward to the definition of two very important nondimensional parameters, which are described below.

### 1.3.1. Nondimensional Parameters

Nondimensional parameters are dimensionless numbers and thus by definition independent of the units employed to measure their variables. Several such numbers are used to characterize fluid flows. Tying in with the introduced example, the ratio

$$\frac{\text{Inertial Force}}{\text{Viscous Force}} \equiv Re \propto \frac{\rho U^2 l^2}{\mu U l} = \frac{Ul}{\nu} \tag{1.2}$$

displays the definition of the Reynolds number, abbreviated with $Re$. Here the kinematic viscosity $\nu$ [m$^2$/s] for fresh water at 20°. Hence, in most situations of interest to naval architects and aerodynamicists, $Re$ will be a high number. Therefore viscous forces are actually small in the bulk of the fluid, nevertheless one has to be careful neglecting them totally. Prandtl developed the boundary-layer theory, confining the area where viscosity plays the dominant role to a very thin layer of fluid adjoin the rigid surfaces. It is there, where large gradients in the fluid velocity occur and where the viscous stresses consequently are large. Outside such boundary-layers the fluid can often be treated as inviscid. That leads to great mathematical simplifications (especially with the further assumption of incompressibility). [New77, p.6]

Now, the ratio of

$$\frac{\text{Inertial Force}}{\text{Gravitational Force}} \equiv (Fr)^2 \propto \frac{\rho U^2 l^2}{\rho g l^3} = \frac{U^2}{gl} \tag{1.3}$$

that directly yields the definition of the Froude number $Fr$ squared is formed. It is an important parameter in cases where gravity plays a significant role. That usually is the case with flows with a free surface. [KC08, p.292]

The third ratio is the one of gravitational to viscous forces. It can be composed from the two others as $Re/(Fr)^2 = \rho g l^2/(\mu U)$. The fact that here a third nondimensional ratio is not independent from the others, can also be seen by Buckingham's Pi theorem.

### 1.3.2. Buckingham's Pi Theorem

In 1914 Buckingham proposed that $n$ variables can always be combined to form exactly $(n-r)$ independent nondimensional variables, where $r$ is the rank of the dimensional matrix. In many cases $r$ equals the number of fundamental dimensions (but not in all cases, since the rank of the dimensional matrix can be less, if e.g. one row in the dimensional matrix can be displayed by a linear combination of the others). [KC08, p.285]

In the introduced problem $n = 5$ and $r = 3$, determining the number of independent nondimensional parameters to exactly two, $Re$ and $Fr$ squared for the chosen case.

### 1.3.3. Drag Force

Drag is defined as the force acting on a solid object in the direction of the relative fluid flow velocity. One distinguishes between different types of drag. [KC08, p.294], [New77, ch. 2 and p. 197] and [Wik11a]

- *viscous drag*
  - *frictional drag*, due to tangential shear stresses
  - viscous *form drag* or *pressure drag*, due to normal pressure stresses[1]
- *wave resistance*, work must be done to generate waves, the associate drag component is known as wave resistance, sometimes called wave drag
- *induced drag*, is arising in conjunction with lifting surfaces since the trailing vortex sheet increases in length at a rate proportional to the free stream velocity. The resulting increase in kinetic energy has to be supplied by the work done to overcome this so called induced drag force. (to be precise, lift results from circulation and without viscosity no circulation, but since one is able to compute the induced drag in the context of potential theory, it is left aside the viscous category)

Here it is assumed that the motion of the body is stationary and that compressibility effects can be neglected, which is generally valid as long as the Mach number (speed of flow / speed of sound in the medium) is smaller than 0.3:

---

[1] This definition is not unique since one can distinguish between two types of forces normal to boundaries: pressure stresses and viscous normal stresses. The latter results from viscosity and the change of the velocity normal to a boundary in the normal direction. See e.g. $F_i = \int_A (-p\delta_{ij} + \mu(\partial_i u_j + \partial_j u_i)) n_i dS$. It might be argued that this formally is not included in the above mentioned 'definition'. On the other hand a force acting normal to and on a surface ($\mathrm{kg\,m^{-1}s^{-2}}$) could also be regarded as a pressure, regardless of its origin. The question is arisen thinking of how a motorboot or a water ski can plane, while a conventional large ship will sink deeper when, velocity is increasing. The reason hides in the viscous forces normal (and not the tangential shear stress) to the vessel's surface, which has to be oriented at an sufficient angle to the waterplane area.

Simply determining for example the drag force of a full-scale ship from a small-size model is an invitational idea. Let $D$ be the drag of a ship hull moving with constant velocity $U$. The drag can be assumed to further depend on the ships characteristic length $l$, the water's density $\rho$ and kinematic viscosity $\nu$ as well as the gravitational acceleration $g$ (since ships generate waves that depend on $g$).

This six quantities sufficiently determine the problem, if dynamic similarity can be assumed. It implies that the flows are assumed to have geometric similarity of the boundaries (all characteristic lengths are proportional) and that the flows are kinematically similar (velocities at the same relative location are proportional). [KC08, p.281]

From Buckingham's Pi theorem the problem has $n = 6$ and $r = 3$, yielding three independent nondimensional ratios. Choosing them to be $\frac{D}{\frac{1}{2}\rho S U^2}$, $\frac{Ul}{\nu}$ and $\frac{U^2}{gl}$ one can write [New77, p.28]

$$\frac{D}{\frac{1}{2}\rho S U^2} = C_D(Re,\ Fr). \tag{1.4}$$

Here the area of the ships wetted surface $S$ is employed. This is not an extra dimensional quantity, since geometric similarity requires it to be proportional to $l^2$.

The drag coefficient $C_D$ is a function of the Reynolds and the Froude number. Aside from the practical difficulty testing small models at the full-scale Reynolds number, scaling $Re$ and $Fr$ simultaneously would require either a superfluid or a change of the volume forces [New77, p.5 and p.28]. Thus, to be able to predict a real-size model's drag from a small-size test, further assumptions are needed.

### Froude's Hypothesis

Here Froude's empirical hypothesis comes in. It assumes that the drag coefficient can be decomposed into two separate components, a frictional-drag coefficient depending on $Re$ only, and a residual-drag coefficient depending only on $Fr$:

$$C_D(Re,\ Fr) \cong C_F(Re) + C_R(Fr). \tag{1.5}$$

The frictional component can be related to a much simpler geometry without having to worry about a free surface, such as the flat-plate frictional-drag coefficient in an unbounded fluid. The literature provides detailed information about $C_F$. The semi-empirical Schönherr line for turbulent boundary-layers on a flat plate [New77, p.95], the laminar Blasius boundary-layer flow [Whi06, p.231] and the recommendations of the International Towing Tank Conference (ITTC) [ITT11] can be mentioned. Figure C.1 is included in the appendix, showing graphs of different recommendation of $C_F$. It is visible that the ITTC line from 1957 predicts higher $C_L$, especially at low $Re$, than the Schönherr line (identical to the ATTC line). This, in the author's point of view, is object to viscous form drag. See also figure C.2 (appendix C) that further illustrates the differences between the Schönherr line, the Blasius boundary-layer theory and experiments. Updated information about the validity of the still widely used 1957 ITTC recommendations are found in [ITT08, p.397]. Sometimes additional corrections are used. One, for example, is an addition due to a roughness allowance. But since this value could occur to be negative, it is preferred to speak from a correlation allowance instead [New77, p.32].

The residual-drag coefficient contains not only the wave resistance, but also the contribution from viscous form drag. That is acceptable since viscous form drag can in case of streamlined bodies assumed to be independent of $Re$ over the range where the boundary-layer is thin compared to the body dimensions, typically for $Re > 10^5$ [New77, p.19]. As it nether depends on $Fr$ it is looked at as being a part of the residual drag without violating Froude's hypothesis (but it also can (partly) be incorporated into the frictional-drag recommendations / corrections). Anyway, the dominant portion of the residual drag is, on all but the slowest ships, mainly caused by wave resistance rather than viscous pressure force [New77, p.29]. Writing Froude's hypothesis in the form $C_{D_{ship}} = C_{D_{model}} - C_{F_{model}} + C_{F_{ship}}$ emphasizes its utilization.

Waves can fairly accurately be described in the course of potential theory. In 1898 Michell published "the wave resistance of a ship" [Mic98], where a purely analytic formula is derived to predict the wave resistance of thin ships. Thin denotes that the beam is small compared to all other characteristical lengths of the problem. The longitudinal slope of a ship hull is not a simple mathematical expression, especially when used in a triple integral equation. Nevertheless a fairly large number of numerical computations of Michelle's integral have been carried out, both, for simple geometries, but also for practical ship geometries. [New77, p.281,282]

Figure **??** attached in the appendix shows a comparison of the wave resistance calculated by Michell's integral and the residual drag coefficient from model tests measurements. Such comparison is questionable since it depends on Froude's hypothesis and on how is dealt with the viscous form drag. But Michell's integral is performing very good where the wave resistance is high. The error there is usually less than that to be expected in experiments (due to scale effects from use of different model sizes) [Tuc98, p.373]. At low speeds, the theory appears to exaggerate the effects of interference, and unfortunately it is this range most ships will be used in. This commonly is explained by viscous effects suppressing the interference effects in a real fluid. Additionally it has to be mentioned that Michell's approximation of a small beam will brake down at low speeds (low $Fr$) since the wave length $\lambda \propto U^2$ can no longer be considered larger than the beam. [New77, p.282]

A study of the total drag coefficient of a fixed Wigley parabolic hull with 1.9m length, 238mm beam and 95mm draft is given by Tuck and Lazauskas [TL08]. It compares $C_D$

from experiments, CFD calculations and from Michell's integral combined with the 1957 ITTC line. And it concludes that CFD using plenty of computing time is not able to give more accurate results than Michell, both are roughly in a 10 % range from the experiments ($Fr > 0.2$).

### Unbounded Fluid

Unbounded denotes the case where no free surface is present and where the bodies characteristic length scales are much smaller than the distance to the nearest boundary or body. The situation becomes simpler since gravity and gravity waves drop out. That might not be obvious, but the role of gravity is to introduce a hydrostatic pressure and a hydrostatic buoyancy force on the body, which is additive to the hydrodynamic drag [New77, p.13].

Under the assumption of dynamic similarity holds $\frac{D}{\frac{1}{2}\rho U^2 S} = C_D(Re)$. It is remarkable that the transition to turbulence decreases the drag of bluff bodies, while it increases the drag of fine bodies [New77, p.20]. This phenomena becomes clear thinking of the two different types of viscous drag. If the boundary layer flow becomes turbulent, the resulting increase of momentum convection increases frictional drag. But in case of a sphere for example it also postpones separation. The latter diminishes the separated region behind the sphere and thus the form drag is dramatically reduced. [New77, p.18]

How separation is defined and when it occurs is topic in the next section 1.3.4. First complementing that on streamlined bodies frictional drag is generally dominant over viscous form drag. The opposite is the case for bluff bodies. In the extremes of a flat plate, aligned or respectively orthogonal to the flow, the pressure or respectively the frictional drag will vanish.

In case of streamlined bodies the drag coefficient diminishes with increasing Reynolds number. That is the case in both the laminar and turbulent regime, but in the transition region from a laminar to a turbulent boundary layer the drag will increase. When exactly such transition occurs can not precisely be predicted. It depends on numerous of parameters like, e.g. roughness and the turbulence intensity of the inflow. For an illustration, consider figure C.2 in the appendix.

Briefly mentioning d'Alembert's paradox that there will be no forces acting upon a body moving with constant translational velocity in an infinite, inviscid and irrotational fluid. Details can be found in chapter 2.3.3.

## 1.3.4. Separation

On bluff bodies it is often seen that the boundary-layer in the decelerating stream (usually on the backside) has a point of inflection and grows rapidly, see also figure 1.1. Under a large enough adverse pressure gradient (diminishing velocity) the flow next to the wall reverses direction and meets the forward flow. The fluid near the wall is transported into the mainstream and the size of the wake becomes much bigger. The separation point is defined as the boundary between forward and backward flow, where the normal shear stress on the surface of the body vanishes. [KC08, p.366]

If, or up to which point, the boundary-layer can withstand without undergoing separation largely depends on the geometry of the flow (body) and whether the boundary-layer is laminar or turbulent. The latter delays the boundary-layer separation, leading to the phenomena described above in the unbounded fluid section (1.3.3). Sharp edges and blunt bodies enforce a steep pressure gradient inevitably leading to quick separation. The gently decreasing shape of streamlined bodies in contrast leads to a weak adverse pressure gradient where the boundary layer remains attached. [KC08, p.367]

Concluding with that, also the ambient turbulence level and the surface roughness play an important role. A golf ball for example only flies that far due to its surface triggering an early transition to a turbulent boundary-layer.

### 1.3.5. Vortex Shedding and the Strouhal Number

A fixed cylinder in a constant flowing fluid (or vice versa) in direction perpendicular to its axis is a classically studied problem that contains several astonishing phenomena.

Figure 1.1 shows the varying behavior at different Reynolds number from creeping flow at very low $Re$ up to the turbulent boundary-layer case that illustrates the drag reducing phenomena discussed above. It might be counterintuitive that such a symmetric problem can have nonsymmetric solutions (in a laminar state). But, as can be seen from the von Kármán vortex street, that is not true, compare to the sketch of the $80 < Re < 200$ regime. Eddies break periodic- and antisymmetrically off from the two sides of the cylinder, resulting in an unsteady, sing-changing and periodic circulation around the cylinder. [KC08, p.370]

The circulation in combination with the incoming velocity field explains why an unsteady lift force acts at some frequency $f = \omega/(2\pi)$. The singing of electricity cables in the wind is an example, where this frequency can be observed in everyday life. There are even constructions that collapsed when the resulting lift force was close to their lateral natural frequency. In nondimensionalized form one can express the maximal lift force $L_{max}$ and $f$ in terms of a lift coefficient and the Strouhal number $Sr$:

$$\frac{L_{max}}{\frac{1}{2}\rho U^2 l} = C_L(Re) \qquad \text{and} \qquad Sr(Re) \equiv \frac{fl}{U} \tag{1.6}$$

Typical values for cylinders with $Re$ in the laminar regime are $C_L \approx 0.5$ and $St \approx 0.22$. [New77, p.38]

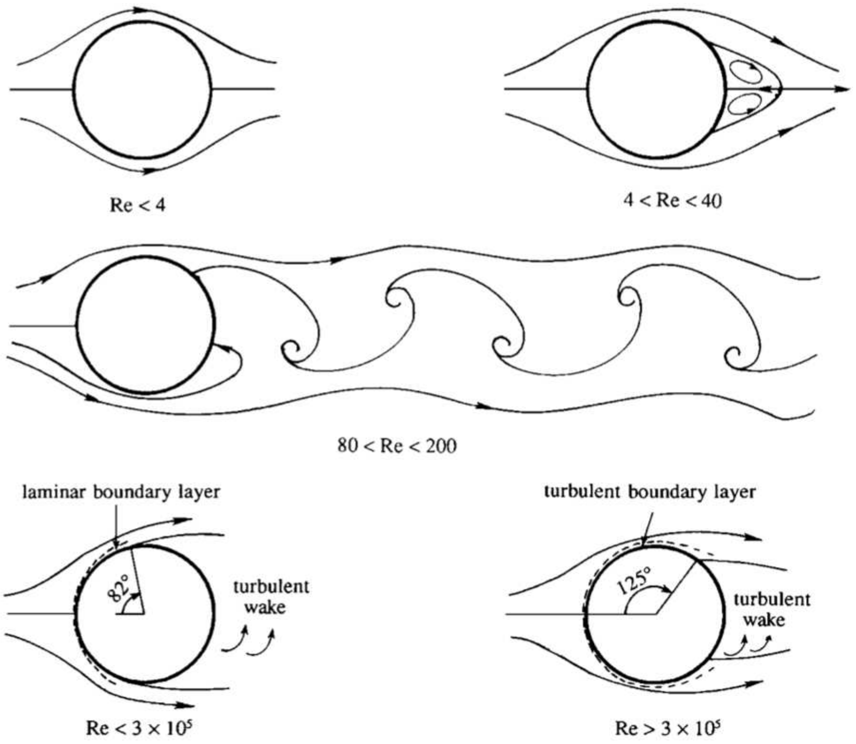

Figure 1.1.: Different regimes of flow over a circular cylinder; source [KC08, p.370]

### 1.3.6. Unsteady Motion

As seen in correlation with the Strouhal number, a body, moving at a constant velocity, can experience nonstationary forces. Considering the relative motion between a body and the fluid to be unsteady the resulting forces obviously will vary with time. To gain more insight into how, one can think about a cylinder and fluid in rest. Under the effect of a theoretically infinite acceleration, the cylinder is then suddenly given a certain velocity $U$ that is be kept constant thereafter. Prandtl carried out this experiment and in 1927 published a series of photographs that illustrate the described situation, see annex figure C.4. Formulating the dimensionless problem with the additional variable $t$ yields

$$\frac{-F}{\frac{1}{2}\rho U^2 l^2} = C_K(Re,\ Ut/l). \tag{1.7}$$

This dynamic drag force from the fluid on the body $F$ is assumed to predominantly act in the direction opposite to that of the body motion, thus the minus. The force coefficient $C_K$ is denoted with the index $K$ to distinguish it from $F$, which is used for friction. The time $t$ is nondimensionalized as $Ut/l$, which is the number of body lengths traveled in a time $t$. [New77, p.35]

In the extremes

$$C_K(Re,\ Ut/l) \cong C_D(Re) \qquad \text{if} \qquad Ut/l \gg 1 \tag{1.8}$$

$$C_K(Re,\ Ut/l) \cong C_K(\infty,\ Ut/l) \qquad \text{if} \qquad Ut/l \ll 1. \tag{1.9}$$

The case $Ut/l \gg 1$ approaches the steady state situation. In the complementary limit inertial effects dominant over the viscous stresses and the inviscid limit is approached. The flow remains attached at $Ut/l \ll 1$ (respectively at small $t$) as it is known from potential theory where $\nu \equiv 0$. Thus the force coefficient in (1.9) effectively is the result of accelerating the body in an ideal fluid where the force from the fluid on the body simply is proportional to the acceleration of the body. The coefficient of proportionality is the added mass, generally expressed as $m_{ij}$, in analogy to Newton's $F = ma$ equation. The subscripts denote the direction of the force and body motion, here (only one direction, no rotation)

$$F = -m_{11}\dot{U}. \tag{1.10}$$

In an unbounded fluid the added mass coefficients (in a body fixed frame of reference) depend only on the body geometry (and fluid density). It can be regarded as a mass of fluid that surrounds the body and must be accelerated with it. [New77, p.34-38 and p.140]

### 1.3.7. Lifting Surfaces

In case of lifting surfaces the drag $D$ is not the only force acting on objects moving at constant speed. There is also an other, often much larger, component contributing to the total force: the lift force $L$. It is defined as the force acting perpendicular to the oncoming velocity (regardless of the orientation in space, or the angle of attack $\alpha$, the object is placed at) and thus perpendicular to the drag, see figure 1.2. Lift results from circulation around an airfoil. The shape does not necessarily need to be the one shown in figure 1.2. Also a flat plate orientated at a nonzero $\alpha$ will give a lift. It is just that a sharp edge leads to separation, leading edge separation in this case, even the flow can reattach, the performance of a flat plate is thus inherently limited. That is not the case in an ideal fluid, where the lifting problem can be reduced to a plate (or in two dimensions a line) of zero thickness, the mean camber line. But as mentioned in 1.3.5, also cylinders can experience lift. Even ships equipped with rotating cylinders (Magnus effect) as sails have been build. (First in 1924, however nether sailing nor such rotor ships could compete against cheap diesel [Wik11c].)

It is assumed that the fluid is unbound, that $\alpha$ and $U$ are constant, as well as that the atmospheric pressure is high enough that cavitation[2] is precluded. The chord length is

---

[2] Cavitation occurs if the pressure is reduced below the vapor pressure of the fluid and the physical state

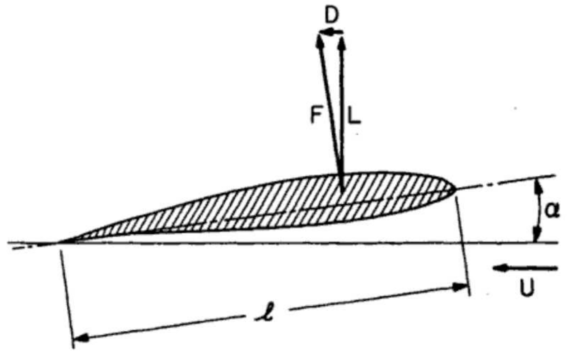

Figure 1.2.: Typical airfoil and the notation used; the angle of attack is generally defined with respect to the 'nose-tail line' between the center of minimum radius of the curvature of the leading edge and the sharp trailing edge; source [New77, p.21]

denoted by $l$. Employing again $S$, which here represents the planform area of the wing and is therefore denoted $S_p$. In the case of a planar hydrofoils, $S_p$ equals the projected surface in the direction of lift at $\alpha = 0$ [New77, p.21]. As geometric similarity is assumed, $S_p$ and $l$ contain the same information since $S \propto l^2$. Summing up, there are $D$ respectively $L$, $S_p$ respectively $l$, $\rho$, $\nu$, $U$ and $\alpha$ yielding three independent nondimensional parameters, writing

$$\frac{L}{\frac{1}{2}\rho S_p U^2} = C_L(Re,\ \alpha) \qquad \text{and} \qquad \frac{D}{\frac{1}{2}\rho S_p U^2} = C_D(Re,\ \alpha). \tag{1.11}$$

As can be seen from figure 1.3, $C_L$ is insensitive to $Re$ until separation occurs, thus one can write

$$C_L(Re,\ \alpha) \cong C_L(\alpha). \tag{1.12}$$

Separation results in tremendous loss of lift, the wing is referred to as stalling. When stall occurs has a major influence on the maximal achievable lift coefficient $C_{L_{max}}$. The latter is obviously dependend on $Re$ and on the boundary-layer (thickness, laminar, turbulent, laminar separation bubble; that is further discussed in chapter 6).

As it often is difficult to preserve $Re$ in model tests, one assumes that the drag coefficient $C_D$ can be decomposed. The drag of an airplane mainly results from induced drag, which is proportional to lift and thus to $\alpha$. The form drag is, as the body is streamlined, independent of $Re$ but will vary with $\alpha$. Frictional drag can be expressed as with help of a flat plate

---

of it abruptly changes to that of a gas [New77, p.4]. That for example can happen on the propeller of a ship. Material fatigue might arise when the cavitation bubbles implode since that generates a micro-jet of the surrounding fluid.

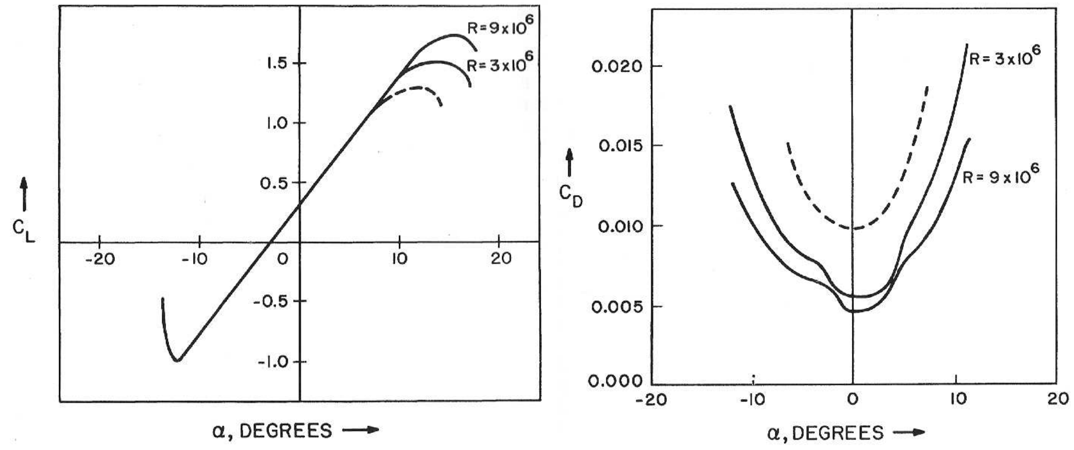

(a) Lift coefficient

(b) Drag coefficient

Figure 1.3.: Lift and drag coefficient of a NACA 63-412 section. The dashed line represents an airfoil with artificial roughness near the leading edge at $Re = 6 \times 10^6$; source [New77, p.22,23]

drag coefficient depending on $Re$ only. Thus, including induced and pressure drag into $C_P$ one can write

$$C_D(Re,\ \alpha) \cong C_F(Re) + C_P(\alpha). \tag{1.13}$$

## 1.4. Sport of Kayaking

There are two Olympic kayak/canoe disciplines – slalom and flatwater racing. Only the latter is discussed. In a kayak, paddlers are seated within the deck, with their legs extended anteriorly, and use a double-bladed paddle to propel the kayak through the water with maximal effort. A canoe, by contrast, is an open boat propelled by one or more paddlers from a kneeling position, using single-bladed paddles. [MSR09, p.167]

This work solely focuses on flatwater sprint kayaking as it is standard at the Olympics, where athletes compete over 200 and 1000 meter.[3] Marathon races exist as well, but are not guided by the same regulations. Furthermore, in this thesis only one athlete kayaking is taken into consideration, commonly referred to as K1 (K=kayak, 1=one person).

The next section briefly touches upon enhancing potentials in the sport of kayaking. Then the motion of the kayak is analyzed with help of sensor data that directly is used describing the motion of the kayak hull. Literature results and own conclusions about the complex propulsion of kayaks are discussed in section 1.4.4. The introduction chapter

---

[3] From 2012 on, the former 500 meter distance is replaced by 200 meters for men. Women will now race over 200 and 500 meters. [Wik11b]

concludes with a short remark on the kayak-rudder, and why it is chosen to be the further object of interest in this master's thesis.

### 1.4.1. Enhancing-Potentials in Kayaking

The ultimate criterion of a kayaker's performance is the time taken to complete the race distance. Aiming to optimize the performance, the sport of kayaking offers a wide field of applications for (fluid) mechanics. First, there is the kayak itself, with its form, trim, surface, seat and seating position. Then, there is the (wing) paddle-blade that undergoes a complex motion. And finally, there is the rudder that supports the stability of the vessels motion and is used to enforce directional adjustments, which become necessary in order to correct for e.g. currents, nonsymmetric propulsion, wind and waves. It of course is also used to perform e.g. turning maneuvers, but the race path is, if considered ideal, a straight line. All equipment is build for kayakers that themselves differ in size, weight and technique. In addition, there are many dependencies, meaning that a change in any of these parameters (and one could identify many more) affects the others.

All of that yields many possibilities for an enhancement of a kayakers performance. But an optimization is a complex process especially since a change in one parameter affects others, and a detailed modeling of the whole interconnected entity is currently far from possible. Nevertheless, and certainly with a good portion of intuition, many improvements have been made throughout the years.

In any case, it is important to not only know physical restrictions but also the ones imposed on the sport by formal obligations. These are given by the official regulations of the International Canoe Federation. The most relevant rules for this discussion are:

- Boats may have one rudder. The rudder has to be placed under the hull of the boat.
- No part of the boat (including the seat and the footrest) may have moving parts which can be used to help propel the boat in a way which would give competitors an unfair advantage (existing moving seat systems already in use are accepted).
- The canoe [N.B. not the kayak!] must be built symmetrically upon the axis of its length.

to be found in the regulations of 2011 [Int11].

### 1.4.2. Motion of a Kayak

Paddling from the start to the finish line took the winner of the 1000 meter K1 Olympics in 2004 exactly 3.25.95 minutes, corresponding to an average velocity of 4.86 m/s, or

17.48 km/h respectively. In a study on five elite kayakers from New Zealand, the averaged velocities ranged from 4.63 to 5.38 m/s [KS92, p.233].

To gain better inside into the instantaneous motion of the kayak, it is auxiliary to first define the coordinate system and the terms used throughout this work. Figure 1.4 shows the conventions adopted from Newman [New77]. It includes a vessel, e.g. a kayak, with its six degrees of freedom. The translational motions defined parallel to $(x, y, z) \equiv (x_1, x_2, x_3)$ are surge, heave and sway. The rotational motions about the same axes are roll, yaw and pitch.

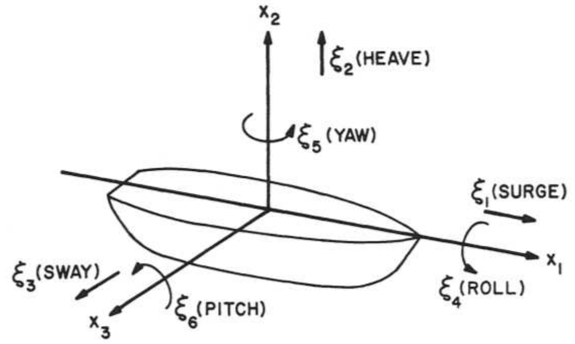

Figure 1.4.: Definition sketch of the six degrees of freedom of the body motion; source [New77, p.286]

Measurement data provided by a former Olympic champion is analyzed to gather basic information about the motion of a kayak. It is presented in figure 1.5. The measurements are taken with help of acceleration- and rate-sensors mounted in front of the paddlers seat, thus near the center of mass of the kayak-paddler-entity.

Note that the coordinate system of the outlined signals is fixed to the hull. In order to compute the respective accelerations for a room fixed coordinate system the knowledge of the rotation convention is required. That can for example be the sequence roll, pitch, yaw, but already pitch, yaw, roll leads to other results. The convention used for the available measurement data is unknown to the author, but that is not of further concern as the angles are small and as the most interesting modes here are the rotational ones.

The sway acceleration (in the sense of an average of half a period) in a room fixed coordinate system can certainly be expected being extremely small since the added mass and the drag coefficient in this direction (orthogonal to the direction of travel) are much large than in surge. The sway acceleration, here in the hull fixed coordinate system, shows the same behavior as the rolling motion, and one therefore can conclude that the sensor is mounted a considerable distance away from the roll axis. Also the yaw motion can directly influence the sway acceleration. But its amplitude is small and the distance between the

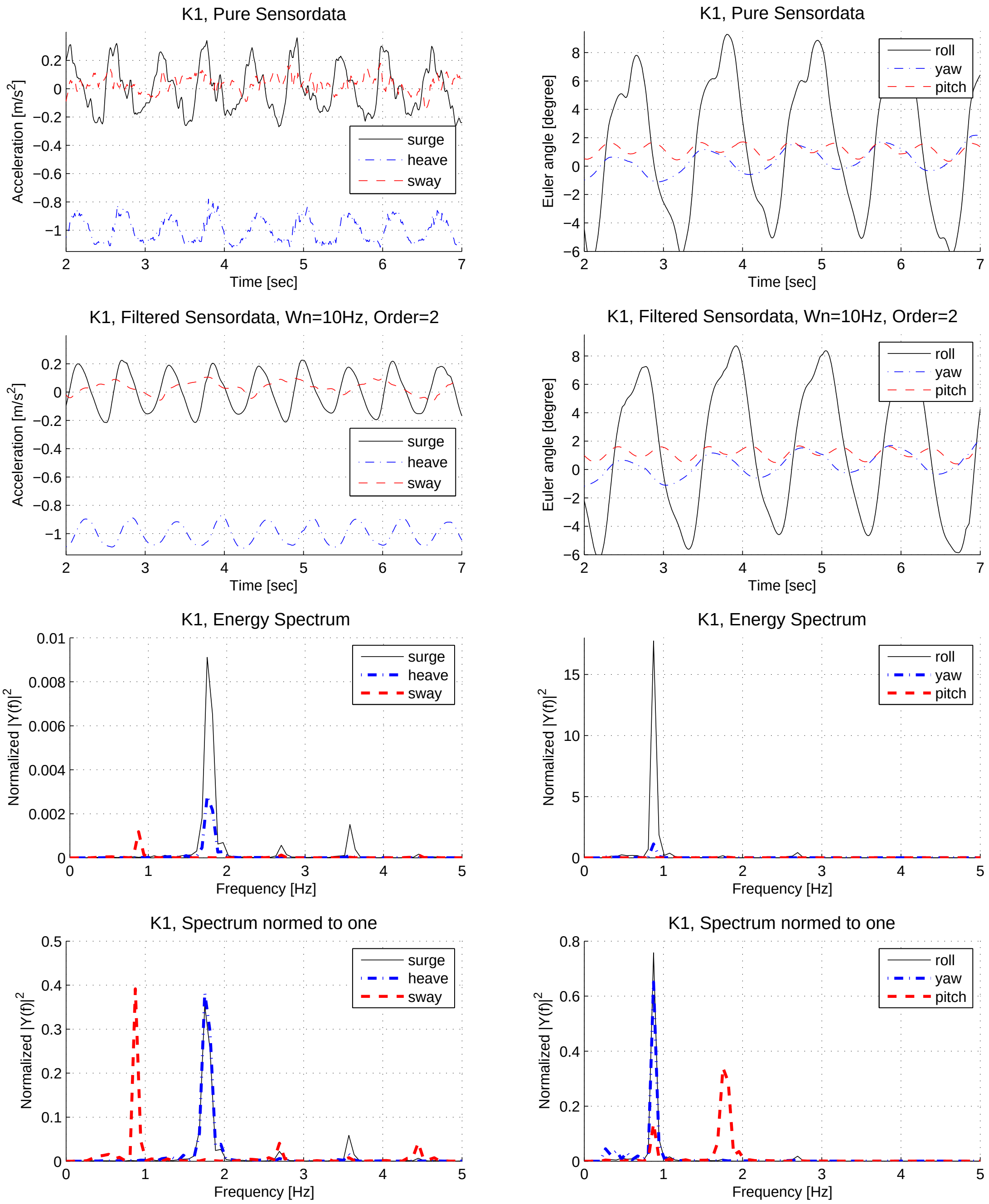

Figure 1.5.: Sensor measurements on a K1 kayak

sensor and the yaw axis cannot be very large for the chosen mount-point.

Essential for further considerations are which frequencies are dominating. That is analyzed best in the frequency domain. The spectra plots are achieved from a discrete Fourier transform, using the fast Fourier transform algorithm (FFT). The sampling rate and length of the time series limits the quality of such analysis. For this available case (100 Hz, 15 seconds) has to be mentioned, that a slight and avoidable error is present. That is because the data is not completely continuously sampled and interpolation becomes necessary.

There are two different spectra given. The classical energy spectra shows the spectral energy density, while the second one per definition does not show an ordinary spectra. It is normed to one, simply, to show the behavior of the modes that are vanishing small in comparison to surge and roll. Alternatively also a logarithmic plot could have been shown. It has to be mentioned that the first three values are manually set to zero since the yaw signal has a considerable drift (the kayaker paddled a curve), which is not of interest here. Two frequencies are dominant. That is 0.88 Hz for the roll, yaw and sway motion oscillating with the frequency of one whole paddling cycle. And the second for pitch, surge and heave is 1.76 Hz, which logically is the double frequency resulting from the two paddling strokes per cycle. (These modes are not to confuse with the low and high frequency limits that can be considered in case of a double body approximation concerning the behavior of damping and added mass in potential theory.)

The spectral energy density of roll and yaw is nearly exclusively confined to 0.88Hz. And even the roll signal does not look like a single sinusoidal function it can by a fairly good approximation be modeled as one. Note the different behavior at positive roll angles compared to the smoother one at negative angles. Of particular interest are the equivalent amplitudes of the different modes. The most scientific way of determining them is to require the artificial signals variance to equal the one of the original signals. That is however not appropriate here since little data is available and the signals (especially yaw) drift. Thus, from a conventional averaging in the time domain one finds the following amplitudes: roll 6.8°, yaw 0.9° and pitch 0.4°.

### 1.4.3. Kayak Hull

The surge acceleration measured in the moving coordinate system is very little affected by the rotations. This is the case because linearly (at small Euler angles) only pitch and yaw can influence surge, and both are small. Thus the velocity fluctuations in surge can precisely be calculated by simply using the given surge acceleration data. Most of the spectral energy is confined to one frequency and it is thus appropriate to conduct an approximation in the from of a single sinus function. Using an amplitude of 0.2 m/s$^2$ for the surge acceleration (compare figure 1.5) combined with the frequency of $f = 1.76$ Hz yields, under a sinusoidal assumption, $0.2/(2\pi f) = 0.02$ m/s maximal fluctuation velocity and under a totally exaggerated square wave assumption $0.2/(2f) = 0.11$ m/s maximal fluctuation velocity. Compared to an average of 4.86 m/s that are 0.4 % and respectively 2.3 %. From Jackson et al. is found:

> Measurements have shown that the the hull speed fluctuation is about 5 % of the mean, so it is both accurate and convenient to assume that both the hull speed and its total drag force are steady [JLB92, p.1197].

Since the conducted approximations indicate even smaller values, assuming the surge velocity as steady is in many cases a reasonable approximation.

In order to describe the effects of the hull fluctuation, one can consider the timescale $Ut/l$. Here only the contribution found from the surge acceleration is considered (rotations are not explicitly taken into consideration). Since the fluctuations are small the author assumes that the velocity scale appropriate to use is the average free stream velocity. For the time scale one can argue that half a period is appropriate since that is the duration of acceleration (that then is followed from a deceleration). The length scale is the kayak length (5.2 m). Then $Ut/l = 4.86/(2f5.2) = 0.5 < 1$. Therefore, the viscous forces can be assumed to be only partly influenced by this fluctuation. Or in other words the dominant contribution regarding the effects of the fluctuation results from inviscid sources (added mass and waves). There exists an widely used engineering approach to a related problem. In order to determin the wave forces on fixed or even moving bodies the Morrison equation simply assumes that it is a sum of the inertial and the viscous force, see [New77, ff.39].

Anyhow, of essential interest here is a (stationary) drag caused by the hull. And that mainly consists of wave and frictional as well as some form drag. As outlined in section 1.3.3 it can be calculated from a Michells equation (wave drag) and then for example be combined with the ITTC line to represent viscous drag. The kayak has a length of 5.2 m and assuming it to be evenly filled with 100 kg, it has a wetted surface of 1.7 $\mathrm{m}^2$. The Froude number is 0.68 and the Reynolds number $2.5 \cdot 10^7$. Thus, with help of the two diagrams in the appendix (figures C.3 and C.1) one approximately gets

$$C_D = C_R + C_F = 0.0027 + 0.0025 = 0.0052 \tag{1.14}$$

$$D = 1/2\, \rho U^2 S C_D = 104 \text{ N}. \tag{1.15}$$

The power needed to overcome this drag force equals 507 Watt ($U = 4.86$ m/s). Considering that further losses caused by propulsion come on top for the paddler, this value is slightly high (88 kg paddler), but not unreasonable since such impressing values are e.g. known from elite cyclists. Nevertheless this only is a rough estimate since it contains many approximations. In [JLB92, p.1197] a K1 kayak with a displacement of 0.093 $m^3$ ($\approx$ 81 kg paddler) is referred to have a total drag of 87 N and therefore 16 % less. Note that this data is from 1992 and that the form of the kayaks changed in between, also because a beam restriction was dropped in 2000. For this case it does however not matter since this rough estimate does not take into account the details of the form.

The form has an influence on the wave drag and on the (small) pressure drag also known as form drag. Check out the freely available software Michlet [Cyb10] that calculates the drag of hulls with the help of Michell's integral for wave resistance and incorporates several options. Frictional drag can be taken from the 1957 ITTC line or from Grigson's algorithm (a planar friction algorithm) and also an additional form factor can be applied (the ITTC line already incorporates some corrections to also take account for some sort of viscous form drag). In comparison to turbulence modeling such computation demands nearly no computational time and allows to optimize the form of the kayak.

The article [MSR09] provides an up-to-date review of previous literature (research related to the sport of flatwater kayaking). It mentions that in rowing the rotational modes, especially yaw and roll, are found to increase the intermittently wetted surface area and thus the hydrodynamic drag. And further:

> Interestingly, however, unwanted movement of the kayak, specifically yaw, pitch and roll, and their effects on mean kayak velocity have been overlooked in the literature [MSR09, p.174].

The increase of the wetted surface area due to a yaw and roll motion is a curious argument. It can be of concern for the roll motion, while it seems unlikely to the author that it has a considerable effect due to the yaw motion.

Thinking of a yaw oscillation (and partly also a roll) it is obvious that waves will be generated and they have the potential to considerably contribute to the energy transferred to the water!

The rotational motions lead to a change in the velocity field relative to the kayak hull, and they thus affect the drag force. Even though the velocity component induced from the rotational motion might be zero in the intended direction of travel, they are a sink of the energy provided by the paddler since (some) viscous forces are present. (A comparison to the ratio $Ut/l$ applied above might relativize this contribution.)

In addition, the author assumes that the resulting velocity field from rotational motions has an other consequence: Consider a roll motion with a roll axis (metacenter height) above the water plane. The induced velocity then results in an induced angel of attack increasing with the draft of the hull. And thus a lift force evolves (total velocity) and additional drag is created!

### 1.4.4. Propulsion, the Paddle-Blade

An mathematically based optimization of the paddle is extremely difficult. Not at least because of the complex three-dimensional and variable motion (differing and adaptable techniques), but also due to its form (wing paddle-blades) and, of course, due to the nonstationary process. There is little research available. Something that partly relates to confidentiality interests, but also to the extremely high hurdles for scientifically based improvement (scientifically here is to be interpreted as standing in contrast to trial and error field-work). Considerably more publications exist on rowing- than on kayak-paddles. That can, besides prestige reasons, also be related to the fact that a kayak-paddle undergoes a more complex motion than a rowing-blade (degrees of freedom).

From the author's point of view the most promising article (accessed) in the field of kayak paddle-blades is from Jackson et al. [JLB92]. It combines mathematical expressions of the paddling efficiency with (nonstationary) laboratory experiments. The latter yields efficiency factors at different angles of attack, depending on stroke lengths (and if conducted of different blades). Since the experimental trajectory is straight, the varying angle caused by the motion of catching, pulling and exiting is not accounted for.

Wing-paddle-blades started their triumph around 1986, quickly replacing the conventional drag-paddle-blades from competitive racing [JLB92, p.1197]. They use a combination of lift and drag to power the boat. Figure 1.6 shows the forces, velocities and angles on a cross section of such a wing-paddle-blade. The blade-velocity relative to the water is denoted with $V_B$ and its drag with $D$. The paddler has to generate the power $P$ to overcome the drag of the ship $D_H$ travelling at hull speed $V_H$ and the work done by moving the blade relative to the water. Thus

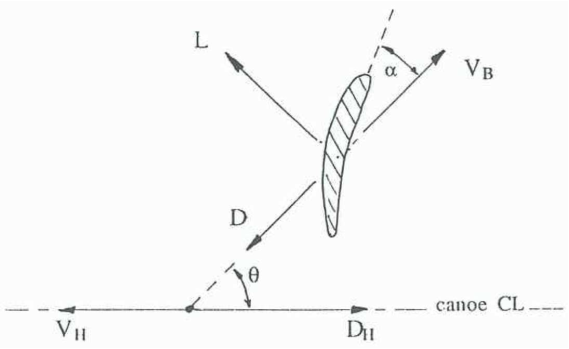

Figure 1.6.: Wing paddle blade with forces, velocities and angles; source [JLB92, p.1197]

$$P = D_H V_H + \frac{1}{T}\int_0^{\Delta} D V_B \, dt. \tag{1.16}$$

Here, $\Delta$ is the time for which the blade is immersed, and $T$ is the total stroke time.

Regarding the propulsion, the last term is unnecessarily lost energy (due to the slip of the paddle through the water). This phenomena is known as the inherent inefficiency in the generation of thrust. It becomes clear thinking of an ideal situation where a paddler would have the possibility to push off from some solid piles above the water. Here the relative velocity to the 'water' would be zero and the last term nonexistent. One can formulate an efficiency factor $\eta$ that relates $P = D_H V_H / \eta$.

With regard to the propulsion the author assumes that *three factors* are of high importance when considering the finally achievable performance of the paddler: The *first* one is the efficiency factor earlier outlined in its most primitive form. Due to the blade work a vortex must arise in the water and in [JLB92] its size is related to the efficiency of the propulsion. Jackson et al. comes to the conclusion that the vortex area in case of the conventional drag-blade-blade is smaller, and that the wing-paddle-blade therefore is inherently more efficient. The consequence is that an *increase in stroke rate* and *vortex area* can be expected to increase the propulsion efficiency. Very interesting is also their experimental result that is shown in figure 1.7. The peak, resulting from the initial acceleration, and the lift (first delayed and thereafter disproportionally increasing to the drag) clearly indicate effects of the nonstationary process. In case of the wing-paddle-blade the thrust is build up from drag and lift (geometrically) while for the classical-drag-paddle-blade that is only the drag of the paddle. Thus, the drag of the wing-paddle can be smaller than the one of the drag-paddle, while both provide the same thrust. The average drag of the blade times its distance moved is the mechanical energy lost to the inefficiency of propulsion. Consequentely the inherit advantage of the wing-paddle-blade.

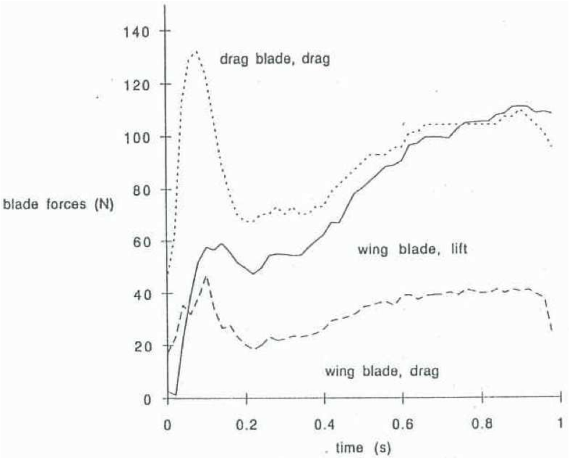

Figure 1.7.: Nonstationary force measurements on a wing- and a conventional drag-paddle-blade; source [JLB92, p.1200]

Getting to the *second* factor, obviously the kayaker's aim is to put as much of his/her energy into forward motion. Thus, regardless if using wing- or conventional paddle-blades, the force (thrust) applied by the paddler to the paddle has to be directed as good as possible into the intended direction of travel. This does not imply that also the paddle has to move in the (opposite) direction of the kayak's intended trajectory. In fact, that would biomechanically be extremely inefficient and, as the hull becomes wider from the bow towards the paddler, also impossible. For both types of blades applies that they catch the water as close to the kayak as possible, and there is good reasons for it. The moment that inevitably is transferred to the kayak leads to an unwanted yaw and roll motion which becomes bigger the larger the distance of the paddle-force to the yaw and roll axis of the kayak. Regarding yaw it is clear that larger amplitudes of the yaw angle will lead to a longer trajectory to the finish line. And, supposably more important, yaw motion contributes to a loss of energy because waves are generated by such oscillation. This is the *second* point. Here, the wing-paddle-blade actually might perform worse than its ancestor since it has a larger normal velocity component and will thus be further away from the yaw axis than the conventional paddle.

But the presumably most important parameter, and therefore also the *third* factor regarding the propulsion, is found outside fluid mechanics: the biomechanical aspects. It is the question which trajectory does fit best to the muscular capacity of the paddler. Obviously many classical parameters enter here as well, that are for example the stroke length and frequency.

There are of course several further important other parameters to optimize like for example the complex process of entering into and exiting out of the water. All water sprayed is a waste of energy. Also the stiffness and the side-to-side wandering (flutter) of the paddle under the strokes is important. And last but not least the weight of the paddle as well as the forces of the air that act on the not submerged paddle play a role.

Articles discussing the optimal blade size can be found and a reasonable hypothesis is for example the following:

> Although not yet documented for kayaking, it is expected that excessive energy will be lost during the main body of the race if the drag force created on the paddle blade during each stroke is not matched with the muscle force–velocity characteristics of the individual [SMM$^+$06, p.147].

However, the study uses an ergometer and does not intend to optimize the paddle itself apart from its size and assumes the path as given. But it discusses a comparison of different skill-levels of paddlers, which shows that the elite ones are able to direct more of their effort in each stroke in the intended direction of travel (>80 %) [SMM$^+$06, p.152]. Further studies on paddling ergometers equipped with senors and camera-tracking systems like [PIG06] and [SRS+02] also state that the best athletes have the smoothest and most symmetric trajectories.

> In kayakists the presence and magnitude of side-to-side asymmetries inversely correlate with performance level [SRS+02].

A wing-paddle-blade will naturally have a more transverse motion than a classical drag blade. Note that also a drag-blade might be used at an angle of attack (different from 90°) or be asymmetric and develops some lift. See for example [SSBH03, p.16] where stationary experiments on different paddle-blades are conducted. The lift coefficients of all blades turns out to be nearly independent of the paddle-blade and it is linear in the studied range (in terms of airfoil theory 70° to 110° angle of attack!). Slight differences are found for the drag coefficients that here naturally decrease eventhough lift is increasing. Eventhough the Norwegian paddle-blade used within this study is described as highly asymmetric and spoon shaped, it remains an uncertainty exactly how it is shaped and how the zero angle of attack is defined. From the author investigated wing-paddles-blades do not have the classical airfoil shape. That is obvious since their usage and purpose is very different from the one of classical airfoils. The upper surface reminds of a wing, while one could say that the lower one basically equals the upper one.

Tying in with the drag of the kayak hull, as argued for in chapter 6.1.1, a fluctuating sway velocity contributes to an increase of the averaged drag. That indicates that an increase in stroke frequency not only has a higher propulsion efficiency, but also a positive contribution to the averaged drag of the kayak.

### 1.4.5. The Kayak Rudder

Rudders are devices, which due to an angle of attack $\alpha$ with respect to the oncoming fluid develop large lift forces $L$. Normally the lift coefficient is linear near $\alpha = 0$, that is $C_L(\alpha) = \frac{\partial C_L}{\partial \alpha}\Big|_{\alpha=0} \alpha$ and the hydrodynamic characteristics of a vessel depend strongly on the rudder, even if $\alpha = 0°$. [TH03, p.20,21]

The kayak-rudder basically is an airfoil where the mean camber is zero, that is, it is symmetric to its planform area. The kayak-rudder contributes to the stability of the kayak. It helps preventing roll and yaw motion and thus decreases the energy loss to for example waves. But the rudder also experiences drag that slows the vessel down. Hence an optimized rudder can enhances the kayakers performance.

Looking at the timescale $Ut/l = 4.86/(2f0.071) = 39 \gg 1$ it is apparent that, for this small body, the viscous forces have enough time to adapt during the oscillating motion.

The rudder is chosen to be the focus of this thesis. That has different reasons, which are now briefly mentioned. The laboratory of the Mechanics Division of the University of Oslo only is equipped for an investigation of the paddle or the rudder flow phenomena since the vessels themselves are too big for the (wave) water tank of the laboratory. The comparison to smaller models, apart from their availability, underlies the crucial assumption of Froude's hypothesis. From the computational point of view, the Reynolds number limits the accuracy achievable within a given computing time. That one could say is a result of the direct growth in size of the geometry and, on the other hand, of the smallest scales in turbulence that decrease as $Re$ grows. They thus demand for finer meshes if the boundary layer is to be resolved. The kayak hull lies on a factor 73 above the (chordlength based) rudder. And a very important point, a simulation of the kayak hull, if not disregarded, incorporates a free surface where waves are generated and that is a further very challenging aspect for simulations. Also the simulation of the paddle-blade is in all points more likely to fail than that of the rudder (The blade has a complex geometry, is shedding large vortices and in order to appropriate model it also the complex motion should be accounted for.). In addition the geometry files are accessible for the rudder while for the paddle the author would have to relay on laserscan images. Lift and drag forces on airfoils (like the rudder and rather not like the paddle-blade) can analytically be described and therefore offer a great possibility for a master's thesis. Consequently the focus in this thesis is put on the rudder flow phenomena.

# 2. Theory Part I: Fundamentals and Analytic Methods

This chapter briefly mentions the notation used throughout the thesis. Fundamentals of fluid mechanics are compactly summarized in section 2.2. The three remaining sections are used to derive the two analytic methods used. That is the slender body theory (section 2.4) and the lifting line theory (section 2.5). Both make use of section 2.3 that contains considerations regarding ideal fluid flow.

## 2.1. Notation

The Notation used throughout this master-thesis is a slightly extended index notation. Meaning that e.g. the velocity vector $\mathbf{u} = \vec{i}u + \vec{j}v + \vec{k}w$ is written like $u_i$ where $i$ is a *free index*, that, in 3 dimensional space, takes the values 1, 2 and 3. A second order tensor, like the linear stress tensor $\mathcal{P}$, writes $P_{ij}$.

Is an index (inside a product or a tensor) repeated then Einstein's summation convention applies. Such an index is called *dummy* or *summation index*. In many cases it is also an advantage to additionally use the abbreviation $\partial_i = \frac{\partial}{\partial x_i}$, with $x$ being a spatial variable. Slightly inconsistent it is also made use of the abbreviation $\partial_t = \frac{\partial}{\partial t}$ for the time derivative. Thus e.g. the Laplacian $\nabla^2 = \nabla \cdot \nabla$ can be written as $\partial_i \partial_i = \partial_1 \partial_1 + \partial_2 \partial_2 + \partial_3 \partial_3$. In terms of potential theory the expression $n_j \partial_j \phi$ is abbreviated as $\frac{\partial \phi}{\partial n}$. For surface integrals the general expression $\iint\limits_S n_i dS$ is cut short to $\int\limits_S dS_i$.

In the second theory chapter (chapter 3) a further notational convention is introduced (see equation (3.3)). It is auxiliary in terms of the statistical description involved in turbulence theory and does not effect the rest of this work.

## 2.2. Fundamentals of Fluid Mechanics

Fluid flow surrounding anything from humans, obstacles, vehicles, birds to fishes can very precisely be described by the *Navier-Stokes* equations. These are first introduced in equation (2.15) and (2.18), respectively, but prior the underlying fundamentals are briefly discussed.

Fluid mechanics is based on the *continuum hypothesis*. That says that matter is continuously distributed throughout the space occupied by the matter. Regardless of how small volume elements the matter is subdivided into, every element will contain matter [Irg08, p.2]. This macroscopic point of view is valid, if the size of the flow system (characterized e.g. by the size of the body around which flow is taking place) is much larger than the mean free path of the molecules [KC08, p.5]. Consult the keyword Knudsen number for more information.

Basic conservation[1] laws for *mass, momentum* and *energy* can be formulated in a direct form, respectively given in terms of a material volume integration [Ber10], the latter means the volume always encloses the same matter while it is deforming and moving,

$$\frac{d}{dt}\int\limits_{V_M} \rho dV = 0 \tag{2.1}$$

$$\frac{d}{dt}\int\limits_{V_M} \rho u_i dV = \int\limits_{S_M} dS_j P_{ij} + \int\limits_{V_M} \rho g_i dV \tag{2.2}$$

$$\frac{d}{dt}\int\limits_{V_M} \rho\left(e+\frac{1}{2}u_i^2\right) dV = \frac{d}{dt}\int\limits_{S_M} dS_j P_{ij} u_i + \int\limits_{V_M} \rho g_i u_i dV + \int\limits_{S_M} k\partial_i T dS_i. \tag{2.3}$$

The domain of integration is thus a function of time with $V_M(t)$ standing for the material volume and $S_M(t)$ for its surface $S$ (sometimes $A$ for area is found in literature). For the momentum balance equations *Newton's second law* has been applied in a continuum sense (Euler's axioms). And for the energy balance equation the *first law of thermodynamics* is used. Further variables are density $\rho(x_i, t)$, internal energy per unit mass $e(x_i, t)$ and the temperature field $T(x_i, t)$. The thermal conductivity $k$ whose units are J s$^{-1}$m$^{-1}$K$^{-1}$ is assumed constant. It emerges from *Fourier's law* of head conduction with the heat flux vector $-k\partial_i T$ describing the heat transport – it's units are J s$^{-1}$m$^{-2}$. As the representative for volume forces, sometimes also referred to as body forces, the gravity vector $g_i$ (force per unit mass) is used. Force per unit volume hence writes $\rho g_i$.

The general *Leibniz-Reynolds transport theorem* that relates the Eulerian (field description) and the Lagrangian (particle description) point of view, writes

$$\frac{d}{dt}\int\limits_{V_G} \rho\Psi dV = \int\limits_{V_G} \partial_t\left(\rho\Psi\right) dV + \int\limits_{S_G} \rho\Psi u_{i_B} dS_i \tag{2.4}$$

---

[1] Instead of the expression *conservation laws* the expression *balance laws* may sound more reasonable for the momentum and energy equations, nevertheless the expression conservation law is used for all of them.

with $u_{i_B}(x_i, t)$ being the velocity of the boundary. Now using it in a material volume sense ($u_{i_B} = u_i$) with the physical variable $\Psi = 1,\ u_i$ and $e + 1/2$ respectively. In these arising equations are then inserted the corresponding equations (2.1), (2.2) and (2.3), yielding the fundamental[2] integral formulations of the conservation laws [Ber10]:

$$\int\limits_{V_M} \partial_t \rho dV + \int\limits_{S_M} \rho u_i dS_i = 0 \tag{2.5}$$

$$\int\limits_{V_M} \partial_t \left(\rho u_i\right) dV \int\limits_{S_M} \rho u_i u_j dS_j = \int\limits_{S_M} P_{ij} dS_j + \int\limits_{V_M} \rho g_i dV \tag{2.6}$$

$$\begin{aligned} \int\limits_{V_M} \partial_t \left(\rho \left(e + \frac{1}{2} u_i^2\right)\right) dV + \int\limits_{S_M} \rho \left(e + \frac{1}{2} u_i^2\right) u_i dS_i = \\ + \int\limits_{S_M} \left(P_{ij} u_j\right) dS_i + \int\limits_{V_M} \rho g_i u_i dV + \int\limits_{S_M} k \partial_i T dS_i. \end{aligned} \tag{2.7}$$

Now using *Gauß's theorem*, also known as the *divergence theorem*,

$$\int\limits_{V} \partial_i \Psi dV = \int\limits_{S} \Psi dS_i \tag{2.8}$$

to convert the surface integrals into volume integrals. That leads to the differential forms of the conservation equations:

$$\partial_t \rho + \partial_i \left(\rho u_i\right) = 0 \tag{2.9}$$

$$\partial_t \left(\rho u_i\right) + \partial_j \left(\rho u_j u_i\right)) = \partial_j P_{ij} + \rho g_i \tag{2.10}$$

$$\partial_t \left(\rho \left(e + \frac{1}{2} u_i^2\right)\right) + \partial_i \left(\rho u_i \left(e + \frac{1}{2} u_i^2\right)\right) = \partial_i \left(P_{ij} u_j\right) + \rho g_i u_i + \partial_i \left(k \partial_i T\right). \tag{2.11}$$

Their validity requires that the integral forms previously given are valid for arbitrary subvolumes and that respectively the (field) variables are sufficiently differentiable [Ber10]. The conservation of mass (2.9) is considered most fundamental of all conservation laws and is commonly refereed to as the (here general) continuity equation.

In the search of a constitutive equation for the stress tensor $P_{ij}$, *Newton's law of fluid friction* is used. It states that the shear stress is a linear function of the velocity gradient, like e.g. $\mu \frac{du}{dy}$ or general $P_{ij} = -p\delta_{ij} + T_{ijkl} S_{kl}$, where $S_{kl}$ is the symmetrical part of the gradient of the velocity field relating to pure deformation. The gradient of the velocity field is commonly decomposed into a symmetric and an antisymmetric tensor:

$$\partial_j u_i = 1/2(\partial_j u_i + \partial_i u_j) + 1/2(\partial_j u_i - \partial_i u_j) = S_{ij} + \Omega_{ij} \tag{2.12}$$

---

[2] The integral forms are considered more fundamental than the differential forms (2.9) to (2.11), since their validity demands further requirements to be fulfilled.

where $\Omega_{ij}$ represents pure rotation, containing the same information as the vorticity $\omega_i$ since

$$\omega_i = -\varepsilon_{ijk}\Omega_{jk} = \nabla \times \mathbf{u} \tag{2.13}$$

with $\varepsilon_{ijk}$ being the cyclic permutation tensor [Pop00, p.24].

Using the most general form of an isotropic fourth order tensor for $T_{ijkl}$ leads to the *constitutive equation of a linearly viscous fluid*, the latter is known as a *Newtonian fluid*,

$$P_{ij} = -p\delta_{ij} + \mu 2S_{ij} + \left(\kappa - \frac{2}{3}\mu\right) S_{kk}\delta_{ij} \tag{2.14}$$

where $\mu$ and $\kappa$ are the Lamé-constants for viscous fluids. Both are functions of temperature. The *dynamic viscosity* $\mu$ represents deformation without change in volume and the *bulk viscosity* $\kappa$ stands for pure expansion [Gje02, p.50]. Equation (2.14) is sometimes referred to as the *Cauchy-Poisson law* and the abbreviation $\lambda = \kappa - \frac{2}{3}\mu$ can be found in some literature [Irg08, p.325]. And $S_{kk}$ is another form of writing $\partial_k u_k$.

Now, from inserting the linear stress tensor $P_{ij}$ (equation (2.14)) into the momentum balance equation (2.10) one obtains the general *Navier-Stokes* equations for compressible flows

$$\partial_t u_i + u_j \partial_j u_i = -\frac{1}{\rho}\partial_i p + \frac{\mu}{\rho}\partial_j\partial_j u_i + \frac{1}{\rho}\left(\kappa + \frac{1}{3}\mu\right)\partial_i\partial_j u_j + g_i \tag{2.15}$$

where $\mu$ and $\kappa$ are assumed constant. Note that this calculation includes an expansion of the left hand side of the momentum balance equation (2.10) by the chain rule and the use of the general continuity equation (2.9). The left hand side in (2.15) can be interpreted as the acceleration of a material particle of fluid, since the *substantial derivative*

$$\frac{D}{Dt} \equiv \partial_t + u_j \partial_j \tag{2.16}$$

expresses the time rate-of-change in a coordinate system moving with the fluid particle [New77, p.60].

The assumption of *incompressibility* $\frac{d\rho(x_i,t)}{dt} = 0$ is introduced here and compressible flows will not be further discussed in the course of this work. Significant simplifications arise: The general mass conservation equation (2.9) becomes the incompressible continuity equation

$$\partial_i u_i = 0 \tag{2.17}$$

and thereby the general *Navier-Stokes* equations (2.15) reduces to the incompressible *Navier-Stokes* equations

$$\partial_t u_i + u_j \partial_j u_i = -\frac{1}{\rho}\partial_i p + \nu \partial_j \partial_j u_i + g_i \tag{2.18}$$

where the *kinematic viscosity* $\nu = \frac{\mu}{\rho}$ is introduced. It's units are $\mathrm{m}^2\ \mathrm{s}^{-1}$.

## 2.3. Ideal Fluid Flow

An ideal fluid flow assumes the fluid to have zero viscosity. The effect of viscosity plays an important role in the regions close to boundaries. Outside such regions the flow analysis can often be simplified by assuming inviscid fluid flow. It was Ludwig Prandtl who introduced the boundary-layer approximation (first in a paper in 1904) distinguishing between the two regions [And05].

The higher the Reynolds number $Re \equiv UL/\nu$, the thinner becomes the boundary-layer. But as the consequence of viscous shear stress, regardless of how thin a boundary-layer is, the fluid velocity on a rigid body must be equal to the velocity of the boundary. This kinematic boundary condition is the no-slip condition.

In an inviscid consideration there are no shear stresses acting within the fluid. Thus there are no restrictions on the tangential velocities. Since the fluid cannot flow through the boundary, solely the fluid velocity component normal to boundaries (right on a rigid body) has to equal the normal boundary velocity (zero if the body is in rest). Such a kinematic boundary condition is often referred to as a free-slip condition.

As the Navier-Stokes equations are already introduced ((2.18)), setting the viscosity to zero yields the momentum equations for inviscid fluid flow, known as *Euler's* equations

$$\partial_t u_i + u_j \partial_j u_i = -\frac{1}{\rho}\partial_i p + \frac{1}{\rho}F_i^v . \tag{2.19}$$

Here the volume forces (force per unit volume) are generally expressed as $F_i^v$. Confining to a conservative[3] gravity field and describing for example the earths gravity force with $F_i^v = \rho g_i = -\rho \partial_i (gy)$, where $g \cong 9.81 \mathrm{m/s}^2$ allows to write Euler's equations as

$$\partial_t u_i + u_j \partial_j u_i = -\frac{1}{\rho}\partial_i \left(p + \rho g y\right) . \tag{2.20}$$

In the simplest case of a hydrostatic equilibrium, $p + \rho g y$ is a constant, since $u$ is zero (or constant). [New77, p.103]

### 2.3.1. Irrotational Flow and the Velocity Potential

Assuming the flow to be irrotational allows the use of potential theory where many powerful computations can be done analytically. For this purpose the underlying framework is listed compactly.

The *circulation* $\mathit{\Gamma}$ is defined as the integrated tangential velocity around any closed

---

[3] A vector field, say $F_i$, is said to be conservative if it has the property that the line integral of $F_i$ around any closed curve $C$ is zero $\oint_C F_i dx_i = 0$ [Mat98, p.28].

contour $C$ in the fluid [KC08, p.63],

$$\Gamma \equiv \oint\limits_C u_i dx_i. \tag{2.21}$$

Lord *Kelvin's circulation theorem* from 1868 states that:

> In an inviscid, barotropic flow with conservative body forces, the circulation around a closed curve moving with the fluid remains constant with time, if the motion is observed from a nonrotating frame.
>
> – Kundu and Cohen [KC08, p.144]

Barotropic means that the density is a function of pressure only. The proof can be found in several textbooks, e.g. [New77, p.103]. Accordingly $\frac{d\Gamma}{dt} = 0$, thus $\Gamma$ has to be a constant. Assuming that the fluid motion started from an initial state of rest sets $\Gamma = 0$ for all time and all material contours within the fluid [New77, p.104].

Stokes theorem for a continuous differentiable vector writes [Mas70, p.23]:

$$\int\limits_S (\nabla \times \mathbf{u}) \cdot d\mathbf{S} = \oint\limits_C \mathbf{u} \cdot d\mathbf{x} \qquad \text{or} \qquad \int\limits_S \varepsilon_{ijk} \partial_j u_k dS_i = \oint\limits_C u_i dx_i \tag{2.22}$$

where the surface integral is taken over any surface $S$ bounded by the contour $C$. The line integral is the definition of circulation (2.21), which from Kelvin's theorem must equal zero (if started from rest) for any material contour lying within the fluid. Hence also the surface integral must equal zero. This can be true only if the integrand is zero. That is the motion of the fluid is *irrotational* [New77, p.105]

$$\nabla \times \mathbf{u} = 0 \qquad \text{or} \qquad \varepsilon_{ijk} \partial_j u_k = 0 \tag{2.23}$$

since the vorticity equals zero throughout an irrotational vector field [Mat98, p.60]. Vorticity is defined as the curl of the velocity (l.h.s. of (2.23)). Noting that the condition of zero viscosity alone is not sufficient to conclude a flow to be irrotational.

Since an irrotational vector can be represented as the gradient of a scalar, irrotational flow is the cornerstone to make use of potential theory. In general this is a result of Helmholtz' theorem in vector analysis, here simply considering the definite integral

$$\phi(x_i, t) = \int\limits_{x_{i0}}^{x_i} u_i dx_i. \tag{2.24}$$

It is independent of the particular path of integration, since the difference between two differing paths between the same two points equals the circulation. And in irrotational flows the circulation around any material contour[4] is zero. Thus the velocity field can be expressed in terms of a scalar variable, say $\phi$,

$$u_i = \partial_i \phi, \tag{2.25}$$

where $\phi(x_i, t)$ is named velocity potential. [New77, p.106]

Backwards it is directly visible that a flow has to be irrotational, if the velocity field is given in terms of a potential, since the curl of a gradient is always zero $\nabla \times \nabla f = \varepsilon_{ijk}\partial_j \partial_k f = 0$.

A useful condition is to require the potential to be Laplacian. It combines the constrains of the primarily introduced assumption of incompressibility (2.17) and the assumption of irrotational flow into one expression:

$$\nabla \cdot \nabla \phi = \nabla^2 \phi = \partial_i \partial_i \phi = 0 \tag{2.26}$$

### 2.3.2. Bernoulli's Equation

Integrating Euler's equations (2.20) leads to an explicit equation for the pressure known as the Bernoulli equation. There are primarily two different cases of the Bernoulli integral found. First, the case of steady but possibly rotational flow, and second the case of irrotational but possibly unsteady flow. In any case the assumption of an inviscid and barotropic[5] fluid is obligatory.

From vector algebra the advective acceleration can be expressed as [KC08, p.118]:

$$\mathbf{u} \cdot \nabla \mathbf{u} = \frac{1}{2} \nabla \mathbf{u}^2 - \mathbf{u} \times \boldsymbol{\omega} \qquad \text{or} \qquad u_j \partial_j u_i = \frac{1}{2} \partial_i u_j u_j - \varepsilon_{ijk} u_j \omega_k. \tag{2.27}$$

Using this equivalency in Euler's equations (2.20) yields

$$\frac{\partial \mathbf{u}}{\partial t} + \nabla \underbrace{\left( \frac{1}{2} \mathbf{u}^2 + \frac{p}{\rho} + gy \right)}_{B} = \mathbf{u} \times \boldsymbol{\omega} \quad \text{or} \quad \partial_t u_i + \partial_i \underbrace{\left( \frac{1}{2} u_j u_j + \frac{p}{\rho} + gy \right)}_{B} = \varepsilon_{ijk} u_j \omega_k. \tag{2.28}$$

In the stationary case the time derivative is zero and the left hand side of (2.28) is a vector normal to the surface $B =$ constant, whereas the right hand side is a vector perpendicular to both $u_i$ and $\omega_i$, thus ([KC08, p.119])

$$p + \frac{1}{2} \rho u_i u_i + \rho g y = \text{constant along stream and vortex lines.} \tag{2.29}$$

---

[4] Also in inviscid flows vortices can be shed, e.g. the starting vortex in the theory of lifting surfaces that is imposed by the Kutta condition. The circulation including the lifting surface and a starting vortex still remains zero. See Newman [New77, p.163]. It is also useful to consider the difference between a rotational and an irrotational vortex, e.g. [KC08, p.139]. The latter is singular at the origin ($u_\theta = \Gamma/(2\pi r),\ u_r = 0$).

[5] Barotropic means that $\rho$ is a function of $p$ only and that implies $\frac{1}{\rho}\partial_i p = \partial_i \int \frac{dp}{\rho}$ where $\frac{dp}{\rho}$ is a perfect differential, and therefore the integral does not depend on the path of integration [KC08, p.118]

If the flow in addition is irrotational, the Bernoulli equation (2.29) is constant everywhere in the fluid.

In the irrotational unsteady case $\omega_i = 0$ and the velocity potential comes into operation. Equation (2.28) simplifies to

$$\nabla \left( \frac{\partial \phi}{\partial t} + \frac{1}{2} \frac{\partial \phi}{\partial \mathbf{x}} \cdot \frac{\partial \phi}{\partial \mathbf{x}} + \frac{p}{\rho} + gy \right) = 0 \quad \text{or} \quad \partial_i \left( \partial_t \phi + \frac{1}{2} \partial_j \phi \, \partial_j \phi + \frac{p}{\rho} + gy \right) = 0. \tag{2.30}$$

Integrating with respect to the three space variable $x_i$ gives

$$\frac{\partial \phi}{\partial t} + \frac{1}{2} \frac{\partial \phi}{\partial \mathbf{x}} \cdot \frac{\partial \phi}{\partial \mathbf{x}} + \frac{p}{\rho} + gy = C(t) \qquad \text{or} \qquad \partial_t \phi + \frac{1}{2} \partial_j \phi \, \partial_j \phi + \frac{p}{\rho} + gy = C(t). \tag{2.31}$$

Since $C(t)$ is a function of time only, it can be included in the potential without changing the velocity field. Thus $C(t)$ may be chosen arbitrarily and can be set equal to zero or to some desired value such as e.g. the atmospheric pressure. [New77, p.108]

The dynamic pressure can thus be written as

$$p - \rho g y = -\rho \left( \partial_t \phi + \frac{1}{2} \partial_j \phi \, \partial_j \phi \right) + (C(t)). \tag{2.32}$$

### 2.3.3. Hydrodynamic Pressure Force

To analytically find the specific velocity field induced by the motion of a body moving with velocity $U_i$, is the target of many theories in the field of fluid mechanics. Once known, the object of interest, the force and moment vectors from the fluid on the body (respectively vice versa) become accessible. In general the force on a body is $F_i = - \int\limits_{S_B} P_{ij} \, n_j \; dS$. Here in the case of an ideal fluid flow the stress tensor $P_{ij}$ reduces to the pressure and thus

$$F_i = \int\limits_{S_B} p \, n_i \; dS. \tag{2.33}$$

Following the convention that positive $n_i$ point out of the fluid volume makes $F_i$ the force acting from the fluid on the body. Substituting Bernoulli's equation for the dynamic pressure (2.32) yields the hydro*dynamic* pressure force

$$F_i = -\rho \int\limits_{S_B} \left( \partial_t \phi + \frac{1}{2} \partial_j \phi \, \partial_j \phi \right) n_i \; dS \tag{2.34}$$

#### Alternate Form

Now seeking an alternate form. One can, with the help of Gauß's theorem (2.8) convert surface integrals to volume integrals. Here the volume $\Upsilon(t)$ shell be bounded by the surfaces $S_B + S_C$ that are considered to form a closed surface. Figure 2.1 sketches the scenario.

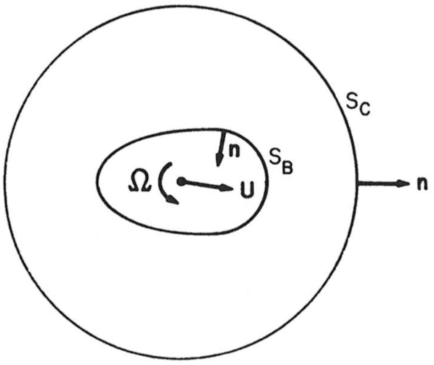

Figure 2.1.: Sketch of the control surface and the moving body; source: [New77, p.132]

Expressing the rate of change of fluid momentum $\rho \frac{d}{dt} \int\limits_{\Upsilon} \partial_i \phi \; d\Upsilon$ with the help of Leibniz-Reynolds transport theorem (2.4), using Gauß's theorem to form only surface integrals and assuming $S_C$ to be fixed ($u_{i_B} = 0$ on $S_C$) yields

$$\rho \frac{d}{dt} \int\limits_{S_B+S_C} \phi n_i \; dS = \rho \int\limits_{S_B} \left( \partial_t \phi n_i + \partial_i \phi U_j n_j \right) \; dS + \rho \int\limits_{S_C} \partial_t \phi n_i \; dS \tag{2.35}$$

Using the boundary condition on the body $\frac{\partial \phi}{\partial n} = n_i U_i$ (kinematic, free-slip) and keeping in mind that $S_C$ is fixed and the time derivative can in case of $S_C$ be taken into the integrand. Thus the surface integrals may be equated separately over $S_C$ and $S_B$ [New77, p.132,133]

$$\rho \frac{d}{dt} \int\limits_{S_B} \phi n_i \; dS = \rho \int\limits_{S_B} \left( \partial_t \phi n_i + \frac{\partial \phi}{\partial n} \partial_i \phi \right) \; dS. \tag{2.36}$$

Adding equations (2.36) and (2.34) and rearranging terms yields $F_i$ in an alternate form

$$F_i = -\rho \frac{d}{dt} \int\limits_{S_B} \phi n_i \; dS + \rho \int\limits_{S_B} \left( \frac{\partial \phi}{\partial n} \partial_i \phi - \frac{1}{2} \partial_j \phi \partial_j \, \phi n_i \right) \; dS. \tag{2.37}$$

By analyzing the last term in (2.37) one can, with the help of Gauß's theorem and the Laplacian (2.26) requirement, show that

$$\rho \int\limits_{S_B+S_C} \left( \frac{\partial \phi}{\partial n} \partial_i \phi - \frac{1}{2} \partial_j \phi \partial_j \, \phi n_i \right) \; dS = 0. \tag{2.38}$$

Thus (2.37) can equally be displayed in a form involving $S_C$ [New77, p.134]

$$F_i = -\rho \frac{d}{dt} \int\limits_{S_B} \phi n_i \; dS + \rho \int\limits_{S_C} \left( \frac{\partial \phi}{\partial n} \partial_i \phi - \frac{1}{2} \partial_j \phi \partial_j \, \phi n_i \right) \; dS. \tag{2.39}$$

In the same manner holds for the moment [New77, p.134]

$$M_i = \int\limits_{S_B} p \left( \varepsilon_{ijk} r_j \, n_k \right) \; dS \tag{2.40}$$

where $r_i$ is a vector originating from fixed coordinates. The alternate expression becomes

$$M_i = -\rho \frac{d}{dt} \int\limits_{S_B} \phi \left( \varepsilon_{ijk} r_j \, n_k \right) \, dS + \rho \int\limits_{S_C} \varepsilon_{ijk} r_j \left( \frac{\partial \phi}{\partial n} \partial_k \phi - \frac{1}{2} \partial_j \phi \partial_j \, \phi n_k \right) \, dS. \tag{2.41}$$

### Unbounded Fluid

Is the fluid unbounded, $S_C$ can be evaluated at infinitely large distance from the body. Considering a spherical radi $r$, the last integrals in (2.39) and (2.41) will be of order $r^{-4}$ and $r^{-3}$ respectively. And as $r$ tends to infinity these integrals will vanish, simplifying force and moment to [New77, p 135]

$$F_i = -\rho \frac{d}{dt} \int\limits_{S_B} \phi n_i \, dS \tag{2.42}$$

$$M_i = -\rho \frac{d}{dt} \int\limits_{S_B} \phi \left( \varepsilon_{ijk} r_j \, n_k \right) \, dS. \tag{2.43}$$

In the special case of steady translation, the integral in (2.42) is independent of time and d'Alembert's paradox becomes directly visible. That states that there act no hydrodynamic forces on a body moving with a steady translational velocity in an infinite, inviscid and irrotational fluid. However, this is not the case for the moment since $r_i$ will depend on time. [New77, p.136]

In the case of lifting surfaces, potential theory can be helped along with e.g. the Kutta condition. It enforces the rear stagnation point to remain at the trailing edge of the airfoil and thus a circulation around the airfoil is induced and consequently a lift force is present. Thus potential theory can be used to describe lift that in a linear analysis equals circulation times density times free stream velocity.

Now let's consider the general case where the body is allowed to freely and unsteadily move within its six degrees of freedom. The motion consists of the translational velocity $U_i(t)$ and the angular velocity $\Omega_i(t)$. The latter is defined with respect to an origin moving with the body. Hence the body boundary condition becomes

$$\frac{\partial \phi}{\partial n} = U_j n_j + \Omega_j \varepsilon_{jkl} r'_k n_l \tag{2.44}$$

where $r'_i$ is the radius vector from the center of rotation. The resulting equations simplify using an indices notation where $U_i$ is indexed from 1 to 6 as $U_i = (U_1, U_2, U_3, \Omega_1, \Omega_2, \Omega_3)$. Thus in this section $i$ will explicitly be used as the index running from 1 to 6, while other indices run from 1 to 3. The boundary condition (2.44) suggests a linear decomposition of $\phi$. Expressing the total potential as the sum

$$\phi = U_i \phi_i \tag{2.45}$$

enables to write the boundary condition as

$$\frac{\partial \phi_i}{\partial n} = n_i \qquad \text{for } i = 1, 2, 3 \tag{2.46}$$

$$\frac{\partial \phi_i}{\partial n} = \left(\varepsilon_{ijk} r'_j n_k\right) \qquad \text{for } i = 4, 5, 6 \text{ while } j \text{ and } k = 1, 2, 3. \tag{2.47}$$

The complete boundary value problem further contains $\nabla^2 \phi_i = 0$ throughout the fluid domain and $\phi_i = \mathcal{O}(r^{-2})$ as $r \to \infty$. [New77, p.137]

Due to the linear decomposition the six potentials $\phi_i$ depend, when expressed in body fixed coordinates ($'$), only on the body geometry (via the boundary conditions (2.46) and (2.47)), but neither on time nor on the velocities $U_i$. Inserting (2.45) into (2.42) writes

$$F_j = -\rho \frac{d}{dt} U_i(t) \int\limits_{S_B} \phi_i(x'_1, x'_2, x'_3) n_j \; dS. \tag{2.48}$$

But due to the body rotation the integral nevertheless depends on time since

$$\frac{dn_j}{dt} = \varepsilon_{jkl} \Omega_k n_l \tag{2.49}$$

where $\Omega_j(t)$ is the rotational velocity vector of the body fixed coordinates. Applying the total derivative in (2.48) gives

$$F_j = -\rho \dot{U}_i \int\limits_{S_B} \phi_i n_j \; dS - \rho \varepsilon_{jkl} U_i \Omega_k \int\limits_{S_B} \phi_i n_l \; dS \tag{2.50}$$

where the accelerations $dU_i/dt = \dot{U}_i$. [New77, p.137]

The corresponding result for the moment is derived with help of a decomposition of the position vector $r_j = r^0_j(t) + r'_j$. Here $r^0_j$ is the vector from the origin of the fixed reference system to the point $r'_j = 0$ which moves with the body. Thus $dr_0/dt = U_j$ while $d(\varepsilon_{jkl} r'_k n_l)/dt = \varepsilon_{jkl} \Omega_k \varepsilon_{lmn} r'_m n_n$ (or for better readability $d(\mathbf{r}' \times \mathbf{n})/dt = \mathbf{\Omega} \times (\mathbf{r}' \times \mathbf{n})$). It can be noted that the need to discriminate between the two coordinate systems can be avoided by assuming that they coincide at the particular instant of time under consideration that is setting $r^0_j = 0$. But prior the total time derivative has to be evaluated, yielding

$$M_j = -\rho \dot{U}_i \int\limits_{S_B} \phi_i \varepsilon_{jkl} r'_k n_l \; dS - \rho \varepsilon_{jkl} U_i \Omega_k \int\limits_{S_B} \phi_i \varepsilon_{lmn} r'_m n_n \; dS - \rho \varepsilon_{jkl} U_i U_k \int\limits_{S_B} \phi_i n_l \; dS. \tag{2.51}$$

Where $r^0_j = 0$ has been used to eliminate one term. [New77, p 138]

Force and moment depend on the body shape and the potentials $\phi_i$ only in terms of the integrals shown in (2.50) and (2.51). With help of the boundary conditions these integrals can be expressed as

$$\int\limits_{S_B} \phi_i n_j \, dS = \int\limits_{S_B} \phi_i \frac{\partial \phi_j}{\partial n} \, dS \tag{2.52}$$

$$\int\limits_{S_B} \phi_i \varepsilon_{jkl} r'_k n_l \, dS = \int\limits_{S_B} \phi_i \frac{\partial \phi_{j+3}}{\partial n} \, dS \tag{2.53}$$

suggesting the definition of the *added-mass* tensor

$$m_{ji} = \rho \iint\limits_{S_B} \phi_i \frac{\partial \phi_j}{\partial n} dS \tag{2.54}$$

where the notation only here exceptionally also allows $j$ to run from 1 to 6. The index $i$ stands for the direction of the body motion and $j$ for the direction of the force respectively moment. Anyhow the added mass tensor is symmetrical, $m_{ij} = m_{ji}$. The expression for force and moment simplify by using (2.52-2.54)

$$F_j = -\dot{U}_i m_{ji} - \varepsilon_{jkl} U_i \Omega_k m_{li} \tag{2.55}$$

$$M_j = -\dot{U}_i m_{j+3,i} - \varepsilon_{jkl} U_i \Omega_k m_{l+3,i} - \varepsilon_{jkl} U_i U_k m_{li}. \tag{2.56}$$

In analogy to Newton's second law, the added-mass can be regarded as a mass of fluid that surrounds the body and must be accelerated with it. That is to be understood as an average value, as particles at different places will be accelerated with varying degree. Unlike in Newton's $F_j = ma_j$, it is generally such that the added-mass coefficients can differ depending on the sign of the direction of the body motion and that the direction of the hydrodynamic force does not necessarily coincide with the direction of the acceleration. [New77, p.141]

Neglecting the rotational effects, the force (2.55) simply writes

$$F_j = -\dot{U}_i m_{ji}, \tag{2.57}$$

as it is mentioned in the introduction chapter 1.3.6. Summing up, the underlying assumptions are that the fluid is ideal (in particular inviscid, incompressible and irrotational), that the body is rigid and of constant volume (its motions are defined by three translation and three rotational velocity components) and that the fluid is unbounded and of infinite extent. Then the added-mass coefficients depend only on the body geometry; "they can be regarded as the most important hydrodynamic characteristics of the body, except in the case of steady translation where (2.55) predicts no force and the viscous drag is clearly more important" (d'Alembert's paradox). [New77, p.140]

## 2.4. Slender Body Theory

Many swimming and flying objects are slender in the sense that one length dimension exceeds the others by an order of magnitude. This is the case for most fishes, vessels or missiles. But also rudders or wings can obey such a slenderness condition if their span length is comparatively small. The hydrodynamic analysis simplifies greatly with such restriction.

In the following first the general problem is outlined. It gives rise to two separately treatable problems – one concerning the longitudinal and the other the lateral one. The fist one is of minor concern to the rest of the thesis and thus only briefly discussed (hints to the derive are found in the appendix). In contrast, the lateral force is of interest and outlined in more detail. The derivations in this section follow Newman [New77, ch.7,sec.1-3].

The lateral motion leads to a derivation of low-aspect-ratio-lifting-surface-theory where the lift coefficient is directly dependent on the aspect ratio. Thus, first defining that the aspect ratio $A$ is defined as the ratio of the span length $s$ to the mean chord length. However, it is more convenient to express $A$ in the form

$$A = \frac{s^2}{S_p} \tag{2.58}$$

where $S_p$ is the area of the planform, which is the projected area of the lifting surfaces on the plane $y = 0$ at zero angle of attack $\alpha = 0$ [New77, p.21,159]. A low aspect ratio lifting surface like e.g. a delta wing is thus necessarily more slender and usually more influenced by three-dimensionality than a high aspect ratio one, like e.g. on gliders.

### 2.4.1. Slender Body in an Unbounded Fluid

Restricting the body to be slender by requiring its maximum lateral dimension $d$ to be much smaller than its length $l$ yields the slenderness parameter $d/l = \epsilon$ that is supposed to be small.

Later in the analysis two coordinate systems become auxiliary, thus defining a space fixed one $(x_0, y_0, z_0)$ and an identically orientated but translational moving one $(x, y, z)$. The latter moves with the body's constant forward velocity $U$ in $x_0$-direction. The body itself may be assumed to further have a lateral motion. It is described by the body's displacement $\zeta(x, t)$ from the $x_0$-axis that is restricted to the $z_0$-direction. In case of a rigid body $\zeta$ will be constant or linear in $x$ while that is not the case for undulatory motions. In any way it is only assumed that $\zeta$ is small compared to the body length and that it is a slowly varying function of $x$. The latter excludes flexural modes[6] with a length scale of order $\epsilon l = d$.

---

[6] Flexural modes (bending vibration) here e.g. denotes an (oscillating) rotation in the plane normal to

Figure 2.2 shows the introduced definitions and sketches a typical slender body. Defining the moving coordinate system in terms of the transformations writes

$$x = x_0 - Ut, \qquad y = y_0 \qquad \text{and} \qquad z = z_0. \tag{2.59}$$

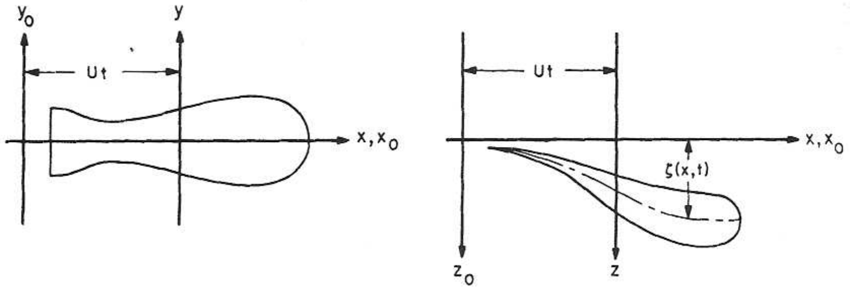

Figure 2.2.: Definition sketch of the slender body setup and coordinates; source: [New77, p.330]

The surface of the longitudinally elongated body is denoted by $S_B$. Planes of $x =$ constant define the cross-section profile $\sum_B(x)$ and the circumscribed area $S(x)$, which is the sectional area of the body. It is assumed that the body ends are such that both $S(x)$ and $S'(x) \equiv dS/dx$ vanish at the ends. (The body end's cross-section area converges slowly to zero, like e.g. for fins, but not for e.g. a cuboid like a box.)

Let the equation $F(x, y, z - \zeta(x, t)) = 0$ describe the body surface. Then the boundary condition on $S_B$ can be written as[7]

$$\frac{d}{dt} F(x_0 - Ut, y_0, z_0 - \zeta(x_0 - Ut, t)) = 0. \tag{2.60}$$

Evaluating the terms yields

$$\frac{\partial F}{\partial \underbrace{x_0 - Ut}_{x}} \left( \frac{dx_0}{dt} - U \right) + \frac{\partial F}{\partial \underbrace{y_0}_{y}} \frac{dy_0}{dt} \quad \dots$$

$$+ \frac{\partial F}{\partial \underbrace{z_0 - \zeta(x_0 - Ut, t)}_{\text{linear in } z_0 = z \text{ and } \zeta}} \left\{ \frac{dz_0}{dt} - \frac{\partial \zeta}{\partial \underbrace{x_0 - Ut}_{x}} \left( \frac{dx_0}{dt} - U \right) - \frac{\partial \zeta}{\partial t} \right\} = 0. \tag{2.61}$$

---

the $y$-axis that also may be caused from deformation.

[7] This derive differs slightly from Newman's way, where the definition of the substantial derivative (2.16) is applied in a more direct sense, writing $\frac{DF}{Dt} = 0$. The author, in this case where the variables are functions themselves, rather prefers to recall, that the definition of the substantial derivative stems from a total derivative, where $(u, v, w) \equiv \left(\frac{dx_0}{dt}, \frac{dx_0}{dt}, \frac{dz_0}{dt}\right)$.

The fluid velocity field (due to the presence of the body) is defined as $(u, v, w) \equiv \left(\frac{dx_0}{dt}, \frac{dy_0}{dt}, \frac{dz_0}{dt}\right)$. Further using the velocity potential $\phi(x_0, y_0, z_0, t)$ to represent the velocities ($u_i \equiv \partial_i \phi$) gives

$$\frac{\partial F}{\partial x}\left(\frac{\partial \phi}{\partial x_0} - U\right) + \frac{\partial F}{\partial y}\frac{\partial \phi}{\partial y_0} + \frac{\partial F}{\partial z}\left\{\frac{\partial \phi}{\partial z_0} - \frac{\partial \zeta}{\partial x}\left(\frac{\partial \phi}{\partial x_0} - U\right) - \frac{\partial \zeta}{\partial t}\right\} = 0. \qquad (2.62)$$

Since $\frac{\partial F}{\partial x_i}$ is a vector normal to $S_B$, dividing (2.62) by $\left|\frac{\partial F}{\partial x_i}\right|$ yields[8]

$$\frac{\partial \phi}{\partial n} = Un_x + \left\{\frac{\partial \zeta}{\partial x}\left(\frac{\partial \phi}{\partial x_0} - U\right) + \frac{\partial \zeta}{\partial t}\right\} n_z. \qquad (2.63)$$

Where $n_i$ is the unit normal vector pointing into the body. The effect of the body on the fluid velocity field will vanish at large distances away from the body, and so also the potential will vanish far away from the body (There exists no other velocity in the fluid than the one induced by the body's motion.)

$$\phi \to 0 \quad \text{as} \quad (x^2 + y^2 + z^2)^{1/2} \to \infty. \qquad (2.64)$$

The boundary value problem is completed by invoking Laplace's equation (see (2.26))

$$\frac{\partial^2 \phi}{\partial x_0^2} + \frac{\partial^2 \phi}{\partial y_0^2} + \frac{\partial^2 \phi}{\partial z_0^2} = 0 \qquad (2.65)$$

throughout the fluid domain.

Before making the slenderness approximation, it is auxiliary to note, that in (2.63) the term $Un_x$ is associated with the boundary condition for the longitudinal-flow problem and the term $\left\{\frac{\partial \zeta}{\partial x}\left(\frac{\partial \phi}{\partial x_0} - U\right) + \frac{\partial \zeta}{\partial t}\right\} n_z$ with the lateral motion. Since the lateral motion is assumed small, the problem can be linearized and the conditions can be treated separately. In particular, the longitudinal-flow problem will be imposed in a "stretched-straight" position ($\zeta = 0$).

Now, simplifying the boundary-value problem ((2.63), (2.64) and (2.65)) by requiring the body to be slender: As $\epsilon \to 0$ the unit normal vector $n_i$ will lie in planes with $x =$ constant, that is

$$n_x = \mathcal{O}(\epsilon), \qquad n_y = \mathcal{O}(1) \qquad \text{and} \qquad n_z = \mathcal{O}(1). \qquad (2.66)$$

From the viewpoint of an inner reference frame with fixed $d = \mathcal{O}(1)$, the body length $l = \mathcal{O}(1/\epsilon)$ will tend to infinity as $\epsilon \to 0$. Accordingly the fluid velocity field appears nearly constant in longitudinal direction ($\frac{\partial}{\partial x_0} = \mathcal{O}(\epsilon)$). Thus, in this inner region $\frac{\partial \phi}{\partial x_0} \ll \left(\frac{\partial \phi}{\partial y_0}, \frac{\partial \phi}{\partial z_0}\right)$. This argumentation holds also for the change in space of the velocities (second

---

[8] Since the coordinate transformation is translational and linear it does not matter if partial derivatives are expressed with respect to $\mathbf{x}$ or $\mathbf{x_0}$.

derivatives) thus Laplace's equation reduces to the two-dimensional form and $\phi$ can be replaced by a two-dimensional potential:

$$\frac{\partial^2\phi}{\partial y_0^2}+\frac{\partial^2\phi}{\partial z_0^2}=0 \qquad \text{with} \qquad \phi=\Phi(y_0,z_0;x_0). \tag{2.67}$$

The dependence on $x_0$ is included as a reminder that the potential will vary slowly along the body length. This variation is a result of a change in body geometry and lateral motion. As both $\epsilon$ and $\zeta$ are assumed small regarding $U=\mathcal{O}(1)$ holds

$$\frac{\partial\phi}{\partial x_0}\ll U. \tag{2.68}$$

As a consequence of (2.66) or respectively (2.67) $\frac{\partial\phi}{\partial n}$ can be approximated by the normal derivative in the $y-z$-plane. Denoting the two-dimensional unit vector normal to $\sum_B$ in the $y-z$-plane with $N_i$ and applying (2.68) and the right side of (2.67) the boundary condition on $\sum_B$ (2.63) simplifies to

$$\frac{\partial\Phi}{\partial N}=Un_x+\left\{\frac{\partial\zeta}{\partial t}-U\frac{\partial\zeta}{\partial x}\right\}n_z. \tag{2.69}$$

In view of (2.69) and the linearity of the boundary value problem it is reasonable to express the solution as the sum of two potentials, one due to the longitudinal ($\Phi_1$) and one due to lateral ($\Phi_3$) motion. The self suggesting choice of

$$\Phi=U\Phi_1+W\Phi_3 \qquad \text{with} \qquad W(x,t)=\frac{\partial\zeta}{\partial t}-U\frac{\partial\zeta}{\partial x} \tag{2.70}$$

yields by inserting in (2.69) the two boundary conditions on $\sum_B$

$$\frac{\partial\Phi_1}{\partial N}=n_x \qquad \text{and} \qquad \frac{\partial\Phi_3}{\partial N}=n_z. \tag{2.71}$$

Under the approximation (2.68), $W(x,t)=\frac{d\zeta}{dt}$ and so $W$ physically is the lateral velocity of a body section, as observed in a fixed frame of reference.

## 2.4.2. Longitudinal Motion

The longitudinal problem is of minor importance to this master's thesis. It therefore is not discussed in detail here, but rather briefly sketched.

Nevertheless, its derivation demands some effort and in appendix A the author provides two hints concerning the rather complex part of the computation.

Comparing the boundary conditions (2.71) of the two reveals that the longitudinal problem does not correspond to a two-dimensional rigid-body motion (all coordinates involved). It necessarily incorporates the dilation of the body, which is represented via source distributions. Their strength (streamlined body, thus source-like on the forebody and sink-like on the afterbody) is found when requiring that the outward flux caused by the longitudinal motion must equal the change of the sectional area of the body.

But its analysis requires the method of matched asymptotic expansions; That is the flow is described two-dimensional close to the body in an inner solution. This has to match an outer solution taking into account the three-dimensionality. The overlap region has to be far from the body in terms of the inner solution and close to the body in terms of the outer solution. The body is slender and thus that is given by $\epsilon l < r < l$.

The solutions can be matched and one arrives at an axisymmetric outer flow solution, while the inner solution (not in its outer region) is not necessarily axisymmetric and reflects the shape of the body geometry. But in the far field that is of no importance.

Illustrating it is noted that it can be deduce that the added mass of a slender body in the longitudinal direction is negligible compared with the body mass – as to be expected.

### 2.4.3. Lateral Force

As shown in chapter 2.3.3 the hydrodynamic pressure force can be expressed in an alternative form (2.39), involving a simpler integral on the body but an additional integral of the surrounding fluid. The latter can be expanded to infinity and often vanishes in the case of an unbounded fluid or double body approximations. Here, however, one is interested in sections of the body and has to consider the surfaces $S_0$ (denote $S_{0_1}$ and $S_{0_2}$). They are indicated in figure 2.3 where also the surface $S_\infty$ of differential thickness $dx_0$ infinitely far away from the body is shown. $\sum_B$ is the profile defined by the limit of $S_\infty$ as $dx_0 \to 0$. Applying (2.39) to this control surface as well as to the differential portion of the body

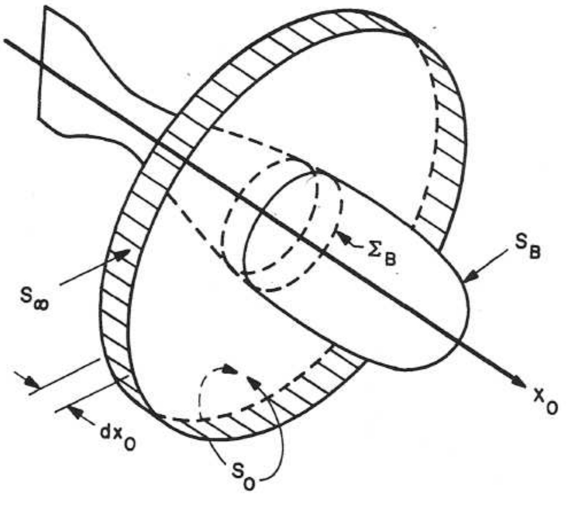

Figure 2.3.: Definition sketch for the control volume of differential thickness $dx_0$ used to compute the differential lateral force $F_z'$; source: [New77, p.338]

surface, the differential lateral force ($z_0$-direction) writes

$$\begin{aligned} F'_z \;=\; \frac{\vec{k}\cdot\mathbf{F}}{dx_0} \;=\; & -\rho\,\frac{d}{dt}\oint\limits_{\Sigma_B} \vec{k}\cdot\phi\,\mathbf{n}\;d\iota \;\;-\rho\oint\limits_{\Sigma_\infty} \vec{k}\cdot\left(\frac{\partial\phi}{\partial n}\nabla\phi \;-\mathbf{n}\,\frac{1}{2}\left(\nabla\phi\right)^2\right)\;d\iota\;\cdots \\ & -\rho\iint\limits_{S_{0_1}}\vec{k}\cdot\left(\frac{\partial\phi}{\partial n}\nabla\phi \;-\mathbf{n}\frac{1}{2}\left(\nabla\phi\right)^2\right)dy_0dz_0-\rho\iint\limits_{S_{0_2}}\vec{k}\cdot\left(\frac{\partial\phi}{\partial n}\nabla\phi \;-\mathbf{n}\frac{1}{2}\left(\nabla\phi\right)^2\right)dy_0dz_0 \end{aligned} \tag{2.72}$$

where $d\iota$ denotes a line integration (it could e.g. be $r(x,\theta)d\theta$). Further evaluation gives

$$\begin{aligned} F'_z = -\rho\frac{d}{dt}\oint\limits_{\Sigma_B}\phi\,n_z\;d\iota\;\;-\rho\oint\limits_{\Sigma_\infty}\left(\frac{\partial\phi}{\partial n}\frac{\partial\phi}{\partial z_0}\;-n_z\,\frac{1}{2}\left(\nabla\phi\right)^2\right)\;d\iota\;\cdots \\ -\rho\left\{\iint\limits_{S_{0_1}}\frac{\partial\phi}{\partial x_0}\frac{\partial\phi}{\partial z_0}dy_0dz_0\;\;-\iint\limits_{S_{0_2}}\frac{\partial\phi}{\partial x_0}\frac{\partial\phi}{\partial z_0}dy_0dz_0\right\} \end{aligned} \tag{2.73}$$

where the terms in the curly brackets can be written in differential form since $dx_0 \to 0$. That is $\frac{\partial}{\partial x_0}\iint\limits_{S_0}\frac{\partial\phi}{\partial x_0}\frac{\partial\phi}{\partial z_0}\;dy_0dz_0$, emphasizing that its contribution can be neglected due to the slenderness assumption $\left(\frac{\partial\phi}{\partial x_0} \ll \left(\frac{\partial\phi}{\partial y_0},\frac{\partial\phi}{\partial z_0}\right)\right)$. The contour integral $\sum_B$ can be evaluated infinitely far from the body where boundary condition (2.64) applies, thus $\phi$ and so the whole integrand vanishes. Thus, the differential lateral force acting along the body length reduces to

$$F'_z = -\rho\,\frac{d}{dt}\oint\limits_{\Sigma_B}\phi\,n_z\;d\iota \tag{2.74}$$

As $\sum_B$ lies on the body, $\phi$ can be replaced by (2.70). Assuming the body to be symmetrical about $z = 0$ simplifies further since the longitudinal velocity than has no contribution to $F'_z$ (and $F_z$) and one can write

$$F'_z = -\rho\,\frac{d}{dt}\left(W(x,t)\oint\limits_{\Sigma_B}\Phi_3\,n_z\;d\iota\right). \tag{2.75}$$

Now employing the boundary condition (2.71) ($\partial\Phi_3/\partial N = n_z$) and using the definition of added mass (equation (2.54)) in the two dimensional sense, the differential lateral force can be expressed as

$$F'_z = -\frac{d}{dt}\left(W(x,t)m_{33}(x)\right). \tag{2.76}$$

The differential operator $d/dt$ is to be interpreted as the time derivative in a fixed reference frame with $x_0 =$ constant. Giving it in terms of the moving reference frame with help of the transformations (2.59) yields partial derivatives and makes the distinction between steady and unsteady motion trivial. The resulting equation

$$F_z' = -\left(\frac{\partial}{\partial t} - U\frac{\partial}{\partial x}\right)[W(x,t)m_{33}(x)] \tag{2.77}$$

has been derived by Lighthill (1960) in analyzing the swimming motion of slender fish, consider [Lig60]. The total force acting on the body can be obtained by integrating Lighthill's 'fish equation'.

### Stationary Lateral Force

In the case where the displacement $\zeta$ is independent of time, which means that there is no lateral motion, the total lateral force is found from integrating (2.77) as

$$F_z \;=\; U\int\limits_l \frac{\partial}{\partial x}[W(x,t)m_{33}(x)]\,dx \;=\; U\,[W(x,t)m_{33}(x)]\Big|_{x_T}^{x_N}. \tag{2.78}$$

The nose $x_N$ of a slender body is a point of zero transverse dimensions and thus $m_{33}(x_N) = 0$. If also the tail is pointed $m_{33}(x_T) = 0$ and in accordance with d'Alembert's paradox no lateral force acts on the body in steady motion. But for a body with a tail fin this is fundamentally different. The two-dimensional added mass of a flat plate

$$m_{33}(x_T) = \pi\rho s^2/4 \tag{2.79}$$

can be used to describe the local added mass at the tail, where the tail span is denoted with $s$.

The displacement $\zeta$ can best be described thinking of a flat plate ($z = 0$) that now is rotated around $y = 0$ by a constant (fixed) angle of attack $\alpha$. (Such a flat surface used to describe the tail fin, rudder or fish in three-dimensional space is not to be confused with the added mass coefficient of a two-dimensional flat plate.) The displacement is then given by $\zeta = \alpha x$, since $\tan(\alpha) \cong \alpha$ for small $\alpha$. Therefore $W = \partial_t\zeta - U\partial_x\zeta = -U\alpha$. It is theoretically sufficient to describe the local angel of attack at the tail $\alpha_T$, thus with help of (2.79) one obtains from (2.78)

$$F_z = \frac{\pi}{4}\rho U^2 s^2 \alpha_T. \tag{2.80}$$

From Lighthill's 'fish equation' (2.77) one obtains the yaw moment acting on the body by using a moment arm in $x$ direction. In terms of the body fixed vertical axis and stationary motion that writes

$$\begin{aligned} M_y &= -U\int\limits_l x\,\partial_x[W(x)m_{33}(x)]\;dx \\ &= U\int\limits_l W(x)m_{33}(x)\;dx \;-\; UxW(x)m_{33}(x)\Big|_{x_T}^{x_N}. \end{aligned} \tag{2.81}$$

Using (2.70) for $W$ and the already derived result for the last term ((2.80) times $x$) yields

$$\begin{aligned} M_y &= -U^2 \int\limits_l \partial_x \zeta m_{33}(x)\ dx \ - \ U^2 x_T \alpha_T m_{33}(x_T) \\ &= -U^2 \int\limits_l \partial_x \zeta m_{33}(x)\ dx \ - \ x_T F_z. \end{aligned} \tag{2.82}$$

The moment caused by the lift force is associated with the last term and vanishes for a body with pointed tail. The remaining term is the moment acting on nonlifting bodies in steady translation. It is known as the *Munk moment* that generally can act on bodies in ideal and stationary flow conditions even though no resulting force is present (d'Alembert's paradox).

What happens to the resulting force (2.80) if the whole body simply is a rectangular flat plate? One could argue that the nose is no longer pointed and $m_{33}(x_N)$ is nonzero and equal to $m_{33}(x_T)$, resulting in zero lateral force. But that is not the correct interpretation of slender body theory. The solution is found in the nature of lifting surfaces. The flow is assumed to be irrotational at each section along the length, thus vortex sheets and separation is excluded in the fluid alongside the body. But as the flow downstream does not affect the analysis such restriction is not obligatory downstream the tail and a trailing vortex sheet may originate from the abrupt trailing edge at the tail. In terms of lifting-surface theory this trailing vortex is directly associated with the lift force.

Further thinking of a planar lifting surface of small aspect ratio $A$ (2.58) with maximum span at the tail, the trailing vortex sheet downstream of the body must be independent of $x$, with a constant downwash velocity (here $z$-direction) proportional to $U\alpha_T$. Provided the angle of attack is constant along the body, it makes thus no difference if the body terminates at the position of maximum span or continues downstream with decreasing span. "For this reason, the low aspect ratio theory holds for uncambered lifting surfaces of more general planform if the maximum span is used (in (2.83)). In this particular case, there is no lift force on the portion of the body downstream of the maximum span." [New77, p.343]

In the case of $\int \partial_x m_{33}(x) dx = m_{33}(x)\big|_{x_T}^{x_N}$ the appropriate added mass to use is therefore the one at $x =$ maximum span, say $x_M$ and $m_{33}(x_M)$. That means that slender body theory in stationary cases yields the same total lateral force for all geometries shown in figure 2.4, where planar lifting surfaces of different span $s(x)$ profiles with the same maximal span are shown.

In the case of planar uncambered lifting surfaces (of small aspect ratio) slender body theory thus reduces to a low-aspect-ratio-lifting-surface-theory, provided no vorticity is shed upstream the point of maximal span. Using the aspect ratio $A$ based on the maximum

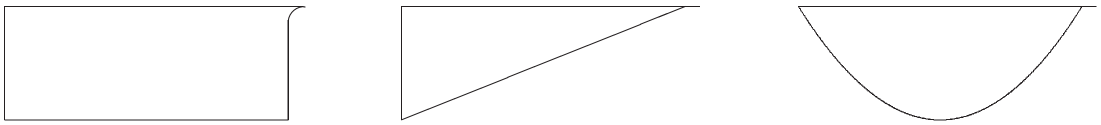

rectangle triangular (delta wing) quadratic

Figure 2.4.: Different profiles of planar lifting surfaces

span and (2.80), the lift coefficient writes

$$C_L = \frac{F_z}{\frac{1}{2}\rho U^2 S_p} = \frac{1}{2}\pi A\alpha. \tag{2.83}$$

With the stationary and planar (equal angle of attack) restriction holds

$$F_z' = -U^2\alpha\,\partial_x m_{33}(x). \tag{2.84}$$

This expression of the differential lateral force shows directly that the longitudinal distribution of the lift force is proportional to the rate of change of added mass. For a triangular delta wing the lift force is hence distributed uniformly along the length. In the case of a rectangular planform, however the center of pressure will be situated at the leading edge. To show that for a rectangular planform all the change of added mass occurs at the leading edge, it is indicated in figure 2.4 that the nose is to be regarded as a point of zero transverse dimension. The differential force for the rectangular planform can be expressed with help of a Dirac delta function $\delta(x-x_N)$. Using (2.79) gives $F_z' = \frac{\pi}{4}\rho U^2\alpha s^2\delta(x-x_N)$. Such limit is not completely physical, "but experiments show that the center of pressure for a rectangular lifting surface of small aspect ratio is very close to the leading edge, particularly in the regime of small angel of attack where leading-edge separation does not occur." [New77, p.343]

In the course of this work, this interpretation of the differential lateral force can be compared to the simulation results. Therefore consider figure 6.12(b) where the pressure distribution along sections of the rudder is shown. It clearly shows the described tendency. Also the comparison to two-dimensional lift theory is adequate as can be seen from figure 6.4.

### Nonstationary Lateral Force

In the general case, where the displacement is nonlinearly time dependent (that is the body accelerates e.g. in z-direction or/and with a yaw acceleration), the added mass coefficients can take the forms

$$m^s_{33} = \int\limits_l m_{33}(x)dx \qquad \text{added mass coefficient due to yaw acceleration} \tag{2.85}$$

$$m^s_{35} = \int\limits_l m_{33}(x)xdx \qquad \text{sway yaw cross}-\text{coupling added mass} \tag{2.86}$$

$$m^s_{55} = \int\limits_l m_{33}(x)x^2dx \qquad \text{added moment of inertia for sway acceleration} \tag{2.87}$$

where the superscript $s$ is inserted to show that these are strip theory results. That is because the velocities correspond to two-dimensional flow problems at each section along the body length. The local force at any section of the body is hence not affected by the shape of the body elsewhere. There are no hydrodynamic interactions between adjacent sections of the body. The sway added mass coefficient for a spheroid for example will be overpredicted by 10 % for a $d/l$ ratio of 0.2 and by 100 % for a sphere. For the moment of inertia the error is even larger, emphasized by the fact that this coefficient is zero for a sphere, while it is predicted nonzero from slender body theory (see (2.87), an even function remains even). But, "it would be naive to suggest that a sphere is slender, and in general a diameter-length ratio of 0.1 to 0.2 is a reasonable upper limit for the slender-body approximation." [New77, p.340]

Concluding this section with the note that, in contrast to the longitudinal problem, the lateral force is of the same order as the body mass.

## 2.5. Lifting Surfaces

Lift results from circulation around lifting surfaces and can be described in terms of potential theory within its ideal fluid flow conditions.

This section derives the lifting line theory. Therefore it makes use of the outcome of two-dimensional thin-wing theory that is presented in the first subsection. It further builds on the two subsections that introduce the general lifting-surface theory and especially treat the induced drag before the finally used lifting line results are achieved.

### 2.5.1. Two-Dimensional

The problem simplifies to a two-dimensional situation when assuming that the aspect ratio (see equation (2.58)) $A \rightarrow \infty$. Let the total velocity field be expressed as $\partial_x \phi - U\vec{i}$, where $U$ is the free stream velocity. The boundary conditions are: the Laplacian throughout the fluid field $\nabla^2 \phi$, a vanishing disturbance at infinity $\partial_i \phi \rightarrow 0$, the free slip boundary condition on the wing $\partial \phi / \partial n = U n_x$ and the Kutta condition $\partial_i \phi < \infty$ at the trailing edge. The latter enforces the velocity at the trailing edge to be finite and thus the physically meaningful circulation around the foil is induced. [New77, p.166,167]

See figure 2.5 and consider chapter 2.3.1 concerning a justification of vortices in potential flow.

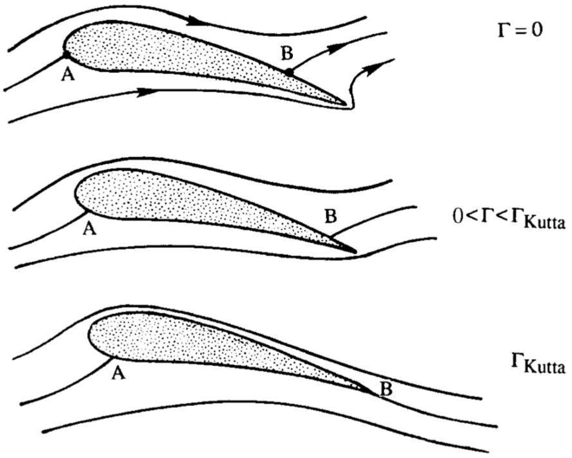

Figure 2.5.: Sketch of the the stagnation points in irrotational flow in terms of the Kutta condition; source: [KC08, p.686]

The denotation of the variables follows the one introduced in the introduction chapter (1), compare to figure 1.2. A compact expression for the lift force can directly be found from (2.33) ($F_i = \int\limits_{S_B} p n_i \, dS$) with the pressure taken from linearizing Bernoulli's equation (2.31) in the steady from:

$$p - p_\infty \simeq \rho u U. \tag{2.88}$$

Thus the lift force, which per definition acts perpendicular to the free stream, writes

$$L = \rho U \mathit{\Gamma} \tag{2.89}$$

where $\mathit{\Gamma} \equiv \oint u_i \, dx_i = \oint u \, dx$ is the circulation; here found from the pressure- respectively velocity-jump between $u$ on and under the wing. This lift-expression is a derivation for linearized thin foils of the more general Kutta–Joukowski theorem. Similarly for the moment about the $z$-axis

$$M = \rho U \oint ux \; dx. \tag{2.90}$$

The body boundary condition can be written as $0 = \frac{D}{Dt}(y - y_u(x))$ where $y = y_u$ describes the upper surface. The first order approximation, valid as long as $|\partial_x \phi| \ll U$, can further be simplified with applying it at $y = 0+$ and writes

$$\partial\phi/\partial y = -U y_u'(x), \qquad \text{on } \; y = 0+, \; -l/2 < x < l/2. \tag{2.91}$$

The same holds for the lower surface $y = y_l$, on $y = 0-$. The potential can be decomposed into an odd and an even function, allowing to write the body boundary condition as

$$\frac{\partial \phi_e}{\partial y} = \mp \frac{1}{2} U (y_u' - y_l'), \qquad \text{on } \; y = 0\pm, \; -l/2 < x < l/2 \tag{2.92}$$

$$\frac{\partial \phi_o}{\partial y} = -\frac{1}{2} U (y_u' + y_l'), \qquad \text{on } \; y = 0\pm, \; -l/2 < x < l/2. \tag{2.93}$$

They correspond to distinctly different physical problems. The first is a thickness-problem ($(y_u - y_l)$ is the thickness of the wing), see also Figure 2.6. It is symmetric and always confined to zero angle of attack, thus no lift force can arise. Consequently all lift can be deduced from problem (2.93), involving the derivative of the mean camber line $\eta = \frac{1}{2}(y_u + y_l)$. Here the velocity at the leading and trailing edge becomes infinite. But at the trailing edge the Kutta condition applies. And at the leading edge one can accept the singularity, since it would be removed from the thickness problem that itself does not effect the lift. [New77, p.166,167,168]

Concentrating on lift and not further emphasizing the difference of $\phi_e$ and $\phi_o$, the body boundary condition for the mean camber line problem writes

$$v = \frac{\partial \phi}{\partial y} = -U \eta'(x), \qquad \text{on } \; y = 0\pm, \; -l/2 < x < l/2. \tag{2.94}$$

As lift results from circulation, it is logical to use a vortex distribution $\phi = Re\{\gamma/(2\pi i)\log(z)\}$ along $y = 0$ to express the velocities (with $z = x - \xi + iy$)

$$u = \frac{\partial \phi}{\partial x} = \frac{\gamma}{2\pi} \frac{-y}{(x-\xi)^2 + y^2} \qquad \text{and} \qquad v = \frac{\partial \phi}{\partial y} = \frac{\gamma}{2\pi} \frac{(x-\xi)}{(x-\xi)^2 + y^2} \tag{2.95}$$

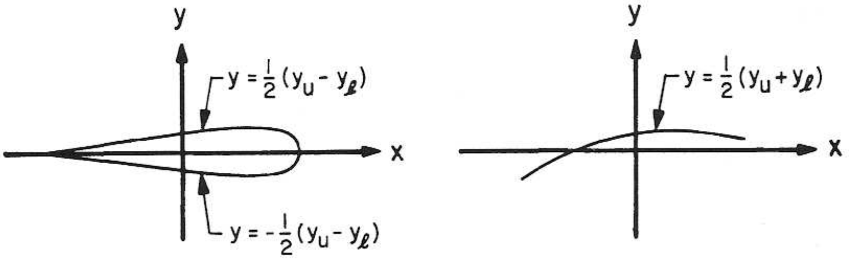

Figure 2.6.: Definition sketch of the thickness and lifting problem; source: [New77, p.167]

where $\gamma$ is the circulation situated at the point $x = \xi$ on the $x-$axis. Integrating along the chord length gives

$$u(x,y) = -\frac{1}{2\pi}\int_{-l/2}^{l/2}\frac{\gamma(\xi)\,y}{(x-\xi)^2+y^2}\,d\xi \quad \text{and} \quad v(x,y) = \frac{1}{2\pi}\int_{-l/2}^{l/2}\frac{\gamma(\xi)\,(x-\xi)}{(x-\xi)^2+y^2}\,d\xi. \tag{2.96}$$

further taking the limit of $y = \pm\epsilon$ where $\epsilon \to 0$, and $y \to \pm 0$ respectively, yields

$$u(x,\pm\epsilon) \simeq \mp\frac{1}{2}\,\gamma(x) \qquad \text{and} \qquad v(x,0\pm) = -\frac{1}{2\pi}\fint_{-l/2}^{l/2}\frac{\gamma(x)}{\xi - x}\,d\xi. \tag{2.97}$$

The latter is to be interpreted as a Cauchy principal value integral and care has to be taken since the singularities are distributed continuously along the cut $-l/2 < x < l/2$ of the $x$-axes. The former states that the discontinuity in $u$ equals the local vortex strength valid for sufficiently small values of $\epsilon/l$. [New77, p.169,170,178]

The boundary condition (2.94) with $v$ from (2.97), forms a singular integral equation since the unknown function $\gamma$ appears in the integrand and the known part of the integrand is singular. A general solution for $\gamma$ can be found with help of the thickness problem that relates to a source distribution $\phi = Re\{\gamma/(2\pi)\log(z)\}$ in the same manner as outlined for the vortex distribution in the mean camber line problem. The velocity components for the source distribution $(u,v)$ are identical to the conjugate pair $(v,-u)$ of the vortex distribution, except that the singularity strengths are the source and the vortex strength respectively. Providing the information that with help of introducing a pseudo velocity a homogeneous solution for $\gamma$ can be found, (for details see [New77, ch.5.7]),

$$\gamma(x) = \frac{2}{\pi\left[\left(\frac{1}{2}l\right)^2 - x^2\right]^{1/2}}\left\{\fint_{-l/2}^{l/2}\frac{v(\xi,0)\left[\left(\frac{1}{2}l\right)^2 - x^2\right]^{1/2}}{\xi - x}d\xi + \frac{1}{2}\,\mathit{\Gamma}\right\} \tag{2.98}$$

with the total circulation around the foil being

$$\mathit{\Gamma} = \int_{-l/2}^{l/2}\gamma(\xi)\;d\xi. \tag{2.99}$$

Up to now $\Gamma$ is unknown and equation (2.98) is not unique. The first denominator in (2.98) contains square-root infinities at $x = \pm l/2$ and thus it is apparent that the vortex strength, and hence the horizontal velocity, tends to infinity at the trailing and leading edge. Here the Kutta condition comes in, that has not yet been applied. It has to ensure a finite velocity at the trailing edge. That can only be true if the terms in the curly parentheses vanish at $x = -l/2$, thus

$$\Gamma = -2 \int_{-l/2}^{l/2} v(\xi, 0) \left[ \frac{\frac{1}{2}l - \xi}{\frac{1}{2}l + \xi} \right]^{1/2} d\xi. \tag{2.100}$$

Having found an explicit expression for the total circulation, all that remains is plug and play. Using the expression for lift (2.89) and the boundary condition (2.94) yields the lift force

$$L = 2\rho U^2 \int_{-l/2}^{l/2} \frac{d\eta}{d\xi} \left[ \frac{\frac{1}{2}l - \xi}{\frac{1}{2}l + \xi} \right]^{1/2} d\xi. \tag{2.101}$$

In terms of chapter 1 the nondimensional lift coefficient per unit length writes

$$C_L = \frac{L}{\frac{1}{2}\rho U^2 l} = \frac{4}{l} \int_{-l/2}^{l/2} \frac{d\eta}{d\xi} \left[ \frac{\frac{1}{2}l - \xi}{\frac{1}{2}l + \xi} \right]^{1/2} d\xi. \tag{2.102}$$

The moment (2.90) consequently displays as

$$M \;=\; \rho U \int_{-l/2}^{l/2} \gamma(x)\, x \; dx \;=\; 2\rho U^2 \int_{-l/2}^{l/2} \frac{d\eta}{d\xi} \left[ \left( \frac{1}{2} l \right)^2 - \xi^2 \right]^{1/2} d\xi \tag{2.103}$$

where $u$ is found from (2.97) and $\gamma$ from (2.98) and (2.100), and the boundary condition (2.94) is used. The corresponding coefficient writes

$$C_M \;=\; \frac{M}{\frac{1}{2}\rho U^2 l^2} \;=\; \frac{4}{l^2} \int_{-l/2}^{l/2} \frac{d\eta}{d\xi} \left[ \left( \frac{1}{2} l \right)^2 - \xi^2 \right]^{1/2} d\xi. \tag{2.104}$$

The *center of pressure* is found from the ratio $x_{CP} = M/L$. [New77, p.171,172]

In the case of the symmetrical airfoils (about $y = 0$), like the kayak rudder, the mean-camber line $\eta$ reduces to the simplest possibility, a straight line respectively a flat plate. Thus $d\eta/dx = \tan\alpha \simeq \alpha$ since $\alpha$ is small. Solving (2.102) and (2.104) (with help the substitution $\xi = \frac{1}{2}l \sin\theta$) gives

$$C_L = 2\pi\alpha \qquad\qquad C_M = \frac{1}{2}\pi\alpha. \tag{2.105}$$

Consequently the center of pressure here is located at the *quarter-chord* point $x_{CP} = l/4$. The precise distribution of the linear pressure jump responsible for the lift distribution is proportional to the vortex strength. The latter is found from (2.98) with help of the boundary condition (2.94) and writes in case of the flat plate

$$\gamma(x) = 2\alpha U \left( \frac{\frac{1}{2}l + x}{\frac{1}{2}l - x} \right)^{1/2}. \tag{2.106}$$

A plot of this equation is shown in chapter 6.2 figure 6.4. where it can be seen that $\gamma(x_T) = 0$, but $\gamma(x_L) \to \infty$ since the Kutta condition only requires the velocity at the trailing edge to be finite. [New77, p.172,173]

### 2.5.2. Basic Lifting Surface Theory

Similar to the two-dimensional problem, also here a thickness problem evolves in terms of a source distribution. The lifting problem reduces to a mean-camber surface $\eta(x, z)$ problem, only that the vortices now no longer are restricted to the same normal direction. The method of complex function theory can not be used here and the variable $z$ and the dummy coordinate $\zeta$ shall denote the coordinates along the span. Like before (2.94), the boundary condition for the normal velocity now becomes

$$v(x, 0, z) = -U \frac{\partial}{\partial x} \eta(x, z) \qquad \text{on the planform area.} \tag{2.107}$$

A solution can be constructed by distributing vortices in the plane $y = 0$. They will in general be of varying strength and orientation angles, thus $\gamma$ here becomes a vector confined to the plane $y = 0$. It shall be decomposed into the *bound* component parallel to the $z$-axis and the *free* component parallel to the $x-$axis. As it can be shown that a line vortex's behavior in the limits very close to its axis is identical to that of a two-dimensional point vortex of the same strength (see [New77, ch.5.8]), the two-dimensional results of the vortex distribution along the $x$-axis apply in three dimensions locally for the bound vortex distribution. The latter is of density $\gamma_B(x, z)$ and induces a discontinuity in the chordwise component of the fluid velocity across the plane $y = 0$

$$u(x, \pm 0, z) = \mp \frac{1}{2} \gamma_B(x, z). \tag{2.108}$$

The distribution of the free vortices similarly induces a discontinuity in the spanwise velocity-component

$$w(x, \pm 0, z) = \pm \frac{1}{2} \gamma_F(x, z). \tag{2.109}$$

For both apply planar distributions of vortices across $y = 0$. Planar vortex distributions are generally known as *vortex sheets*, here the bound and free vortex sheet. And they are not independent, since the velocity field adjacent to the sheets must be irrotational. From (2.23) one can state that $\partial_z u - \partial_x w = 0$, thus

$$\partial_z \gamma_B - \partial_x \gamma_F = 0. \tag{2.110}$$

A change in the bound vorticity along the $z$-axis thus has to be balanced by a corresponding change in the free vorticity. [New77, p.191,192,193]

The linearized pressure induced by these vortex sheets is equal to (2.88), since $w$ only gives a second order contribution: $p - p_\infty \simeq \rho u U = \mp\frac{1}{2}\rho U \gamma_B(x,z)$. Thus the pressure jump across the sheet is proportional to the bound vorticity, while the pressure associated with the free vortex sheet is continuous in this linear analysis and does not disturb the pressure jump. Thus the free vortex sheet can exist in a state of dynamic equilibrium within the free stream – that is where its name stems from. The bound vortices induce a pressure jump that requires the existence of an external balancing force, the lift force. [New77, p.193]

Integrating the pressure from the trailing to the leading edge leads to the sectional lift force[9]

$$L(z) = -\rho U \oint \underbrace{\mp\frac{1}{2}\gamma_B(x,z)}_{u(x,\pm y,z)}\ dx = \rho U \int\limits_{x_T(z)}^{x_L(z)} \gamma_B(x,z)\, dx = \rho U \mathit{\Gamma}(z) \tag{2.111}$$

and a further integration along the span gives the total lift

$$\overline{L} = \rho U \int\limits_{-s/2)}^{s/2} \mathit{\Gamma}(z)\ dz. \tag{2.112}$$

Now exploring the appropriate distribution of bound and free vortex sheets to find information about $\mathit{\Gamma}$: Integrating (2.110) along the chord writes

$$\int\limits_{x_T(z)}^{x_L(z)} (\partial_z \gamma_B - \partial_x \gamma_F)\ dx = 0 \qquad \text{that is} \qquad \mathit{\Gamma}'(z) + [\gamma_F(x,z)]\Big|_{x_T}^{x_L} = 0. \tag{2.113}$$

This states that any spanwise change in the total circulation $\mathit{\Gamma}(z) = \int\limits_{x_T(z)}^{x_L(z)} \gamma_B\ dx$ must be reflected in a corresponding jump of the free vortex density across the section. The total circulation must vary in $z$ since the wing is finite and at the latest $\mathit{\Gamma}$ has to change at the tips $x = \pm\frac{1}{2}s$ from a nonzero value to zero. The resulting free vorticity must be *conserved* and leaves behind a thin wake region of free, or *trailing*, vorticity. The total circulation can be looked at as to be balanced by an equal and opposite starting vortex. Thus, ideally the

---

[9] According to the author's calculations Newman uses $\mathit{\Gamma} = -\oint u\ dx$ since $\mathit{\Gamma} = -\int (u^+ - u^-)\ dx$ and from (2.108) $u^+ = -\frac{1}{2}\gamma_B$ and $u^- = \frac{1}{2}\gamma_B$ and thereby $\mathit{\Gamma} = \int \gamma_B\, dx$

system of bound and free vortices is rejoined downstream in a closed loop. The surrounding is assumed uniform and undisturbed. Setting the free vorticity to zero upstream of the leading edge ($\gamma_F(x_L, z) = 0$) determines the free vortex density ($\gamma_F(x_T, z) = \gamma_T(z)$) to be the trailing vortex density. Thus

$$\gamma_T(z) = \mathit{\Gamma}'(z). \tag{2.114}$$

Noting that $\gamma_T(z)$ is independent of $x$, as can be seen from (2.110), shows that there can be no bound vorticity in the wake. [New77, p.194]

Figure 2.7(a) sketches a lifting surface, or precisely speaking only its projection in the plane $y = 0$, where discrete bound and free vortices are indicated as lines in $z$- and $x$-direction respectively. The free vortex sheet extends downstream while the bound vortices are confined to the planform area. Note that even working with the linearized problem that is confined to $y = 0$, the lifting surface's shape and angel of attack enter via the boundary condition (2.107).

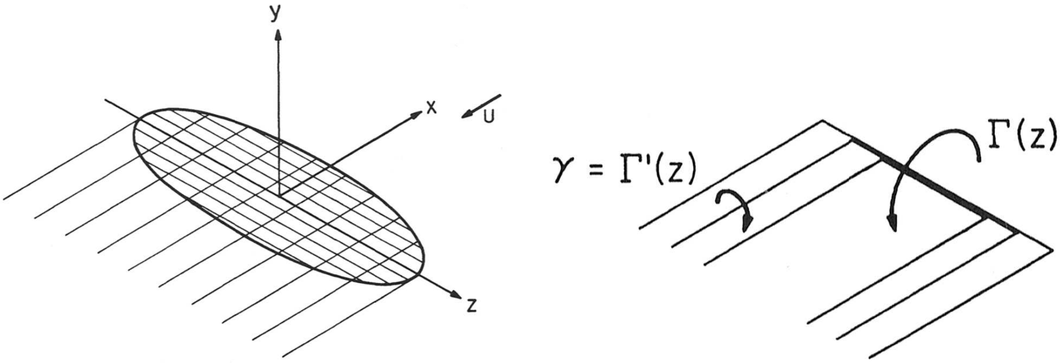

(a) Discrete vortices

(b) Sketch to the lifting line approach

Figure 2.7.: Lifting surface theory; source: [New77, p.195,196]

In the case of large aspect ratio, which is e.g. small chord length in comparison to the span, $\mathit{\Gamma}$ will change dramatically close to the tips since it has to equal zero thereafter. Thus the trailing vortices will in spanwise-direction mainly be confined to the region close to the tips. This supports the picture that the resulting vortex distribution reminds of a form of a horseshoe. As the trailing vortices of the sides have to be opposite in sign, a similar picture also generally evolves and the name *horseshoe* vortex applies also here.

The trailing vortex sheet is an inevitable consequence of the three-dimensional effects. It will always be detrimental to the performance of a lifting surface. First the lift is reduced since the trailing vortices induce a *downwash* velocity, reducing the effective angle of attack in comparison to a two-dimensional case without downwash. Secondly the induced drag is the result from the continuous energy needed to form the trailing vortices.

There are different ways horseshoe vortices can be superposed in order to model a realistic wing. The special case where horseshoe vortices of varying span are distributed along the same chordwise position marks the approximation behind lifting line theory. As indicated by the thicker line in figure 2.7(b) one single bound vortex $\Gamma(z)$ is formed and, in order to satisfy the conservation of circulation the trailing vortices are constrained to (2.114). Such assumption is valid if the span is long compared to the chord length, thus the lifting line theory is of practical importance especially for wings with larger aspect ratio $A$ and is finally deduced in section 2.5.4. [New77, p.196,197]

### 2.5.3. Induced Drag

The trailing vortex sheet increases in length at a rate proportional to $U$. Thus the kinetic energy in the fluid increases due to the work done to overcome the drag force and the drag equals the kinetic energy of a slice of fluid (with unitlength in $x$) far downstream.

Applying (2.39) to an infinitely large control volume covering the whole lifting surface in terms of the drag ($x$-component), shows directly that the body integral vanishes. The control volume shall be composed by two plains at $x$ = constant, then the contribution from the remaining surface vanishes as $y^2 + z^2 \to 0$ and one is left with

$$D = \frac{1}{2}\rho \int\limits_{S_C} \left\{ (\partial_x \phi)^2 - (\partial_y \phi)^2 - (\partial_z \phi)^2 \right\} n_x \, dy \, dz. \tag{2.115}$$

As the same is true far upstream and as the trailing vortex sheet is independent of $x$ one can write

$$D = \frac{1}{2}\rho \int\limits_{-\infty}^{\infty} \left\{ (\partial_y \phi)^2 + (\partial_z \phi)^2 \right\} \, dy \, dz \tag{2.116}$$

where evaluation shall apply at $x \to -\infty$. The integral describes the two-dimensional energy in a *Trefftz plane* where $x$ =constant (far downstream). [New77, p.197]

The velocity induced from the trailing vortex sheet far downstream is independent of $x$ and as $\nabla^2 \phi = 0$ one can write

$$D = -\frac{1}{2}\rho \int \nabla\phi \cdot \nabla\phi \, dy \, dz = -\frac{1}{2}\rho \int \nabla \cdot (\phi \nabla \phi) \, dy \, dz = -\frac{1}{2}\rho \oint \phi \frac{\partial \phi}{\partial n} \, dl \tag{2.117}$$

where the last step makes use of Gauß's theorem to transform to a line integral that equally can be applied on trailing vortex sheet, or the cut $|z| < \frac{1}{2}s$. In contrast to $\phi$ the $v-$velocity $\frac{\partial \phi}{\partial y}$ is continuous (see 2.107-2.109) and one can write

$$D = -\frac{1}{2}\rho \int\limits_{-s/2}^{s/2} (\phi^+ - \phi^-) \frac{\partial \phi}{\partial y} \, dz = -\frac{1}{2}\rho \int\limits_{-s/2}^{s/2} [\phi]_-^+ \frac{\partial \phi}{\partial y} \, dz. \tag{2.118}$$

The jump in the potential $\phi$ can be related to the bound vorticity. The pressure jump across the wake has to vanish and it therefore remains valid to evaluate from $-\infty$

$$\begin{aligned} \Gamma(z) &= -\oint u\,dx = -\int\limits_{x_T}^{x_L} \left(u^+ - u^-\right) dx \\ &= -\int\limits_{-\infty}^{x_L} \left( \left(\frac{\partial\phi}{\partial x}\right)^+ - \left(\frac{\partial\phi}{\partial x}\right)^- \right) dx = [\phi]_-^+ \Big|_{x=-\infty} \end{aligned} \tag{2.119}$$

where the last step incorporates that the pressure jump, and thus the jump in the potential, has to vanish at the leading edge. [New77, p.198]

The vertical velocity far downstream can be expressed from the two-dimensional vortex distribution (2.97). Here the plane is $y$-$z$ and not $x$-$y$, leading to a change in sign (right hand rule). Further using (2.114) to substitute for the trailing vortex density leads to

$$\frac{\partial\phi}{\partial y} = \frac{1}{2\pi} \fint\limits_{-s/2}^{s/2} \frac{d\Gamma(\zeta)}{d\zeta} \frac{d\zeta}{\zeta - z}. \tag{2.120}$$

Substituting (2.119) and (2.120) into (2.118) yields the drag in terms of only the bound circulation

$$D = \frac{1}{4\pi}\rho \int\limits_{-s/2}^{s/2} \Gamma(z) \underbrace{\fint\limits_{-s/2}^{s/2} \frac{d\Gamma(\zeta)}{d\zeta} \frac{d\zeta}{z - \zeta}}_{*}\; dz. \tag{2.121}$$

Also the lift force already given in (2.112) can be derived in terms of the Trefftz plane. [New77, p.198,199]

Lift (2.112) and drag (2.121) can now be computed, if the spanwise distribution of the circulation $\Gamma(z)$ is known. Lift is linearly proportional to $\Gamma$ and thus (induced) drag is proportional to the square of lift. Since $\Gamma$ depends on the angel of attack and camber, the ratio $L/D$ is inversely proportional to the angel of attack and camber. Thus $L/D$ tends to infinity at zero angle of attack and camber! Recalling that this is an ideal flow computation. Nevertheless this indicates that $\alpha$ should be kept small in order to have maximal lift in comparison to the induced drag (and also to avoid stall, cavitation and nonlinear effects). An other indicator for such merit, which is well behaved, can be defined as

$$K \;=\; \pi A \frac{\overline{C}_D}{\overline{C}_L^2} \;=\; \frac{\pi}{2}\rho U^2 s^2 \frac{\overline{D}}{\overline{L}^2} \;=\; \frac{s^2}{8} \frac{\int \Gamma(z) \fint \left[\Gamma'(\zeta)/(z-\zeta)\right]\, d\zeta\, dz}{\left(\Gamma(z)\; dz\right)^2}. \tag{2.122}$$

Here the most efficient lifting surface is the one with smallest $K$. The coefficients

$$\overline{C}_L = \frac{\overline{L}}{\frac{1}{2}\rho U^2 S_p} \qquad\qquad \overline{C}_D = \frac{D}{\frac{1}{2}\rho U^2 S_p} \tag{2.123}$$

are defined with respect to the planform-area $S_p$, as is the aspect ratio $A$ (2.58). The limits of the integrals are $\pm\frac{1}{2}s$. [New77, p.199]

The circulation $\Gamma(z)$ and its derivative $\Gamma(z)'$ can be assumed to be continuous along the span and $\Gamma(z)$ to be zero at the tips $z = \pm\frac{1}{2}s$. Thus it can be expanded in a Fourier series of the form

$$\Gamma\,(s/2\ \cos\theta) = 2Us\sum_{n=1}^{\infty} a_n \sin n\theta \tag{2.124}$$

with $z = \frac{1}{2}s\cos\theta$. One can also deduce this precise form from the Fourier series expansion that can be used in two-dimensional analysis. The latter series is found in Newman [New77, p.187] and an outline of the arguments is given in [Aya10, p.14]. Nevertheless, requiring the coefficients to be expressible in the most simple form makes this choice quite self-suggesting. Using the expansion in (2.112) and evaluating yields

$$\overline{L} \;=\; \rho U \int\limits_{-s/2)}^{s/2} \Gamma(z)\ dz \;=\; \rho U^2 s^2 \sum_{n=1}^{\infty} a_n \int\limits_{0}^{\pi} \sin n\theta\, \sin\theta\ d\theta \;=\; \pi\frac{1}{2}\rho U^2 s^2 a_1 \tag{2.125}$$

since an orthogonality relation with m and n positive integers states

$$\int\limits_{0}^{\pi} \sin n\theta\, \sin m\theta\ d\theta = \begin{cases} \frac{1}{2}\pi & \text{if } m = n \\ 0 & \text{if } m \neq n. \end{cases} \tag{2.126}$$

The drag is calculated similarly from (2.121). But as it involves a more complicated integral, for simplicity indicated with $*$ (compare (2.121)), its solution requires the use of a Glauert integral

$$G_n(\theta) = \fint\limits_{0}^{\pi} \frac{\cos n\phi}{\cos\phi - \cos\theta}\ d\phi \qquad \text{where} \qquad G_n = \pi\frac{\sin n\theta}{\sin\theta}. \tag{2.127}$$

Then the drag (2.121), with help of (2.124), writes

$$\begin{aligned} D &= \frac{\rho}{4\pi} U s^2 \sum_{n=1}^{\infty} a_n \int\limits_{0}^{\pi} \sin\theta \sin n\theta\ \underbrace{4U \sum_{n=1}^{\infty} n a_n \fint\limits_{0}^{\pi} \frac{\cos n\phi}{\cos\phi - \cos\theta}\ d\phi}_{*}\ d\theta \\ &= \pi\frac{1}{2}\rho U^2 s^2 \sum_{n=1}^{\infty} n a_n^2 \end{aligned} \tag{2.128}$$

where $\phi$ is the equivalent to $\theta$ used in cases involving the dummy variable $\zeta$. This drag and lift expressions further simplify giving them in terms of its coefficients (2.123):

$$\overline{C}_L = \pi A a_1 \qquad \text{and} \qquad \overline{C}_D = \pi A \sum_{n=1}^{\infty} n a_n^2. \tag{2.129}$$

The lift coefficient depends only on the first Fourier coefficient $a_1$ while the drag coefficient depends on all $a_n$ squared. Thus all Fourier coefficients will contribute to an increase of drag, while only $a_1$ influences lift. Hence it is apparent that the optimum spanwise distribution of $\Gamma$ is found if $a_n = 0$ for $n \geq 2$ and that corresponds to an elliptical spanwise distribution of the circulation. Thereby the merit $K$, see equation (2.122), becomes one. For any other spanwise loading $K$ will be larger and essentially the lifting surface will be less efficient (in terms of induced drag). [New77, p.200]

### 2.5.4. Lifting Line Theory

The planar vortex sheets described in section 2.5.2 represent the linearized lifting problem for general three-dimensional lifting surfaces with help of the general vortex density $\gamma(x, z)$. The boundary condition (2.107) describes $v$ that itself will be a surface-integral equation in terms of the unknown vector $\gamma(x, z)$ (similar to the line integral in the two-dimensional case, see $v$ in equation (2.97) ). As $\gamma$ now involves two coordinates, closed-form solutions can not be derived. One is left with the possibility of a numerical solution or further assumptions have to be considered. The latter is topic of this section.

Assuming the aspect ratio $A$ to be large suggests a strip-theory approach. But such two-dimensional approximation would also yield the two-dimensional results, since it neglects that the trailing vorticity must be shed as the wings simply are not of infinite span, respectively $l(z)$ is a function of $z$. The trailing vorticity gives rise to the induced drag and diminishes the lift force. The latter is evident since the trailing vortices induce a downwash velocity that reduces the effective angle of attack of the lifting surface.

It was Prandtl who developed the lifting line theory (LLT). The lifting line approach can be regarded as a second approximation to correct the strip-theory results, and is an outstanding example of the use of asymptotic approximations. [New77, p.201]

Thinking of a large aspect ratio wing, and looking locally at the chordlength as a first order quantity gives rise to assume a slowly varying chordlength that can locally be regarded as constant. This perspective is referred to as the *inner region* where the three-dimensional effects are slowly varying and will be taken into account by a suitably corrected inflow and not directly by the two-dimensional computations. This can thus be described as a second order approximation with help of an inflow velocity and direction unknown in advance.

From the perspective of the *outer region* the spanlength is of order one and the details of the foil geometry are of minor concern. The trailing vortex sheet, absent in the two-dimensional case, governs the outer solution. Thus the situation can be approximated as sketched in figure 2.7(b) where the bound vortices are regarded to be situated along a straight line. From the outer view the planform surface thus reduces to the segment $(-\frac{1}{2}s, \frac{1}{2}s)$ of the $z-$axis. This is a line, the *lifting line*. In regard of figure 2.7(b) it is obvious that a straight line assumption helps simplifying the analysis, but also assumes that there is *no sweepback angle*. [New77, p.202]

The trailing vortices occupy lines from $-\infty < x < 0$ in the trailing vortex sheet $(y = 0,\ z = \zeta)$ but are otherwise independent of $x$. Thus the velocity induced in this plane is exactly half the one from the two-dimensional case where the lines occupy $-\infty < x < \infty$. The two-dimensional result is already used for the vertical velocity in the Trefftz plane (2.120). Taking half its value and denoting it with the subscrip $T$ as the velocity due to the trailing vortices writes

$$v_T(0,0,z) = \frac{1}{4\pi} \int_{-s/2}^{s/2} \frac{d\mathit{\Gamma}(\zeta)}{d\zeta} \frac{d\zeta}{\zeta - z}. \tag{2.130}$$

For conventional planforms and averagely also in general $v_T$ is negative for $|z| < \frac{1}{2}s$ and therefore a *downwash*. Before using $v_T$ to correct the inflow velocity vector is has to be assured that this is by far the most important contribution to the downwash. There are two other influencing sources. First the free vortices within the foil. Their length equals the local chordlength. The latter is small compared to the span and this will have a negligible influence on the downwash compared to the trailing vortices. Secondly it are the bound vortices. From the Biot-Savarat integral, see [New77, p.191], it can be shown that also the correction due to $\gamma_B$ is negligible compared to $v_T$. [New77, p.202,203]

Thus the most significant three-dimensional effect to correct the inner solution is to impose the vertical velocity component $v_T$. This is equally satisfied if considering the change of inflow-angle. Thus calculating the *induced* angle in order to change the effective angle of attack (as it is small: $\tan \alpha_i \cong \alpha_i$). Former simply writes

$$\alpha_i(z) \equiv \frac{v_T}{U} = \frac{1}{4\pi U} \int_{-s/2}^{s/2} \frac{d\mathit{\Gamma}(\zeta)}{d\zeta} \frac{d\zeta}{\zeta - z}. \tag{2.131}$$

From the two-dimensional results (e.g. (2.99) with (2.106)), the circulation of an uncambered airfoil is given by $\mathit{\Gamma} = \pi U l \alpha$. The two-dimensional circulation referred to in the inner solution ($\mathit{\Gamma}_{2D}(z)$) can thus be corrected by the amount of circulation caused by $v_T(z)$ with help of $\alpha_i(z)$ using this flat plate result. This circulation used to correct $\mathit{\Gamma}_{2D}$ equals $\pi U l \alpha_i$ and is generally negative since $v_T$ is negative. [New77, p.203]

Thus, arriving at *Prandtl's lifting line* equation, the corrected local circulation expresses

$$\mathit{\Gamma}(z) = \mathit{\Gamma}_{2D}(z) + \frac{1}{4} l(z) \int_{-s/2}^{s/2} \frac{d\mathit{\Gamma}(\zeta)}{d\zeta} \frac{d\zeta}{\zeta - z}, \qquad -\frac{1}{2}s < z < \frac{1}{2}s \tag{2.132}$$

where $\mathit{\Gamma}_{2D}(z)$ is the two-dimensional circulation including the effect of camber and geometric angle of attack, while the last term represents the correction due to the induced angel of attack. Similarly to the Kutta condition in the two-dimensional case, here the circulation has to vanish at the tips $\mathit{\Gamma}(\pm\frac{1}{2}s) = 0$ making the equation unique. In (2.132) appears the derivative of the unknown function in the integrand. Such equations are named integrodifferential equation and this one can not be solved analytically for general planform geometries. [New77, p.203]

Applying the same Fourier series as before, see (2.124) and use the Glauert integral (2.127) yields the induced angle of attack

$$\alpha_i(\underbrace{s/2\ cos\theta}_{z}) = -\frac{1}{\pi}\sum_{n=1}^{\infty} na_n \fint_0^{\pi} \frac{\cos n\phi}{\cos\phi - \cos\theta}\, d\phi = -\sum_{n=1}^{\infty} na_n \frac{\sin n\theta}{\sin\theta}. \tag{2.133}$$

Using $\alpha_i$ in (2.132) yields (2.134) and consequently the system of linear equations

$$\mathit{\Gamma}(s/2\ \cos\theta) = \mathit{\Gamma}_{2D}(s/2\ \cos\theta) - \pi U l(s/2\ \cos\theta) na_n \frac{\sin n\theta}{\sin\theta} \tag{2.134}$$

$$\sum_{n=1}^{\infty} a_n \sin n\theta = \frac{1}{2Us}\mathit{\Gamma}_{2D}(s/2\ \cos\theta) - \frac{\pi}{2s} l(s/2\ \cos\theta) \sum_{n=1}^{\infty} na_n \frac{\sin n\theta}{\sin\theta}. \tag{2.135}$$

$$0 < \theta < \pi$$

Now restricting to an elliptical spanwise distribution of $\mathit{\Gamma}$. That is $a_n = 0$ for $n \geq 2$, for which in the previous section already is shown to have the highest lift / induced drag ratio. Then (2.135) directly yields

$$a_1 = \frac{1}{2Us}\mathit{\Gamma}_{2D}(s/2\ \cos\theta) \left\{ \sin\theta + \frac{\pi}{2s} l(s/2\ \cos\theta) \right\}^{-1} \tag{2.136}$$

In case of an *uncambered* foil $\mathit{\Gamma}_{2D} = \pi U \alpha l(z)$. That, together with requiring the planeform surface to be *elliptical*[10]

$$l(\underbrace{s/2\ \cos\theta}_{z}) = l_0 \sin\theta \tag{2.137}$$

enables to eliminate the dependence of $a_1$ (and therefore $\alpha_i$) on $z$ and equation (2.136) becomes

$$a_1 = \frac{\pi\alpha}{2s} l(z) \left\{ \sin\theta + \frac{\pi}{2s} l(z) \right\}^{-1} = \frac{\pi\alpha}{2s} l_0 \left\{ 1 + \frac{\pi}{2s} l_0 \right\}^{-1}. \tag{2.138}$$

The surface of an ellipse is $S_p = \frac{\pi}{4} s l_0$, thus the aspect ratio (2.58) here writes $A = 4s/(\pi l_0)$ and (2.138) becomes

$$a_1 = \frac{2\alpha}{A+2}. \tag{2.139}$$

---

[10] Note that $z = s/2\ \cos\theta$ and therefore $l(z)$ is not proportional to $\sin(z)$ but to $\sin\theta$. That defines an ellipse and the planform is therefore elliptical. Integrating $\int_{-s/2}^{s/2} l(z)\, dz = -\frac{1}{2} s l_0 \int_0^{\pi} (\sin\theta)^2\, d\theta = -\frac{\pi}{4} s l_0$ yields the surface of an ellipse (equally $-\pi$ could have been used as the upper limit leading to a positive sign). Similarly the prior introduced expansion of $\mathit{\Gamma}(z)$ (see (2.124)) is elliptical if the only nonzero $a_n$ is $a_1$.

Consequently the equations (2.125), (2.128) and (2.129) reduce accordingly to the uncambered, elliptical planform results for wings without sweepback angle

$$\overline{L} = \pi\rho U^2\alpha\frac{s^2}{A+2} \qquad \text{and} \qquad D = \frac{1}{2}\pi\rho U^2\alpha^2\frac{s^2}{A+2}, \tag{2.140}$$

$$\overline{C}_L = \frac{2\pi\alpha A}{A+2} \qquad \text{and} \qquad \overline{C}_D = \frac{4\pi\alpha^2 A}{(A+2)^2} = \frac{\overline{C}_L^2}{\pi A}. \tag{2.141}$$

The two-dimensional results are recovered as $A \to \infty$. That is the induced drag vanishes and the lift coefficient approaches $2\pi\alpha$. [New77, p.204]

# 3. Theory Part II: Turbulence Modeling

The chapter turbulence modeling deals with the needed theoretical basics regarding the turbulence modeling used in this thesis.

## 3.1. What Turbulence Really Is

It is difficult to briefly, but precisely, state what turbulence really is. Descriptions vary from: a fluctuating, disorderly motion [Whi06], a flow that is not laminar[1], or:

> Turbulence is a state of fluid motion, a flow regime [not a fluid property]. It is an irregular condition in which physical quantities vary nearly randomly in time and space.
>
> – B. A. Pettersson Reif

But there is no general definition of turbulent flow and it is thus common to describe its characteristics: The most important ones are (taken from [DR11], [Whi06]):

- High Reynolds number $Re = \frac{UL}{\nu} \gtrsim 10^3$, where U and L are the characteristic velocity and length scale respectively (ratio of inertial to viscous forces).
- Diffusive; mixing is much stronger than that due to laminar (molecular) action.
- Dissipative; turbulent kinetic energy is transformed into internal energy by viscous stresses.
- Vorticity is a crucial feature of turbulence; the fluctuations are never irrotational.
- Self-sustaining; once triggered, turbulent flow can maintain itself by producing new eddies to replace those lost by viscous dissipation.
- Three dimensional; turbulence cannot sustain itself in one or two dimensional flows.[2]

---

[1] Laminar (from lamina “plate”) meaning a fluid streaming in layers without mixing, thinking about perfect streamlines like they are known from potential theory.

[2] It can be shown from the vorticity transport equation. And precisely speaking two dimensional flows only exist in theory. For modeling reasons it is important to keep this fact in mind.

- Satisfies the continuum hypothesis, meaning the smallest scales are bigger than the mean free path.

A classical illustration refers to Osborne Reynolds who, in 1883, performed pipe flow experiments. Stokes, at that time, had shown that Poiseuille pipe flow is a solution to the Navier-Stokes and continuity equations ((2.18) and (2.17)). Poiseuille's formula for the pressure drop versus flow rate agreed with experiments up to some certain velocity, after which the flow rate was unpredicted. Reynolds injected a thin stream of dyed water into the main flow. As long as the dye filament remained thin throughout the length of the pipe, Poiseuille's law was valid. The fluid flow in cylindrical layers which moved relative to each other; it was in a laminar regime. At higher speeds the colored fluid line became unstable and eventually disintegrated into a complex flow, which could give the fluid in the pipe a general colored look. Nowadays one would say, Reynolds experiment became unstable and made a transition to turbulence above a critical Reynolds number. [DR11, p.46], [Irg08, p.304,305]

Also in order to confirm that the Navier-Stokes and continuity equations not only govern the laminar flow, but also the turbulent flow regime, Reynolds invented the so called 'Reynolds averaging', see section 3.4. Today, the doubts if these equations ((2.18) and (2.17)) are the equations of turbulent fluid flow have been laid to rest.[3] [DR11, p.46]

## 3.2. The Turbulence Problem

> The turbulence problem[..]is not a problem of physical law; it is a problem of description. Turbulence is a state of fluid motion, governed by known dynamical laws – the Navier-Stokes equations in case of interest here. In principle, turbulence is simply a solution to those equations.
>
> – Durbin and Reif [DR11, p.4]

But the exact solutions are under most circumstances impossible to find. Analytic solutions are only known for a few special (laminar) cases. Thanks to an increased computer power, numerical solutions of the complete flow phenomena have in a (very) limited range become approachable. They are called *direct numerical simulations* (DNS).

White [Whi06, p.401] states (in 2006) that with supercomputers meshes with 100 million nodes can be solved, but DNS requires extremely fine meshes and is thus still restricted to Reynolds numbers below $10^4$. The reason is that a DNS must resolve both, the largest, and smallest eddies and scales that are dynamically significant in the flow [Rey90]. And the

---

[3] The concerns that have arisen were whether large accelerations that violate the linear stress strain relation for Newtonian fluids could occur, or even violate the continuum assumption [DR11, p.46].

smallest scales, known as Kolmogorov microscales, become even smaller with increasing Reynolds number.

To give more insight into such illustrating relations the next section proceeds with more information about their origin, dimensional analysis. And it also shows why the smallest scales become smaller with increasing $Re$.

## 3.3. Dimensional Analysis and Scales of Turbulence

This section makes use of dimensional arguments to derive different scales of turbulence and discusses the concept of the *energy cascade*. If not mentioned otherwise, the information in this section cites to Durbin and Reif [DR11].

Considering a fully developed shear layer, one can assume the largest eddies to be in the order of the thickness of the layer itself $l_0$ and to have a characteristic velocity $u_0$. Imaging a length scale for the smallest eddies $\eta \ll l_0$, then the associated local Reynolds numbers $u\eta/\nu$ is much smaller than $u_0 l_0/\nu$. That emphasizes the importance of viscous forces on small scales.[4] Upon this argumentation it seems reasonable to assume that the largest scales are produced by mean shear and the smallest scales dissipated by viscosity. Kolmogorov argued that this requires an intermediate range of scales, called *inertial subrange*, across which the energy is transferred without being produced or dissipated. Further thinking of an equilibrium state, the energy flux through this range then must equal the rate at which energy is dissipated at small scales. In such an equilibrium state, the rate of energy dissipation per unit mass, denoted $\varepsilon$,[5] equals the rate at which energy cascades across the inertial subrange. Since in practice an equilibrium state only is present in special cases, the assumption of a *local equilibrium* in the inertial subrange and in the dissipation range usually is invoked. That is assuming that the small scales adapt almost instantaneously to such an equilibrium, while the large scales might depart from it.

Now seeking arguments for a dimensional analysis to describe the inertial subrange region: It is an overlap region between the large scale, energetic range and the small scale dissipative range. Since the large scales are not directly affected by molecular dissipation, the inertial subrange can also not depend on it and thus has to be independent of viscosity.

It is reasonable to assume that the small scales are of a fairly universal form, independent of the flow width. Since the inertial subrange region also shares its range with the small scale region, it can neither depend on the flow width. Then the variable left for dimensional arguments is $\varepsilon$ the rate of energy dissipation. Considering a characteristic eddy size $r$ for an

---

[4] The Reynolds number displays the ratio between inertia and viscous forces, this is directly visible writing $Re = \frac{\rho U^2 L^2}{\mu U L} \left(= \frac{UL}{\nu}\right)$.

[5] The rate of energy dissipation per unit volume hence writes $\rho\varepsilon$

eddy in this region, it's energy then is in the order $(\varepsilon r)^{2/3}$. This is known as Kolmogorov's 2/3 law, which in Fourier space becomes the -5/3 law.

Figure 3.1 shows the spectral energy density $E(\kappa\eta)$ by a log-log plot. Here, $\kappa$ stands for the wave number being inversely proportional to length $\kappa \sim 1/l$. It is further normalized with Kolmogorov micro-lengthscale $\eta$, so that the dissipation range lies around $\kappa\eta = \mathcal{O}(1)$. Precisely formulated $E(\kappa\eta)$ is the energy density per unit wave number per unit mass, here, normalized by the micro-lengthscale $\eta$. In physical space that is the distribution of energy across the scales of eddies. As it can be seen (and measured) in Fourier space, Kolmogorov's -5/3 law, shown as $k^{-5/3}$, matches exactly the behavior of the experimental data in the inertial subrange.

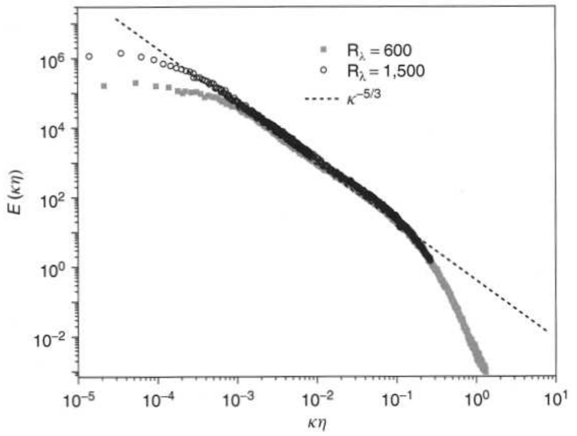

Figure 3.1.: Experimental spectra measured by Saddoughi and Veeravalli (1994) [SV94] in the boundary layer of an enormous wind tunnel; therefore at very high Reynolds number and thus showing the -5/3 law over several decades; source [DR11, p.17]

A turbulent time scale, denoted $T_0$ can be formed from the turbulent kinetic energy $k$ and the rate at which it is dissipating ($\varepsilon$). It is $T_0 = k/\varepsilon$ and is sometimes referred to as eddy lifetime or integral time-scale. As is formed by the overall turbulent kinetic energy, which is mainly contained by the large scales, $T_0$ is a scale of the larger, more energetic eddies. Also a turbulent Reynolds number can be found. It is defined as $Re_T \equiv k^2/\varepsilon\nu$.

The thesis already made use of Kolmogorov's microscales, the smallest scales in turbulence, however these are yet to introduce. As this scaling applies to the dissipation range, they are not to confuse with Kolmogorov's -5/3 respectively 2/3 law, which is applied at scales larger than the dissipation scales. These smallest scales have little energy (see also figure 3.1) thus turbulent kinetic energy $k$ is no appropriate scaling. But viscosity $\nu$ plays an important role in the dissipation range and also $\varepsilon$, which is defined as the rate of energy dissipation by unit mass, is the right scale here. Kolmogorov's microscales for length, velocity and time thus respectively read:

$$\eta \equiv \left(\frac{\nu^3}{\varepsilon}\right)^{\frac{1}{4}} \quad , \quad u_\eta \equiv (\nu\varepsilon)^{\frac{1}{4}} \quad \text{and} \quad \tau_\eta \equiv \left(\frac{\nu}{\varepsilon}\right)^{\frac{1}{2}} . \tag{3.1}$$

Forming a Reynolds number of Kolmogorov's microscales $\eta u_\eta/\nu = 1$. That shows the importance of viscous forces and is indicating that this scales characterize the very smallest, dissipative eddies [Pop00, p.185].

Since $\varepsilon$ also bridges the gap to larger scales, it plays a dual role. Expressing $\varepsilon$ in terms of the larger scales $\varepsilon \sim u_0^3/l_0$ and inserting into Kolmogorov's microscales (3.1) yields

$$\eta/l_0 \sim Re^{-3/4} \quad , \quad u_\eta/u_0 \sim Re^{-1/4} \quad \text{and} \quad \tau_\eta/\tau_0 \sim Re^{-1/2}. \tag{3.2}$$

All ratios show a similar behavior of decreasing microscales with increasing Reynolds number, a knockout argument for DNS. Figure 3.2 sketches this difference schematically.

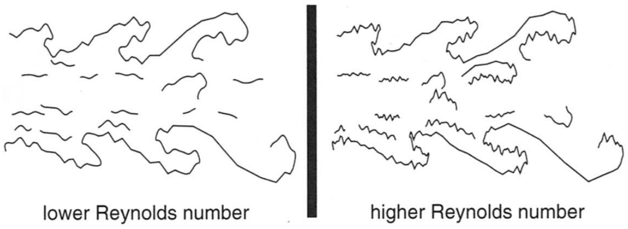

Figure 3.2.: Schematic difference of high and low Reynolds number turbulence; source [DR11, p.13]

Following Reynolds tracks of averaging, the next section talks about the statistical framework used in “Reynolds averaging”.

## 3.4. Statistical Tool: Averaging

As the equations of turbulent fluid flow are known (discussed earlier in section 3.1), turbulence is in principle *deterministic*. But thinking of the chaotic, nearly random motion that can be found in turbulent flows, it also seems to have some sort of *stochastic nature*.

In any turbulent flow field there are, unavoidably, perturbations in initial conditions, boundary conditions and material properties. The evolution of flow at high Reynolds numbers is extremely sensitive to such perturbations. That is illustrated, considering Lorenz equations, a set of ordinary differential equations. Lorenz studied the solutions these equations deliver, when their initial conditions are marginally changed (e.g. by 0.001 %). By numerical integration in 1963, Lorenz showed that their solutions first are indistinguishable but then, beyond some point, begin to differ completely. As the consequence of this extreme sensitivity to initial conditions, the state of the system beyond such a point in time[6] cannot be predicted. [Pop00, p.37]

Not only that it usually is unfeasible to solve all details of a turbulent flow field, and that it, due to small perturbations in initial conditions, boundary conditions and material properties, simply is unpredictable what a system after a long enough time instantly will look like, but for many purposes it only is of concern what the general flow behavior is like.

In the sight of this using a statistical approach to simplify the problem is somewhat logical. In order to be able to better describe turbulent flows, averaging the exact laws is promising and the classical approach. But it leads to more unknowns as equations, and therefore modeling is needed, as will be seen.

First introducing the concept of Reynolds averaging, *averaged* or, in other words, *mean* variables are either indicated by capital letters, e.g. $U$, or by an overline, essentially needed in cases where the average is to be taken of a product and not just of single variables, e.g. $\overline{uu}$. In contrast to all other chapters, the notation for *total* variables here makes use of a tilde, like e.g. $\widetilde{u}$. This notation provides better readability, as it is in most cases not necessary to carry along additional signs. Subtracting the mean variables from the total variables yields the so called *fluctuating* variables. They are indicated with lowercase letters, e.g. $u \equiv \widetilde{u} - U$ where $U \equiv \overline{\widetilde{u}}$. Thus, using this so called *Reynolds decomposition*, the total velocity and the total pressure field respectively write

$$\widetilde{u}_i = U_i + u_i \qquad \text{and} \qquad \widetilde{p} = P + p. \tag{3.3}$$

The general definition of mean variables is the *ensemble average*, given for some field variable $f(x_i, t)$ that writes

$$\overline{f(x_i,t)} = \lim_{N \to \infty} \frac{1}{N} \sum_{m=1}^{N} f_m(x_i,t)\,. \tag{3.4}$$

This implies that an experiment has to be repeated infinitely often and that the variables have to be recorded at all times at all points in space, in order to form averages of all experiments at all times at all points in space, the mean values. A fairly difficult approach.

But there are circumstances that provide simplification: *statistical stationary*[7] turbulence. That is the statistics are independent of the time origin and $f(t)$ and $f(t+t_0)$ have

---

[6] In the particular example the initial conditions are known only within $10^{-6}$ resulting in no further useful predictions after $t = 35$.

[7] In other words, stationary means translational invariance in time [DR11, p.20], homogeneity in time [DR11, p.10]

the same statistical properties for any $t_0$, thus $\overline{f(t)} = \overline{f(t+t_0)}$ [DR11, p.20]. Then, and only then the ensemble average coincides with the time average

$$\overline{f(x_i)} = \frac{1}{T}\int_{t_0}^{t_0+T} f(x_i,t)\,dt \tag{3.5}$$

given also $T \to \infty$. The time average is essentially an average over an ensemble of times where $T$ is a suitable time scale much larger than the time scale of any turbulent fluctuations [Fos09, p.13]. Figure 3.3 visualizes the effect of averaging.

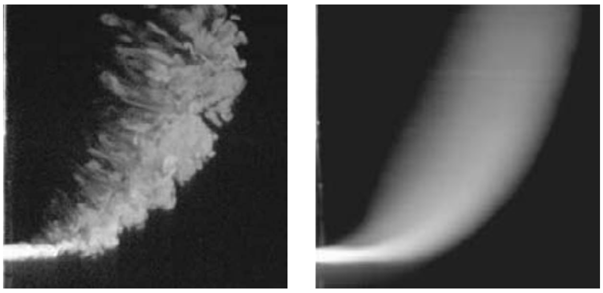

(a) Instantaneous (b) Time averaged

Figure 3.3.: Instantaneous and time averaged views of a yet in a cross flow. Measured in an updraft wind tunnel with air as crossflow fluid and nitrogen as jet fluid; source [SM04, p.9,10]

But most flows are not statistically stationary and than equations (3.4) and (3.5) are not equivalent. An illustrating example of unsteady turbulent flow is the flow in a tidal estuary. Here T is easily chosen to be much smaller than the tidal time scale and $\overline{f(x_i)}$ is then slowly varying in time [Whi06, p.406]. Figure 3.4 sketches the differences between steady and unsteady laminar and turbulent flow.

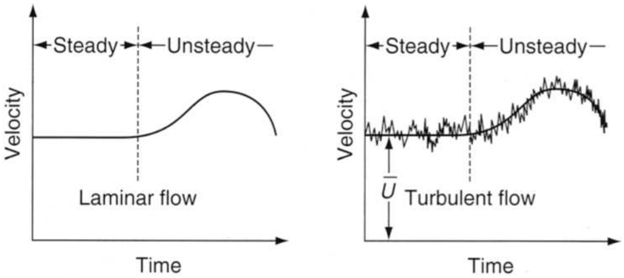

Figure 3.4.: Sketch of steady and unsteady laminar and turbulent flow; source [Whi06, p.407]

It is important to note that ensemble averaging is a linear operation. The following relations illustrate the consequences. Note that the left and the right column contain the same statements, but the ones to the right use the notation introduced above (equation (3.3))

$$\overline{\overline{f}} = \overline{f} \qquad \overline{U} = U \tag{3.6}$$

$$\overline{f - \overline{f}} = 0 \qquad \overline{u} = 0 \tag{3.7}$$

$$\overline{af} = a\overline{f} \qquad \overline{a\widetilde{u}} = aU \tag{3.8}$$

$$\overline{f + g} = \overline{f} + \overline{g} \qquad \overline{\widetilde{u} + \widetilde{v}} = U + V \tag{3.9}$$

$$\overline{fg} = \overline{f}\,\overline{g} + \overline{(f - \overline{f})(g - \overline{g})} \qquad \overline{\widetilde{u}\widetilde{v}} = UV + \overline{uv}. \tag{3.10}$$

An essential point is noting that per definition $\overline{u} = 0$ and also $\overline{Uu} = 0$, but $\overline{uu} \neq 0$.

## 3.5. Governing Equations

As discussed earlier the governing equations of turbulent fluid flow are the Navier-Stokes and the continuity equations introduced in chapter 2.2 (equations (2.18) and (2.17)). Applying the tilde notation and including the volume forces into the pressure term those equations write

$$\partial_t \widetilde{u}_i + \widetilde{u}_j \partial_j \widetilde{u}_i = -\frac{1}{\rho}\partial_i \widetilde{p} + \nu \nabla^2 \widetilde{u}_i \tag{3.11}$$

$$\partial_i \widetilde{u}_i = 0. \tag{3.12}$$

The latter is achieved by using a gravitational potential, say $\Phi$.[8] It represents the effect of gravity (or any other conventional volume force). For the earths constant gravity field holds $\Phi = gy$ with $g \cong 9.81$ m/s$^2$ (in a coordinate system with an upward pointing y-axes). Thus the gravity vector writes $g_i = -\vec{j}g = -\partial_i \Phi$. Using $\widetilde{p}^{\#}$ to denote the unmodified pressure, a *modified pressure* term $\widetilde{p} = \widetilde{p}^{\#} + \rho\Phi$ can be formulated and is accounted for in the outlined Navier-Stokes equations.

As outlined, numerical (and analytical) solutions to these equations are in most real cases not achievable. Introducing the outlined Reynolds averaging yields further equations that are suited for modeling. The next subsections introduce the famous Reynolds averaged Navier-Stokes as well as further transport equations. Thus generally speaking all are Reynolds averaged equations.

---

[8] $\Phi$ stands for the potential energy per unit mass associated with gravity.

### 3.5.1. Reynolds Avaraged Navier-Stokes

Reynolds averaged Navier-Stokes (RANS) equations are found by introducing the Reynolds decomposition (3.3) into (3.11) and (3.12) and averaging the equations. That yields

$$\partial_t U_i + U_j \partial_j U_i = -\frac{1}{\rho}\partial_i P + \nu \partial_j \partial_j U_i - \partial_j \overline{u_j u_i} \tag{3.13}$$

$$\partial_i U_i = 0. \tag{3.14}$$

As a result of the averaging, $U_i$ and $P$ only vary in time if the flow is statistically unsteady.

The last term in (3.13) evolves from the advective term ($\widetilde{u}_j \partial_j \widetilde{u}_i$). The continuity equation allows to write it in the given form ($\overline{u_j \partial_j u_i} = \partial_j \overline{u_j u_i}$). One can thus state that this term represents the *averaged effect of turbulent advection on the mean flow field.* Multiplying the density back to the l.h.s. explains why this term is the derivative of the so called *Reynolds stresses* or *Reynolds stress tensor* $\rho \overline{u_j u_i}$ that has the dimensions $[\mathrm{kg}/(\mathrm{m\,s}^2)]$.

This nine component tensor contains, due to symmetry ($\overline{u_j u_i} = \overline{u_i u_j}$), six unknowns. In contrast to the not averaged set of equations one is now left with unclosed equations. There are four equations ((3.13) and (3.14)) with a total of 10 dependent variables ($U_i, P$ and $\overline{u_j u_i}$). Thus this closure problem forms the need for turbulence modeling.

Before looking at possible closures further usefull transport equations are presented.

### 3.5.2. Further Reynolds Averaged Equations

More usefull transport equations equations can be found. All outlined transport equations relate the total rate of change of some quantity to a physical phenomena describing the transport or respectively the distribution of this quantity.

Subtracting (3.13) from (3.11) yields the momentum equation of the fluctuating field

$$\partial_t u_i + U_k \partial_k u_i + u_k \partial_k U_i + \partial_k (u_k u_i - \overline{u_k u_i}) = -\frac{1}{\rho}\partial_i P + \nu \partial_k \partial_k u_i. \tag{3.15}$$

This equation is especially helpful since it can be used to form a transport equation for the Reynolds stresses. Evaluating $\overline{(3.15)_i(u_j)} + \overline{(3.15)_j(u_i)}$ after some algebra yields

$$\begin{aligned}\underbrace{\partial_t \overline{u_i u_j} + U_k \partial_k \overline{u_i u_j}}_{\text{total rate of change}} = -\frac{1}{\rho}\underbrace{\left(\overline{u_j \partial_i p} + \overline{u_i \partial_j p}\right)}_{\text{redistribution}} - \underbrace{2\nu \overline{\partial_k u_i \partial_k u_j}}_{\text{dissipation}} \\ \underbrace{-\partial_k \overline{u_k u_i u_j}}_{\text{turbulent transport}} \quad \underbrace{-\overline{u_j u_k}\partial_k U_i - \overline{u_i u_k}\partial_k U_j}_{\text{production}} + \underbrace{\nu \nabla^2 \overline{u_i u_j}}_{\text{viscous diffusion}}\end{aligned} \tag{3.16}$$

These are the *Reynolds stresses transport equations* (RSTE). Note that (solving for the Reynolds stresses) these equations come up with three unclosed terms: the redistribution, dissipation and the turbulent transport.

Once the RSTE equations are found, one obtains a transport equation for the turbulent kinetic energy ($k \equiv \frac{1}{2}u_iu_i$) by setting the indices $i = j$ (thus summing over $i$) as well as multiplying with 1/2, which yields

$$\begin{aligned}\partial_t k + U_k\partial_k k = -&\underbrace{\frac{1}{\rho}\partial_i\overline{u_ip+}}_{\text{pressure-diffusion}} \quad -\underbrace{\nu\overline{\partial_k u_i\partial_k u_i}}_{\text{dissipation}} \\ &\underbrace{-\frac{1}{2}\partial_k\overline{u_ku_iu_i}}_{\text{turbulent transport}} \underbrace{-\overline{u_iu_k}\partial_k U_i}_{\text{production}} + \underbrace{\nu\nabla^2 k}_{\text{viscous diffusion}} \end{aligned} \tag{3.17}$$

Alternatively $\frac{1}{2}\overline{u_i(3.15)}$ brings up the same result (abbreviated TKE). The turbulent kinetic energy $k$ is a scalar quantity and effectively describes the kinetic energy per unit mass due to the fluctuations.

## 3.6. Categories of Turbulent Flow

There are different possibilities to classify turbulent flow. Presented here are the categories used in [Rei10]. They might suite best from a theoretical point of view and have no sole claim. In any case, table 3.1 provides an overview over different categories used in turbulence modeling. As indicated by the complexity-arrow, there are approximations that allow further simplification of the problem and thus further (mathematical) insight. For example, isotropic flows are used to find constants of some turbulence models. That is possible since the isotropy assumptions leads to to great mathematical simplifications [DR11, p.10]. The meaning of these categories is described as follows:

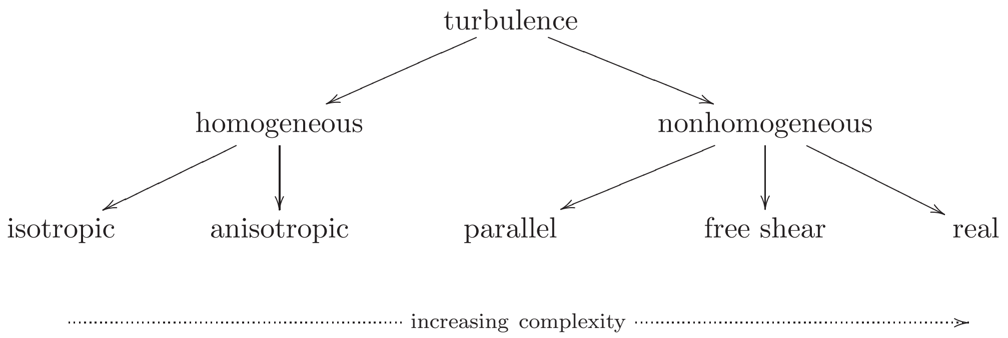

Table 3.1.: Categories of Turbulent Flow

- Homogeneous: stands for spatial homogeneity; that is the statistics, in particular the correlations of fluctuating components are not functions of position. E.g. $\partial_1\overline{u_1u_2} = 0$ (while $\overline{u_1u_2}$ generally is nonzero). That implies that the turbulent diffusion is zero; a classical example is homogeneous parallel shear flow; homogeneity causes

$k(t \to \infty) \to \infty$ and $\varepsilon(t \to \infty) \to \infty$! But that is a logical consequence since one describes an ideal, infinite source ($\frac{dU}{dy} = \text{const.}$).

  - Isotropic: means that the correlations of fluctuating components have no directional dependence, that is $\overline{u_1^2} = \overline{u_2^2} = \overline{u_3^2}$ while all nondiagonal elements are zero. It is a special subset of homogeneous turbulence since isotropic turbulence necessarily is homogeneous. Isotropic turbulence describes decaying turbulence since the production becomes zero (since it here can be written as $\overline{u_1^2}(\partial_k U_k) = 0$).
  - Anisotropic: here consequently the fluctuations have no directional dependence and are not confined to have the same magnitude in all directions.

- Nonhomogeneous: the correlations of the fluctuations components depend on the spatial position. Thus they necessarily have to be anisotropic.
  - Parallel: in the sense of self-similar flows, e.g. fully developed plane channel flow.
  - Free shear and boundary layer flows.
  - Real: standing for fully realistic flows; the real life so to speak.

## 3.7. Closure Modeling

DNS requires way too much computational power to be of general applicability. In addition, the information of interest usually is not the one shown in figure 3.3(a), but the time-averaged counter part 3.3(b). Simply averaging the governing equations to obtain the averaged view leads to unclosed equations. That is the case since the Navier-Stokes equations are nonlinear (advective term). Now it remains the task to find relations that somehow close the RANS equations. Constitutive relations are sought and necessarily will somehow have to rely on empirical information. Note that the aim is to describe $\overline{u_i u_j}$ without ever knowing the instantaneous fluctuations.

Different strategies exist and are summarized in figure 3.5. It also reveals which type of fundamental theories the individual models are build on.

### 3.7.1. Boussinesq Eddy Viscosity Hypothesis

But what can be used to model the Reynolds stresses? Turbulence is not a property of the fluid, but of the flow. So the Reynolds stresses should depend on a quantity related to the flow. They should also be independent of the coordinate system, which generally speaking requires Galilean invariance.

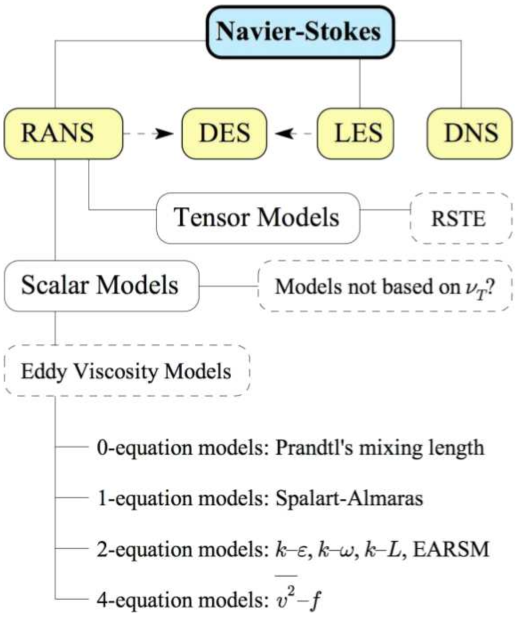

Figure 3.5.: Overview over turbulence models and its relations; source [Fos09, p.24]

The mean rate of strain tensor $S_{ij} = \frac{1}{2}(\partial_j U_i + \partial_i U_j)$ fulfills these two loose criteria and can thus be used to formulate a general linear model. The first one to do so was Boussinesq who in 1877 formulated the Boussinesq eddy viscosity hypothesis [Sch07]. It reads

$$\overline{u_i u_j} = \frac{2}{3} k \delta_{ij} - 2\nu_T S_{ij} \tag{3.18}$$

where $\nu_T$ is the eddy viscosity. This hypothesis is found by requiring the tensor to be of a general form, say $\overline{u_i u_j} = a\delta_{ij} + bS_{ij}$. The special case of $\overline{u_i u_i}$ essentially equals two times the definition of $k$. Since $S_{ii} = 0$ it remains only $a3 = 2k$ and thereby the first constant is determined (by the unknown $k$). $b$ has to have the same dimensions as viscosity $\mathrm{m}^2/\mathrm{s}$ and Boussinesq choice felt to $b \equiv -2\nu_t$. Now the closure problem is reduced from six to two unknowns, $\nu_T$ and $k$, and it exist many models to predict those.

### 3.7.2. Models with scalar variables

The eddy viscosity hypothesis forms the backbone of numerous scalar variable models ($\nu_T$ and $k$ are scalars).

There are zero equation models like Prandtl's mixing length model, one equation models like Spalart–Allmaras and two equation models like the k-epsilon or the k-omega model. Several more exist, also models with more than two equations, like the four equation $v^2 - f$ model.

A very classical one is the k-epsilon model. It contains transport equations for $k$ and $\varepsilon$ and models the eddy viscosity with help of dimensional arguments. The relations are deduced from the TKE equation (3.17). They employ a constitutive gradient model for the pressure diffusion and the turbulent transport. In total, five parameters evolve. Those are determined with the help of theoretical considerations under different assumptions of e.g. isotropic turbulence (decaying and homogeneous), plane channel flow, homogeneous shear flow, the constant stress layer (inner region see section 3.9) and, of course, by experiments.

The shear stress transport turbulence model (SST) is mainly used in the simulations of this thesis. Briefly stated it is a mixture of $k$–$\epsilon$ and, close to walls, a $k$–$\omega$ type of modeling. The main developer behind this model is Menter, see for example [Men09] for his (2009) review of the SST model.

### 3.7.3. Models with tensor variables

Even though not applied here it must for the sake of completeness be stated that there is also a different branch of models modeling the Reynolds stresses. They are based on tensor variables and do not build on the eddy viscosity hypothesis. Instead, closure models for the Reynolds stresses based on the the Reynolds stress transport equation (RSTE) are used to close the problem in a more advanced way. One can find different names for it like second-moment closure (SMC), (differential) Reynolds stress modeling (RSM) or Reynolds stress transport (RST).

The price of increased complexity brings several advantages e.g. regarding anisotropic turbulence (now modeling a tensor and not scalar quantities). And also the situation concerning the intrinsic assumption of eddy viscosity based models that $\overline{u_i u_j}$ is locally determined with $S_{ij}$, which is referred to as an instantaneous equilibrium (missing memory effect of turbulence), is enhanced. More information can for example be found in [DR11, ff.155] or [HJ02].

In the comparative study of Viti and Schetz [VS05] it is concluded that eddy-viscosity based models are simpler to use compared to Reynolds stress models and it is also mentioned that the computing time of, here in particular the Wilcox's Reynolds-stress model, is found to be ca. 2.5 times longer than with the $k-\omega$ Wilcox model. The latter uses ca. 10 % more computing time than the one-equation Spalart-Allmaras model.

## 3.8. Large Eddy Simulation

Large Eddy Simulation (LES) is a combination of DNS and turbulence modeling. Since in a DNS the grid has to resolve all scales, most of the computational expenses of a DNS go to the smallest scales. In LES just the bigger eddies are resolved while the smaller scales (refer to subgrid scale (SGS)) are modeled. That seems promising since one can expect that the small scale eddies are more universal than the large scale eddies, which are directly affected by the flow geometry. Especially in flows over bluff bodies, where unsteady separation and vortex shedding is involved, LES is expected to be more reliable than Reynolds stress models [Pop00, p.558].

Conceptual steps in LES are (with reference to [Pop00, p.559]):

- A filtering is applied to decompose the velocities into a filtered (resolved) and a residual (SGS) component that will be modeled.
- Filtering the Navier Stokes equations gives the equations of evolution for the filtered velocity field. These equations contain an unclosed term, the residual stress tensor (SGS stress tensor).
- Closure is obtained by modeling this residual stress tensor, e.g. most simply by an eddy viscosity model.

There are different SGS models, the oldest one is the Smagorinsky model. It has an important parameter referred to as $C$. By a supplement first developed by Germano [GPMC91], the so called dynamic Smagorinsky model, $C$ is dynamically and automatically determined. This is an advantage since e.g. $C$ automatically reduces close to walls. (It has to be smaller close to walls to account for anisotropy). Before, this was achieved manually, or with e.g. van Driest damping. The Smagorinsky constant vanishes for well-resolved laminar flows. Negative values of $C$ are possible and can be viewed as backscatter. But the resulting “backward diffusion” can generate numerical instability so that it is often simply limited to $C \geq 0$. [FR02]

## 3.9. Boundary Layer and Wall Treatment

Naturally, the boundaries cause major challenges in turbulence modeling. The velocity of the fluid right on a rigid boundary equals the velocity of the boundary itself. Thus, the velocity gradient close to boundaries is large and the viscous effects play a dominant role.

In turbulence modeling it often is necessary to imply wall functions in order to capture the (averaged) flow phenomena close to boundaries. Some models like the $k$–$\omega$ model can, if the grid is fine enough, be used all the way to boundaries and do thus not necessarily rely on additional wall treatment. That is not the case for the $k-\varepsilon$ models and neither in general for SMC models (section 3.7.3). One reason is that the turbulent timescale $k/\varepsilon$ tends to zero at the wall. [Fos09, p.35]

Guidance for the necessary wall treatment is found engaging the delighting outcome of the analysis of a classical problem – fully developed plane channel flow, driven by a constant pressure gradient. That is the simplest nonhomogeneous problem. The equations simplify due to the geometry and the statistically stationary situation ($U_i(y)$) as well as the symmetry. The detailed derivation is found in several textbooks, e.g. [DR11, ff.57] or [Pop00, ff.264]. Here, the most important outcomes are illustrated.

From a force balance across a channel section, the wall shear stress is described by $\tau_w = -\frac{dP}{dx}h$, where $h$ is half the channel-width. Defining the frictional velocity $u_* \equiv (\tau_w/\rho)^{1/2}$ and thereby nondimensionalizing the variables of interest yields: wall distance $y_+ = yu_*/\nu$, velocity $U_+ = U/u_*$ and $\overline{uv}_+ = \overline{uv}/u_*^2$. These variables are often referred to as given in dimensionless 'wall', 'plus' or 'inner units'. In addition, defining the 'frictional' Reynolds number $Re_\tau \equiv u_*h/\nu$, allows to write a stress balance in the form

$$1 - \frac{y_+}{Re_\tau} = \underbrace{\frac{dU_+}{dy_+}}_{\text{visoucs}} + \underbrace{\overline{uv}_+}_{\text{turbulent}} \quad . \tag{3.19}$$

Thus the sum of viscous and turbulent stresses varies linearly across the channel. The viscous term is, for all except the very lowest Reynolds numbers, only important close to the walls ($y_+ < 40$). And note that turbulence cannot be maintained when $Re_\tau \lesssim 100$ [DR11, p.59].

From equation 3.19 one can deduce different regimes of $U_+(y_+)$. Figure 3.6 shows a schematic overview of those regimes and the regions close to the wall.

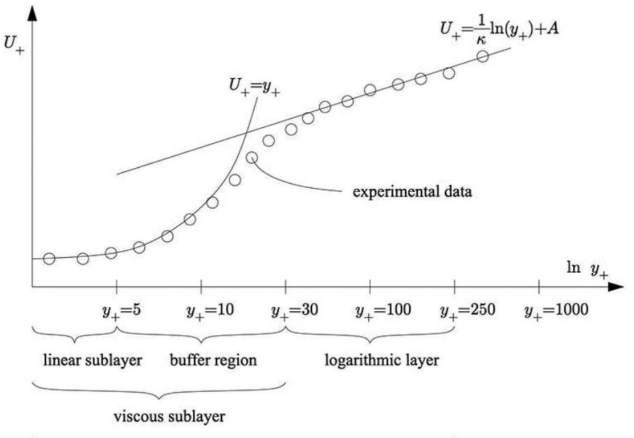

Figure 3.6.: Sketch of the wall regions with graphs of the linear and the log layer; the experimental data is only exemplified; source [Fos09, p.36]

The quasi equilibrium constant stress layer at the smallest $y_+$ gives rise to $U_+ = y_+$ (linear sublayer). The turbulent stresses are zero at very small $y_+$. At the point where turbulent and viscous stresses are equal (ca. $y_+ = 10-15$) the rate of energy production is maximal. A little further away from the wall, say at $y_+ \approx 40$, one enters the logarithmic layer where $U_+ = \frac{1}{\kappa} \ln y_+ + A$. The constants are determined by experiments ($\kappa \backsimeq 0.41$ is the von Kármán constant, $A \backsimeq 5.1 - 5.5$). Note that between the linear sublayer and the logarithmic layer a buffer region is found. That is the region where none of those two approximations are adequate. Here, for example Spaldinger's 'regularization procedure' can be employed.

On the basis of such mathematical (and empirical) descriptions of the boundary-layer CFX allows to employ wall functions to account for the flow phenomena close to boundaries. In comparison to older versions of CFX (versions above 5.4.1) scalable wall functions are used. Earlier, the dimensional distance to the first node, also simply called $y_+$, had to be ensured to not fall below 20 in order to make the blending work (log-layer), as an upper limit 200 was given. Due to the use of a scaling it is no longer problematic to employ wall functions even though $y_+$ is much smaller than 20. For $\omega$ type of models, in particular the SST model an automatic switch to an additional treatment of the viscous sublayer is possible. That requires that a minimum of 15 nodes to fall in the boundary-layer. However, if the near wall grid resolution is below $y_+ < 2$ also a strict low-$Re$ implementation of the model is possible. [ANS09a, ff.117]

# 4. Simulations

Numerical simulations of turbulent fluid flow mainly depend on two fundamental fields of research. The first one is the physical modeling described in chapter 3. The numerics used to solve the stets of equations is the second one. The quality of a numerical solution to given (partial differential) equations not only depends on the scheme used to solve them, but on the quality of its discretization.

In the course of this work the numerical simulations are carried out using Ansys CFX 12. They are based on discretizations obtained with the help of ICEM 12 engaging CAD-data of specific kayak rudders.

This chapter describes the simulations in terms of the tools and methods used to achieve the simulation results. It presents the numerical and discretization methods as well as the challenges that were faced in producing satisfying meshes. Yet, the final simulation results are presented within the results chapter (chapter 6).

## 4.1. Numerical Method

In order to numerically solve the partial differential equations Ansys CFX employs an *element-based finite volume method*. The discretization is based on dividing the fluid domain into numerous small subdomains, the computational cells. The result of this process is referred to as *mesh* or *grid*. Such a mesh is used to construct finite volumes, which are used to conserve relevant quantities such as mass, momentum, and energy.

Ansys CFX is capable to use second-order discretization schemes in space and time. In the course of this work, the high resolution option is used for all final computations. It gives a higher accuracy but is numerically less stable than first order schemes.

Ansys CFX applies a coupled algebraic multigrid algorithm to solve the linear systems that arise from the discretization. The coupled solver uses a fully implicit discretization approach to solve the hydrodynamic equations (for $u$, $v$, $w$, $p$) as a single system. This reduces the number of iterations needed to reach convergence as compared to a segregated solver (in transient computations the steps used to reach convergence of a time step), but it uses more memory. For a steady state problem the time-step behaves like an parameter determining how fast convergence is reached. [ANS09b, ch.1,2]

### 4.1.1. Solver Options

All final stationary computations are carried out with the automatic time step option enabled. Wall functions are always set to automatic. The heat transfer is chosen to be isothermal with the fluid confined to 20° Celsius. Viscosity and density consequently follow the material properties for water at 20°, which is $\rho \cong 998.2$ and $\nu \cong 10^{-6}$.

As a starting point, the whole flow field is initialized with the inflow velocity. The boundary conditions at the inflow wall are a normal velocity and a medium turbulence intensity (5 %). Transition models are not employed, consider chapter 6.3, especially 6.4.3, as well as the conclusions 7 on a discussion of the interesting phenomena regarding transition and (laminar) separation. The walls of the box are free slip walls and at the outflow wall the average static pressure is set as a boundary condition. It is averaged over the whole outlet and the pressure profile bend parameter is chosen to be 0.05. The pressure values referred to are to be seen relative to the reference pressure. The latter is chosen to equal the atmospheric pressure. For all final numerical schemes the high resolution option is chosen. In CFX that means that whenever possible second order approximations are used. In the case of transient calculations the second order backward Euler scheme is explicitly chosen.

### 4.1.2. Convergence

The discrete and iterative nature of numerical simulation leads to a step by step approximation of solutions. If such solutions are correct or not is often unknown. Apart from a direct physical way of evaluating simulation results, there are further measures to give an indication if a possibly correct solution has been reached. The most important one is the residuals. Residuals give the imbalance in the linearized system of discrete equations. One can say that they show how much the left-hand-side of an equation differs from the right-hand-side at any point in space. Such imbalance should approach zero, but already due to the finite precision of computers that can never be true. A simulation is said to be *converged* if the residuals of consecutive iterations approach a small enough finite value. That is not always the case. Such diverging solution can have different reasons, like for example unsatisfactory quality of the mesh, or that a stationary computation is applied on a problem that requires transient consideration.

Ansys CFX provides the maximal and root-mean-square (RMS) residuals. The latter are the weighted average over the domain, since they are computed from squaring, averaging and then taking the square root of the mean. In order to obtain a meaningful convergence criteria both types of residuals are normed. Such normalization divides the raw residuals by appropriate scales in order to e.g. have them independent of the initial guess and, in stationary computations, also of the time step. [ANS09b, ch.9]

## 4.2. Discretization

In order to be able to numerically solve the equations derived in chapter 3 it is necessary to provide a discretization, the mesh. It fills the whole fluid domain and bounds on the used boundaries. In particular here that is a box and the geometry.

This section describes the demands on the mesh and the methods used for its generation. The challenges involved in satisfying this requirements are topic of the next section.

### 4.2.1. Requirements of the Mesh

For numerical simulations the quality of the mesh is vital and the meshing process often makes up the biggest part of CFD projects. There are many different ways one could divide a volume into thousands of subvolumes, the computational cells and respectively nodes and computational points.

In order to meet the demands of the numerical scheme and the physical phenomena involved, the mesh has to fulfill certain requirements. These are that the cells have to be well-shaped. That means to have little skewness and smooth intersections between different cells. The latter signifies that the differences in e.g. volume of neighboring cells should not be too big. It is also required that the cells are sufficiently small to be able to smoothly enough describe the physical phenomena. Thus, if physical quantities are rapidly changing in space, the mesh has to be very fine in that direction. This is generally the case near impermeable surfaces where the velocity gradient is very large. Further there is the aspect ratio of cells that should not exceed appropriate limits depending on the flow velocity and its gradient as well on the used modeling approach. Depending on the aim, when resolving the boundary layer, the first node away from a no slip boundary should be within a certain length measured in wall distance units y-plus.

And not to forget, of course, the limiting requirement of the available computational power. It is therefore necessary to generate a mesh that has a fine enough resolution, while it at the same time should consist of as few nodes as possible. This dilemma calls for a smart distribution of the mesh.

The factor with the computational time becomes even more picky in the case of transient simulations where the Courant number ($u\,\Delta t/\Delta x$) should be kept smaller than one. That requires the timesteps to become smaller as the mesh ($\Delta x$) becomes finer. If a finer mesh is used, the computational time therefore does not only directly increases because the number of computational points is increased, but also because it takes more timesteps to come to a certain point in time.

In order to determine if a mesh (or grid) is adequate enough and leads to valid results, the concept of *grid independence* is introduced. It denotes the case where the simulation accuracy of for example the lift force of the rudder is no longer changing by altering different parameters concerning the grid. (For LES, strictly speaking, a grid independence can first be found when a DNS is achieved, since the gridsize here determines which scales are directly solved and which ones are modeled.)

In general, not only grid independence but a complete *sensitivity analysis* can be accomplished for numerous parameter, not only those directly concerning the grid. The focus of this work lies not on the underlying numerical schemes and the effects of using different schemes are not analyzed. To nevertheless ensure that the inaccuracy regarding the numerical schemes is minimal, all schemes are chosen to use higher resolution, usually denoting second order approximations.

In the course of this work the effects of different closure models, the size of the domain and the grid density as well as the grid quality are analyzed. Further parameters that can be object to investigation are the turbulence intensity, the type of boundary used at the outlet and the timestep size and so on. But, as the time horizon of this work is very limited, solely the foremost mentioned ones are studied. In the authors point of view, these are the most important and interesting ones with regard to the aims of this work.

### 4.2.2. Methods Used for Meshing

The kayak rudder with its surfaces that are curved in both directions, or more precisely stated the curvature is changing in both directions, is the boundary of interest for the meshing process. In many scientific cases the geometry is artificial, simplified or quasi two-dimensional and can be discretized with help of structured meshes. That is not the case here, where it in addition is crucial that the exact form of the rudder is reflected by a fine mesh close to the boundary. Hence, due to the geometry of the kayak-rudder, an *unstructured* mesh is used.

Unstructured implies that the connectivity between the cells is irregular and has to be stored explicitly for each cell. Therefore the form of the cells can vary more freely than in structured meshes where all elements are restricted to be of hexahedral form (in three-dimensions). The latter defines cells to be build of six faces. Unstructured meshes in contrast are build of tetrahedra (in three-dimensions). A tetrahedron is always composed of four triangular faces. Meshes based on tetrahedra thus allow the adaption to more general forms and are also automatically be generated.

Such automatic generation of unstructured meshes can be based on different algorithms like for example the Delaunay triangulation and Octree methods (compare [Per06]). In the course of this work mainly the latter is used. Octree stands for building a tree by refining either by eight or zero children. Thus a cube is divided into eight cubes or remains as it is. Icem uses tetrahedra and divides them. Thereafter its algorithm is cropping and warping the edge points to the boundary and refines the mesh with help of a smoothing. One advantage is that the cell size automatically will, wherever possible, not be smaller than constrained. An other one is that it with Octree is possible to neglect small details in the geometry if the mesh is chosen coarse enough. See [ANS09c, ff.25] and [Pho02].

In Icem unstructured volume meshes can for example be generated under the so called Tetra/Mixed tag. That denotes that pure tetrahedra meshes can be combined with for example hexahedral parts or prism. The latter arises when extruding for example a hexagon-surface to a volume. Note that in Icem the underlying surface may be curved and the needed prism will in general not be a ‘right prism’ but an ‘oblique prism’ since its extruded surfaces can not be hold parallel to each other in order to close the mesh. Prism is especially useful close to boundaries, where a purely tetrahedral mesh is not very satisfying.

Such methods like the inflation layer technique prism and the tetrahedra meshing have to somehow be restrained in order to enforce the generation of the desired form of a mesh. Therefore different techniques are available. Used in the course of this work are constrains in the form of

- lines,
- surfaces,
- density lines and boxes as well as
- the inflation layer technique prism.

All of these techniques come with a bundle of adjustable parameters. In addition there are also a few global parameters like the global scaling of a maximum seed size. A method that has not been mentioned is the combination of a hexahedral core with tetrahedral surrounding including a possible prism-mesh at the boundaries. With this so called Hexa-core method (hybrid mesh) the author however did not at any parameter achieve satisfying smooth meshes of acceptable size.

It is important to note that the tetrahedra have to be grown in size steps of the form $2^n$ (before smoothing takes place). Thus the smallest tetrahedron restriction determines the possible sizes of the others.

The process of meshing is engaged in an iteration loop of simulating, checking the results and working on the geometry. The author kept track of the parameters used for the different meshes and the resulting pros and cons of certain achievements. This track-list contains around 100 files. And behind each noted file usually hide multiple trials of mesh generations. As the full generation of a volume mesh, including the inflation layers, easily can take half an hour on the PC available (depending on the number of nodes and further parameters like the layers of prism), one can say that already the computational time only generating the meshes took weeks.

## 4.3. Challenges in the Discretization

The previous section describes the methods used and the requirements behind the mesh generation. This section outlines its process in the evolution of this master's thesis. It is divided up into two parts: One concerns the challenges mainly related to the geometry and the other one the challenges directly related to the meshing. Both nevertheless work hand in hand.

### 4.3.1. The Geometry in Regard to the Mesh

The geometry data available is of iges format (Initial Graphics Exchange Specification). Importing the given files into Icem yields kayak rudders with surfaces that are no longer continuous. Especially the surfaces along the edges (mentioned as curvature surface) of the rudder are no longer of the intended form, as can be seen from figure 4.2(a).

To generate an appropriate mesh, not only the geometry of the intended form is required, but also its surfaces have to be exact and error-free enough to allow the generation of a surface-mesh of a certain quality.

The rudder is symmetric about the $xy$-plane, see figure 4.1(a). For information about the coordinate system used, consider figure 4.1(d). That differs from the introduction-figure 1.4 only in terms of the equal but opposite direction of forward motion. The first is chosen in order to be able to define a positive free stream velocity in the simulations.

The geometry of the rudder is reflected by three different surfaces. The two symmetric sides leave in average a gap of 0.2 mm that is filled by the third, highly curved surface. Since the latter in large parts is incorrect, it has to be replaced. And as this curvature surface also forms the by far most curved surface of the geometry it also gives rise to the biggest challenge in meshing.

The first approach tried, was constructing a simple flat connection between the unchanged sides. But, as also the side-surfaces were not free of error this approach did not lead to immediate success. Thus also the sides had either to be repaired or constructed new. The latter approach was followed and all surfaces were newly constructed. Therefore the target not only was to ensure error free closed surfaces, but, that the form remained

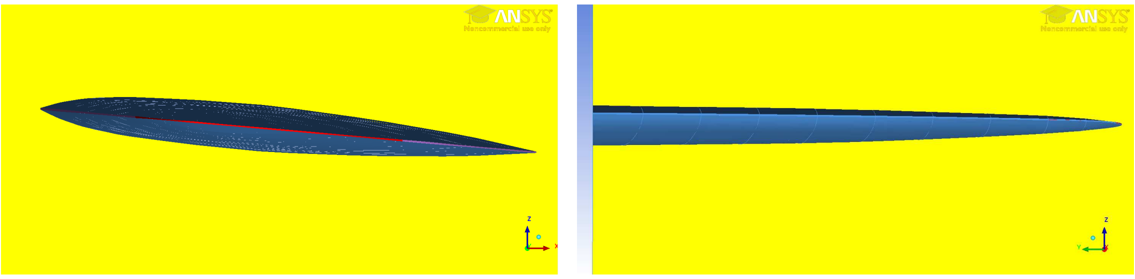

(a) View from the bottom

(b) View from the front

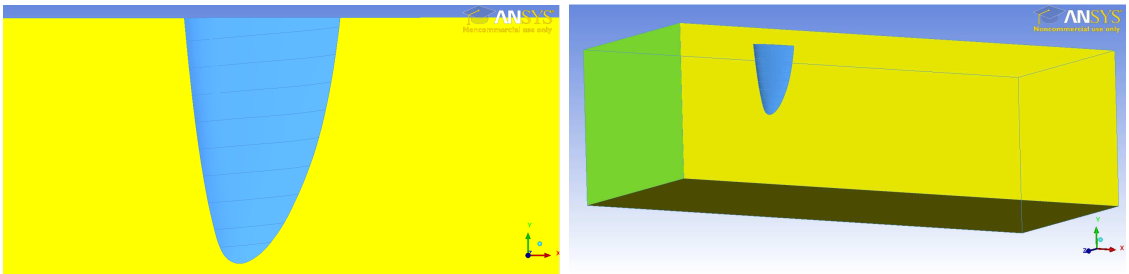

(c) View from the side

(d) View of the whole setup

Figure 4.1.: Three views of the setup and the general layout; angel of attack $\alpha = 5°$

unchanged[1] at the greatest possible accuracy.

Fitting curves along the surface of the rudder and the edges enables to construct new surfaces. In order to achieve maximum accuracy a high number of lines was distributed in chord- and spanwise direction of the rudder side surface. Since the rudder is symmetric, luckily only one side had to be constructed and the other one is gained from mirroring. Within the accuracy of Icem it is thus also ensured that the problem is totally symmetric. As the mesh is generated in a symmetric manner one can expect the lift force to approach zero in the cases where $\alpha = 0$.

The resulting surface constructed with a very fine distribution of fitted lines is shown in figure 4.2(b). The surfaces of every square had to be constructed one by one. But as a higher number of surfaces promised an increased accuracy in reflecting the real geometry, it seemed worth the time spent. Nevertheless, it turned out that too many of the surfaces constructed with Icem were corrupt themselves, and a coarser distribution had to be used. That can be evidenced in all other images as for example 4.1(c) (color print needed).

At this point it seems important illustrating involved problems by a simple example. Consider three vertical lines and two horizontal lines that both are curved and intersect such that they form the boundary of two squared adjoining surfaces. When constructing

---

[1] Unchanged in terms of achieving the intended form of the rudder. Several parts of the geometry were heavily changed due to errors involved in the process of Icem importing the geometry. These errors were pronounced most close to the tip of the rudder where the curvature is increased.

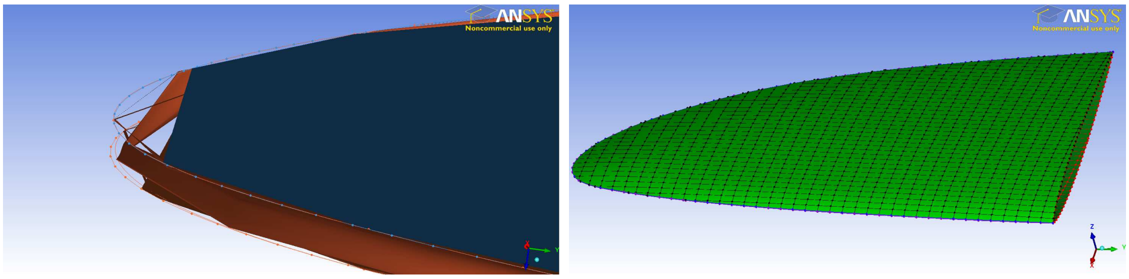

(a) Raw imported geometry (b) Mapping of the side surfaces

Figure 4.2.: Challenges with the geometry

such a squared surface, it regularly happens that the lines will not remain as they were. Often such generation of surfaces on the basis of four (or more) slightly curved lines (not even talking about large curvature as found at the curvature surface) leads to the automatic generation of secondary lines. Thus constructing surfaces with help of boundaries that align to each other will result in the fact that they do not perfectly align. This is of no further concern as long as the error is small enough. How small it has to be to be irrelevant depends mainly on the size of the surface mesh used on the particular surface. Luckily there are automatic repair functions. But they have to be used carefully and with the right parameters. Applying the build topology repair function with a too big tolerance will destroy parts of the geometry. Using it with a very fine tolerance in contrast causes that many surfaces can not be adjoined and one is left with a modified geometry that is full of wholes. Applying the repair function with a very fine tolerance and thereafter with a bigger one will consequently lead to different results than directly using the bigger one. In the authors estimation, the errors then have the tendency to remain whereas when using the adequate repairing tolerance right away, the best results are achieved. It sometimes also helps to simply run the repair automatism twice.

The curvature surface filling the gaps between the two sides of the rudder is heavily curved. Nevertheless, as long as the curvature is restricted to one direction, as in the case of a flat connection, Icem works fine. As soon as this surface however is to be curved in both directions, the above described problems arise.

This problem transfers directly over to the finally chosen solution that is following in the next section since it is directly relevant for the mesh.

### 4.3.2. The Mesh in Regard to the Geometry

In the process of this work hundreds of meshes have been generated. Finally presented in the thesis are the meshes based on two geometrical setups. The chronologically earlier achieved one (preliminary) is based on a larger version of the kayak-rudder, while the finally used one fuses on the smallest version of this type of rudder. The first one is used to evaluate turbulence models and is based on a flat surface along the edges. Its mesh is much coarser and less smooth. Higher angles of attack did however not converge and a better mesh was needed.

The curvature surface connecting the edges of the two sides plays the major role in the quality of the mesh. It is this curvature surface that leads to the most important improvements in the mesh compared to the preliminary one. Besides that the rudder in the preliminary mesh has a longer span (see table 6.3), several other optimizations lead to much finer resolution at the positions where it is needed most, while the total grid size remains the same.

Figure 4.3(a) compares the flat plate solution with a slightly rounded surface. Note that the size of the gap is exaggerate in this view. It is averagely only 0.2 mm wide, while the rudder has a thickness of 8 mm.

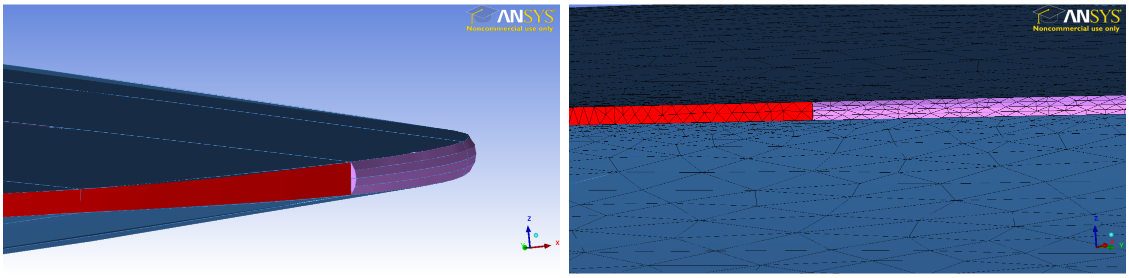

(a) Two solutions

(b) and the resulting surface mesh

Figure 4.3.: Edge of the rudder

The resulting mesh is displayed in the three different views, see figure 4.4, 4.5 and 4.6. In all figures the most critical and important regions are shown in detail. Figures 4.4(c) and 4.4(d) evolve from the advanced curvature surface, while figures 4.4(e) and 4.4(f) show the resulting mesh of the flat curvature surface. It is obvious that the latter leads to a much rougher transition and a coarser resolution.

But why the need for such a change in geometry, if simply the surface mesh could have been required to be finer? The answer hides in figure 4.5. One reason of minor importance is that the finer the surface mesh on the curvature, the more nodes occur. And here they are only needed in the directions lying in the $xz$-plane. The velocity gradient in the $yz$-plane is small and does not demand for such high resolution, thus the gird size is drastically enlarged without benefit (except close to the tip). The really important reason however is that the extrusion of the prism is stretched in the $xz$-plane, but not in the $yz$-plane. Thus

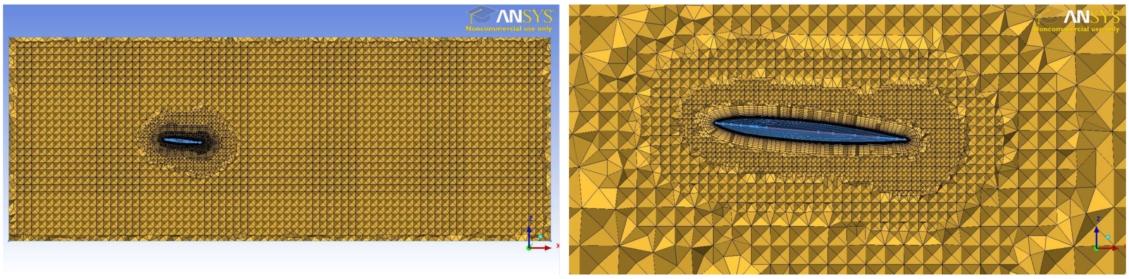

(a) Overview

(b) Overview closer perspective

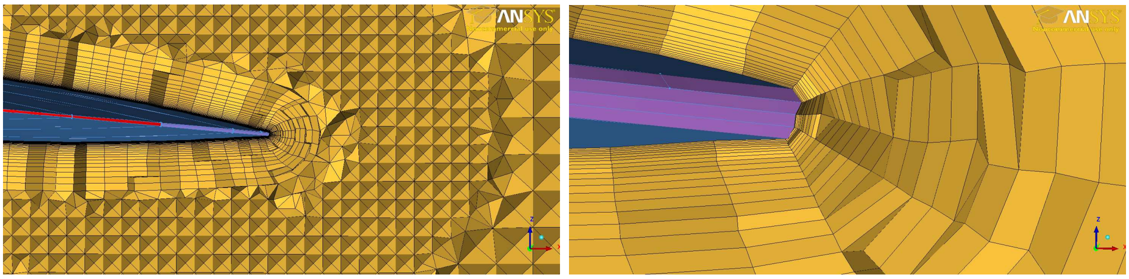

(c) Most problematic region with modified edge surface

(d) Detailed effect of modified edge surface

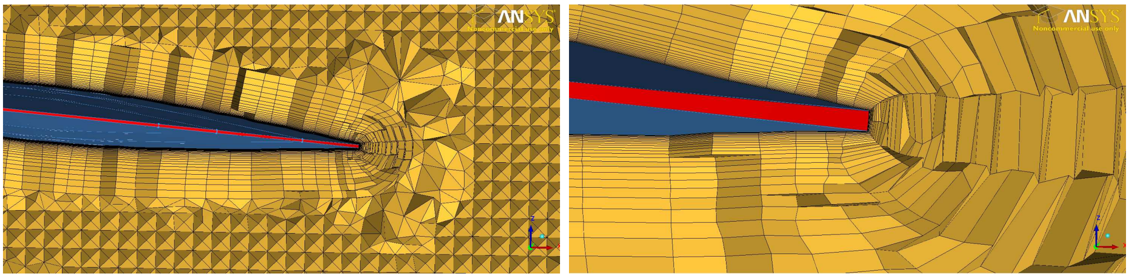

(e) Most problematic region with straight edge surface

(f) Detailed effect of straight edge surface

Figure 4.4.: Mesh $xz$-plane

the transition from the prism to the tetrahedral mesh becomes extremely harsh (in the $yz$-plane) if the curvature surface mesh is chosen too fine. In figure 4.5(b) the upper part is build on the modified curvature surface and the lower part on the flat solution. And even on the flat part the surface mesh size is twice as large as on the modified part, it still shows a worse transition.

Why becomes visible by considering figure 4.3(b). On the flat surface tetra mesh size 0.35 is applied and on the modified one 0.175. Nevertheless the mesh on the modified surface is stretched longer and leads therefore to a slightly coarser and therefore smoother behavior in the $yz$-plane. The author did not find any other possibility to enforce Icem to stretch the tetra surface mesh than modifying the geometry. The curvature is divided into four thin stripes that all stand at slight angles to each other. Therefore Octree, depending on the specification of the surface mesh size, puts nodes on the edges of these little surfaces and, if chosen smartly, also stretches them as shown in figure 4.3(b).

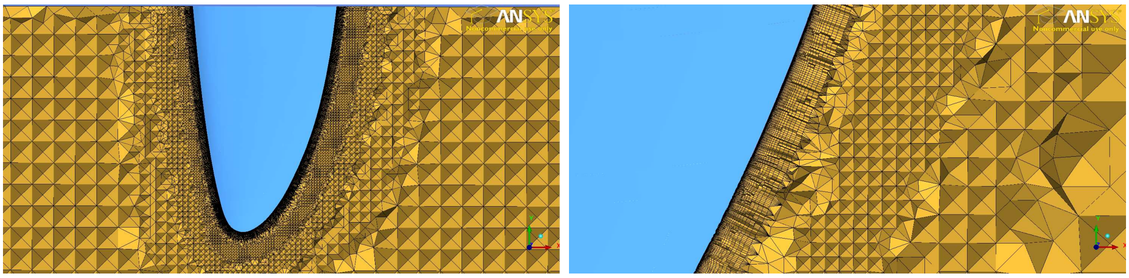

(a) Overview

(b) Most problematic region shows also the different meshes resulting of the two different solutions for the surface along the edge

Figure 4.5.: Mesh $xy$-plane

With help of this trick the mesh becomes much smoother. And even though it still has harsh transitions, combined with the other improvements, the simulation now converges even at higher angles of attack (7.5°) at full scale Reynolds number. Something that is not the case with the preliminary meshes.

The modification is implemented on the biggest part of the edges. But close to the tip (especially on the trailing side) the curvature of the edge is higher and those striped surfaces could not be generated or, respectively, could not be made error free. Consequently, on many sections different work-arounds were needed to reach the exact same target. That becomes clear considering an interesting behavior of Icem regarding the work with geometry, or more precisely the work with in both direction curved surfaces. The example is the following: Assume such surface is present without bounding lines. Then one automatically constructs the bounding lines on the basis of the surface. When the surface thereafter is deleted and one tries to generate a surface from these lines, it may happen that it simply is not possible. It is such time consuming behavior that made it necessary to find endlessly many different work-arounds in order to finally arrive at the intended closed geometry.

With regard to the curvature surface one can also think of other solutions. At least at the trailing edge it would be reasonable to extend prism further downstream. But that is only possible, if the trailing edge is sharp. That is not the case for the given geometry of the rudder. Nevertheless, the author also worked on a different approach tackling the problem. For example extruding the side surfaces such that they meet and no particular curvature surface exists. But, not only that it was not possible to achieve such error free surface all along the rudder, they also lead to a much worse mesh and were therefore not further pursued.

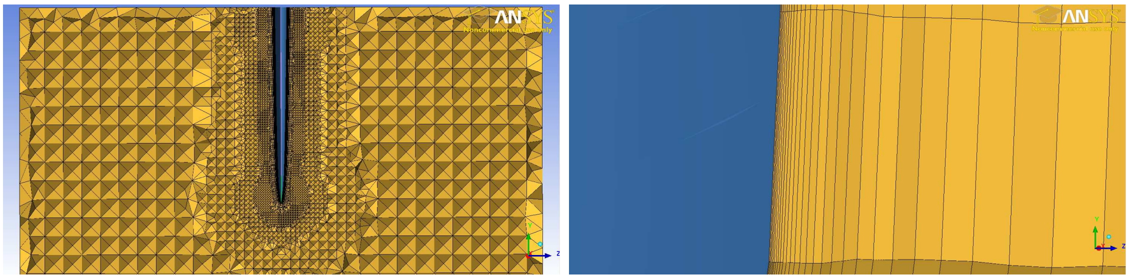

(a) Overview

(b) Maximal existing aspect ratio is ca. 280

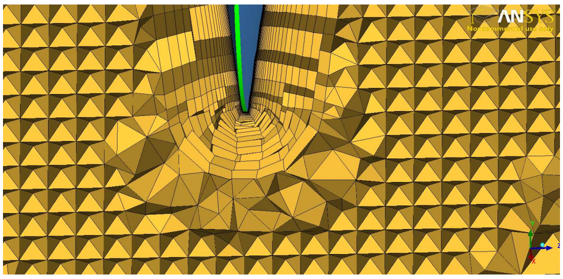

(c) Problematic region: tip

Figure 4.6.: Mesh $yz$-plane

Within the $yz$-plane figures, the maximum aspect ratio is presented in figure 4.6(b). It occurs on the two sides of the rudder where the surface mesh is on its coarsest and is approximately 280.

Table 4.1 gives an overview over the most important parameters used in the meshes. In addition there are several more parameters concerning the expansion and growth rate of the surface meshes, line meshes and density boxes. These sizes are usually given in mm and have to be seen in regard to the volume of the cells. They are thus proportional to the third root of the volume. There is also a big box version of the normal mesh. It uses the same parameters as the normal one but all lengths of the box are doubled. That results in 1 410 000 nodes.

Before concluding this section, one last remark on the use of (poly)lines in Icem. The number of points that can be used to define them is of course limited. Thus lines have to be split regularly in order to prevent the loss of information. That has to be kept in mind, also when assembling several lines together.

The simulation results gained from the efforts presented in this chapter are presented in the results chapter (6.3.2). While this chapter does not contain any figures on the preliminary meshes, the results chapter holds one figure presenting the preliminary discretization with regard to the magnitude of the velocity (6.9). That can be compared to its normal mesh counterpart shown in figure 6.11.

|  | preliminary | prel. fine | normal | fine |
|---|---|---|---|---|
| max size | 11.2 | 5.6 | 11.2 | 11.2 |
| surface: |  |  |  |  |
| max size sides | 1.4 | 0.7 | 1.4 | 0.7 |
| max size curv. | 0.175 | 0.0875 | 0.175/0.35 | 0.175/0.175 |
| prism: |  |  |  |  |
| first height | 0.05 | 0.025 | 0.005 | 0.0025 |
| growth rate | 1.15 | 1.15 | 1.175 | 1.175 |
| num. layers | 18 | 18 | 30 | 30 |
| box size [m] | 0.8×0.3 ×0.3 | 0.8×0.3×0.3 | 0.8×0.25×0.3 | 0.8×0.25×0.3 |
| num. nodes | 781 000 | 1 161 000 | 780 000 | 2 130 000 |

Table 4.1.: The most important parameters used for the meshes

# 5. Experiments

The third major part of this master's thesis is an experiment. The aim is to experimentally measure the forces acting on the kayak-rudder at different angles of attack and different velocities.

This chapter describes the approach and procedure that are used for the experiment. Regretably the amplifier did break down right after the first measurements were conducted. Consequently a new one was ordered, but, turned after several weeks unfortunately out to finally not be available within the timeframe of this work. As the deadline was already close, the further work load of searching, ordering and adjusting another amplifier was not conducted. Therefore, the outcome of the experiment is only of limited gain to the comparison of the lift and drag coefficients found from theory and simulation. However, time and energy to build the experimental setup and make it function in the first place, is already invested. In addition the data analysis is build up, but lacks the input. Nevertheless, the principle challenges and possible improvements can be deduced and the conditions for possible further measurements are strongly enhanced.

## 5.1. Equipment

The hydrodynamic laboratory at the University of Oslo is equipped with a wave tank. It is 25 m long, 0.5 m wide and can be filled with water up to a height of approx. 1 m. Rails are mounted on the top of the sides of the tank such that it is possible to pull objects through the tank. And even tough it is not build as a classical towing tank, it is certainly wide and deep enough to justify the study of a kayak rudder.

The target is to measure drag and lift (horizontal) at different angles of attack and at different (constant) velocities. The vertical lift is of minor interest and very small, thus its measurement is not pursued.

To the hydrodynamic laboratory belongs a workshop that allows to prepare for all kinds of advanced experiments. It has a lot of materials in stock and the mechanical part of the experiment is build up from available resources. Since however the force has to somehow be measured, different equipment had to be ordered.

### Load Cell and Mechanical Assembly

It is desired to measure both, lift and drag. Since that can also mechanically be accounted for, by simply repeating the experiment with a different setup, one one-dimensional force sensor is purchased. A single point load cell from Hottinger Baldwin Messtechnik GmbH (HBM), namely PW4MC3/500-G1 is chosen. It is based on strain gauge measurement and inherently corrects for the applied moment in order to measure only the force. That is referred to as off-center-load compensated and is made possible by its geometry, see also figure 5.1 for a picture of the load cell.

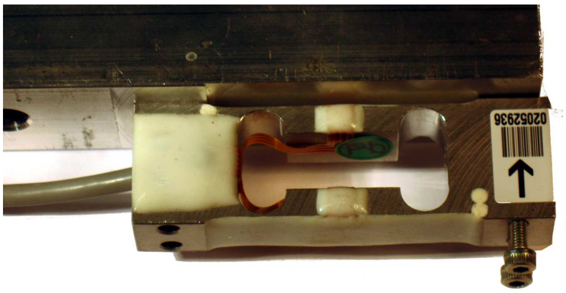

Figure 5.1.: Single point load cell PW4MC3/500G-1 mounted on the square bare with 0.4 mm wide air gap to ensure against overload

Thus, the measured value ideally does not change, if the applied force is parallel displaced away from the actual position of the load cell. That however has its limits, and the aim therefore has to be having the resulting force from the rudder as close to the force sensor as possible. The off center load error is described as ±0.0233 % of the sensivity ($1.0 \pm 0.1$ mV/V) (according to international recommendation OIML R 76). HBM's recommendations also demand the platform size to be no larger than 200 × 200 mm. That means for the particular usage that the force of interest (perpendicular to the plane of the load cell) is supposed to not be placed further away from the load cell than 100 mm.

The drag force expected from kayak-rudders is very small, especially at the low velocities realistically achievable in the tank. Therefore the load cell has to be very sensible in terms of its load, but, of course, neither too vulnerable. Consequently the version with a maximal load of 500 gram (or 4.9 N) is chosen.

The error caused by a lateral force is not explicitly given since it does not appear in its most common usage. But the cell is prescribed to withstand values of a stationary lateral force that are smaller than 200 % of the maximal load in the intended direction ($2 \cdot 4.9$ N). The sensor is guaranteed not to damage due to normally directed load below 300 % of the maximal load. That equals 1.5 kg and makes the cell vulnerable. Therefore a construction is designed that mechanically guaranties that the displacement of the cell is restrained. The deflection at maximal load is stated to be $< 0.4$ mm. Accordingly the cell is mounted such that it can not exceed 0.4 mm deflection in positive load direction. In addition the case connecting load cell and rudder-rod-carrier is equally designed so that a deflection in opposite direction as well cannot exceed 0.4 mm. Yet, that does not guarantee for the lateral load not to be exceeded, but here the deflection is unknown (and smaller). Nevertheless an adjustment screw is placed so that this deflection could be restrained as well.

As shown in figure 5.2 the rudder-rod is enchased from a carrier, which then is fixed to the case mounted to the load cell. The carrier allows the rod to be adjusted in terms of rotation (angel of attack) and in terms of the vertical distance to the cell or respectively the water.

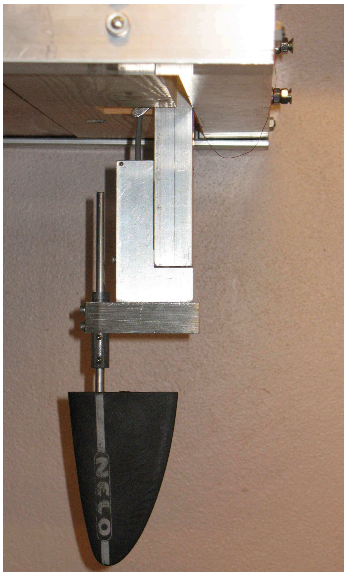

Figure 5.2.: Experimental setup; the rudder with the rod and its carrier, the case housing the load cell, the square bar on which the load is is fixed and parts of the frame used to host all equipment

On the other side the load cell is mounted to an aluminum square bar that is connected to a frame that hosts all equipment. This square bar can be turned by 90 degrees. That allows for drag or lift measurements.

Also the frame is build from aluminum material and is constructed so that it fits on the already existing trolly. It has a floor plate made from wood and can host other necessary equipment.

The whole experiment is constructed in a way allowing everything to be moved with the trolley, which has the benefit that no trailing cables are needed. That is possible since the laptop runs on battery power and supplies the NI-USB 6211, while for the amplifier (and thus for the load cell) two 12 V snowmobile batteries are used.

The trolly, on which the frame with all the equipment quickly can be fixed, is, with regard to its four bearings, 600 mm long and 720 mm wide. It is fixed via ball-bearings to the rails and is pulled by a very stiff rope commonly used in sailboat racing. The rope is attached to one side of the trolly. In combination with the small length to width ratio that, independent off whichever bearings are used, is not beneficial for the friction coefficient of the trolley itself. The rope is driven by a 0.55 kW motor from SEW Eurodrive (R17/DT80K4). The frequency converter is from the same brand, a Movitrac 31C. The maximal velocity with the current gear ratio is approx. 0.85 m/s.

### Data Acquisition

An adequate amplifier is also found from HBM, the RM4220. Its filter can be adjusted up to 5 kHz (±5 %) via soldering in adequat resistors. Its gain and zero is adjustable via DIP-switches and potentiometers. As all cables are short, the voltage output is used. The gain is adjusted to a scaling of 50 gram per Volt. The different weights used for calibration are found from a calibrated high precission scale.

In order to digitize the signal from the amplifier, it is made use of National Instruments (NI) data acquisition (DAQ) systems. Here precisely, a NI-USB 6211 connected to a conventional laptop via USB and NI's software LabVIEW are used to capture the measurement data.

The sampling rate in all presented cases is set to 1 kHz, while the amplifier's filter is supposed to have a cutoff-frequency of approx. 500 Hz.

In order to precisely measure the local velocity of the trolly, an electro-optical sensor is installed. It is fixed to a box, and via magnets (and a steel plate) to the trolly, and can be triggered from small plates of known length (or/and distance between each other). Such plates have to be placed along the side of the tank. As they were not yet fixed to the wave tank at the time the only measurements were taken (the amplifier broke down afterwards), the accurate velocity measurements are not available for these preliminary results. The approximate 0.85 m/s are deduced from the overall time and distance accomplished in a whole run.

## 5.2. Measurements

Due to the above stated reason only four considerable measurements are available and can be used within this work. All of them are conducted with zero angle of attack ($\alpha = 0°$) and the (with this settings) maximal available velocity of the trolley of approximately 0.85 m/s.

The measured signal is directly proportional to the drag force on the rudder. Figure 5.3 shows the resulting force in Newton found from the load cell. It displays the whole cycles from rest, acceleration, the phase of constant speed of the motor and the more abrupt stop. All runs start at precisely the same position, while the point of stop is not exactly the same for all runs. The graph shows three runs with the rudder submerged 8 mm under the waterplane, which means that the rudder-rod is also submerged by 8 mm. The fourth measurement is taken with the rudder at the same position, but without water. The accelerating process lasts for ca. 3.5 s. Here, in the phase where the trolly is accelerating, the difference between the runs with and without water at first is not visible but then it increases as time is increasing. That is to be expected since the viscous forces are negligible at very small timescales (see Prandtl's famous photographs C.4). The signal for the acceleration without water clearly indicates that the approximate acceleration of the trolly is constant up to ca. 3.5 s. Thereafter the average force of the waterless measurements drops to nearly zero (0.00167 N) while the three other measurements fluctuate around an average of 0.0759 N.

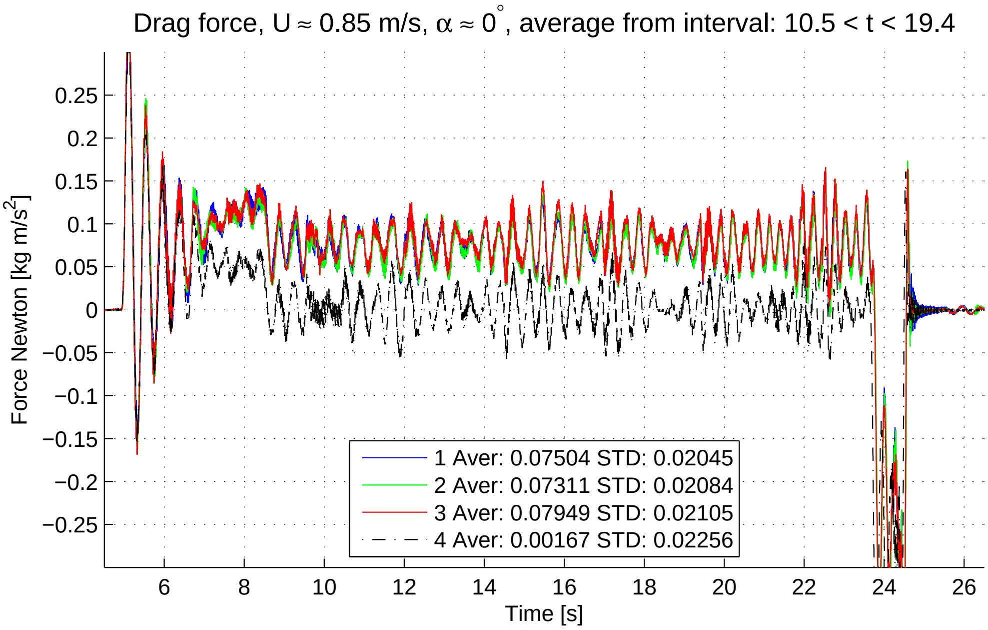

Figure 5.3.: Experimental force measurements; comparison and overview of whole runs

The stop is more abrupt than the starting-acceleration. The signals from the runs with water show the presence of an additional frequency, after the trolly is already stopped, that is not found without water. It frequency is approximately 2 Hz. That can be expected since the waves generated from the rudder have a frequency in this order. By using linear wave theory and neglecting the surface tension as well as the finite water depth, the dispersion relation is found to be $\omega^2 = gk$. The wave number $k$ is found from $k = \omega/c$, where $c$ is the phase speed, which can be assumed to correlate with the velocity of the rudder. Than $f = g/(2\pi c) \approx 1.8$ Hz. Here, both, the error of determining the velocity and the actual frequency is present, while the approximation of neglecting the surface tension is justifiable since the wavelength $\lambda_l = 2\pi/k \approx 0.46$ m is much larger than the minimal wavelength found from the theory including surface tension (here that is 0.017 m). Also the neglected effect from finite waterdepth is fully arguable for since $\tanh(kh) \cong 1$ because $kh \approx 13$. Linear theory is applicable if $ka = 2\pi a/\lambda_l \ll 0.1$, where $a$ is the unknown but small amplitude. Wave theory can for example be found in [GPT10].

Figure 5.4 shows the range of (desired) constant velocity in more detail. The noise to signal ratio is very high. The oscillation amplitude is around half the size of the average. These are far from ideal conditions in order to achieve valid results. Nevertheless, comparing the three runs with each other, it becomes clear that the noise is barely changed from run to run. And the noise is not at all due to the rudder flow phenomena, as also the run without water shows the precise same pattern.

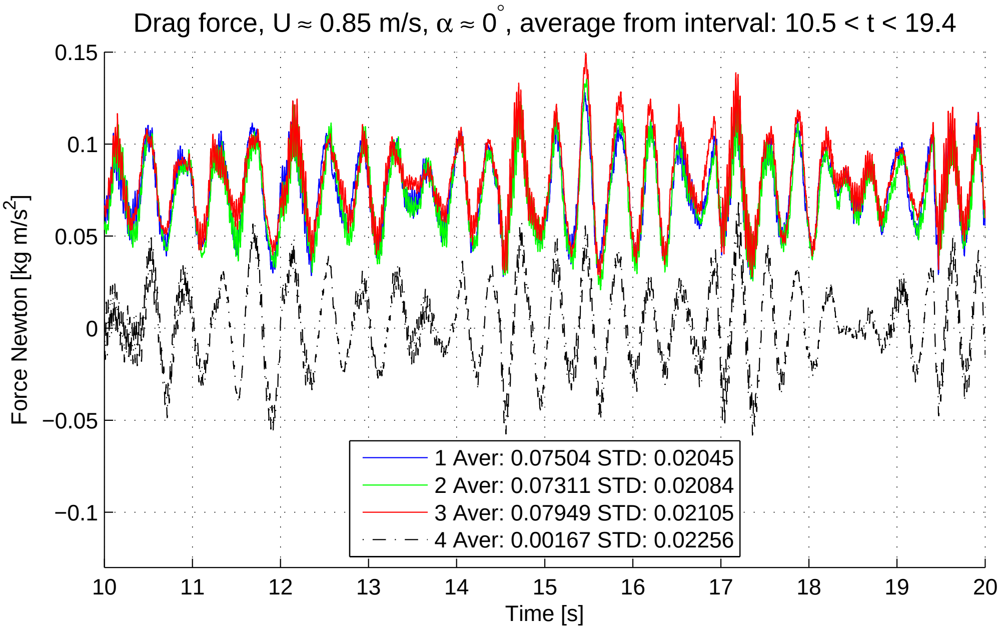

Figure 5.4.: Experimental force measurements; detailed comparison of runs

The dominating frequency of the noise is very similar to the one deduced for the waves. That best can be seen in figure 5.5, which shows the energy spectra of all runs. The minor figures show two interesting regions in more detail. All runs concentrate most of their spectral energy density between 2.6 and 2.8 Hz.

The only contribution from higher frequencies visible in this linear scale, is found at ca. 41 Hz. That is caused by a resonance frequency of the setup. Barely visible in the time domain plots is the high frequent oscillation that is permanently present, especially right after the trolly is stopped. It corresponds to the frequency shown in the second minor figure. It is interesting that the runs with water here have a slightly reduced resonance peak frequency in comparison to the ones without water. That could be due to a damping effect. But it is very uncertain since there is no statistical support available. Yet also the first run where water is present tends to the behavior of the one without water. That brings up the suspicion that the resting time could have something to do with these slight differences since run number 2 and 3 followed in relatively short periods after run 1.

Indeed, looking at overall peak frequency range ($\approx 2.7$ Hz), a distinct difference is visible between run 2 and 3, as compared to run 1 and the one without water. Here the first and the waterless run peak at a lower frequency, while the peak frequency of run 2 and 3 is still distinctly pronounced. The oscillation in this range is the result of the induced noise from the bearings since the behavior is approximately equally found with and without water. The bearing system is very precise but overconstrained and does have a lot of friction. Due to the first run the bearings become warmer and might behave slightly different in the upcoming run. This can serve as a reasonable explanation for the differences in behavior observed at the frequencies 2.6 – 2.8 Hz.

There is a third frequency of interest. As the circular rod is submerged in the water, the classical Strouhal frequency described in chapter 1.3.5 is expected to occur. But, as the rod is only 8 mm submerged and due to the surface tension, its effect can only be very limited. Nevertheless, if present it has to be found at a frequency of $f = Sr\,U/l$. As the rod has a diameter of 6 mm, the appropriate Reynolds number is $5.1 \cdot 10^3$ and therefore $Sr \approx 0.21$. That predicts a Strouhal frequency of 30 Hz. And indeed, as can be seen from figure 5.6, there is a little but distinct peak found. For the run without water it is much less but still present. That is reasonable since the Strouhal number for this rod in air also is approx. 0.21 (based on the diagram found in [Wik11d]).

The indicated averages and standard deviations for each singel run are calculated from the interval $10.5\text{ s} < t < 19.4\text{ s}$ (compare to figure 5.3). The standart deviation (STD) of the pure signals in this range is averagely 0.0208. That are 27 % of the mean value! But, three runs do not allow for much justifiable statistical computations of their averages. Presenting a confidence interval for example is not adequate here. Nevertheless, the average of the average of the three runs where water is present is 0.0759 N. Its STD is 0.0033, which are 4 % of this avarage. So this at least indicates that there is some hope left to find statistcally significant avarages, even with this large signal to noise ratio.

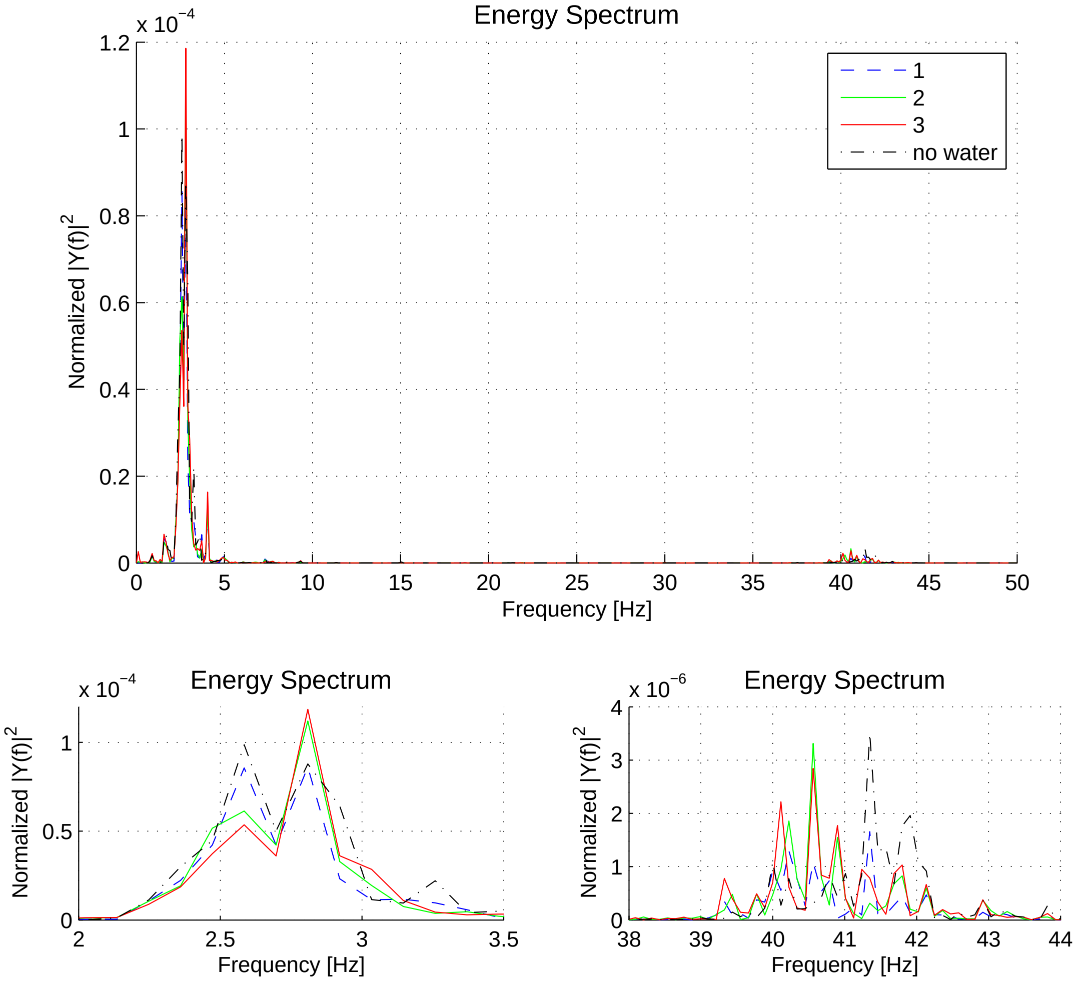

Figure 5.5.: Spectra of the experimental drag measurements

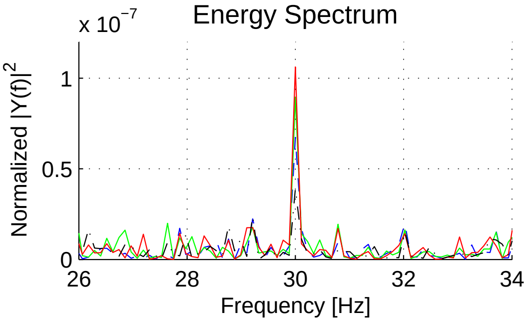

Figure 5.6.: Spectra of the experimental drag measurement; Strouhal region for the rod in air and water

# 6. Results

The results chapter presents a theoretical analysis of the velocity field at the rudder (section 6.1). The next section (6.2) discusses the theoretical methods with regard to the kayak-rudder. Before its outcome is compared to the simulation results in section 6.4, the simulation results themselves are presented (6.3). Furthermore it follows a comparison of the experimental outcome with the simulation results (6.5). Combining the dynamic angle of attack described in the first section, section 6.6 'Lift, Drag and Power Loss' makes use of it in combination with the simulation results. The chapter concludes with a discussion on the optimal form of kayak rudders (6.7).

Note that especially the section regarding the efficiency (6.4.3) comes up with critical arguments pertaining to the simulation results. They are further discussed in the outlook of this master's thesis (consider the conclusion chapter on the further suggestions (7.2)).

## 6.1. Velocity Field and Angle of Attack of a Kayak Rudder

This section applies the knowledge gained about the motion of the kayak hull in order to approximate the velocity field in the region of the rudder. The dynamic induced-angle of attack is approximated and the assumptions concerning the boundary-layer of the kayak hull are discussed. It concludes with an outline of the arguments involved in determining the optimal longitudinal position of the rudder at the kayak hull.

### 6.1.1. Induced Velocity and Angle of Attack

The angle of attack of the kayak rudder can be adjusted by the kayaker in order to steer. As the aim is to reach the finish in the shortest possible time, it is auxiliary to cover this distance in a preferably straight line. Therefore the kayaker uses the rudder to correct for reasons influencing the averaged trajectory of the kayak. That can for example be streaming, waves from neighboring kayaks or unbalanced propulsion. The kayaker usually does not adjust the rudder in order to diminish the periodic motion resulting from the paddling propulsion. In the studied case the dominant frequency is 0.88 Hz and, depending on which degree of freedom, respectively 1.76 Hz.

The motion of the kayak is described in chapter 1.4.2. How strong the periodic motion is depends on the kayaker's technique. In general, the higher the amplitudes the more energy is lost to related energy sinks. That is the case for the yaw motion that directly generates waves as well as for the viscous drag since it scales with the velocity squared. In terms of the conventional wave drag (due to forward motion) the situation is more complicated. That is because kayaks operate on high Froude numbers and the residual drag coefficient has a distinct maximum. Nevertheless, for the kayaks average forward velocity $Fr = U/(gl)^{1/2} \cong 0.7$, and that is clearly behind the peak of the coefficient, which also here is normalized with $U^2$ (see in the appendix figure C.3 on wave resistance). In the region of $Fr \sim 0.7$ the gradient of the gradient of the residual (or purely wave resistance) coefficient is negative and therefore the total residual drag can only increase with increasing amplitude of the forward velocity-fluctuation. Consequently, the interest in small amplitudes is justified for all fluctuating components.

The kayaker does not adjust the rudder within every period and it is auxiliary to assume the rudder to be fixed in its neutral position and analyze the angle of attack caused by the motion of the kayak hull. On top of this analysis a correction embracing an adjustment of the kayaker can always be superposed.

The kayaks position due to the yaw motion directly mirrors an angle of attack, say the geometrical angle of attack. But these positions result from a nonstationary process and do not reflect the effective angle of attack of the rudder. As the kayak rudder moves with the kayak, it is exposed to the same motion as the kayak within all its six degrees of freedom. This motion is neither only straight forward nor stationary. The kayak rudder thus, in addition to the geometric angle, faces an induced angle of attack.

In order to analytically model the velocity field at the kayak rudder the different motions have to either be of negligible size or an analytic representation has to be found. The translatory accelerations are negligible here since:

- The resulting fluctuation of the forward velocity (surge) is small compared to the average (below 5 %).
- The vertical motion heave obviously has a minor influence on the angle of attack of the kayak rudder since it acts in spanwise directions. But this is an assumption, since in reality it will have an influence on the instantaneous forces.
- The lateral sway motion is extremely small since the added mass and also the drag coefficient in this direction are enormous compared to surge. (In figure 1.5 its amplitude results mainly due to the fact that the sensor is not fixed at the actual center of rotation or respectively that the accelerations are not transformed to a fixed coordinate system.)

The rotational mode pitch is very small ($< 0.5°$) and in addition a similar argument as for heave applies. It can thus be neglected.

The two remaining modes are roll and yaw. Linearly they induced a velocity only in $z$-direction. Since the angles are small that is justifiable. Their spectral energy density is concentrated to one single frequency, therefore it is reasonable to model them with single sinusoidal signals. Now one needs to determine their amplitude, frequency and phase-shift.

The most scientific way of determining the appropriate frequency is to integrate along the energy spectrum and use the surface's center point to define the appropriate frequency. The amplitude could be found from requiring that the artificial signal (with the already found frequency) results in the same variance as the measurement data. But, in consideration of the little amount of data, neither the representation is statistically general nor the outlined computations. Thus it is sufficient to use the appropriate frequencies found from the dominant peak in the spectra. For the outlined computation of the appropriate amplitude one faces the uncertainty that the signals drift and therefore, if not corrected for, the variance is larger than adequate. That is especially true for the yaw signal since the kayaker's heading in this data-set changed slowly in time. Thus the amplitude is taken from a conventional averaging of the raw signals max and minimums. This yields that yaw motion has an amplitude of approximately 1 degree and roll of 6.8 degrees.

It remains the problem of determining the distance of the rudder to the corresponding rotational axes. In order to find an approximation for the yaw axis, the axes of inertia for a the kayak filled with 100 liter water are used. The kayak itself is assumed to be of zero weight. But the part of the kayak that remains under the waterplane is assumed to equal 100 kg and therefore a displaced volume of $\sim 100$ liter. This remaining volume's yaw axis of inertia is used as a fictive yaw axis (2.15 m distance to the rudder). This is of course a rough assumption. But neither the added mass of the submerged kayak hull nor the inertia of the kayaker-kayak entity is known. Using it is inviting. Not only since further useful information can be deduced from the information found from the submerged part of the kayak, but also justified since the distance of the rudder to the, say geometric middle of the hull, is larger than two meters. Thus it is not important if the yaw axis estimation is exposed to an error of a few decimeters.

For the roll axis the situation is fundamentally different. For the first the rudder is situated close to it and for the second it is defined by the metacentric height. This height changes with the roll (and pitch) angle and is thus difficult to compute on a real geometry. Especially if it should depend on the current position of the hull. Therefore the height of the roll axis is assumed to not depend on the position of the kayak. Its computation demands that the $x$ inertia of the waterplane surface in $x$-direction, say $I_{xx}$, and the height of the center of buoyancy, say $B$, is known. The center of mass for the 100 liter (0.1 m$^3$)

volume equals $B$ and also $I_{xx}$ is found from CAD-data. Then $I_{xx}/0.1$ yields the distance from the center of buoyancy to the metacentric height. Comparing that to the height at which the rudder is fixed to the kayak hull yields a distance of 0.13 m.

Now amplitudes, frequencies and distances to the roll axes are determined. It remains the phase-shift between roll and yaw, which is found from the data in figure 1.5. Roll is 0.18 seconds delayed in comparison to yaw and that corresponds to a phase-shift of 57 degrees.

### Induced Velocity

Figure 6.1 shows the resulting velocity in $z$-direction based on the outlined assumptions. All functions are sinusoidal and have the frequency in common. The distance to the roll axis is chosen such that it corresponds to the midsection of the rudder. That is half its draft (or span) and can therefore be assumed to be an average value for the whole rudder.

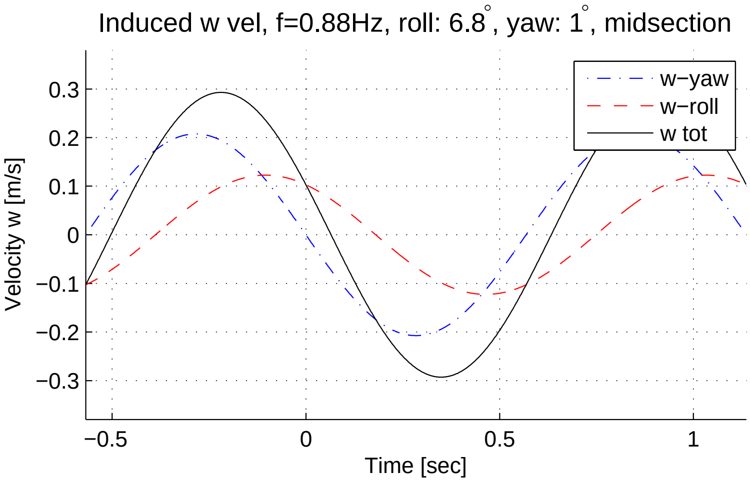

Figure 6.1.: Linearized induced velocity in $z$-direction due to roll and yaw motion; roll is based on 6.8°, 0.88 Hz and a distance of (0.13+0.056) m (spanwise midsection); yaw is based on 1°, 0.88 Hz and 2.15 m distance; yaw to roll phase-shift is 57°

The largest contribution stems from the yaw motion, even though its amplitude is only 1°. It is the long distance to the yaw axis that leads to a yaw-induced lateral velocity of maximal 0.21 m/s. The roll motion has a much higher amplitude but, as the roll axis is barley 20 centimeters above the rudders midsection, it does contribute with an amplitude of only 0.12 m/s. Due to the phaseshift the resulting amplitude is not the direct sum of the two velocities. It equals 0.29 m/s. This maximum consequently is reached after the yaw max value passed and before the roll max value arrives (in time).

The induced velocities scale with the frequency, or more precisely, the angular frequency $2\pi f$. That is obvious since, assuming a very low frequency, the resulting velocities would have to approach zero. For the geometric angle this situation is different.

### Angle of Attack

The geometric angle's amplitude is independent of the frequency and, as roll does not enter here, it also is equal all along the spanwise position of the rudder (the chordlength is of negligible size).

The induced angles not only depends on the induced velocity $w$ but also on the free stream velocity $U$. They compute $(\alpha_w \cong) \tan \alpha_w = w/U$ and are shown in figure 6.2. In this figure it is distinguished between the yaw and roll induced angle. The latter is based on the midsection of the spanwise length of the rudder.

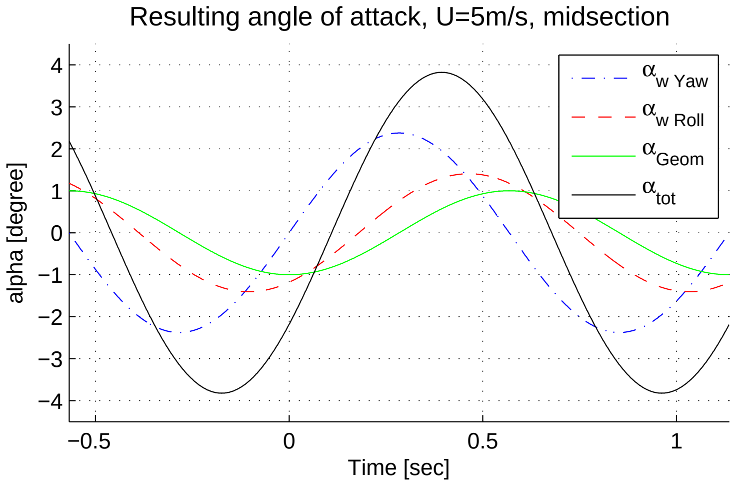

Figure 6.2.: Resulting angle of attack ($\alpha_{tot}$) at the spanwise midsection of the rudder found from the superposition of the geometric angle ($\alpha_{geo}$) and the induced angles from yaw velocity ($\alpha_{w\ yaw}$) and from roll velocity ($\alpha_{w\ roll}$); the distance to the roll axis used is (0.13+0.056) m that equals the spanwise midsection of the rudder

But what does this imply for the lift force? The lift depends linearly on the angel of attack. A positive angle of attack induces a positive lift force and the total lift can assumed to be proportional to the resulting angle of attack, shown as the black solid line $\alpha_{tot}$. For a justification see chapter 1.4.5.

The yaw velocity and its induced angle of attack result from the derivative of the yaw position that itself is responsible for the geometric angle of attack. Therefore the yaw-velocity-induced angle of attack is shifted -90 degrees in phase as compared to the geometric angle of attack. Physically one can interpret the geometric angle of attack as always resulting in a force that tends to bring the kayak to zero yaw angle. The opposite would be true if the rudder was situated in front of the yaw axis.

The yaw-velocity-induced angle of attack results in a force that can be looked at as always pulling the kayak to a state of no yaw motion. That is obvious since e.g. it only exists if the the yaw velocity is nonzero. The faster the yaw velocity, the higher this force. That is positive since it permanently damps the yaw motion, while the geometric angle of attack tries to bring the yaw angle to zero. One could say the force caused by the geometric angel of attack has ‘no damping’ and could in an idealized view contribute to an oscillation. That is not the case for the always damping force caused by the yaw-velocity-induced angle of attack.

One can thus state that, any angle of attack whose phase-shift lies in between the one from the geometric angle of attack and the one from the yaw-velocity-induced angle of attack, contributes to diminish the yaw motion. That, of course, implies that its amplitude is of the same sign.

Indeed the roll motion is oriented such that it lies in between the two. Precisely, with its 57 degrees it is closer to the geometric angle of attack than to the yaw velocity induced one. Thus with regard to the yaw motion its contribution is more on the side of reducing the yaw angle than damping the yaw velocity. With regard to the roll motion, of course, that is different. Here the lift due to roll induced angle of attack will always try to bring the roll velocity to zero.

The amplitude of the total angle of attack is 3.8 degrees. That is 2.8 degrees more than the geometric angle of attack. The extremes, where the distance to the roll axis corresponds to the position of the tip of the rudder and respectively to the position on the hull surface (where the rudder is fixed upon), are shown in figure 6.3. The maximum total angle of attack is thus found at the tip of the rudder with 4.2 degrees, while it at the other end of the rudder only is 3.4 degrees.

But, this analysis has only a certain degree of validity. There are two main reasons for that. The first and already mentioned one is the linearization of the motions and the neglecting of the other modes as well as the modeling in the form of single sinusoidal equations. But the second, and in the author’s point of view here more important reason, is that the real fluid is not ideal. That essentially means that the kayak is sourrounded by a (turbulent) boundary layer and in contrast to the ideal point of view, a real fluid reacts differently. The kayak is cambared and has to involve a slightly adverse pressure gradient. In addition the boundary layer is influenced by the dynamic motion of the hull. And also the vortex shed from the paddle-blades can have an influence. In the extrem that could for example mean that separation occurs when the adverse pressure gradient exceeds a certain (unknown) limit. That is certainly unlikely to happen on the kayak hull (but is much more

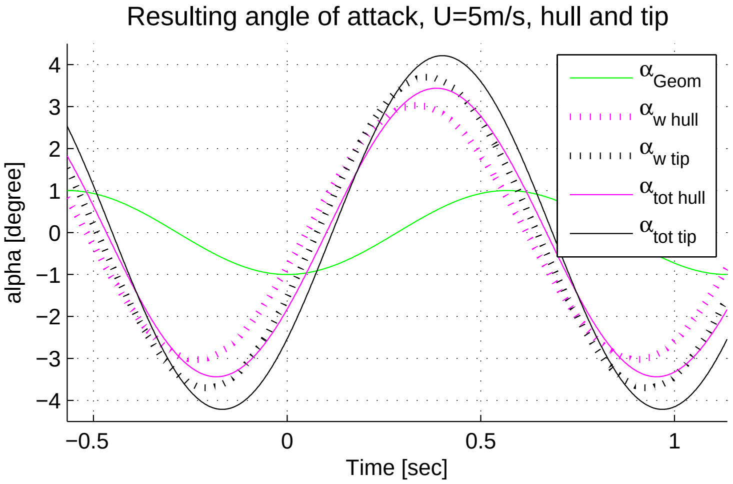

Figure 6.3.: Maximal and minimal resulting angle of attack ($\alpha_{tot\ tip/hull}$) due to the geometric angle ($\alpha_{geo}$) and the resulting induced angle from yaw and roll velocity ($\alpha_w$); the distance to the roll axis is evaluated at the hull (0.13+0.0) m (denoted hull) and the tip of the rudder (0.13+0.112) m (denoted tip)

likely for the rudder). Nevertheless, one could imagine that the boundary layer thickness locally increases due to for example the pitch motion.

### 6.1.2. Influence of the Kayak Hull

The kayak's wetted surface is surrounded by a boundary layer, which is laminar only on the first few centimeters and continues turbulent thereafter. That, compared to a fictive laminar case, increases the drag (streamlined body), but also the boundary layer thickness. The rudder is situated approximately 4.6 m behind the nose of the kayak.

The curvature of the keel is very small and the boundary layer along the kayak remains attached all the way to the tail. That is a necessity in order to be competitive and to not increase the drag. That effectively is the main reason for the streamlined form of kayaks. The turbulent boundary layer thickness of a flat plate can be estimated with an approximate formula $\delta = 0.16\,x\,(Re)^{-1/7}$ [Whi06, p.434]. Then the resulting thickness at the position of the rudder ($x$ = 4.6 m) is approximately 65 mm. That is slightly more than half the spanlength of the smallest rudder, yet the influence of the oscillations and the curvature of the kayak (adverse pressure gradient) are not even taken into account! Anyhow it is clear that the turbulent boundary layer certainly has an important influence on the lift achieved by the rudder. But, even though the turbulent boundary layer thickness is large, the averaged velocity at, say, half the height of the boundary layer height, will still be approximately 80 % of the free stream velocity. This data is taken from a diagram in [Whi06, p.415] assuming a mild adverse pressure gradient. The latter is certainly mild since the curvature of the kayak is small.

The boundary layer is influenced by the oscillating motions of the kayak. In the previous section the pitch motion could be neglected, but with regard to the boundary layer of the kayak hull it is reasonable to consider pitch. Using an approximate pitch axis close to the center of mass of the kayak and 0.4° pitch amplitude, the rudder is displaced by an amplitude of 15 mm. But pitch is not the only reason for the rudders motion in $z$-direction. Also heave motion is present. Simply using a sinusoidal approximation and an amplitude of 0.15 m/s$^2$ combined with $f = 1.76$ Hz (see chapter 1.4.2) yields an amplitude of the displacement of 1.2 mm. That, in the authors point of view, is surprisingly little and could result from the fact that the pitch acceleration used is not corrected for the rotational effects (hull fixed coordinate system). In addition there are all the other modes of motion. Even if they do not directly (linearly as the angels are small) influence the motion in $z$-direction, they will have an distinct influence on the boundary layer.

One can also look at the distance traveled within one period of, for example the largest rotational mode, roll. That is $x = U/f = 5/0.88 = 5.7$ m and respectively 2.8 m for the double frequency as in heave. Thus right on the order of one or respectively half a kayak lengths (5.2 m).

Apart from this brief outline on the kayak's boundary layer and its influence on the kayak rudder, it is neglected in the rest of this work. That is an approach whose validity only partly can be vindicated. But it certainly is the logical approach to investigate the given problem.

### 6.1.3. Optimal Position of the Rudder

The kayak rudder does not only contribute to the kayak's behavior by enableling the kayaker to steer, but it is essentially stabilizing the vessel. Not only in yaw, but also in roll.

The aim of the kayaker is to spend as much of its power on the forward motion and as little as possible to other sinks. Not only the forward motion, but also the yaw motion generates waves that limit the averagely achievable velocity of the kayak.

What is the best longitudinal position of the rudder? At first glance that obviously is the very sternmost end of the kayak since here the distance to the yaw axis is at is maximum. That implies, that not only the lift force acts with the longest possible arm of lever, but also that the yaw-velocity-induced angel of attack is maximum. But at the end of the kayak, the rudder necessarily is situated much closer to the roll axis. That means that the roll-velocity-induced angle of attack is smaller and therefore also its contribution to the lift of the rudder. In addition it is such that also the turbulent boundary layer of the kayak is thicker at the tail. It has manifold effects on the achieved lift and drag of the kayak rudder (e.g. laminar vs. turbulent behavior). It reduces the (averaged) velocity, but not equally in all directions. Thus the angle of attack can locally be very different from the ideal assumptions made. In addition behave turbulent boundary layers differently than laminar ones. That, in certain situations, can even lead to improvements regarding the performance of the rudder. Nevertheless, the velocity enters quadratically and is, along with the angle of attack, essential for achieving a high lift force with the rudder.

An argument against the position at the stern of the kayak can be that also roll contributes to an unwanted energy loss to the water (even though one can argue that the wave generation due to roll motion might be little, it is certainly not zero and neither is the viscous drag). Roll motion is affected by the rudder in terms of its distance to the roll axis. As this arm of lever is decreased, decreases the roll reducing effect of the rudder. But, for example, it is not unreasonable to assume that the roll motion can be of biomechanical importance to the paddler and that its reduction finally could turn out contraproductive.

The discussion has not touched upon one essential optimization criteria. That is, that the lift force does not come without a downside. As the rudder is finite, the lift achieved results in a trailing vortex. This vortex has to be generated and the energy used to do so gives rise to the (lift-) induced drag. That cannot be disregarded, even though the ratio lift to induced drag is (very) high. And, in addition, there is of course the viscous drag of the rudder that depends linearly on the surface of the rudder. It is a function of the Reynolds number and can at this small $\alpha$ be expected to have the largest contribution to the total drag of the rudder.

This shows, that even only an optimization of the longitudinal position of the kayak-rudder is a very complex problem that is hard to realistically tackle by using analytic (and also other) methods.

The nest section deals with the interpretation of the analytic methods studied in order to describe the lift and drag force on lifting surfaces like kayak-rudders.

## 6.2. Analysis of the Analytic Methods in Regard to Kayak Rudders

This section analysis the outcomes derived in the theoretical analysis of chapter 2. Therefore the most important results are included within this argumentation. One of them is the lateral force and its coefficient found for slender bodies

$$F_z = \frac{1}{4}\pi\rho U^2\alpha s^2 \qquad \text{and} \qquad C_{L_{SBT}} = \frac{1}{2}\pi\alpha A, \tag{6.1}$$

where the subscript SBT denotes its origin the slender body theory.

It is the lifting line theory (LLT) that has an analytical solution if the planform geometry is elliptical. The then resulting lift coefficient for uncambered airfoils $\overline{C}_L$ yields a powerful analytic tool as it comes along with a drag coefficient. The latter gives the induced drag due to the, for finite wings inevitable, trailing vortices. The forces and its coefficients accordingly write

$$\overline{L} = \pi \rho U^2 \alpha \frac{s^2}{A+2} \qquad \text{and} \qquad D = \frac{1}{2}\pi \rho U^2 \alpha^2 \frac{s^2}{A+2}, \tag{6.2}$$

$$\overline{C}_L = \frac{2\pi\alpha A}{A+2} \qquad \text{and} \qquad \overline{C}_D = \frac{4\pi\alpha^2 A}{(A+2)^2} = \frac{\overline{C}_L^2}{\pi A}. \tag{6.3}$$

As derived in chapter 2.5.3, the elliptical planform that is used to form these solutions is the optimal form in terms of the lift-to-induced drag ratio in terms of the general linearized lifting surface theory. The latter is the backbone of lifting line theory. LLT then uses an asymptotic approximation in order to be able to deduce further relations that then end up having an analytic solution for elliptical planforms.

A further useful result is the chordwise pressure distribution and the resulting moment on the wingsection. Since the general three-dimensional lifting theory does not come up with analytical solutions, one can refer to the simpler two-dimensional case that also is incorporated in the lifting line theory. The kayak rudder is symmetric in $z = 0$, thus the mean-camber line (surface) reduces to a straight line (plane surface) and the two-dimensional vortex distribution is given by (2.106). The latter is shown in figure 6.4. The plot can be regarded as a lift distribution since the linearized pressure jump, responsible for the (linear) lift force, is proportional to the vortex strength. For uncambered foils, the two-dimensional lift force and moment for a unit spanlength and respectively its coefficients

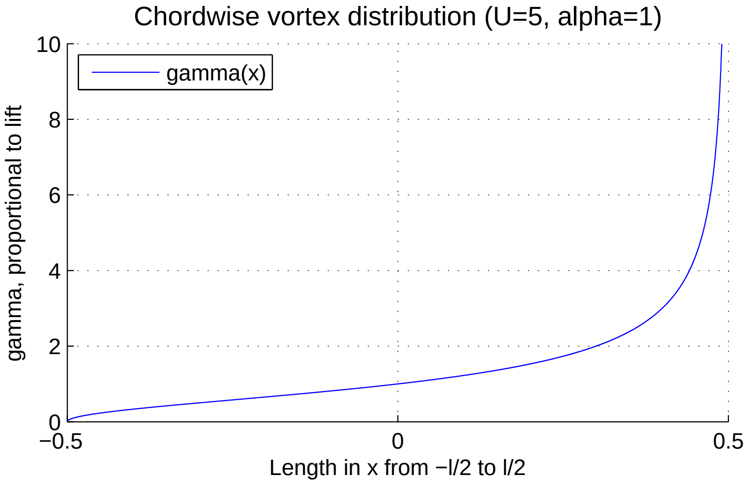

Figure 6.4.: Vortex distribution of an uncambered two-dimensional foil

express as

$$L = \pi \rho U^2 \alpha l \qquad \text{and} \qquad M = \frac{1}{4}\pi \rho U^2 \alpha l^2, \tag{6.4}$$

$$C_L = 2\pi\alpha \qquad \text{and} \qquad C_M = \frac{1}{2}\pi\alpha. \tag{6.5}$$

It follows that here the center of pressure $x_{CP} = M/L$ is located at the *quarter-chord* point, $x_{CP} = l/4$. The kayak rudder studied in the course of this work is fixed to the kayak by a rod. As it has to be constructed such that it does not yaw on its own, this rod has to coincide with the axis of zero moment as closely as possible. The rod exits the rudder slightly before the quarter chord point. That is the safe side in order to prevent instability. A comment on this this can be found in the final conclusion of the thesis.

### 6.2.1. Comparison of the Analytic Methods

First of all it must be noticed that all expressions have two things in common. They scale linearly with the angle of attack and linearly with the inertia forces. The latter are $\rho U^2$ times some surface, or, respectively in the two dimensional extreme, times a lengthscale (and unit width).

Figure 6.5 illustrates the behavior of all three lift coefficients in terms of the aspect ratio $A$ (2.58). As all of them scale linearly with the angle of attack, it is sufficient to analyze only one case with $\alpha$ fixed to a certain value, here, chosen to be one. The two dimensional results are independent of the aspect ratio as they refer to an infinite spanlength and a constant chordlength. The slender body theory scales linearly with the aspect ratio and keeps on growing to infinity as $A \to \infty$. Only the lifting line theory results (of the elliptical planform) are zero for $A = 0$ and approach the two dimensional limit for $A \to \infty$. That is obviously the most reasonable overall behavior.

In the limit of $A \to 0$ the lifting line coefficient shows a nearly linear behavior that has twice the gradient of the slender body theory. The next step is analyzing how and why the theories behave like indicated, what that physically means and which theory is applicable where.

**The Ratio LLT / SBT in the Extreme:** In order to compare the (stationary) slender body theory and the results of lifting line theory one can analyze their ratio. The ratio $\overline{C}_L/C_{L_{SBT}}$ yields its limiting behavior in terms of the aspect ratio by the use of l'Hôpital's rule, which allows to write it as $8/(A+2)^2$. In the limit of $A \to 0$ this ratio becomes two and lifting line theory predicts twice the lift of slender body theory. This difference is not surprising, since lifting line theory assumes $A \gg 0$. In the two-dimensional extreme ($A \to \infty$) the outlined ratio becomes zero. Neither that is very surprising since $C_{L_{SBT}}$ obviously becomes

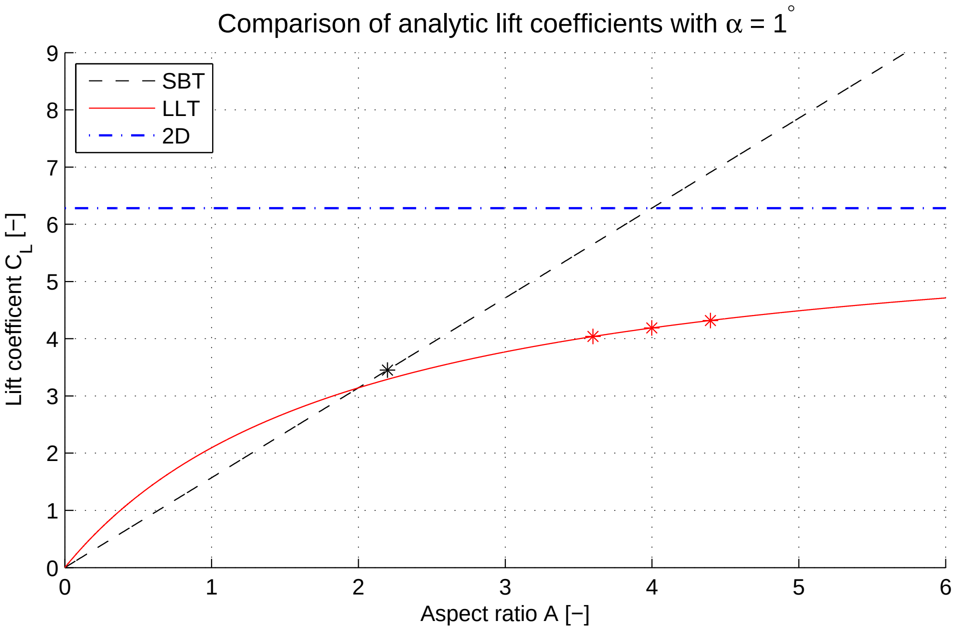

Figure 6.5.: Analytic lift coefficients over the aspect ratio

infinite as $A \to \infty$. This behavior is nonphysical but a logical consequence of the heavy violation of the slenderness approximation.

**LLT as $A \to \infty$:** When looking at the situation where $A \to \infty$, it is from a physical perspective most reasonable to keep the spanlength fixed, say $s = \mathcal{O}(1)$. Then the chordlength $l = \mathcal{O}(1/A)$. That means also that the lifting line theory approaches its two-dimensional counterpart. There, the lift is proportional to $l$, while $C_L$ is independent of $l$. Physically this is reasonable as long as the thickness of the wing is of an order smaller than the chordlength, say $t = \mathcal{O}(1/A^2)$. In other words, the wing is streamlined. While this does not affect the potential theory lift results, here the streamlined form is intrinsically assumed since the lifting theory is linearized not only in terms of the pressure, but also in terms of the applicability on the plane $y = 0$. It intrinsically builds up on a situation where the boundary layer remains attached. Also nonlinear and viscous effects (other than the circulation) are neglected. The latter leads for example to stall and gives rise to viscous drag.

**SBT as $A \to \infty$:** In case of the slender body theory, the lift force $F_z$ depends on the geometry only in terms of the spanlength squared ($s^2$). The chordlength is thus of no importance other than to ensure the existence of the slenderness. That is physically reasonable as long as the three-dimensional effects are dominant ($A \to 0$), that means the downwash and trailing vortex are of high importance. At large $A$, where the two-dimensional lift theory becomes valid, it is obvious that the lift force cannot scale with $s^2$ since it will depend linearly on the surface that in the two-dimensional limit simply writes $sl$. The proportionality of (stationary) SBT to $s^2$ evolves from the slenderness approximation allowing the total lateral force to be based on the two-dimensional added mass of a flat plate applied at the maximum span. It thus can intrinsically not take into account what the complete geometry looks like, except by requiring it to be slender. Note until normalizing the SBT lift force, the surface of the airfoil enters the equation and the coefficient then depends linearly on $A(= s^2/S_p)$.

**LLT and SBT at minor $A$:** Here, where $A \to 0$ the two-dimensional results become completely invalid. Also the lifting line theory assumes $A \gg 1$ and predicts for very small aspect ratio, say $A < 0.2$, twice the lift of slender body theory. It is here, slender body theory has its best validity. At such small $A$ the size of the surface looses its importance since the trailing vortices are dominating and the slender body theory, which disregards the chordlength while using the maximum span, is justifiable. Nevertheless, lifting line theory has to be regarded as an outstanding result of asymptotic approximations. Newman states as follows “Thus, while Prandtl’s approximation is not systematic, the most important higher order effects seem to have been included through good luck or shrewd insight or a combination of the two.” [New77, p.206].

As directly visible in figure 6.5, slender body theory has three intersection points with the other theories. First of all at $A = 0$ with lifting line theory, which it then again crosses at $A = 2$. From this perspective and, knowing that LLT tends to overpredict the lift, it is inviting to use slender body theory instead of lifting line theory up to $A = 2$. The underlying assumptions of lifting line theory demand $A \gg 1$ (even though it matches $\overline{C}_L(A = 0) = 0$). In the case of $A = 2$ one can argue that the slenderness approximation is already violated. Assuming a delta wing, the slenderness parameter $\epsilon = d/l = s/l = 1$; and that is not slender. Newman [New77, p.340] states that the upper limit of SBT in the general time dependent case is in about reached at a diameter length ratio of $d/l = s/l = 0.2$. For a delta wing that corresponds to $A = 0.4$ and for an elliptical planform to $A = 0.25$.

Once again consulting literature on the accuracy of lifting line theory: Table 6.1 gives the approximate errors caused by overprediction of the lift coefficient by the LLT depending on $A$ as stated in [New77, p.206].

| $A$ [-] | 0 | 2 | 4 | 8 |
|---|---|---|---|---|
| Error [%] | 100 | 20 | 10 | 5 |

Table 6.1.: Approximate error of lifting line theory depending on $A$

Looking at the error values for $A \geq 2$ it can be seen that they correspond to the function

$$100/(2.5A) \qquad \text{for A} \geq 2 \tag{6.6}$$

while the maximal error at $A \to 0$ is not infinite but equals 100 %. The latter could be displayed by a function $100/(2.5A + 1)$. This however would lead to an error of this error-description concerning the other discrete values found in table 6.1 of size $100/(6.25A^2 + 2.5A)$. The point where LLT and SBT predict the same lift coefficient is $A = 2$. Here table 6.1 predicts a 20 % error for the LLT. But to conclude that thus also the SBT would overpredict the lift by 20 % at $A = 2$ is correct only if the form of the airfoil is elliptical! As deduced before, the SBT predicts half the lift of LLT at $A \to 0$. Here, at the limit $A \to 0$, it is reasonable to conclude that SBT is fully valid since also the slenderness approaches infinity.

The next section relates this analysis to the kayak rudder. Prior to that it remains to also mention the last intersection point of SBT. It is at $A = 4$, where SBT intersects with the two-dimensional results. Here, SBT, as well as the two-dimensional result, is completely invalid. The two-dimensional theory alone basically only applies in the laboratory to analyze wing-sections, and on wings with a very large span compared to the chordlength. That can be seen by requiring the maximal error compared to LLT to be of a certain percentage. Such error constrain can be written as $A > 200/\%$. Thus, a maximum acceptable error of for example 5 % restricts the two-dimensional theory to $A > 40$, and that corresponds to $s = 51\, l_0$.

### 6.2.2. Lift Coefficient for the Kayak Rudder

The kayak rudders planform geometry is shown in figure 4.1(c) (chapter 4.3). Its spanlength is referred to as $d$, like draft. Since it is only one-sided, this is auxiliary in order to distinguish it from $s$, which is in lifting theory generally used for the total span.

In order to find the most appropriate aspect ratio for both SBT and LLT, the possible elliptic solutions and the direct use of span and surface are considered. This has three reasons: Firstly, LLT is based on elliptical planform surfaces. Secondly, such surfaces and aspect ratios are analytically given and, thirdly, the most important reason, the rudder reminds of an ellipse.

The elliptical planform area is $S_p = \pi s l_0/4$. For the given kayak rudder all three parameters are known, but the form is not fully elliptical. Thus one can calculate different possible aspect ratios ($A = s^2/S_p$), always referring to two values, which are geometrically given by the kayak rudder. Those, along with the rudders measured values (real), are given in table 6.2. Depending on which two out of the three scales are used, the third one adapts accordingly and is therefore marked bold. As the kayak rudder ends on the kayaks rigid surface it is one-sided and care has to be taken when referring to the appropriate aspect ratios.

| - | real | $2S_p,\ 2d$ | $2d,\ l_0$ | $2S_p,\ l_0$ | $S_p,\ d$ | $d,\ l_0$ | $S_p,\ l_0$ |
|---|---|---|---|---|---|---|---|
| $S_p$ [m$^2$] | **0.00568** | 0.01136 | **0.0126** | 0.01136 | 0.00568 | **0.00628** | 0.00568 |
| $s$ [m] | **0.112** | 0.224 | 0.224 | **0.203** | 0.112 | 0.112 | **0.101** |
| $l_0$ [m] | **0.0714** | **0.0646** | 0.0714 | 0.0714 | **0.0646** | 0.0714 | 0.0714 |
| $A$ [$-$] | - | 4.4 | 4 | 3.6 | 2.2 | (2) | (1.8) |

Table 6.2.: Theoretical aspect ratios and resulting geometric measures

Constrains of the used LLT coefficient are uncambered hydrofoils, which is intrinsically satisfied by kayak rudders; symmetric sides of the wing, which is neither a problem; then it is the elliptical planform. The rudder's planform surface $S_p$ reminds of a section of an ellipse. Yet it is not an half ellipse since it terminates too early. That is $l(z)$ still has a considerable gradient at the position of maximum $l = l_0$. And it is also not elliptical since the leading edge would correspond to an ellipse of a higher $A$ than the trailing edge. The elliptical planform here also incorporates that the sweepback angle has to be zero. That is fulfilled for the rudders, mainly analyzed in the course of this work. But there are also kayak rudders with a pronounced sweepback angle. They are used in conditions with grass in the water since the risk of grass getting trapped in such rudders is heavily reduced compared to conventional ones.

Following a comparison of all these different aspect ratios (shown in table 6.2) and their implycations in terms of the two different theories is conducted. Therefore figure 6.6 shows the resulting lift coefficients from all $A$ for both SBT and LLT.

For the lifting line theory it is required that the airfoil's tips are of zero chordlength and symmetric. Thus, the three minor aspect ratios are certainly not appropriate in order to refer to the kayak rudder. That is not a problem for the three larger aspect ratios since one could say that they are based on a double body approximation of the rudder. But using these aspect ratios in the LLT remains an approximation since the form of the rudder is not fully elliptical. And that does not change whichever approximation is chosen. So which

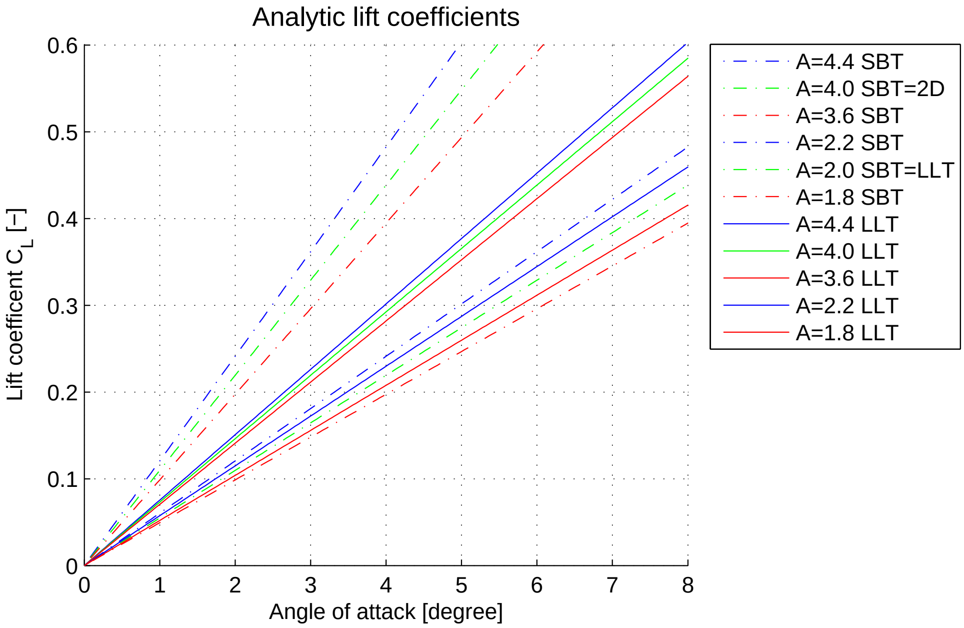

Figure 6.6.: Analytic lift coefficients in case of the kayak rudder

of the three approximations left is most physical? $A = 4.4$ fuses on the planform and the spanlength, $A = 4$ on the spanlength and the chordlength and $A = 3.6$ on the planform and the chordlength. The latter is not appropriate since the spanlength is considerably reduced and that obviously reflects an airfoil where the three-dimensional effects are more pronounced than on the rudder of interest. The case of $A = 4$ reveals that the fictive surface becomes bigger. That, if the real rudder would obey an elliptical form, means that the rudder only displays a section of an (half) ellipse. And even though the rudder is not fully elliptical, it is true that the change in chordlength does not approach zero at the end of the rudder, see figure 6.7. Thus, from the standpoint that the rudder's surface is more fundamental than the adaption of a chordlength according to the elliptic representation, the aspect ratio $A = 4.4$ is most reasonable. This argumentation can easily be supported by two-dimension lifting theory since here the total lift depends linearly on the surface of an airfoil. But the requirement for the LLT solution is the elliptical planform and from the perspective of the three dimensional effects, $A = 4$ might be more appropriate. In order to use the solution for this kayak rudder, one has to violate against one of the arguments. Left with the choice, one or the other, the author, as to the fact that $A$ is considerably larger than 2, tends to $A = 4.4$ since the surface gains in importance with increasing $A$.

Slender body theory does not depend on the body geometry other than having to obey the slenderness approximation (precisely, also a constant angle of attack and a nose of zero transverse dimension is assumed). The dependence on the surface enters first with the coefficient. Therefore SBT does not at all relay on an elliptical planform and the most appropriate aspect ratio is certainly based on the real span and real planform surface ($A = 4.4$ and $A = 2.2$). But an aspect ratio of 4.4 is not justifiable since the slenderness approximation would be totally disregarded and heavily violated. It remains $A = 2.2$, which directly is based on the rudders geometry without any further interpretation. Apart from the violation of slenderness the question remains, if this, for the case where the rudder is fixed on the kayak, really is appropriate. That is discussed in section 6.4.

## 6.3. Simulation Results

The simulation results divide into five parts. First the setup is briefly presented, followed by the comparison of different closure models employing a mesh based on a large kayak rudder. The 'final simulation results' present the outcome of an improved mesh that is based on a small kayak rudder. Consequently the next subsection compares these two results and therefore kayak rudders. The most illustrating subsection is the one concluding. It presents and analyzes the resulting force coefficients from a bundle of computations.

### 6.3.1. Setup, Rudders and Meshes Analyzed

The studied kayak rudder is found in at least three different sizes. If not mentioned differently, the analysis is based on the smallest one. Yet, they only differ in terms of their profile being cut shorter, see figure 6.7. The dimensions of these three rudders are given in table 6.3, where the Reynolds numbers are based on the maximum chordlength, a velocity of 5 m/s and the viscosity $10^{-6}$, corresponding to 20° Celsius warm, fresh water.

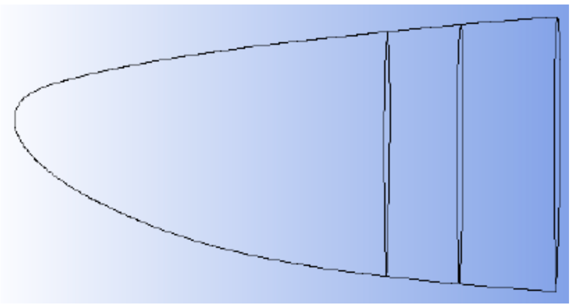

Figure 6.7.: Different sizes of the kayak rudder

| | $d$ [m] | $l_0$ [m] | $S_p$ [m$^2$] | $Re$ [$-$] |
|---|---|---|---|---|
| small, finally used | 0.112 | 0.0714 | 0.00568 | $3.57 \cdot 10^5$ |
| medium | 0.134 | 0.0757 | 0.007300 | $3.79 \cdot 10^5$ |
| large, used for comparison | 0.163 | 0.08 | 0.009559 | $4.00 \cdot 10^5$ |

Table 6.3.: Different sizes of the analyzed kayak rudder

The simulation-results presented are based on two different sizes of the rudder. The largest and the smallest one. Meshes called preliminary are based on the larger rudder, while in all other cases it is the small one. That has also historical reasons, since the preliminary meshes are not only much coarser, they also are less smooth than the finally used ones. The smaller size of the rudder is one, but not the main reason that made the incorporation of the improvements in the final mesh possible (even though the preliminary and the final mesh have approx. the same number of nodes).

The underlying simulation and discretization are described in chapter 4. Of particular interest is the used mesh; compare to chapter 4.3.2. Nevertheless, the discretizations with regard to the resulting boundary layer of both, the preliminary and the final mesh, are presented within the next three sections of this chapter.

All simulations are based on constant inflow and respectively constant position of the rudder. This is justifiable with regard to the timescale outlined in chapter 1.4.5. The transient calculations accomplished could serve as a first step into a simulation including the dynamic motion of the rudder and, of much higher interest, if the whole kayak could be taken into account. As argued for in chapter 1, transient calculations incorporating the dynamic motion of the rudder alone, are not necessarily needed. And, they use distinctly more computational time. A simulation of the whole dynamic kayak-hull and rudder entity could therefore certainly provide more information. But it is questionable if the computational limitations allow such simulation to validly be performed within a reasonable time. The Reynolds number for a typical K1 kayak lies at about $2.6 \cdot 10^7$. And a further challenge, if taken into account, is that it incorporates a free surface! Therefore, the simulations performed for this master's thesis never included a kayak, but use a free slip box instead.

The dynamic effects on airfoils become especially important in the regime where separation begins. In wind turbine modeling the resulting dynamic behavior is often modeled by constitutive dynamic stall models. The phenomenon is that, if the angle of attack is suddenly increased to a point where the wing stalls, it will for a short moment not stall since the boundary layer remains attached for a certain timescale (see chapter 1.3.6). Thus, at first also the lift will be extremely high and thereafter small. A similar behavior holds when the angle of attack changes out of the stall regime. From the constitutive perspective such process hence has a certain hysteresis. In terms of turbulence theory one could say turbulence has a memory. But, as shown in the beginning of this chapter 6.1.1, the resulting angles of the kayak rudder are small. Therefore the dynamic phenomena of stall is not expected to occur. At least as long as the rudder is not adjusted over a certain limit (or the kayaker's technique is changed). But that remains an assumption since the behavior of the boundary layer is complex especially at this small $Re$. Regarding the simulations no transition model is applied. Anyhow, accurate transition prediction is a highly challenging topic for CFD.

### 6.3.2. Comparison of Different Closure Models

The comparison of different closure models is based on the preliminary mesh and therefore on the larger rudder. These simulations are carried out with the angle of attack $\alpha = 0°$ and $\alpha = 1°$, both at $U = 0.5$ m/s and $U = 5$ m/s. Thus the chord based Reynolds numbers are $4 \cdot 10^4$ and $4 \cdot 10^5$ respectively. They are chosen to be in the order of the laboratory scale and the race pace respectively.

The most interesting outcomes of the simulations are the drag ($D$) and lift forces on the rudder. They allow to directly compare different turbulence models and are summarized in table 6.4. There are two different lift forces. $L$ is the one in the intended direction, directly influencing the yaw (heading). The upward pointing vertical lift force is denoted $L_y$.

The transient simulations depend on more parameters than the stationary computations. The here included LES computation is run with a timestep of 0.1 ms. This value is chosen to ensure that the max Courant number barely exceeds one.[1] Due to computational limitation that is slightly disregarded for the transient k-epsilon model. It is computed with a fixed timestep of 0.5 ms. That causes the Courant number to be approx. 0.85 for the RMS and 7.2 for the maximum.

#### The fast velocity case $\mathbf{U = 5}$ $\frac{\mathbf{m}}{\mathbf{s}}$

In the fast velocity case the laminar solution does not converge, indicating that the flow supposably no longer is laminar. That is expected since the Reynolds number is high enough to indicate a turbulent boundary layer (closer to the trailing edge, note that also an adverse pressure gradient is present). One can compare to figure C.2 found in the appendix (Frictional drag coefficient of a flat plate).

In the case of $\alpha = 1°$ the forces show a very good match between k-epsilon and SST as they always lie under 3 % difference. SST is checked on grid independence with a grid with 49 % more nodes. It shows a very good agreement in D (0.06 % difference) and $L$ (1.57 %) while the smallest force, $L_y$ with 22 % is extremely far of. The author assumes that in the case of $L_y$ the grid differences resulting from the edge (especially closer to the tip) is responsible for this behavior. It has to be stated that this gird check is by far not satisfying since it is based on approximately half the volume size of the cells. That leads only to a 21 % decrease of the average side lengths of the cells and is thus not the appropiate way to test the grid independence. With the finally used mesh, a more advanced check of a more advanced mesh is conducted.

---

[1] Note that also an automatic timestep can be defined to ensure a desired size of the Courant number. The author made use of this possibility with regard to the final mesh computations, but it is not further presented within the thesis.

| Case/ Model | $\alpha = 0°$ $U = 0.5\ \frac{\mathrm{m}}{\mathrm{s}}$ | $\alpha = 0°$ $U = 5\ \frac{\mathrm{m}}{\mathrm{s}}$ | $\alpha = 1°$ $U = 0.5\ \frac{\mathrm{m}}{\mathrm{s}}$ | $\alpha = 1°$ $U = 5\ \frac{\mathrm{m}}{\mathrm{s}}$ |
|---|---|---|---|---|
| laminar | $D = 0.0270$<br>$L_y = 0.00672$<br>$L = 0.000105$ | failed<br>not<br>converging | $D = 0.0274$<br>$L_y = 0.00685$<br>$L = 0.0525$ | - |
| k-epsilon | failed<br>not<br>converging | $D = 1.739$<br>$L_y = 0.542$<br>$L = -0.0265$ | failed<br>not<br>converging | $D = 1.783$<br>$L_y = 0.599$<br>$L = 9.134$ |
| transient k-epsilon | $D = 0.0263$<br>$L_y = 0.00507$<br>$L = -0.000223$ | - | - | - |
| k-omega | - | $D = 1.845$<br>$L_y = 0.559$<br>$L = -0.0173$ | - | - |
| SST | $D = 0.0280$<br>$L_y = 0.00616$<br>$L = 0.000128$ | $D = 1.691$<br>$L_y = 0.585$<br>$L = -0.0213$ | $D = 0.0277$<br>$L_y = 0.00631$<br>$L = 0.0867$ | $D = 1.738$<br>$L_y = 0.599$<br>$L = 9.162$ |
| finer grid SST | - | - | - | $D = 1.739$<br>$L_y = 0.489$<br>$L = 9.020$ |
| LES | - | - | $D = 0.0293$<br>$L_y = 0.00626$<br>$L = 0.0696$ | - |

Table 6.4.: Resulting forces in Newton for different closure models; preliminary mesh; drag $D$, horizontal lift $L_y$ and lift $L$

Figure 6.8 shows the contour plot of the SST results (normal preliminary mesh). The pressure distribution is reasonable, while the dimensionless wall distance y-plus reveals a major downside of this mesh. It indicates the (dimensionless) distance from the boundary to the first node in the fluid and is, at its biggest, 18. That is not sufficient to resolve the boundary layer behavior. Consequently the blending of wall functions makes this computation possible. In earlier versions of CFX the wall functions were not scalable and one had to ensure that y-plus did not fall below 20 and not above 200 in order to apply the wall functions. That is no longer the case, since the wall functions became scalable. For k-omega type models (like SST in the inner region of the boundary-layer), the wall function switches automatically to a more precise, low *Re* near-wall treatment if the boundary layer contains at least 10 nodes, see [ANS09a, ff.118]. Low Reynolds number here denotes more or less only that the mesh resolves the boundary layer flow in detail, something that due to the computational limitations becomes increasingly difficult with growing *Re*.

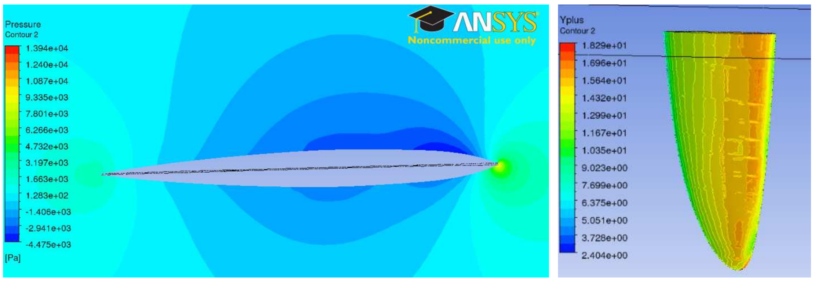

(a) Relative pressure $P$ $p$

(b) y-plus (max 18)

Figure 6.8.: SST contour plots; preliminary mesh; $\alpha = 1°$ and $U = 5\ \frac{\mathrm{m}}{\mathrm{s}}$

The boundary layer and its sourrounding is presented in figure 6.9. It directly reveals what the y-plus plot indicates. It is not resolved. A commen definition of the boundary layer is that it ends at the point where the velocity reaches 99 % of the free steam velocity. That is very demonstrative for the case of a flat plate, but here, the rudder has a thickness, a circulation and is bounded by a box. The latter leads to a speed up in the in the region where the rudder is present. The box is at minimum 38 times wider than the rudder thick, but it still contributes to a small speed up. In this case the velocity at the sides of the box is 5.0098 m/s and respectively 5.03566 m/s. That is a 0.18 % and respectively 0.71 % difference to the 5 m/s of the free stream. These values are taken at the vertical top of the box, where the rudder is at its maximum thickness of about 0.008 m. The difference from the two sides of the rudder mirros the effect of the circulation leading to a higher velocity on the suction side of the wing. Assuming a two-dimensional argumentation one can, with help of the conservation of mass state, that the averaged increase in the velocity is 2.7 %

compared to the inlet velocity. It effects both sides and can, if small, be assumed to not further worsen[2] the simulation results except inducing a slightly increased velocity on both sides of the rudder.

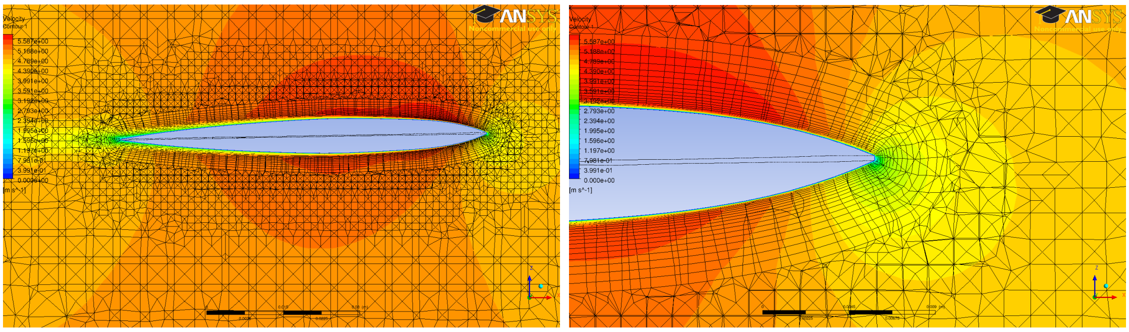

(a) Overview

(b) Overview detailed

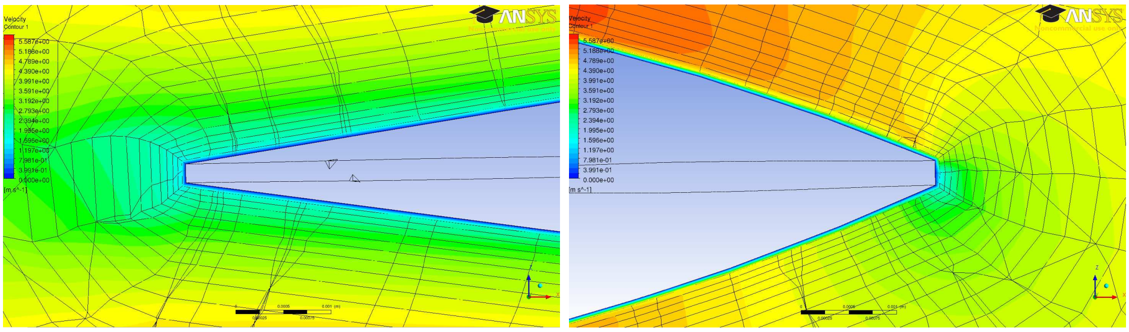

(c) Trailing edge

(d) Trailing edge detailed

Figure 6.9.: Discretization preliminary mesh and the total velocity $|U_i|$; contour plot in $xz$-plane; $\alpha = 1°$ and $U = 5\ \frac{\text{m}}{\text{s}}$; SST model

Figure 6.9(d) reveals that even at the tail, where the boundary layer already reached a certain height,[3] the major amount of the velocity gradient still is situated between the boundary and the first node. The height of the first cell is 0.05 mm (see table 4.1 in chapter 4.3.2).

For the case of $\alpha = 0°$ k-epsilon, k-omega and SST are carried out. All differences are below ca. 6 %, except for the lift. It has a maximal difference of 34 %. But this difference is of no further concern since $\alpha = 0°$ and $L$ therefore is supposed to approach zero. Especially

---

[2] Note that this is not generally true.

[3] One can compare to the flat plate boundary layer height, say for $x = 80$ mm (max chordlength). In case of a laminar Blasis boundary layer ($U = 5$ m/s) that reveals $\delta^* = 1.7208\, x\, (Re_x)^{-1/2} = 0.22$ mm, while an estimation of a turbulent boundary layer thickness can be $\delta = 0.16\, x\, (Re_x)^{-1/7} = 2.0$ mm [Whi06, p.232,434]. But this argumentation anyhow can only serve as a comparison since the rudder is cambared and three dimensional. Note that there are further phenomena evolving and that the simulation does not make use of a transition model.

since the geometry should theoretically be completely symmetric since it is mirrored. But neither that is the case, nor is the discretization necessarily symmetric. In addition, the accuracy of the computation is finite and one can thus not expect the lift to be zero.

### The slow velocity case $\mathbf{U = 0.5\ \frac{m}{s}}$

In the slow velocity case both laminar simulations converged. That is reasonable since the Reynolds number based on the maximal chordlength only is $4 \cdot 10^4$, and the geometry is streamlined, especially at such small angle of attack.

The k-epsilon model did not converge in both low Reynolds number computations. That is expected since the k-epsilon model has problems at low $Re$ where its behavior is known to have a stagnation point anomaly. Looking at figure 6.10 reveals what exactly that means. Here turbulent kinetic energy $k$ is shown for exactly the same setup differing only in terms of the used model. The k-epsilon model overestimates $k$ at the leading edge, where it punctually is very large. Comparing it to the SST results shows what a more appropriate distribution looks like. But note that also the SST model is not free of such behavior. The turbulent kinetic energy field distribution can be expected to show a growing $k$ (band) downstream of the leading edge that builds a slowly vanishing wake behind the rudder. A similar behavior holds for the eddy viscosity that also is overestimated at and close to stagnation points. Detailed information can be found in [DR11, ff.139]. The transient k-epsilon computation converged, but its result is under no circumstances thrustworthy. It differs from the stationary case in terms that the time term is part of the computations. The author assumes that the reason for convergence can be found in diffusive numerical effects.

The LES computation (Smagorinsky constant set to $C \geq 0$) is the second transient computation and is even more questionable. Its drag and vertical lift are similar to the SST model, but the lift is 25 % smaller ($\alpha = 1°$). The LES-lift value lies between the laminar and the SST model. That is reasonable from the point of view that LES models the subgrid scale and directely solves the Navier-Stokes equations for the larger scales, while the laminar computation attempts to directly solve the Navier-Stokes equations. But this mesh is not adequate for an LES computation since it is coarse and not smooth. For example large aspect ratio cells can lead to a problematic situation since this hybrid approach has to distinct and match between the two scales (the distinction is found from a filtering of the discretization). The boundary layer is not at all resolved and neither the laminar computation, especially for nonzero angle of attack, can be regarded as fully thrustworthy.

A k-omega model is not used here, but it can be expected to converge since it has no stagnation point anomaly. The SST model essentially is a combination of k-omega

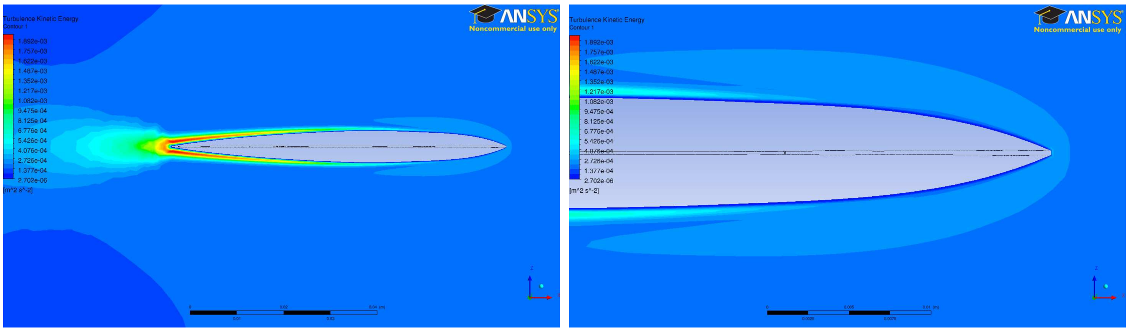

(a) SST (b) SST leading edge

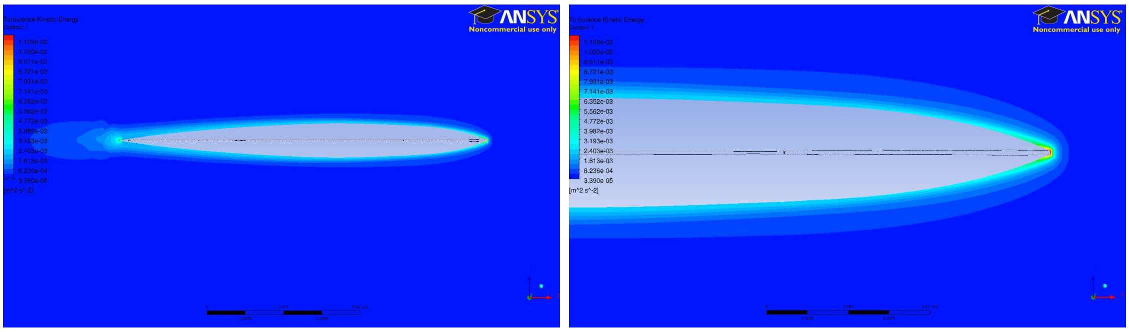

(c) k-epsilon (d) k-epsilon leading edge

Figure 6.10.: Stagnation point behavior; contour plot of turbulent kinetic energy $k$; preliminary mesh in $xz$-plane; $\alpha = 0°$ and $U = 0.5\ \frac{\mathrm{m}}{\mathrm{s}}$

modeling in the inner region of boundary layers and a k-epsilon approach in the free stream. The k-omega model is known to be sensitive to the inlet free stream turbulence properties [CFD11]. Therefore, the natural choice, combining the advantages of both classical models, is the SST model. It is thus also the model of first choice in the futher analysis of the fluid flow behavior following in the next sections.

### 6.3.3. Final Simulation Results

The preliminary mesh does not resolve the boundary layer phenomena. A distinctly improved mesh is used to compute the force coefficients presented in the upcoming section 6.3.5. In this section its detailed results, also with regard to the discretization, are presented.

The discretization along with contour plots of the absolute velocity $|U_i|$ is shown in figure 6.11. From the two first figures (6.11(a) and 6.11(b)) it can be seen how the grid is build. The mesh size increases away from the rudder. Attention, besides for the prism, only $2^n$ size steps are possible (before the smoothing is applied). Along the trailing edge, the mesh keeps the smallest tetrahedral size longer in order to allow a better resolution in this vital region of the flow. The total velocity, as compared to the free stream, is observably reduced on the pressure side in the region around the nose. At the suction side the total velocity is increased. That is especially the case in the region of the first half part of the chord, and thus slightly further downstream than for the decrease region of the pressure side of the rudder. Both is reasonable since this picture matches very well the effect of a circulation around the wing.

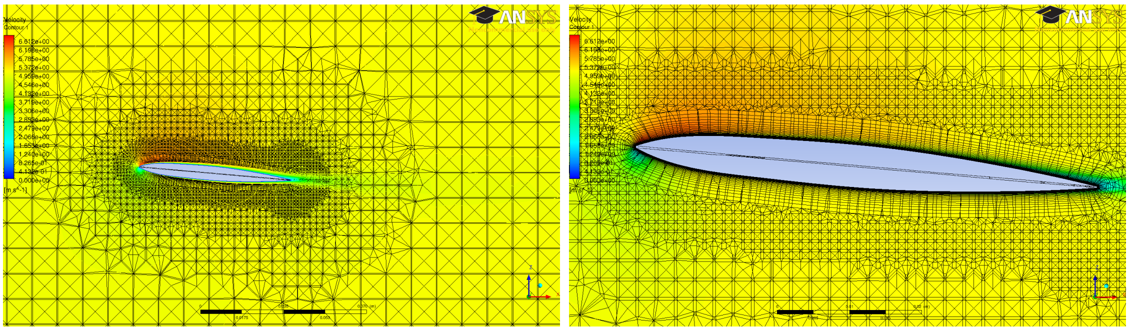

(a) Overview (b) Overview detailed

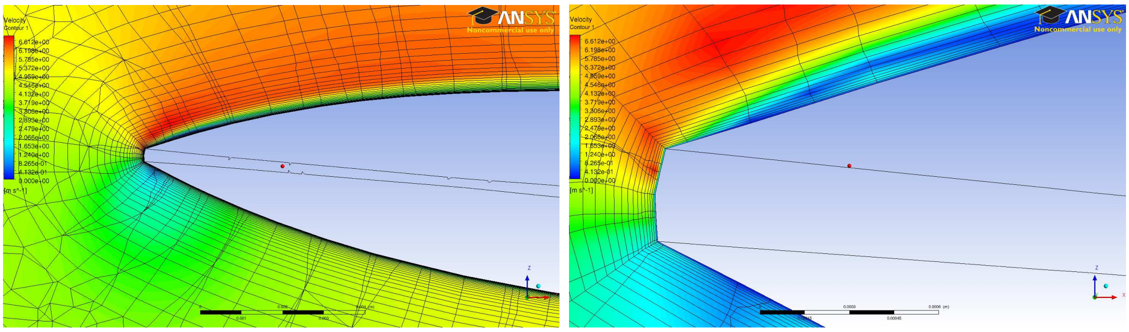

(c) Leading edge (d) Leading edge detailed

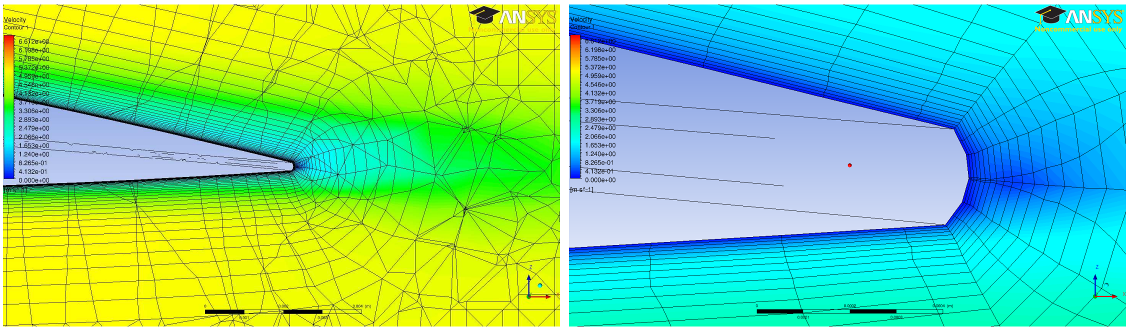

(e) Trailing edge (f) Trailing edge detailed

Figure 6.11.: Discretization and the total velocity $|U_i|$; contour plot in $xz$-plane; $\alpha = 5°$ and $U = 5\ \frac{\mathrm{m}}{\mathrm{s}}$; final mesh with SST model

The inflation layers (prism) are grown as far out as the smoothness of the transition to the tetrahedral mesh allowes. From figure 6.11(e) one could argue that 29 instead of 30 layers might have led to a slightly better transition. Nevertheless the boundary layer here is much better resolved than with the preliminary mesh. The detailed images reveal that many layers are within the major gradient of the velocity. Note that the smallest cells are hardly visible, even in the most detailed images.

The first height of the inflation layer mesh is equal all over the rudder (0.005 mm see chapter 4.3.2). It therefore is obvious that the boundary layer is resolved worst where it is at its thinnest. Consequently also y-plus is at its maximum at the upper side of the leading edge.

Figure 6.12 shows the y-plus, pressure and turbulent kinetic energy distribution along two polylines shown in the first of the figures (6.12(a)). The y-plus value referred to is the distance to the first node away from the wall in dimensionless y-plus units. It peaks right at the leading edge in a value $< 5$. Apart from that it is continuously below 2. That is an acceptable value in order to resolve the boundary layer, or respectively to allow CFX to apply the low $Re$ near wall treatment instead of the scalable wall functions.

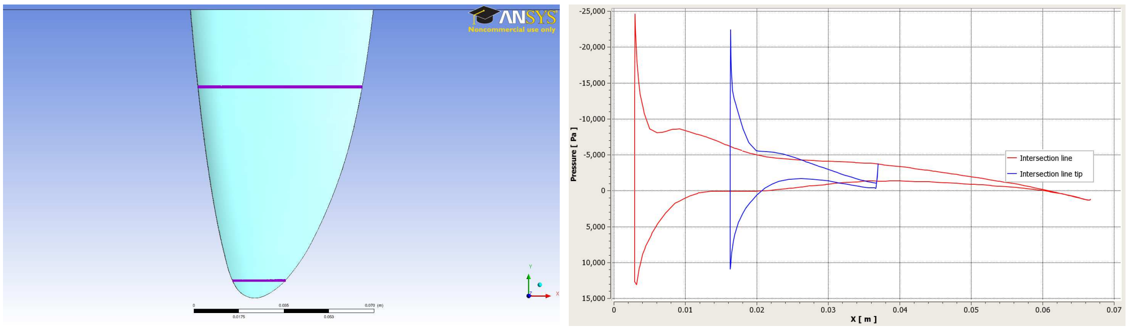

(a) Position of polyfit-curves

(b) Relative pressure $P$

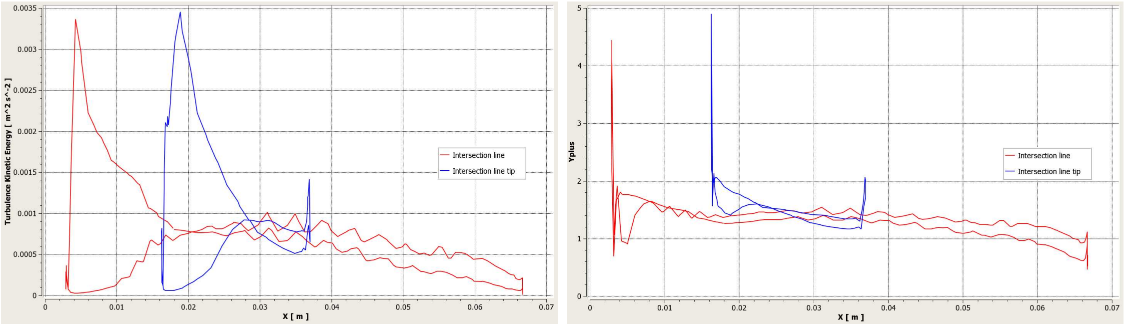

(c) Turbulent kinetic energy $k$

(d) Wall scale y-plus

Figure 6.12.: Different measures at polyfit lines along rudder sections ($z$=constant); $\alpha = 5°$ and $U = 5\ \frac{\text{m}}{\text{s}}$; final mesh with SST model

The local turbulent kinetic energy $k$ along the polylines on the rudder surface is reasonable since it is higher where the boundary layer is thin. The pressure distribution 6.12(b) shows the classical behavior. Note that the pressure axis points downwards and that the relative pressure is shown. The majority of the lift is thus concentrated in the region right behind the leading edge. That is in agreement with inviscid theory: For a two-dimensional lift distribution see figure 6.4 or consider the interesting interpretation of slender body theory on the basis of equation (2.84) (chapter 2.4.3). Notice the peak at the trailing edge that is visible in all quantities. It is more pronounced closer to the tip since it results from the three-dimensional effects of the finite wing.

The pressure field is presented in figure 6.13. The plane shown in the slightly adjusted front view (6.13(b)) intersects with different relative chordlengths of the rudder, thus the lower pressure in the region closer to the tip. Anyway, here, the region right at the tip is the most interesting section. It shows the effect of the free vortex (resulting in the trailing vortex sheet) that inevitably has to exist on finite wings. In the authors point of view it can be made responsible for a tip suction force that makes up a part of $L_y$. More on that in the interpretation on the force coefficients (section 6.3.5).

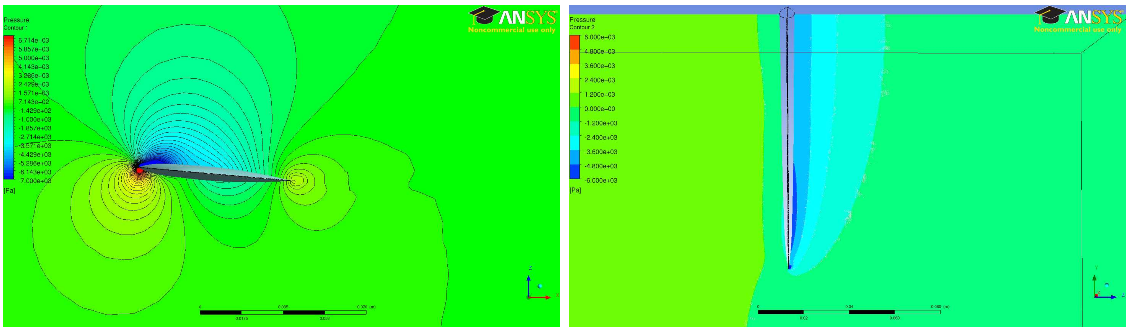

(a) $xz$-plane

(b) $\sim yz$-plane

Figure 6.13.: Relative pressure $P$; contour plot; $\alpha = 5°$ and $U = 5\ \frac{\mathrm{m}}{\mathrm{s}}$; final mesh with SST model

Concluding the attempt to prove the grid and box independence is presented. The resulting force coefficients along with their percentaged difference are presented in table 6.5. Regarding the grid independence it is essential to take into account that neither the geometry nor the computational power allows an infinite increase of the resolution. The meshes are described in 4.3.2. This fine one is build up so that all essential sizes are set to half the value (except the surface mesh size used on the modified curvature surface). Firstly, that does not generally lead to an improvement of the smoothness and the transitions in the mesh. Secondly, the mesh size on the curvature surface along the edge may not fall below a certain limit since the geometry is error free only up to a finite limit. And the smoothness effect of the implemented, modified curvature surface is lost if the mesh size is not adequate. In the particular case the mesh smoothness is improved in the area of the modified curvature since the sourrounding mesh is finer, but the increase in smoothness does not affect the tip in equal manner. In pure grid nodes the size increased with 173 %. The differences between the forces are marginal. The only significant change is found in the drag value. It essentially depends on the resolution of the boundary layer. As the y-plus value is approximately half of the normal mesh, this difference is reasonable.

| | $\alpha = 5°$ | | | $\alpha = 0°$ | | |
|---|---|---|---|---|---|---|
| | standard | diff. | fine | standard | diff. | big box |
| $C_D$ | 0.0248 | -2.1 % | 0.0243 | 0.0137 | -1.5 % | 0.0135 |
| $C_{L_y}$ | 0.00895 | +0.1 % | 0.00896 | 0.00577 | -1.2 % | 0.00570 |
| $C_L$ | 0.3303 | -0.5 % | 0.3287 | -0.000204 | -44 % | -0.000113 |

Table 6.5.: Comparison of SST based force coefficients from the standard (final), fine and big box mesh; $U = 5\ \frac{\mathrm{m}}{\mathrm{s}}$, $Re = 3.6 \cdot 10^5$

The independence of the box should essentially be much easier to verify, but the achieved mesh is based on $\alpha = 0°$. That is theoretically totally symmetric and thus the whole attempt is not as significant as with a nonzero angel of attack. The reason why no other big box simulation is performed is simple: already the change of the box or the rotation of a body in Icem leads to the requirement of again repairing (some) surfaces. As this is timeconsuming and the master's thesis finite, the box independence is not generally shown. Nevertheless, this computation based on a box with a doubling of all side length delivers positive results. The large difference in the lift coefficient is acceptable since $L \to 0$ as $\alpha \to 0$. Its justifications are described in section 6.3.2. The drag is diminished by 1.5 %. That is likely to relate to the decreasing influence of the speed up. It is interesting that also the increase of the mesh resolution has an diminishing effect on the drag and one can discuss if there is a correlance between this behaviour.

### 6.3.4. Comparison of the Rudders

This section compares the rudders with help of the results from the preliminary and the final meshes. Since they are respectively based on the large and the small rudder, this not only allows to discuss their validity against each other, but also the effects of the rudder size.

The preliminary setup does not converge for angles of attack $\alpha \geq 5°$ and its mesh is less smooth and much coarser than the finally used one. Nevertheless, the resulting force coefficients are in good agreement with the finally achieved ones.

They are presented in table 6.6, where the SST computations are compared against each other. The rudder in the preliminary mesh has a higher aspect ratio and one expects a higher lift coefficient (less three-dimensional). That indeed is found from the simulations (13 % at $U = 0.5$ m/s and 12 % at $U = 5$ m/s).

The lift in vertical direction results from two sources: viscous forces and the free vortex distribution. As both can be expected to approach zero if the aspect ratio goes to infinity, it is obvious that the bigger rudder (preliminary mesh) experiences a smaller vertical lift coefficient. That is supported by the fact that also the tip of the two rudders is the same. Indeed $C_{L_y}$ is reduced by 16 % and 15 % for respectively $U = 0.5$ m/s and $U = 5$ m/s for both angles of attack. If one assumes the simulations to be accurate enough, one could thus assume that, at this small angel of attack, the viscous forces make up the dominant portion of the vertical lift. That hypothesis is supported by the finally achieved force coefficients presented in the next section, see figure 6.16.

The drag consists of viscous and induced drag. Thus it can be related to the lift superposed with the viscous drag of nonlifting streamlined bodies. The viscous drag coefficient diminishes with increasing Reynolds number and increases due to the transition to a turbulent boundary layer (see chapter 1.3.3). While the induced drag (ideally) is not affected by the Reynolds number. It is interesting that in the high velocity case the smaller rudder yields a 6 % and respectively 4 % (at $\alpha = 1°$ and $\alpha = 0°$) smaller drag coefficient than the large one. While in the high velocity case its opposite (3 % more for both $\alpha$). That, for the case of $\alpha = 1°$, one can explain by the change in the lift coefficient relative to the two rudders since the induced drag enters in a quadratic manner. However, the same argumentation does not hold for $\alpha = 0°$. But here the change is also smaller and, of course, the mesh quality of the preliminary mesh is not allowing for the same quality of drag prediction than the final mesh.

An intersting behavior is that all simulations where $\alpha = 0°$ predict a small negative lift force, apart from the preliminary mesh with the SST and the laminar computation for $U = 0.5$ m/s; thus only the low *Re* case. Since the preliminary mesh used in the high and low *Re* cases is the same, it is not the discretization alone that determines which sign this force gets (with the fine mesh it is always negative). However the lift force and coefficient is supposed to approach zero here since the rudder is theoretically completely symmetric.

Concluding also the preliminary mesh as compared to the final one has reasonable results. Anyhow, the work put into the final mesh has a double pay off, since it not only acts as a certain validation of the preliminary results but now simulations with higher angle of attack become possible. And that, even without increasing computing time since the pure mesh size remained unchanged.

| $\alpha = 1°$ | | | | | | |
|---|---|---|---|---|---|---|
| | $U = 0.5\ \frac{m}{s}$ | | | $U = 5\ \frac{m}{s}$ | | |
| | final small rudder | diff. | preliminary large rudder | final small rudder | diff. | preliminary large rudder |
| $C_D$ | 0.0248 | -6 % | 0.0232 | 0.0141 | +3 % | 0.0146 |
| $C_{L_y}$ | 0.0063 | -16 % | 0.0053 | 0.0059 | -15 % | 0.0050 |
| $C_L$ | 0.0640 | +13 % | 0.0727 | 0.0681 | +12 % | 0.0768 |
| $\alpha = 0°$ | | | | | | |
| $C_D$ | 0.0244 | -4 % | 0.0235 | 0.0137 | +3 % | 0.0141 |
| $C_{L_y}$ | 0.006161 | -16 % | 0.00516 | 0.00577 | -15 % | 0.00490 |
| $C_L$ | -0.00027 | +140 % | 0.00011 | -0.00020 | +10 % | -0.00018 |

Table 6.6.: Comparison of SST based force coefficients of the preliminary and the final mesh

### 6.3.5. Resulting Force Coefficients

This section presents the resulting force coefficients achieved with the final mesh. It also includes the results from the simulation with the finer mesh used to check the grid independence. Here, all results are based on the smallest rudder (see table 6.2) that is also studied in the theory sections 6.1 and 6.2. The geometry is (theoretically) totally symmetric and therefore it is justifiable to mirror the results onto negative angles of attack. With help of this artifice it is ensured that the minimum of all polyfit lines is situated at zero angle of attack. These negative counterparts are not explicitly plotted. Of course, all simulation results are given precisely at their unchanged values within 5 digits.

#### Lift Coefficients

The lift coefficients are shown in figure 6.14. They can be compared to the polyfit lines. Since the theory predicts the lift coefficients to depend linearly on $\alpha$, the polyfit line is based on a first order polynominal. The differences between the straight interpolated lines and the simulation results is barely visible in the plot. Nevertheless, there is a tendency observable: The higher the angle of attack, the more differ the simulation results from their ideal theoretically linear behavior based on the results of the lower angles of attack. Or, in other words, they behave not completely linear but predict slightly less and less lift, the higher the angel of attack becomes. That is reasonable since viscosity plays a major role in real fluids and is (besides of enforcing the Kutta-condition) neglected in the outlined

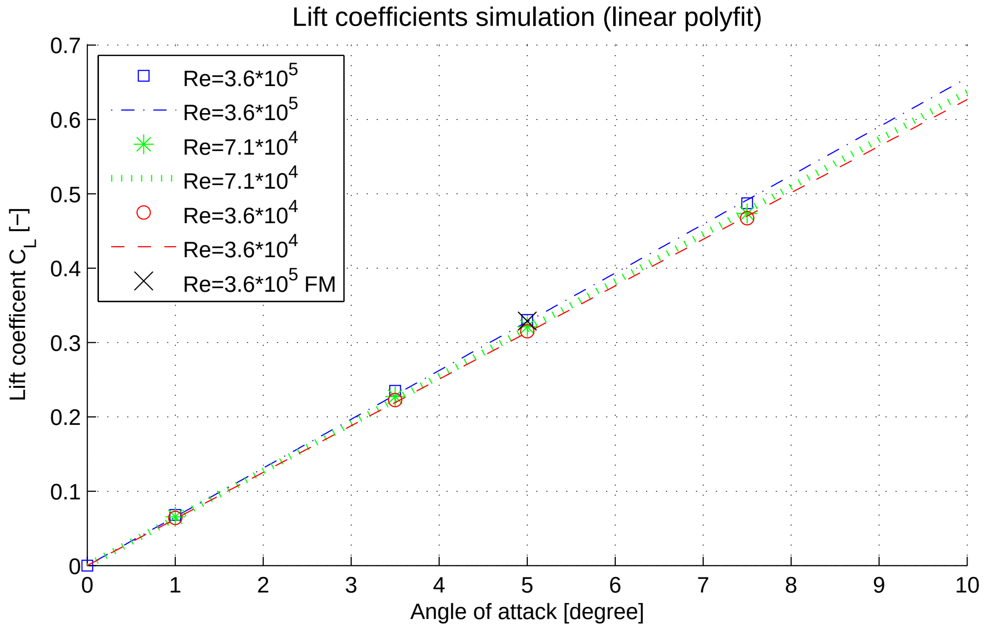

Figure 6.14.: Lift coefficients from the simulation results

theory.

Thinking of the situation where the angel of attack keeps on increasing, one slowly starts to approach the angle where stall occurs. And at $\alpha = 7.5°$ this critical angle of attack is much closer than for the other simulation results. Comparing to experimental results, see figure 1.3, shows that stall is not necessarily a sharp process. It develops since the boundary layer begins to separate more and more from the foil.[4] Note that the rudder is symmetric and one can thus assume that it cannot achieve as high lift coefficients as its cambered counterparts since separation will set in earlier (but that does not necessarily mean that the rudder cannot reach higher angles of attack without stalling).

The (max) chordlength based $Re = 3.6 \cdot 10^5$ and corresponds to an inlet velocity of $U = 5$ m/s, $Re = 7.1 \cdot 10^4$ to $U = 1$ m/s and $Re = 3.6 \cdot 10^4$ to $U = 0.5$ m/s. The difference between those three bundles of simulations is noticeable. For all $\alpha > 0°$ the simulation with the higher $Re$ predicts slightly higher lift coefficients and this behavior increases with angle of attack. Physically speaking that is logical, noting that the boundary layer remains attached longer as the $Re$ is increased. Again, consider the experimental results shown in figure 1.3 (Note that the artificial roughness also shown in this figure represents a change in the foil surface and that, the author assumes, here contributes to a thicker boundary

---

[4] In the sense that separation does not simultaneously have to occur over the complete span of the foil, and that separation neither necessarily has to start at the leading edge. Whereas leading edge sparation certainly leads to an abrupt loss of lift.

layer and an earlier separation as for the others since the boundary layer of them can also be expected being turbulent in large parts of the foil; certainly for higher angles of attack.).

The simulations make not use of a transitional model and it remains the question how much of the effects of a, at such $Re$ in reality (partly present), laminar regime the simulation covers. More on that in the next section (mainly 6.4.3) and the conclusion.

From the perspective of ideal flow theory the following argumentation is applicable: The theory assumes zero viscosity and as $Re$ increases, decreases the importance of viscous forces as compared to the inertial forces. From this point of view the high Reynolds number simulation fits best to the theory. But note that the higher the Reynolds number, the more difficult it becomes to resolve the boundary layer in the simulations (disregarding the effects of transition). For example here y-plus is maximum only 1.0 in the $U = 0.5$ m/s simulation, whereas it is maximum 5.3 for $U = 5$ m/s (with $\alpha = 5°$).

### Drag Coefficients

For the drag coefficients the polyfit-lines are based on a quadratic polynominal since the theory predicts the induced drag to quadratically increase with $\alpha$. All results are shown in figure 6.15 Here the difference between the different Reynolds number cases is much more

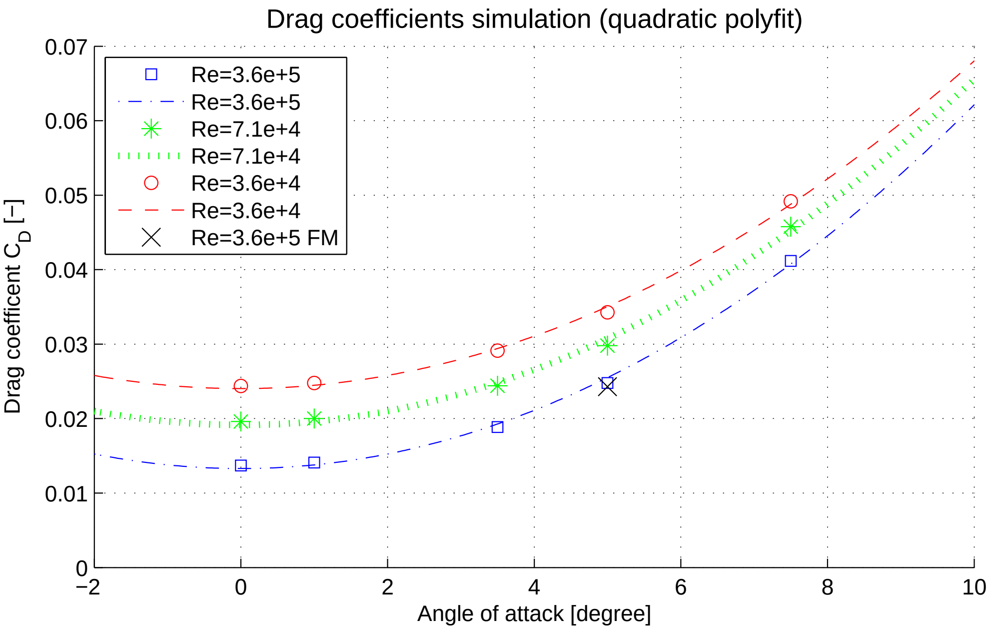

Figure 6.15.: Drag coefficients from the simulation results

pronounced. That is obvious since the drag not only results from lift, but also from viscous drag. The latter can be related to a flat plate since the rudder is streamlined. As the geometry is unchanged, the viscous drag coefficient depends on the Reynolds number only.

Ideally thus the viscous drag is independent of $\alpha$ and only leads to the different offsets for the different cases of $Re$. It is interesting that the medium $Re$ line is nearly situated in the middle, while its $Re$ value is much closer to the minimal $Re$. That, in reality, could be explained by a shift to a turbulent boundary layer. Consider figure C.2 for the drag coefficients of a flat plate. But note that this simulation does not use a transition model and that not 'laminar', but 'turbulent' flow is modled.

It can be observed that the parabolas slowly approach each other with increasing $\alpha$. That is to be explained by two reasons: First, with the help of the previously described behavior of the lift coefficients. The lift enters quadratically into the induced drag and one can thus expect the parabola of the higher $Re$ drag coefficients to be steeper than the lower counterparts. Note that this referres to the simulation results. In reality and precisely stated, the quadratic approximation only holds locally. Secondly, the viscous drag is not completely independent of $\alpha$ and, as at the same time the dependence on $Re$ is given, it is possible that the parabolas slightly diverge from each other. The real boundary layer behavior is especially difficult to predict at such Reynolds numbers where the boundary layer is not generally turbulent.

### Vertical Lift Coefficients

The vertical lift coefficients obviously follow, like the drag, a quadratic behavior. That might not be obvious at first glance since the lift is linearly dependent on $\alpha$. But the vertical lift not only results from viscous forces. One can say that this simulation is based on a one sided wing. Consequently the averaged total vertical force is not obliged to vanish due to symmetry reasons. As the wing is finite a trailing vortex has to inevitably exist if lift is present. The trailing vorticity, or on the wing referred to as free vorticity, induces a circulation mainly confined to the tips of the wing that is equal the change in bound circulation, see equation 2.114. The drag is caused by the trailing vorticity. As the drag (coefficient) is proportional to the lift (coefficient) squared it is logical that also the vertical lift (coefficient) caused from such 'tip suction force' follows a quadratic behavior.

The vertical lift coefficients offsets result from viscous forces (at $\alpha = 0°$). Similarly like a waterski can plane, here, the rudder is opposed to the opposite effect.[5] The viscous part of the vertical lift coefficient is dependend on the Reynolds number, but also heavily on the form of the geometry. Here it might also be interesting to refer to the thickness based Reynolds number that is considerably lower than the chordbased one (11 times for each's maximum geometric value here). This argumentation can serve as an explanation for why the three $Re$ cases are relatively close together.

---

[5] In contrast to a waterski the flow around the rudder does not separate and sourrounds smoothly the whole streamlined rudder.

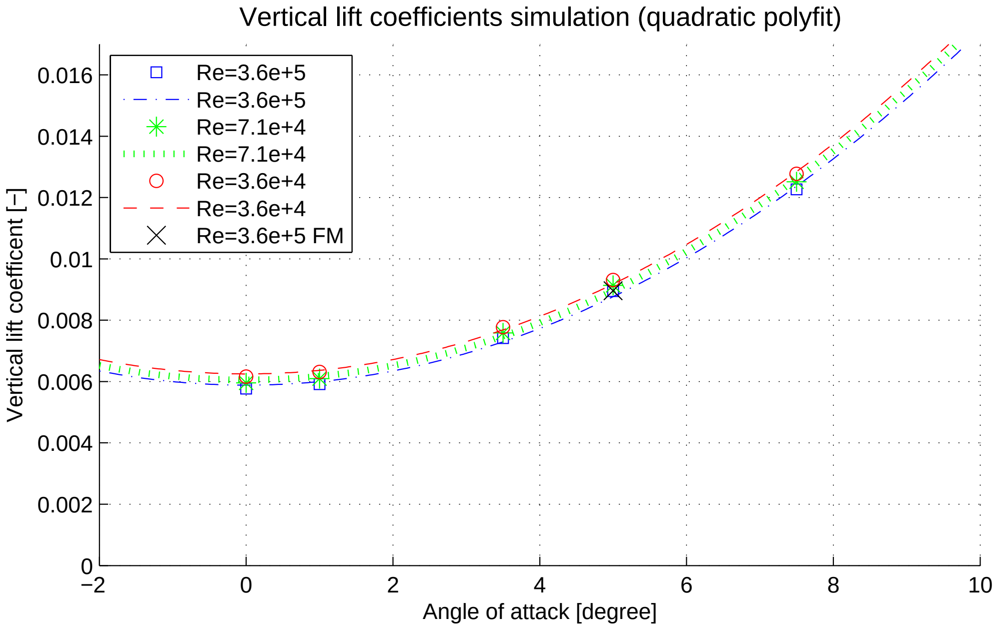

Figure 6.16.: Vertical lift coefficients from the simulation results

If all hypothesis are correct, it remains the question 'why do the vertical lift coefficients not show the same diverging behavior like the drag coefficients'? The viscous part of the vertical lift is, in contrast to the viscous drag force, heavily dependend on the form. The size of the surface orthogonal to the free stream changes immediately if $\alpha$ moves away from zero, that is not the case for the planform surface that is aligned with the free stream. And is is the former surface that is of importance for the viscous part of the vertical lift. The tip suction force depends quadratically on $\alpha$, but also the viscous part of the vertical force depends on $\alpha$ in a manner that is unknown and has to dependend on the geometry. Thus, while the change in drag over $\alpha$ relates mainly to the induced drag, the change in vertical lift over $\alpha$ does not necessarily mainly relate to the tip suction force, but can also be caused by the change of the viscous force.

Note that a tip suction force can also be induced from a roll motion if the roll angle is $\pm \gg 0°$.

### Efficiency: Lift Drag Ratio

The polylines found from the drag and lift coefficients can be used to construct lift-to-drag ratios as shown in figure 6.17. As one naturally is interested in minimal drag and maximal lift this serves as an indicator of merit. As not only the drag coefficient is smallest for the highest $Re$ computation but also the lift is slightly higher, it is clear that the highest $Re$ leads to the best performance. It also represents the race pace and peaks at $\alpha = 5.1°$ with

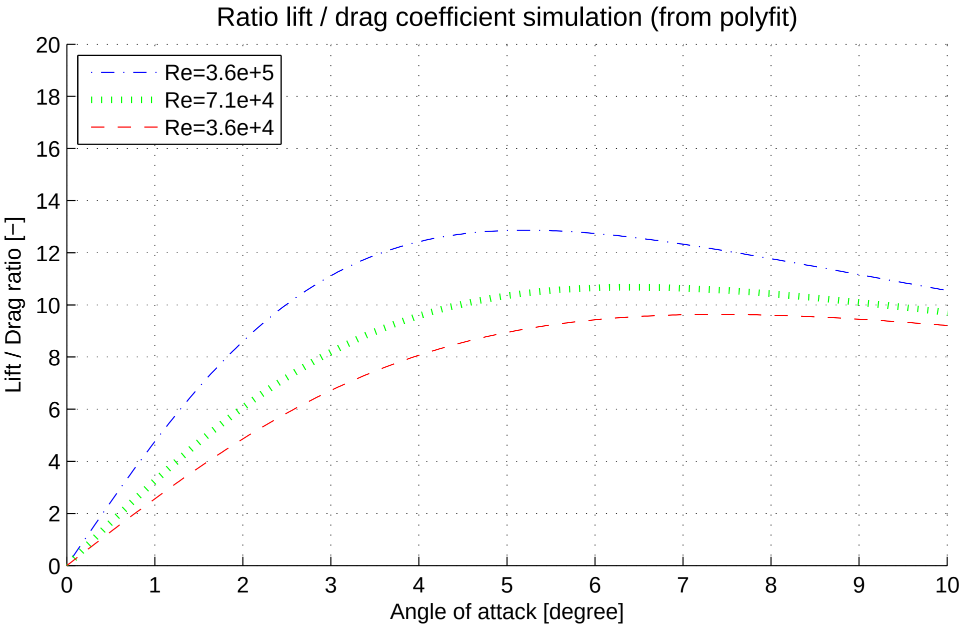

Figure 6.17.: Lift to drag ratio based on the simulation results

a maximal ratio of 12.9. With the polyline representing the 10 times smaller Reynolds number, or respectively velocity, the peak is shifted to higher angles of attack since the viscous drag forces are much higher (quasi offset on the induced drag). Its maximum is reached at $\alpha = 7.3°$ degrees with a ratio of 9.6. Those maxima marks the point where the drag coefficient reaches double the value of its size at $\alpha = 0°$. This behavior is caused by the linear approximation of lift combined with the in $\alpha = 0°$ symmetric parabola of the form $ax^2 + c$ for the drag. Consequently the point of highest merit and double drag compared to the drag at $\alpha = 0°$ is situated at $(c/a)^{1/2}$.

In the big picture this behavior implies that an increase in Reynolds number leads to a better performance of the airfoils. That indeed is true, see for example [Lis83]. But, not only that scaling effects are very important, in terms of kayaking the chordbased $Re$ can only be influenced by changing the chordlength and this is adequate only in a very limited range.[6] It is possible that an other local maximum is hidden in between the achieved calculations (that might exist in the real world, while it by these simulations, that do not employ additional transition models, possibly never can be found). Especially the phenomena of the boundary layer (separation, transition, reattachment, thickness) have a complex influence on drag and lift.

---

[6] In order to maintain a similar lift force, an increased chordlength will have to be balanced with a diminished spanlength. Thus a rudder with a smaller aspect ratio would evolve. And the smaller $A$ the smaller the lift coefficient (see figure 6.5).

This section concludes by remarking that the lift coefficients found from the simulations are not totally independent of the Reynolds number. The magnitudes of the drag coefficients are heavily dependent on $Re$ since, assuming (for illustration purposes) the viscous drag in this range to be totally independent of $\alpha$, the viscous drag first becomes the minor contributor to the drag above $\alpha = 5.1°$ (high $Re$ (race pace) computation). The vertical lift is roughly 3.5 times smaller than the drag and, most important, it is orthogonally directed toward the intended direction of travel and is therefore no (direct) power sink.

Also note that these coefficients are found for the specific geometry. Only rudders with the same form (but different size) can be assumed to obey these coefficients for the specific $Re$. That is called the principle of geometric similarity (geosim), see chapter1.3.3.

## 6.4. Comparison of the Simulation and the Analytic Results

The analytic and the simulation results can be verified and analyzed against each other. As the coefficient graphs from the simulations are based on the small rudder, the whole comparison occurs with respect to the smallest rudder, which is also treated in the theory section 6.2.2. In order to have clear figures, only the two simulation results for the maximal and minimal Reynolds number are presented.

### 6.4.1. Lift Coefficients

The analytic lift coefficients are based on the approximate aspect ratios relating to the kayak rudder and the specific theory. An overview on those aspect ratios and the corresponding geometric measure is previously introduced, see table 6.2 in section 6.2.2. There also an argumentation is presented that, for the elliptical lifting line results, argues for $A = 4.4$. That indeed is a compromise since also $A = 4$ has a similar degree of justification. For the slender body theory it is noted in section 6.2.2 that $A = 2.2$ is the only considerable aspect ratio. It is based on the surface and the direct length of the rudder. But attention has to be payed since the rudder is not 'swimming' alone in an unbounded fluid.

First considering figure 6.18. It compares the three higher aspect ratios in terms of LLT and the three minor $A$ in terms of the SBT with the simulation results. It is clearly visible that SBT with $A = 2.2$ only slightly underestimates the simulation results, while the two

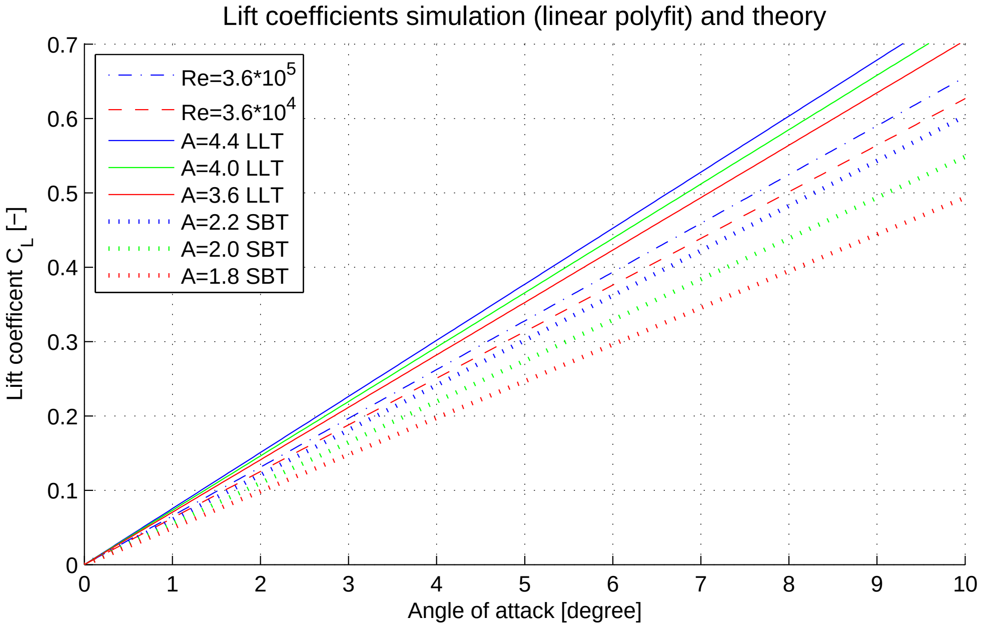

Figure 6.18.: Lift coefficients; comparison of theory and simulation results

remaining aspect ratios lie considerably further off. All information regarding the kayak-rudder entering the SBT results is its maximal span and, due to the representation as a coefficient, the planform surface. SBT's main restriction is that the body is slender. Other than that SBT does neither take into account what the body's geometry looks like, nor how large the surface is.[7] Considering the span length as fixed, SBT is at its maximum validity if the chordlength $l_0 \to \infty$. One can state that SBT remains valid as long as the achieved force remains unchanged as $l_0$ (and therefore the planform surface) becomes smaller. That can be regarded as the region where three-dimensional effects are dominating. Obviously, SBT will overestimate the lift force as the aspect ratio is growing (see also figure 6.5). This tendency starts, even though negligible for very small $A$, right away as $A$ is growing (when comparing to LLT, note that LLT overestimates the lift by 100 % as $A \to 0$). Thus at $A = 2.2$ one certainly expects the SBT to clearly overestimate correct results. That is not the case here and it has a very reasonable explanation.

Here it is not appropriate to employ $A = 2.2$ in terms of the SBT since the upper side of the rudder is fixed to the kayak (or a no-slip box) and thus the three dimensional effects correlate to a situation where the rudder also is mirrored to the other side of the box (or kayak)! Therefor, also for SBT, the higher aspect ratios are appropriate (here in particular $A = 4.4$) and they are obviously way too far away from the region where SBT is close to be valid. Thus, even the SBT results on the first glance seem to be reasonable since they nearly coincide with the simulation results, they are no appropriate representation. This match is only a coincidence since the body here is regarded as swimming alone without a kayak above it. By accident it has an aspect ratio that in terms of SBT yields similar results. Concluding even the smallest kayak rudder analyzed is not slender enough to obey the limitations of slender body theory. Nevertheless, it has to be stated that regarding the whole kayak, slender body theory displays a powerful analytic tool. But that is not the focus of this work.

Comparing the elliptical lifting line theory to the simulation results, it is clear that LLT regarding all aspect ratios overestimates the simulation results by a considerable amount. As to be expected $A = 4.4$ predicts the highest lift since it also represents the geometry where three-dimensional effects are least dominating. The overprediction is expected since it is known that LLT overestimates the lift force more and more as the aspect ratio is decreased. In section 6.2.1 a function describing the approximate error is deduced, see equation 6.6. It exactly represents the discrete errors found from literature for $A \geq 2$ (presented in table 6.1). That allows to correct the LLT lift results for the

---

[7] Precisely stated, here the angle of attack is assumed constant all along the body, and the nose is assumed to be a point of zero transverse dimension. Anyhow, in the force (not coefficient) enters only the maximal spanlength.

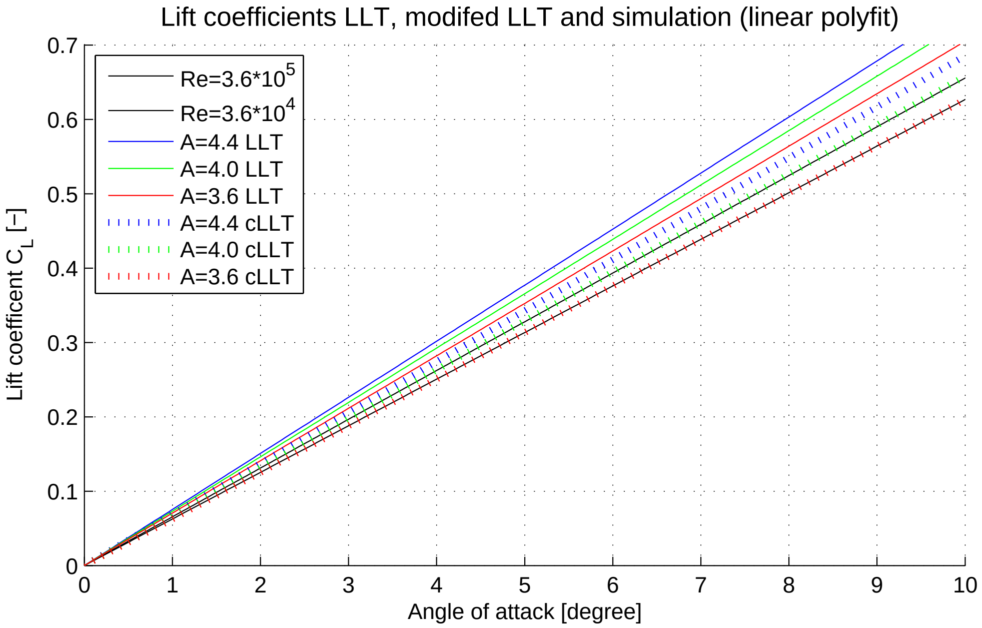

Figure 6.19.: Lift coefficients; comparison to error corrected lifting line results

appropriate amount. Using this error correction, the corrected lift coefficient writes $C_{Lc} = C_L\left(1 - \frac{1}{2.5A}\right)$ and is appropriate for all $A \geq 2$. Its results are presented in figure 6.19 and are astonishing. The corrected LLT for $A = 4$ exactly matches the simulation results of the higher Reynolds number, while the corrected LLT for $A = 3.6$ matches the low Reynolds number simulations. The aspect ratio $A = 3.6$ is described as not appropriate, which is also found here: Since LLT theory fuses on the approximation of zero viscosity, it is more appropriate to be compared with situations where the Reynolds number is high. The race pace chord based $Re$ is 0.36 millions. That is not very high for an airfoil. Consider for example a conventional passenger airplane at 800 km/h with a chordlength of 2 m and dry air at 20° Celsius, here $Re = 66 \cdot 10^6$. And that, even though the kinematic viscosity of air is much higher than that of water.

The corrected LLT results for $A = 4.4$ still overestimate the high $Re$ results by 4.6 %, while it are 15 % for its unchanged LLT counterpart. In the last section (6.3.5) it is argued that $A = 4.4$ might be slightly more appropriate than $A = 4$, while the best theoretical approximation might lie in between the two. The simulations show the tendency of increasing lift with increasing $Re$. That would certainly bring the results closer to the $A = 4.4$ corrected LLT results if even higher $Re$ computations are performed. From this perspective the corrected LLT with $A = 4.4$ might be the one closest to a higher $Re$ simulation.

Nevertheless, in the case of the kayak rudder at its specific $Re$, the corrected elliptic

LLT with the aspect ratio based on the span and chordlength ($A = 4$) fits perfectly to the simulation results. The actual difference to the polyfit lines generated by the simulations is 0.37 %. Therefore, assuming the simulation result to be correct, the corrected LLT result with $A = 4$ can be recommended in order to predict the rudders lift. Note that this assumes ideal conditions regarding the fluid flow as e.g. the neglected boundary layer of the kayak and, of course, the uncertainties of the simulation results. The latter is questionable mainly because the *Re* regime that is critical in terms of transition. And these simulations do not employ transition models.

If the LLT correction also is usefull in terms of the drag coefficient is discussed in the next section.

### 6.4.2. Drag Coefficients

The analytic drag coefficients found from lifting line theory represent the induced drag due to the lift of finite wings. It depends quadratically on the lift and is caused by the trailing vortices.

Figure 6.20 contents several different drag coefficients. First the ones of the two polyfit lines from the simulations. Then unmodified induced drag from analytic LLT solutions. There it is shown: $A = 4.4$ and $A = 4.0$, the corrected version introduced in the previous section for $A = 4.0$, while the two remaining aspect ratios $A = 2.97$ and $A = 2.66$ evolve from requiring the LLT lift coefficient to equal the simulation result for the high and low *Re* respectively. The two letter drag coefficients are then also shown in a further modified form. They are given an offset in order to artificially incorporate a viscous drag by using the simulation results at $\alpha = 0°$.

As can be seen in figure 6.20 $A = 2.97$ and $A = 2.66$ have nearly the same gradient. It is noticeably higher than for $A = 4.4$ and also as for the $A = 4.0$ case. This is reasonable since the more three-dimensional the wing, the more induced drag evolves relatively to its surface. The drag based on the corrected LLT results ($A = 4.0$ cLLT) has a far lower gradient than all others. Also that is reasonable since $\overline{C}_D = \overline{C}_L^2/\left(\pi A\right)$; and for the cLLT $\overline{C}_L$ is diminished but divided by the unchanged $\pi A$.

The reason why the two parabolas from the simulations not have the same gradient and offset is explained in the previous section (6.3.5).

Instead of using an offset based on the simulation results, it might be inviting to use a frictional coefficient from the literature in order to describe the total drag. But attention is required when taking this offset from the friction coefficients of a flat plate. In the case of the rudder, the planform surface is used to normalize and it does not equal the real surface that is more than twice as large. Then, the appropriate Reynolds number is not an absolute value since the chordlength is a function of $z$. And, of course, the rudder is not

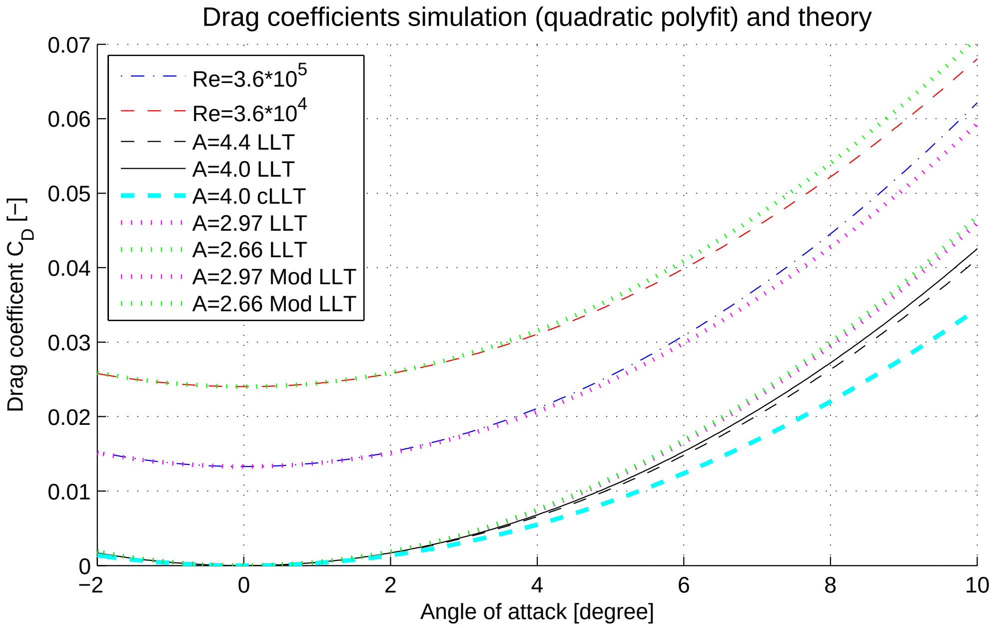

Figure 6.20.: Drag coefficients; comparison of theory and simulation results

flat! In reality, the viscous drag coefficient thus also has a component due to form drag. And, separation (transition, reattachment) can occur due to the adverse pressure gradient. Critical is not only the leading edge, but especially for laminar flows the whole part of the chord downstream of the thickest position, where ideally the pressure carfully is brought back up to the normal level (see e.g. figure 6.12(b)).

The two modified lines are of little scientific value since the LLT overestimates the lift. Thus, simply reducing the aspect ratio to make it fit to the simulation results, remains a purely constitutive approach since the induced drag does no longer correspond to the appropriate geometry (but an ideal elliptical one that has a minor aspect ratio). In addition, and that is the case for all outlined theoretical approximations of the total drag, the viscous drag is not independent of the angle of attack. It is build on two different types of viscous drag. As $\alpha$ increases, more and more viscous form drag will occur, while the percentage of the frictional drag is decreased. It is thus difficult to validly determine how much viscous drag exactly contributes to the total drag at different $\alpha$. Nevertheless, the theoretical assumption of a constant viscous drag yields an acceptable fit for the matched aspect ratios. For the low $Re$ simulation also the LLT with $A = 4.0$ fits well, and one can discuss this further in terms of the efficiency.

### 6.4.3. Efficiency: Lift Drag Ratio

The arguments involving separation are highly interesting in terms of the state of the flow (laminar or turbulent). A turbulent boundary layer can withstand a higher adverse pressure gradient than a laminar one where separation quickly sets in. Is a laminar flow separating, then it is very likely to turn turbulent and a reattachment can occur. If the latter scenario occurs and the now turbulent flow reattaches, then the recirculation region is referred to as a *laminar separation bubble*. Such phenomena are critical to the performance of airfoils (or rudders). In order to reattach a Reynolds number of about 70 000 is needed. At $Re \approx 10^5$ the laminar separation bubble usually extends across 20-30 % of the lifting surface. One can look at the flow outside the boundary layer as a potential flow. Is the bubble present over a large part of the wing, then the 'potential' stream, and in consequence the pressure distribution, is changed distinctly as compared to a case without such bubble. At higher $Re$ this bubble may be a lot shorter as compared to the chordlength and therefore have an minor effect. But, is the angle of attack increased over a critical limit, then this bubble can burst and a sudden stall sets in. This information is found in [Lis83, ff.229]. It must not necessarily be a bursting separation bubble that triggers stall. At larger Reynolds numbers for example, the flow anyhow is turbulent before the adverse pressure gradient sets in.

The efficiency of a lifting surface can be expressed with the help of the lift-to-drag ratio (the ratio naturally reveals the same dimensionless result, no matter if one uses the coefficients or only the forces). For a quantitative overview on the maximal achievable efficiency of airfoils see figure 6.21. It clearly shows that the Reynolds numbers the kayak rudder is operated in are in the critical region. It is exactly in this transition region, the modeling of the lift and drag behavior is especially difficult (of course also other regimes come up with interesting phenomena like cavitation or the effects of approaching mach speed).

Luckily the maximal achievable lift to drag coefficient is not the crucial parameter for the kayak rudder. It is symmetric, since it has to perform equally for both directions, and is mostly operated at moderate angle of attacks. Thus it is of higher importance that the lift-to-drag ratio is already maximal for small lift forces.

A low drag force (not coefficient) certainly is achieved if no separation occurs and if in addition the boundary layer remains laminar. But laminar boundary layers lack the ability to withstand stronger adverse pressure gradients. That is the actual reason for the dramatically reduced performance shown in figure 6.21. In order to avoid separation in a laminar regime not only $\alpha$ has to be small, but in case of the symmetric kayak rudder one can also say that the thickness to chordlength ratio must be small as well (and nevertheless the leading edge round). That is that the adverse pressure gradient has to be small enough

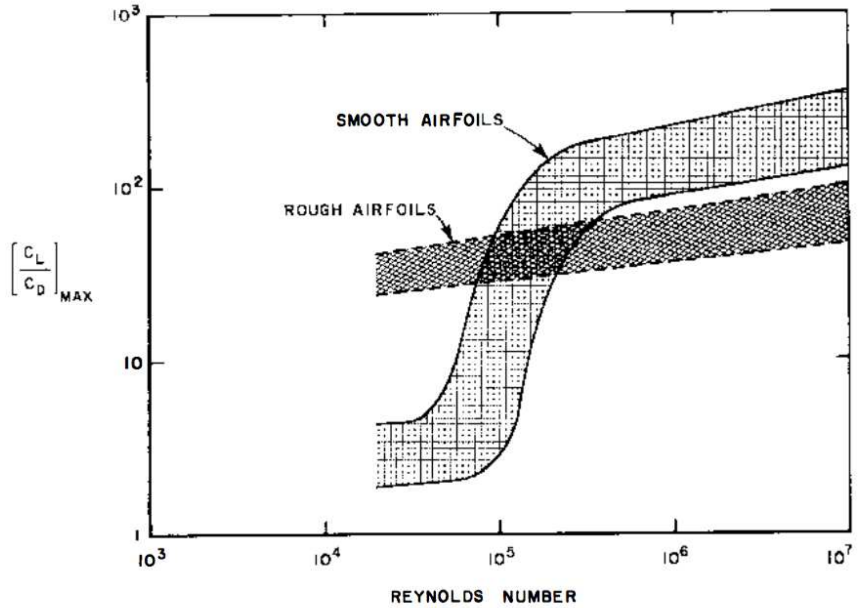

Figure 6.21.: Maximal efficiency of airfoils over the Reynolds number; source [Lis83, p.226]

so that the (laminar) boundary-layer can withstand.

It is generally a huge challenge for CFD to predict the correct point where transition takes place. There exist (mostly purely empiric) models that can provide help. But not only do they have to be used with care, also the validity is somewhat uncertain. If separation occurs is extremely dependend on the conditions of the boundary layer (laminar or turbulent, thickness, surface roughness, etc.) and thus also very difficult to predict in such transitional *Re* regime. Note, that a fully laminar flow can be solved without turbulence modeling, see chapter 6.3.2.

Figure 6.21 also implies that the separation occurs early in laminar flows and sets much lower limits than in the turbulent regime (at similar *Re* already at a factor roughly around 20! (log scale)). The simulation results, especially for the lowest *Re*, predict higher maximal lift drag ratios than displayed by the stripe for smooth airfoils in this graph. That does not mean that the rudder is rough, its surface is assumed smooth in the calculations, but it is an indicator for the turbulent flow modeled. The simulation is based on turbulence modeling without employing transition models. The flow is given a 5 % turbulence intensity at the inlet and, even though transition models exist, laminar turbulent interaction is a huge challenge for turbulence modeling.

Figure 6.22 shows the ratio of lift to drag, and therefore the efficiency of all the coefficients introduced in the previous section. In terms of lifting line theory it is clear that, as $\overline{C}_L \to 0$ also the induced drag coefficient approaches zero. As the latter quadratically depends on the former, their ratio tends to infinity as $\alpha \to \infty$. The purely theoretical coefficients are only indicated in the north-east corner since they, as just outlined, quickly become extremely large.

The more realistic results are gained from either pure simulation or from modifying the analytic induced drag with help of the drag coefficient predicted from the simulations at $\alpha = 0°$ (as described in the previous section).

As to be expected, both, the LLT and the cLLT (error correction formula) for $A = 4.0$ overestimate the efficiency of the simulations clearly for all $\alpha \gtrsim 2.5°$. That difference results from the prior outlined underestimation of the drag in case of cLLT, and, for the LLT, from the more distinct underestimation of the drag in combination with the overprediction of the lift as compared to the simulations. The two from the artificial adaption of the aspect ratio, constructed results go very well with the simulation results. Anyhow, all theory based efficiencies not only build on the assumptions taken in order to derive the LLT, but also on the assumption that the viscous drag would be independent of $\alpha$. That is not the case.

It also remains the uncertainty of how realistic the simulation results are (especially at higher angle of attack). As outlined, the regime the rudders are used in is not only critical to their maximal performace, but also a huge challenge for the turbulence models.

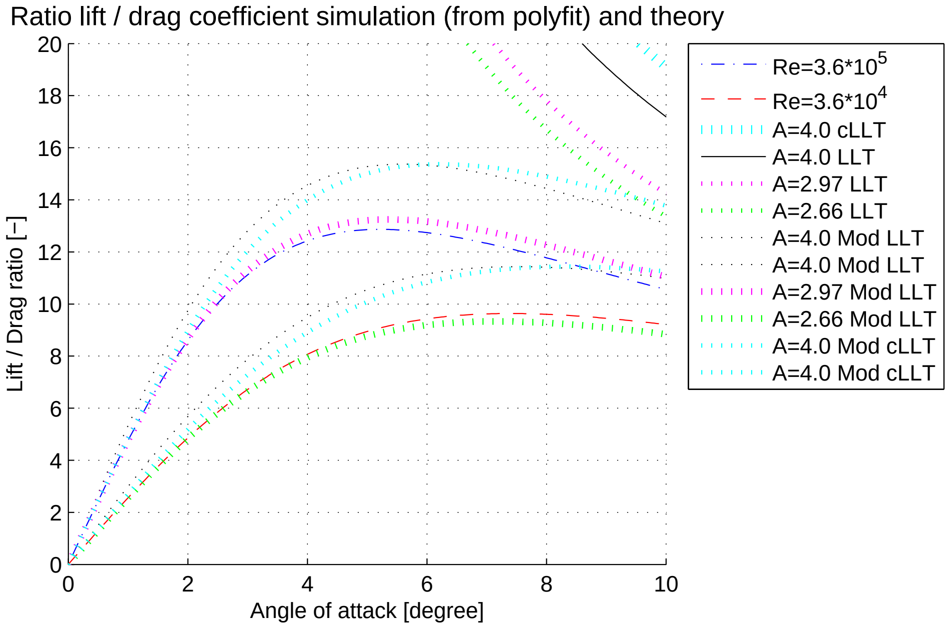

Figure 6.22.: Lift to drag ratio based on theory and simulation results

## 6.5. Comparison of the Experimental Outcome to the Simulations

Due to the cessation of the experimental work after the amplifier broke down, the experimental results are only preliminary. Nevertheless, the drag value for zero angle of attack can be compared to the simulation results.

In this setup the rudder is submerged 8 mm under the waterplane. The resulting drag force in Newton is shown in figure 6.23, where the average value is indicated by two different filtering techniques. The simulation result for the drag at 0.85 m/s does not exist. An approximate drag coefficient is thus found from linear interpolation between the simulation results for 0.5 and 1 m/s. That yields $C_D = 0.021$. The rudder used in the simulations is identical to the one used in the experiment. Evaluating $C_D$ for the given rudder yields $D = 0.043$ N. That are 57 % less than the 0.0759 N averagely predicted by the experiments. Note in figure 6.23 only one run is shown. For an analyses in the frequency domain with interesting outcomes and for more information on the experiment conduct the expirement chapter (5).

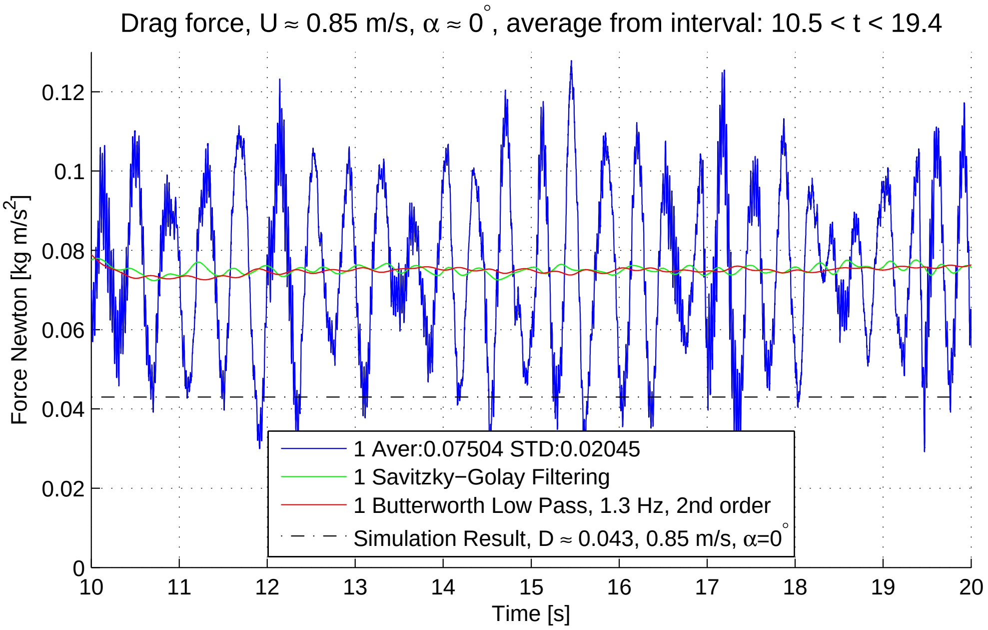

Figure 6.23.: Experimental force measurements; comparison to simulation results

First of all the simulation results go under an uncertainty. Especially since the mainly in section 6.4 discussed complications of the boundary-layer phenomena apply. Nevertheless, here $\alpha = 0°$ and $Re \leq 7.1 \cdot 10^4$, both indicating for minor difficulties due to a in reality possibly laminar regime.

Secondly the force measurements are not precise. The force is applied off the center of the cell and also a lateral exposure is put on the force sensor due to the weight of the system. In addition the whole process oscillates at different frequencies. That all does not contribute to the precise measurement of the drag force.

But, these sources of error all are not the main reason for the big difference. It is found at the principle problem of the free surface. Waves are generated that cause a distinct increase of the drag. Unfortunately Michells equation does not apply here, since the rudder is submerged and the rod is far from continuous in terms of the rudder.

Due to the submerged rudder also the rod contributes to the drag, both, in form of wave drag and viscous drag. And there is one more contribution that is not present in the simulation. And that is caused by the surface of the rudder normal to the rod at the end of the rudder – read, the surface that usually is adjoin the kayak hull. And even though the rod is nearly as wide as the rudder thick, it contributes to the drag. (The rod does not cover the whole surface but only a fraction of it.)

The idea behind submerging the rudder is that the values of a submerged rod without the rudder can be subtracted from such measurements in order to find the drag of interest. This solution is chosen since mounting the rudder right at the surface causes wave drag as well as surface-tension effects directly on the rudder. Both do not arise in the simulation and neither (in this form) at the real kayak. And certainly 8 mm are not enough ensuring the rudder's contribution to the generation of waves to be small. Nevertheless, a compromise has to be found between the eccentricity of the force and the distance to the free surface.

There are several possibilities to deal with this dilemma. Certainly, a wind (water) tunnel test can make those problems obsolete right away. But that is not available and one can certainly find satisfying solutions here.

One would be to submerge the whole sensor and rudder, another one could be to redirect the drag force via a lever and have the rudder deeply submerged. That solution simultaneously gives the possibility to scale up the drag force for the sensor. Another possibility is to use a certain body on the waterplane area that might resamble a part of the kayak. In either of the two last named solutions one would have to subtract the drag found at runs without rudder from the runs with rudder. That leaves a small uncertainty behind since the contact surface of the rudder to such a geometry is covered in the runs with rudder, but not in the runs without rudder.

The other source of error is the noise induced from the trolly. That problem is solveable since the overdetermined bearings do cause a lot of unnecessary friction that even is increased since the trolly is shorter than wide. The rails currently used are of such high precision as usually found in e.g. milling machines. The author assumes that it is not necessary to change to other rails since one here could compensate with a modified trolly.

It can contain further bearings that give the system the necessary degree of freedom back to smoothly glide over the rails. Combined with a length to width ratio of, say, 3-to-1 that is assumed to distinctly improve the quality of the signal.

A last remark concerns the single point load cell. Ideal a further study ought include the analysis of the influence of lateral forces on the load cell since within the frame of this work no appropriate analysis could be conducted. That unfortunately holds even though the influence of off-centered-load and tangential forces has briefly been looked at before the amplifier was destroyed.

## 6.6. Lift, Drag and Power Loss

Combining the simulation results with the semianalytically found induced angel of attack allows to compute the dynamic lift, drag and power loss caused by the resulting forces on the rudder.

These results are very illustrating, but they do follow all assumptions introduced in the simulations and in the description of the induced angle of attack. The latter and its assumptions are presented in section 6.1.1. The resulting force coefficients used to compute lift and drag are presented in section 6.3.5.

Figure 6.24 shows the resulting quantities of the three different sizes of the rudder (for the dimensions of the rudders see table 6.3). All are based on the assumption of a constant free stream velocity of 5 m/s (as argued for in chapter 1.4.3). The results of the small rudder are in total agreement with the simulation results. But, the in figure 6.24 presented results for the medium and the large rudder introduce a further approximation. Here, the lift and drag coefficients are not, or only partly, known from simulations. The results for the medium and large rudder are therefore based on the coefficients found for the small rudder. The appropriate coefficients would be very similar to the one of the small rudder, but, certainly not equal. Therefore their results are indicated with parentheses.

Note that section 6.3.4 compares the large and the small rudder simulations on the basis of the available results of the large rudder (preliminary mesh, $\alpha = 0°$ and $1°$). Here it is argued that the lift coefficient of the bigger rudders must be higher than of the smaller rudder. That indeed is found (12 % at $\alpha = 1°$). This difference can be assumed to remain approximately constant since the lift behaves linear in $\alpha$ in this range. The drag coefficients of the larger and the small rudder can be assumed to be very similar at $\alpha = 0°$, but the difference will naturally increase as the induced drag (respectively $\alpha$) increases. But, as $\alpha$ is small here (below 4° see figure 6.2), the error introduced for the drag (and power loss) can be assumed smaller than for the lift.

Figure 6.24(a) shows that 17.8 N maximal lift occur, while the results for the medium

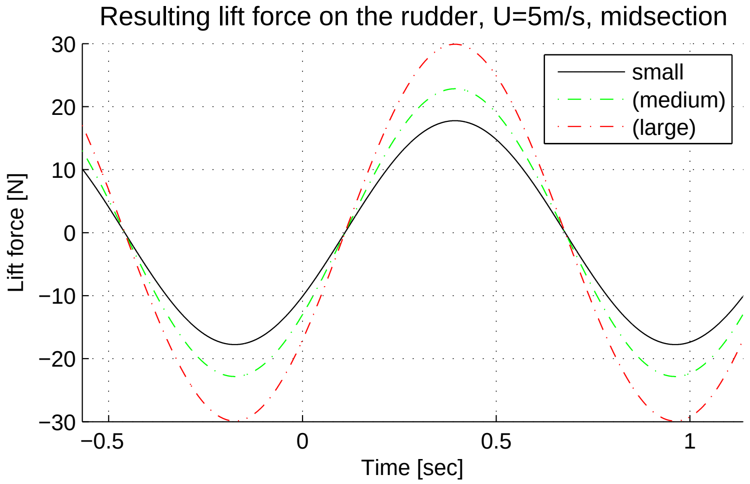

(a) Lift

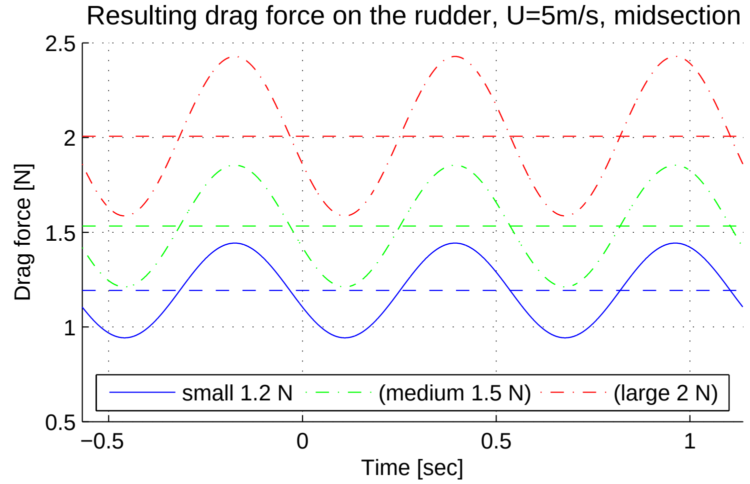

(b) Drag

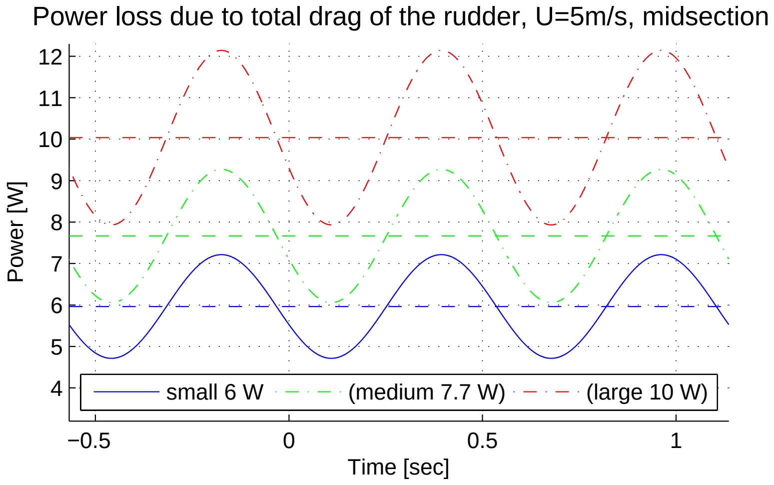

(c) Power loss

Figure 6.24.: Lift, drag and power loss for the different rudders; $U = 5\mathrm{m/s}$, $\alpha > \pm 3.8^\circ$

and large rudder have to be expected higher. Here, the large rudder develops 29.9 N. Assuming the 12 % error found in section 6.3.4 being correct, one could state that 33.5 N are more appropriate. In figure 6.24 the difference between the small and the large rudder is generally +68 % of the quantities of the small rudder (absolute +168 %). Using this 12 % error correction increases this value to +88 %, with validity only for the lift (absolute +188 %). For the medium rudder no simulation results are available. Compared to the small rudder its difference for lift, drag and power loss is thus +29 % (absolute +129 %).

The average drag force is 1.2 N for the smallest and 2 N for the biggest rudder. Naturally the frequency of the drag force is doubled compared with the lift. Its amplitude is a result of the absolute lift force and is 0.25 N for the small rudder. The drag of the large rudder has an approximate amplitude of 0.42 N.

The drag naturally is proportional to the power loss. The average rate at which energy is transferred to the water is 6 W for the smallest and 10 W for the largest rudder. Compared with a total power output of an elite athlete, which is in the order of magnitude of 500 W (over a few minutes), the rudder would contribute 1.2 % for the small and respectively 2 % for the large rudder. How much energy the rudder prevents being lost to e.g. waves is the deductive question that arises here. An estimation of the losses to waves can seminumerically be computed within potential theory, but that is not part of this master's thesis.

Note that the power loss is proportional to the velocity cubed. That makes a percentaged enhancement of the race time at an elite level extremely difficult compared with one at lower speeds since for the same percentaged improvement in speed a much higher gain of power output is required. This is one reason why elite kayakers', cyclists' or skiers' performances seem so similar regarding the achieved times.

## 6.7. Optimal Form

What is the optimal form of the rudder?

**Ideal Case:** First looking at the ideal case of the lifting line theory. The answer is simple – first of all an elliptical planform. The derive is conducted in chapter 2.5.3. The LLT luckily has the studied analytic solution for exactly this planform, where the theoretical lift-to-induced drag ratio is optimal.

It remains to determine what the ellipse should look like. That is, how large are the major and minor axis of the ellipse ($l_0/2$ and $s/2$) supposed to be. Here the answer is obvious – it has to approach the two-dimensional limit. That is $A \to \infty$, see for example figure 6.5.

Other planforms can be solved numerically or with help of a (quasi iterative) simplification method. The latter puts on further assumptions but allows for analytic treatment of planeform surfaces of more general form. It uses the first order circulation (two-dimensional) and inserts it for the unknown derivative $\partial \Gamma / \partial \zeta$ in (2.132). Thereby the second approximation is found and, theoretically, one could go on like this with the next correction. But that however would not be consistent with the approximations already incorporated in Prandtl's lifting line equation [New77, p.204]. An example of the application of this simplification method can be found in [Aya10, p.20].

Back to the predicted ideal case of $A \to \infty$. First of all, this case is technically impossible to build. Any material will at some point reach its limitations. And a wing with an extremely large span combined with a short chordlength (and a corresponding small thickness!) is very fragile. Examples where efficiency is very important are gliders or in the field of birds e.g. albatrosses or storks. All of them have relatively large aspect ratios. A concrete example is found considering a state of the art glider like the DG-1001 S [Flu11]. Its spanlength is 20 m with a surface of 17.51 m$^2$, thus $A = 22.84$. For this particular aspect ratio the two-dimensional lift coefficient is 9 % higher than the one from elliptical solution of the LLT.

But assumed the materials allow even longer and narrower (and thinner) wings, would it really be more efficient to keep on increasing $A$ beyond a certain point?

**Effects of the Viscous Fluid:** The induced drag is not the only force that the paddler has to overcome. Viscous drag is not present in an ideal fluid, but will contribute to the drag of any real airfoil. In the extreme of zero lift ($\alpha = 0°$ for the symmetric kayak rudder), the induced drag is zero and all drag origins from viscous forces.

The next step could be the assumption that the viscous drag coefficient (say $C_{D_V}$) is constant. Then the only free parameter left is the surface and it should be as small as possible. And again, the optimal form would be to approach the two-dimensional limit.

Now introducing the kayak motion. Thinking of the kayak's roll motion, it is clear that, the bigger the distance to the roll axis gets, the higher the roll induced angle of attack. As the efficiency of the rudder is a function of the angle of attack, the first optimization criteria arises here. At some point, $\alpha$ exceeds the critical angle of attack and stall occurs. See figure 6.3 for the difference between the induced angle of attack at the tip and at the position where the rudder is fixed to the kayak hull. If a rudders truly has such a large spanlength that separation occurs due to roll motion in the region close to the tip, then it certainly is appropriate to consider mounting the rudder at the very last point of the vessel – the stern (there it is closer to the roll axis).

The viscous drag coefficient is dependend on the Reynolds number. Generally (for streamlined bodies) one can say that it decreases with increasing $Re$. For the rudder where $A \to \infty$, the lift coefficient is high (if not stalling), but $Re$ is low and that implies a high $C_{D_V}$ (but a small surface). Therefore, also here, an optimization problem evolves. Taking a look at the experimental results for the frictional part of $C_{D_V}$ (figure C.2) however reveals that the transition region necessarily will be difficult to predict. And that is just for a flat plate; the real wing is not flat and has camber and therefore also pressure drag (viscous form drag), even though it is comparatively little at small $\alpha$.

That leads to the assumable most important factor for airfoils in the $Re$ regime of kayak rudders. It drastically increases the complexity and has to do with the fact that a laminar boundary layer cannot withstand larger adverse pressure gradients and will quickly separate. The separated flow then is likely to turn turbulent and thus a reattachment becomes possible. The described case leads to what is called a 'laminar separation bubble'. Depending on its size the lift is dramatically altered. But also the drag is affected – both directly and indirectly by the change of induced drag. Where exactly such a separation bubble occurs is very difficult to predict. There are transition models that can provide help, but for multiple reasons they are not employed in these simulations.

Back to the optimization criteria. The drag and the (mostly maximal) lift coefficient strongly depend on $Re$, but also on $\alpha$, and on other factors like the ambient turbulence level, or the roughness of the rudder's surface. And in the limits, which in this regime are quickly reachable, only slight changes in one of the parameters can result in dramatic changes of the coefficients.

Using a turbulator on parts of the kayak rudder, for example in form of an artificial roughness, may hold the possibility gaining higher maximal lift-to-drag ratios. In a case where separation is avoided that would certainly be beneficial, but for the usually present small angles of attack, separation is expected to not occur and thus the drag would unnecessarily be increased. And, of course the risk of an overall worsening behavior as shown in figure 1.3 always remains.

One important point is not mentioned yet. The boundary layer of the kayak is turbulent and a large part of the rudder is situated within it. This at first glance negative starting point could in specific situations theoretically turn out beneficial in terms of preventing from a laminar flow and thus from a laminar separation (bypass transition). But also here one has to distinguish since for example a thicker turbulent boundary layer does not only increase the drag but also is less resistant against separation than a thinner turbulent boundary layer. Such a negative effect can arise due to for example a turbulator. Figure 1.3 shows that not only the drag is increased (that is inevitable compared to a nonseparating laminar flow), but also the maximal lift coefficient is diminished here.

The velocity in the boundary layer of the kayak is reduced (and the flow is turbulent) compared with the free stream. That causes, in situations where stall is prevented, a lower absolute lift and drag, while the lift coefficients can remain unchanged. But also the resulting angle of attack can be affected.

In addition, the kayak's boundary layer is time dependend since the kayak is moving (oscillating) in all degrees of freedom. That applies also for the resulting angle of attack described in chapter 6.1. In the case of separation time dependens becomes extra interesting since it incorporates a distinct hysteresis.

There is another factor that disturbs the fluid flow – the vortices shed from the propulsion. It is possible that those periodically interfere with the fluid in the region of the rudder.

All these parameters make an optimization of a kayak rudder an astonishing complex process that in order to guarantee realistically results ought to involve experiments. Simply referring to the possibility of turbulence modeling in order to optimize the problem is not as appropriate as it might seem since the transition, separation and reattachment process may play a major role.

Nevertheless, a feature any kayaker easily can influence, is that the trailing edge of the rudder is sharp. Due to the manufacturing process some rudders have a flesh along the edges. That can be removed with grinding. In contrast, for the leading edge one naturally has to recommend making it smooth and round in order to provide the best conditions for maximal circulation. Nevertheless, in this $Re$ regime, it is not completely certain that a roughness could provide for a better behavior with regard to the boundary layer (transition in order to prevent laminar separation later on the wing). Concerning the risk of trapping grass in the rudder, no doubt is left that the leading edge should be as smooth and round as possible; not only for the circulation, but in order to minimize those devastating risks.

There exist kayak rudders that are especially made for conditions with a lot of grass in the water. Those have a distinct sweepback angle. That is also known from high speed airplans. As they approach the speed of sound a form of wave drag arises that is minimized by such geometry. This argumentation is however not at all relevant for kayak-rudders, and the grass rudder can be expected to have a worse efficiency compared with traditional kayak rudders.

Concluding the author should like to mention an often seen feature of modern airfoil: winglets. Its idea dates more than hundred years back in time ([Wik11e]) and is a logical consequence of the recognition of the effects of the trailing vortex. They effectively reduce the downwash velocity on the wing induced from the trailing vortex and therefore lead to a higher efficiency of the flight. Nevertheless, it took them decades to become standard. In case of the kayak rudder, winglets at first glance also could be of relevance. However here the average lift force is naturally close to zero and therefore the benefit reduced. And the devastating effect arising of grass, or other things that might be in the water, possibly getting trapped in the winglet unfortunately make winglets directly obsolete.

# 7. Conclusion

The conclusion briefly summarizes the main achievements, gives further suggestions on possible improvements regarding the different topics treated and concludes with ideas that evolved while working on this master's thesis.

## 7.1. Résumé

Lifting line theory (LLT) and slender body theory (SBT) are derived and applied to kayak rudders. Of these two *analytical methods* only LLT can cope with the studied kayak rudders' aspect ratios ($A$). And even though $A$ is small compared with many conventional airfoils, it still heavily exceeds the slenderness approximation essential to SBT. The LLT principally assumes $A \gg 1$ but its asymptotic nature yields a powerful result, even for relatively small $A$. An empiric error correction function, based on approximate errors found in the literature, is introduced. With its help the LLT excellently matches the simulation results.

The successful *simulations* are the result of intense work with the meshing. And it has to be stated that the Reynolds number range of the studied kayak rudders is very sensible. That is because the real flow's transition from a laminar to a turbulent boundary layer occurs in this region. In this context is to mention the processes of laminar (and turbulent) boundary layer separation, transition and reattachment, where a laminar separation bubble can evolve. That has essential effects on the airfoil's performance, which is very difficult to capture using CFD.

However that is inherently included in the *experiment*. It is build up and preliminary results for the drag at zero angle of attack are available. They are reasonable compared with the simulation results, yet they are not directly comparable since the wave drag could not be accounted for. That mainly results from the fact that the amplifier was destroyed, and thereafter no further measurements have been conducted.

The motion of the *kayak* is studied with help of measurement data and information provided by former Olympic champion Eirik Verås Larsen. It is compared to information found in the literature and used to approximate the dynamic angle of attack. The latter is combined with the simulation results and then used to compute the power loss due to the drag of the rudder (approx. 6 W for the small rudder). Also the dynamic lift that diminishes the oscillating motion of the kayak in yaw and roll is found by this calculation. The enhancing potentials in flatwater kayaking are briefly described. Essential is the effectivity of the propulsion and the energy losses due to waves as well as due to viscous forces. Literature on the kayak-paddling propulsion is studied and the outcome summarized. The author's perspective of an enhancement of the propulsion is presented. The drag of kayak hulls can for example be optimized by freely available tools, and even though that is not the topic of this work, it is an interesting opportunity for further research.

## 7.2. Further Suggestions

This master's thesis studies the rudder flow phenomena and uses analytic, simulative and experimental methods to describe the force coefficients of kayak rudders. Gaining further inside into the effect of those on the kayak is a topic that naturally arises. A description of the energy loss to waves generated from e.g. the yaw oscillation and the analysis of how the yaw motion is influenced by the rudder (and hull and technique of the paddler) could along with the results of this work be used to form an optimization criteria concerning the size of the rudder.

All *simulations* are conducted with constant angle of attack. To consider the dynamic changes in inflow can be a next step, but with regard to the arguments presented in chapter 1.4.5 that is not necessarily more beneficial to the final outcome. Another point is of much higher interest. That is to take into account the effects of transition, but:

> Modelling of laminar-turbulent transition in boundary layers has proven one of the most challenging tasks in CFD for many decades. Although many industrial flows are in the range of $10^4 < Re < 10^6$ [...] there was simply no reliable way of including these effects even to first order in general purpose CFD codes. [Men09, p.308]

Menter and its group developed an empiric transition model, see [MLV06]. It is implemented in CFX. Today, this transition model is excessively validated together with the SST model [ANS10b, p.108]. Thus, indeed relying on empirical, experimental correlations, it nevertheless possibly allows to realistically compute the phenomenon of transition that can be so crucial for the performance of kayak-rudders. Its usage is of course connected to requirements of the simulation. They are that symmetry planes should be used (not slip walls) and that the mesh provides approximately $y_+ = 1$, ca. 75-100 gird nodes in the streamwise direction and a wall normal expansion ratio of approx. 1.1. Here, in order to model it adequately, it is crucial to know what the realistic turbulence intensity should be (attention, it is decaying in the streamwise direction of the inlet) [ANS10a, ff.126]. The turbulence intensity brings up the question that reveals how the simulation really could be put onto another level. That is the boundary layer of the kayak. Requiring an appropriate resultion of the boundary layer quickly exceeds the computational limits. Note that necessarily also the question of how to deal with the free surface arises; that one will cause further challenges to a simulation. Nevertheless, if a successful compromise could be found, further insight into an important factor influencing the performance of the rudder might be gained.

Besides turbulence modeling with all its advantages, also another tool that does not at all demand much computational time exists and can be of interest if one e.g. aims to change the form of an airfoil. Consider the so called panel method, as for example in [Fea08]. It relies on potential theory and does therefore inherently not take into account all effects of a real fluid.

A further comment in the simulation context concerns the meshing. The author assumes that considering another format than iges to import CAD-data into ICEM can be beneficial. In case iges is the only available source, try at least to first use another program converting the data into another format. Moreover, even though ICEM's geometry editing tools are easy to understand, the author recommends finding access to an ordinary CAD program, in order to conduct the first part of the editing of the geometry.

At some point it certainly becomes necessary to verify the simulation results with experiments. The *experimental approach* itself has to be further improved and validated. A further use of the setup ought to for example include a study of the effect of lateral and longitudinal forces on the single point load cell (due to e.g. lift or drag and weight). Another point is the increase of the velocity of the trolley (or the size of the rudder, temperature of the water) in order to accomplish the experiments at the intended Reynolds number. That is of importance especially in this transitional regime. Nevertheless, simulation results of lower $Re$ could also be verified against respective experiments. Also the turbulence level plays an important role at the real kayak-rudder, and one certainly has to find a solution if it is to be included in the experiments (use of e.g. fencing, measurement with PIV). A further thought is that it has to be shown that the intended solution regarding the treatment of the wave drag is satisfying. If that turns out to be false, another handling must be found. Apart from the increase of distance to the free surface, also other possibilities arise. One can for example think of a geometry put on the rudder-rod. Or another idea is covering major parts of the watersurface with plates of some light swimming material in order to suppress waves. Anyhow, as long as the rudder is submerged, a way to deal with the effect of the part of the rudder's surface that usually is adjoin to the kayak hull has to be found. But maybe it even is possible to use slightly larger rudders and measure without submerging them. A critical point that certainly needs to be modified is the trolly system. Its improvement is necessary in order to reduce the noise to signal ratio (and may be possible at very low costs). Some ideas are described in chapter 6.5.

The *theoretical approaches* studied within this work could form the basis for further research in the field of kayaking. The slender body theory can be applied to the kayak hull. The author for example has conducted a nonstationary computation on the basis of SBT (equations 2.77 and 2.85–2.87) to approximate the lateral force caused by the dynamic motion of the kayak rudder. But as the rudder does not fullfill the slenderness criteria, it is not further considered. Nevertheless, for the kayak hull SBT is applicable. An additional challenge that could be taken into account, is the free surface. It anyhow gives rise to many interesting research questions. A promising topic, for example, is the computations regarding different aspects of the wave drag.

The lifting surface theory applied to kayak-rudders fuses on elliptical lifting line theory. Kayak rudders have no perfectly elliptic planform. More general planform surfaces can be taken into account conducting numerical solutions. Comments on these are found in chapter 2.5.4. Another, however less promising method, is the simplification method mentioned in chapter 6.7.

One last suggestion affects the analysis of the *kayak's motion*. The deductions made in this work fuse on one single measurement covering 15 seconds only. It would be interesting to measure several kayakers with exactly defined position(s) of the sensor(s) in order to then be able to model the precise dynamic motion of the kayak. A computation of the kayak's energy losses to waves, for example, could then make use of precise input data. Nevertheless, it remains uncertain what effects on the rudder the boundary layer of the kayak and the vortices from the propulsion have. This study, most likely, will be good advised conducting advanced experiments.

## 7.3. Creative Comments

During this master's thesis several ideas evolved, especially on how the rudder, apart from higher efficiency caused by optimization of its form, could contribute to a better performance of the kayaker. This section presents them. They might quickly turn out to be unrealistic and even counterproductive! But one never knows and in sports it often are marginal differences that decide if a race is won or lost.

In order to minimize the yaw motion and the thereby resulting losses of energy, the kayak rudder not only needs to have the optimal size, but also functionality. If the angle of attack could permanently be adjusted such that a higher lift force is achieved that could increase the positive effect of the rudder without increasing its size. That might automatically be achieved using the periodic changing pressure difference between the left and right foot. Or, of course, by the kayaker permanently adjusting the rudder. But it is essential to match the appropriate phase (see chapter 6.1.1) and to not exaggerate.

The rudder rod is logically placed at the center of pressure. That is the first choice since it guarantees that no moment due to the lift (and drag) force acting on the rudder, acts on the steering system. In two dimensional analysis this point for uncambered foils like the rudder is the quarter-chord point.

If the rudder rod would be placed in front of the center of pressure, for example at the leading edge or even further away, the rudder could theoretically contribute to the propulsion of the kayak. Besides that this is prohibited by the regulations, the kayaker would also then be demanded to permanently ensure the position (and for an extra propulsion, motion) of the rudder. And it is very ineffective as the resulting angle of attacks are (and have to be) small and thus the resulting force (of drag and lift) might still have a negative $x$-component. (Fishes on the contrary are flexible and can gain a much higher efficiency from such propulsion.)

Is the rod displaced towards the leading edge, as proposed above, then the moment tends to rotate the rudder to zero angle of attack. The opposite is true for rod positions closer to the trailing edge. This variant is essentially instable. But one here could think of an advantage. This moment automatically tends to increase the angle of attack. If they system is flexible, say within one degree, and thereafter stiff, then $\alpha$ would jump by one degree every time zero is crossed. Thereby the average angel of attack is automatically increased. But attention is required since this is an instable process and its functionability relies on the fact that the slack in the system only allows a motion in the order of a fraction of the periodically existing angle of attacks amplitude.

Another idea, which is not realted to the rudder, also evolves from the thought of reducing the yaw motion, but relates to the propulsion. The submerged paddle has a considerable vertical orientation and the paddler attempts to direct its resulting force to the intended direction of travel. Naturally, a yaw moment on the kayak evolves. If the paddler could transfer a certain yaw moment into the opposite direction that could decrease the yaw motion. That is the direction of attempting to open ‘screw caps’ that ‘swim’ in the water or, mentioned the other way around, the paddle-rod has to ‘attempt’ to wring the paddlers hands further around the rod. It is questionable if such attempt is in accordance with the given biomechanical conditions and if it at all could have a considerable contribution.

Certainly, such a moment could automatically be induced by using an appropriate paddle-blade (similar principle as for the rudder-rod).

When reading the statues of kayaking one can notice that the symmetric form of the boat's hull is required for the canoe, not however for the kayak. Assume a paddler had a distinct difference between the propulsion of the left and right side, and, therefore his rudder would usually be adjusted more to one side. Then, this could be incorporated in a marginally asymmetric kayak hull, and therefore a slightly higher performace could possibly be reached.

# A. Note on Slender Body Theory

### First Note

Equation A.1 (7.30 in [New77, p.336]) can be shown with help of a Taylor expansion.

$$\left\{\left(\frac{\xi-x}{r}\right)+\underbrace{\left[\left(\frac{\xi-x}{r}\right)^2+1\right]^{1/2}}_{*}\right\} \simeq \frac{r}{2|\xi-x|} \qquad (\xi-x)<0 \tag{A.1}$$

Consider rewriting $*$ in the following way

$$\left[\left(\frac{\xi-x}{r}\right)^2+1\right]^{1/2} = \left[\left(\frac{\xi-x}{r}\right)^2+\left(\frac{\xi-x}{r}\right)^2\left(\frac{r}{\xi-x}\right)^2\right]^{1/2} \tag{A.2}$$

$$= \frac{|\xi-x|}{r}\underbrace{\left[1+\left(\frac{r}{\xi-x}\right)^2\right]^{1/2}}_{\bullet} \tag{A.3}$$

then using a Taylor expansion of the above term marked with $\bullet$ around $\left(\frac{r}{\xi-x}\right)^2=0$. Resulting it writes

$$\left[1+\left(\frac{r}{\xi-x}\right)^2\right]^{1/2} \simeq 1+\frac{1}{2}\left(\frac{r}{\xi-x}\right)^2 (\text{+h.o.t.}) \tag{A.4}$$

and all that remains to show the relation of (A.1) is inserting the approximation.

### Second Note

Also equation A.5 (7.27 in [New77, p.336] is not straight forward to solve.

$$\frac{d}{d\xi}\log\left\{\frac{\xi-x}{r}+\left[\left(\frac{\xi-x}{r}\right)^2+1\right]^{1/2}\right\} = \left[(x-\xi)^2+r^2\right]^{-1/2} \tag{A.5}$$

$$= \left\{ \frac{1}{r} + \frac{\xi - x}{r^2} \left( \left( \frac{\xi - x}{r} \right)^2 + 1 \right)^{-1/2} \right\} \left\{ \frac{\xi - x}{r} + \left( \left( \frac{\xi - x}{r} \right)^2 + 1 \right)^{1/2} \right\}^{-1} \tag{A.6}$$

When the derivative (A.6) first is computed, then it is auxiliary to expand the equation with $\left\{ a - (a^2 + 1)^{1/2} \right\}$ where $a \equiv \frac{\xi - x}{r}$.

# B. Additional Simulation Results

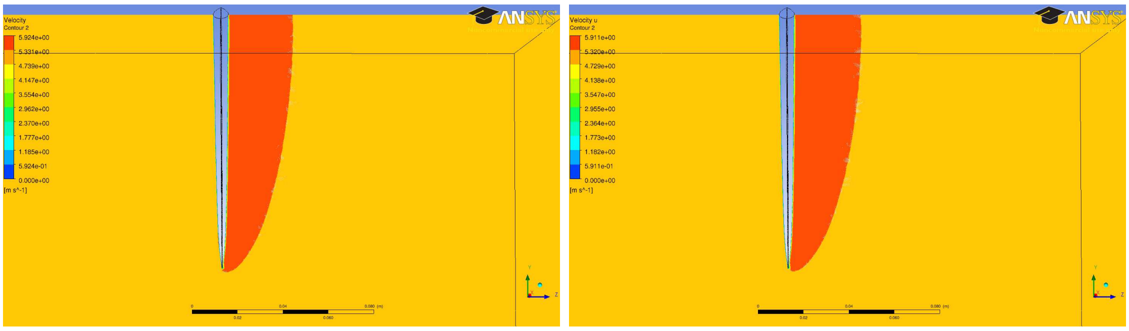

(a) contour zyplane totvel

(b) contour zyplane u

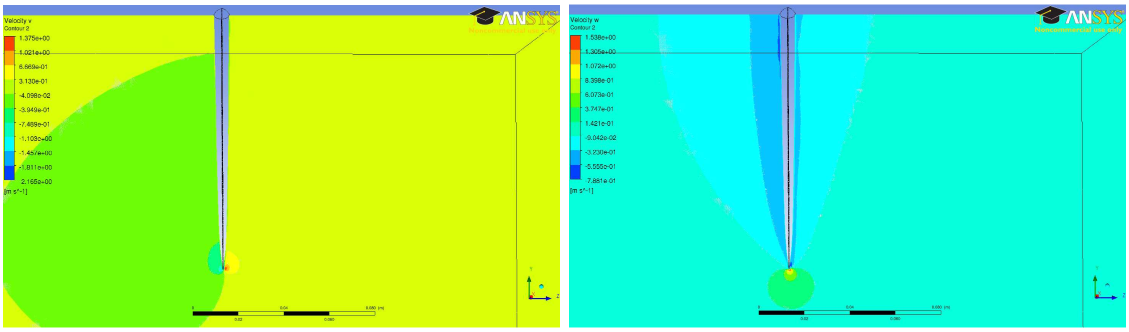

(c) contour zyplane v

(d) contour zyplane w

Figure B.1.: Contour plots of the velocities; slightly aligned front view ($\sim zy$-plane); final mesh with SST model; $U = 5\text{m/s}$, $\alpha = 0°$

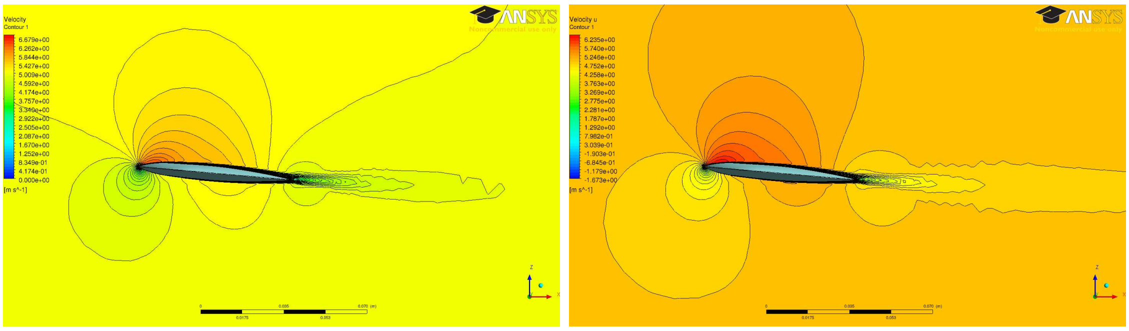

(a) contour totvel

(b) contour u

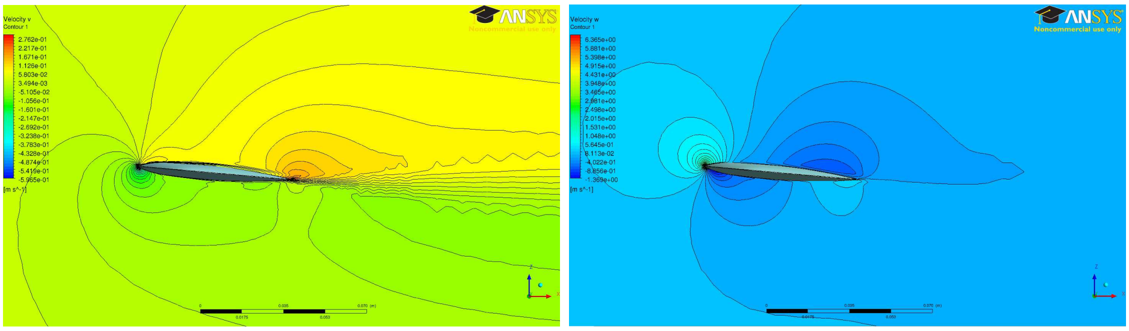

(c) contour v

(d) contour w

Figure B.2.: Contour plots of the velocities; final mesh with SST model; $xz$-plane; $U = 5\text{m/s}$, $\alpha = 0°$

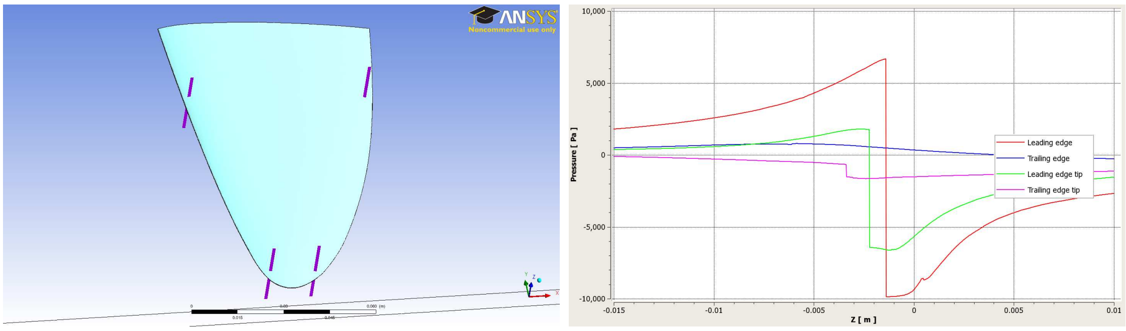

(a) Measurement lines

(b) p

Figure B.3.: Pressure along transvere lines at different position of the rudder; final mesh with SST model; $U = 5\text{m/s}$, $\alpha = 0°$

# C. Diagrams from other Sources

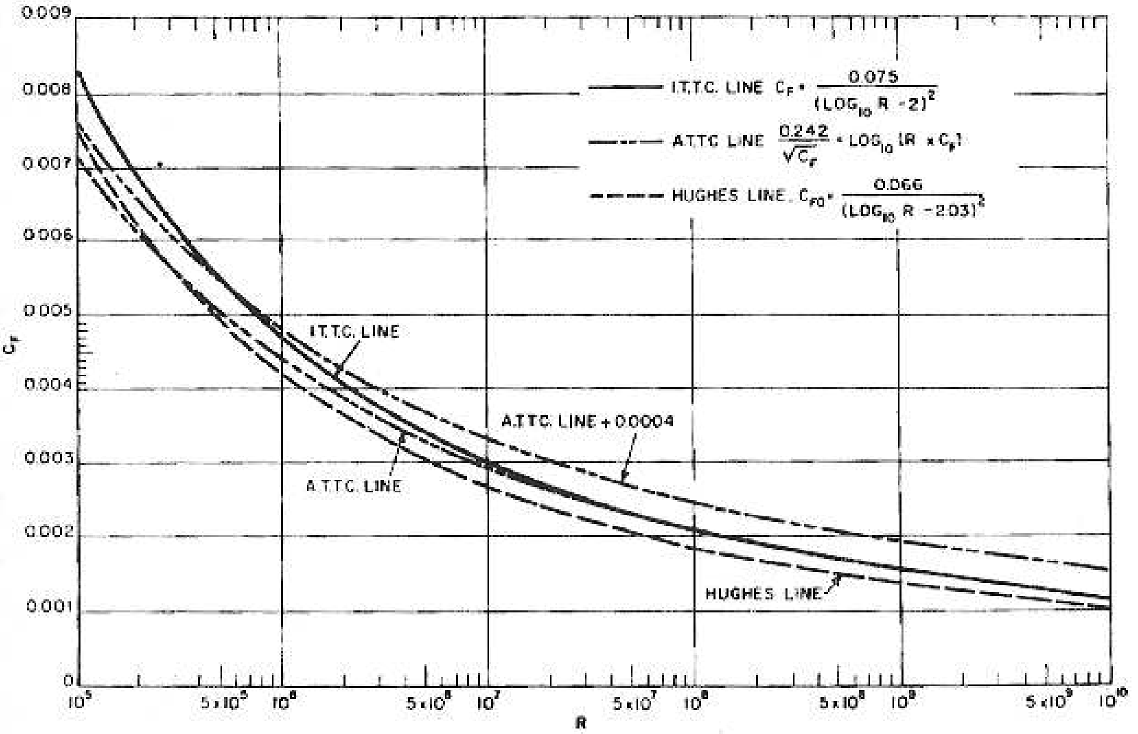

Figure C.1.: Frictional drag coefficients and extrapolators. The ITTC line is recommended by the International Towing Tank Conference, the ATTC line by its American equivalent. The latter equals the Schönherr line; source [New77, p. 31]

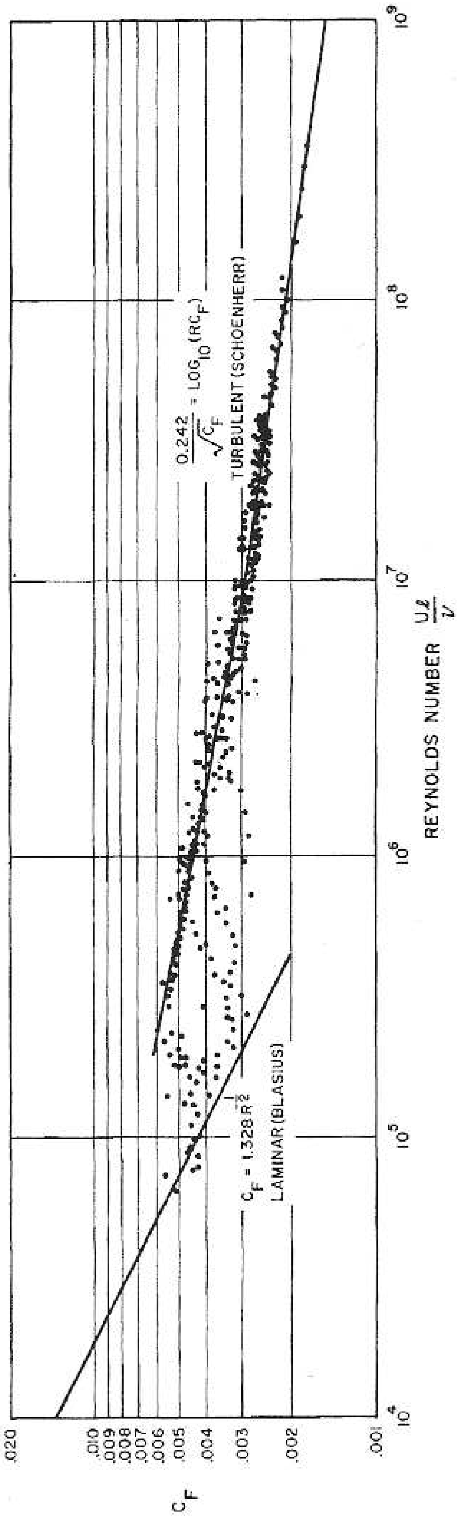

Figure C.2.: Schönherr's flat plate frictional drag coefficient compared with the (laminar) Blasius boundary theory and experiment results; source [New77, p. 17]

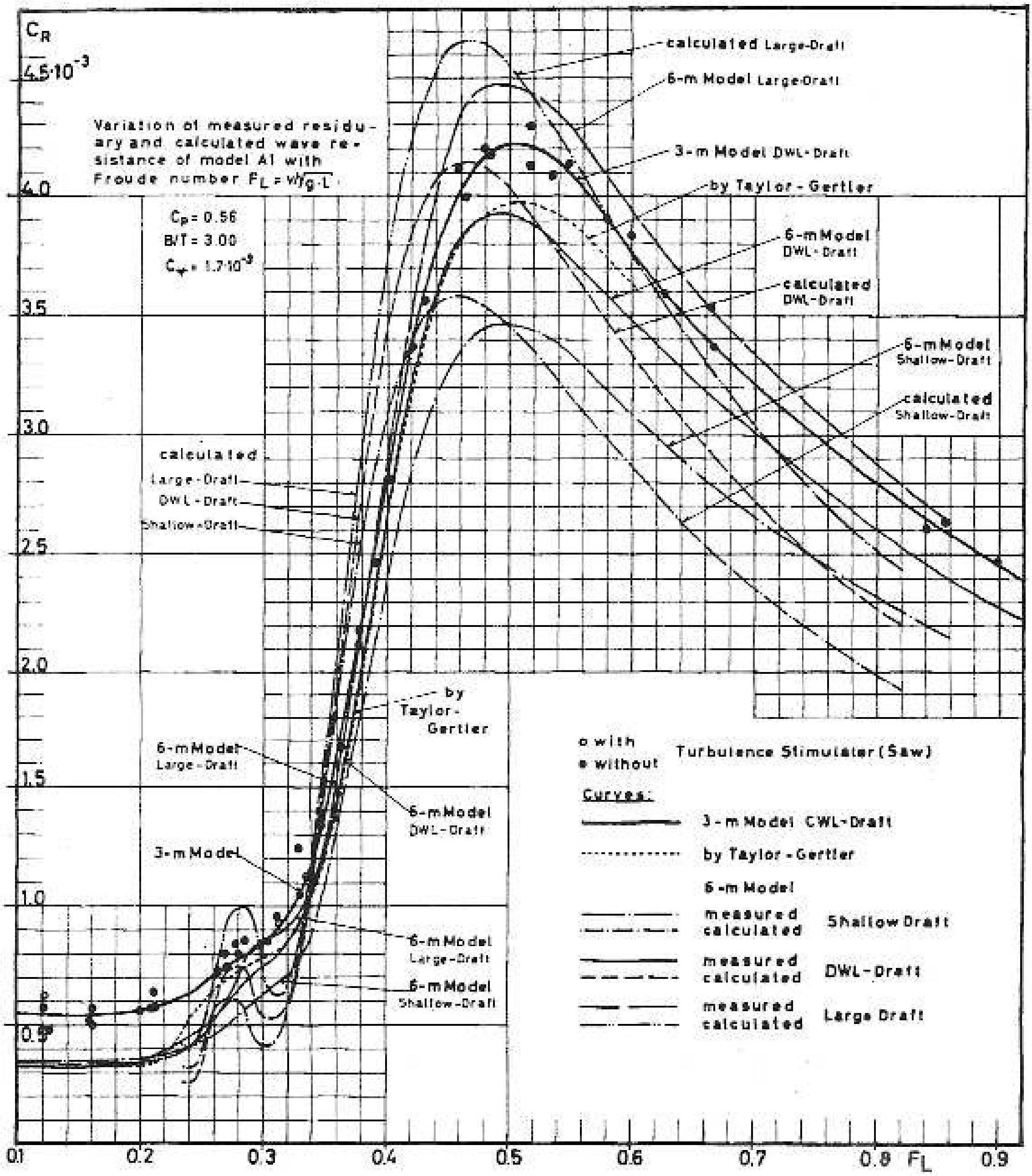

Figure C.3.: Comparison of the wave resistance calculated from Michell's integral with the residual drag coefficient measured from different model tests; source [New77, p. 283]

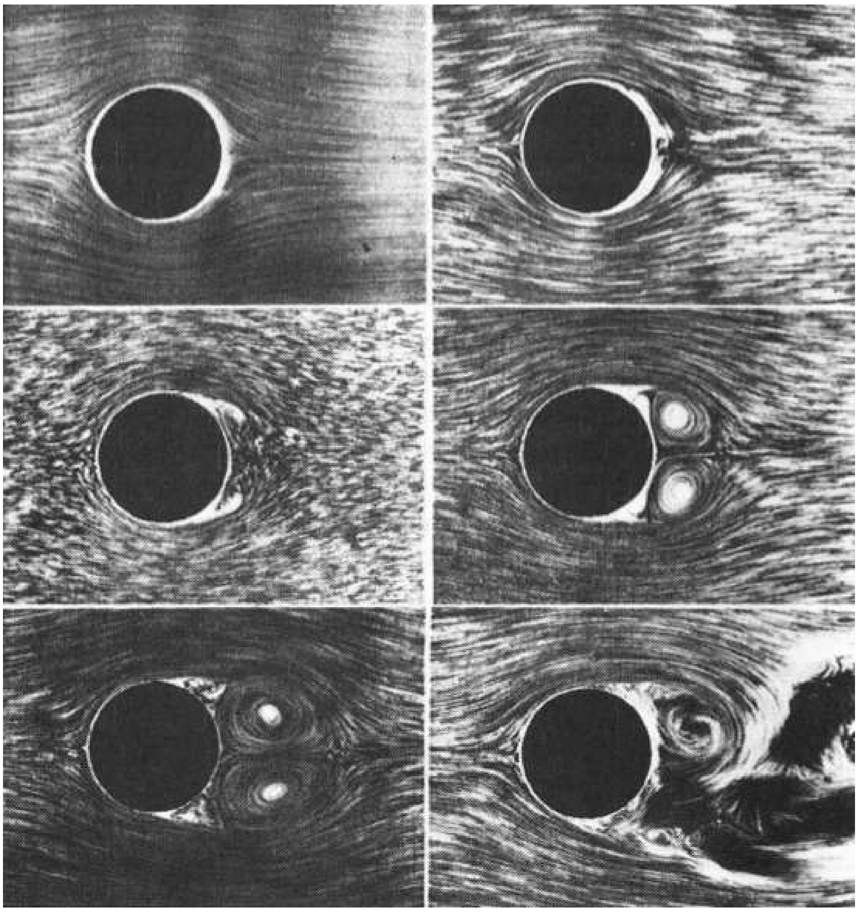

Figure C.4.: Photographs from Prandtl 1927 showing the initial stages of the flow past a circular cylinder, which is from a state of rest impulsively accelerated to a constant velocity; source [New77, p. 36]

# Bibliography

[And05] John D. Anderson, Jr. Ludwig prandtl's boundary layer. *Physics today*, pages 42–48, 2005.

[ANS09a] Inc ANSYS. *ANSYS CFX-Solver Modeling Guide*, 2009. Relase 12.0.

[ANS09b] Inc ANSYS. *ANSYS CFX-Solver Theory Guide*, 2009. Relase 12.0.

[ANS09c] Inc ANSYS. *User Manual — ANSYS ICEM CFD*, 2009. Relase 12.0.

[ANS10a] Inc ANSYS. *ANSYS CFX-Solver Modeling Guide*, 2010. Relase 13.0.

[ANS10b] Inc ANSYS. *ANSYS CFX-Solver Theory Guide*, 2010. Relase 13.0.

[Aya10] Anis Awal Ayati. Aerodynamic effects on wind turbine blades using the lifting-line theory. Master's thesis, University of Oslo, 2010.

[Ber10] Arnold Bertelsen. Mek4300 - viskøs strømning og turbulens. lecture notes, 2010.

[Cyb10] Cyberiad. *Michlet — User's Manual*, 2010. Michlet is research code.

[DR11] P. A. Durbin and B. A. Pettersson Reif. *Statistical theory and modeling for turbulent flows*. John Wiley & Sons Ltd., Chichester, second edition, 2011.

[Fea08] Richard L. Fearn. Airfoil aerodynamics using panel methods. *The Mathematica Journal*, 10:4:725–739, 2008.

[Fos09] Hannibal Eie Fossum. Predicting particle deposition in the human airways with rans turbulence modeling. Master's thesis, University of Oslo, 2009.

[FR02] J. Frölich and W. Rodi. Introduction to large eddy simulations of turbulent flows. In B.E. Launder and N.D. Sandham, editors, *Closure Strategies for Turbulent and Transitional Flows*, pages 267–299. Cambridge University Press, 2002.

[Gje02] Bjørn Gjevik. *Viskøse Væsker og Elastiske Stoffer.* UiO, Departement of Mathematics, Norway, Oslo, 2002. Compendium used in MEK4220, in 2010.

[GPMC91] Massimo Germano, Ugo Piomelli, Parviz Moin, and William H. Cabot. A dynamic subgrid-scale eddy viscosity model. *Physics of Fluids AIP.*, pages 1760–1765, 1991.

[GPT10] Bjørn Gjevik, Geir K. Pedersen, and Karsten Trulsen. *Hydrodynamic Wave theory.* UiO, Departement of Mathematics, Norway, Oslo, 2010. Compendium used in MEK4320.

[HJ02] K. Hanjalić and S. Jakirlić. Second-moment turbulence closure modelling. In B.E. Launder and N.D. Sandham, editors, *Closure Strategies for Turbulent and Transitional Flows*, pages 47–101. Cambridge University Press, 2002.

[Int11] International Canoe Federation. Canoue sprint competition rules. Technical report, ICF, 2011.

[Irg08] Fridtjov Irgens. *Continuum Mechanics.* Springer, 2008.

[ITT08] *25th International Towing Tank Conference*, volume 2, 2008.

[JLB92] P. S. Jackson, N. Locke, and P. Brown. The hydrodynamics of paddle propulsion. In *11th Australasian Fluid Mechanics Conference*, pages 1197–1200, 1992.

[KC08] Pijush K. Kundu and Ira M. Cohen. *Fluid Mechanics.* Academic Press, USA, fourth edition, 2008.

[KS92] Selina J. Kendal and Ross H. Sanders. The technique of elite flatwater kayak paddlers using the wing paddle. *Journal of Applied Biomechanics*, 8(3):233–250, 1992.

[Lig60] M. J. Lighthill. Note on the swimming of slender fish. *Journal of Fluid Mechanics*, 9(02):305–317, 1960.

[Lis83] P. B. S. Lissaman. Low-reynolds-number airfoils. *Ann. Rev. Fluid Mech.*, 15:232–239, 1983.

[Mas70] George E. Mase. *Theory and Problems of Continuum Mechanics.* Schaum's outline series. McGraw-Hill, 1970.

[Mat98] P. C. Matthews. *Vector calculus.* Springer Undergraduate Mathematics Series. Springer-Verlag London Ltd., London, 1998.

[Men09] Florian R. Menter. Review of the shear-stress transport turbulence model experience from an industrial perspective. *International Journal of Computational Fluid Dynamics*, 23:305–316, 2009.

[Mic98] John Henry Michell. The wave resistance of a ship. *Philosophical Magazine*, 45:106–123, 1898.

[MLV06] F. Menter, R. Langtry, and S. Völker. Transition modelling for general purpose cfd codes. *Flow, Turbulence and Combustion*, 77:277–303, 2006. 10.1007/s10494-006-9047-1.

[MSR09] Jacob S. Michael, Richard Smith, and Kieron B. Rooney. Determinants of kayak paddling performance. *Sports Biomechanics*, 8(2):167–179, 2009.

[New77] John Nicholas Newman. *Marine Hydrodynamics*. The MIT Press, Cambridge, Massachusetts, and London, England, 1977.

[Per06] Per-Olof Persson. *Unstructured Mesh Generation*, 2006. MIT Lecture 2 in Advanced Topics in Numerical Methods for Partial Differential Equations.

[Pho02] Phoenix Analysis and Design Technologies. *Tet-Meshing: ANSYS vs. ICEM*, 2002. The Focus, a Publication for ANSYS Users.

[PIG06] Nicola Petrone, Andrea Isotti, and Guglielmo Guerrini. Biomechanical analysis of olympic kayak athletes during indoor paddling. In Eckehard Fozzy Moritz and Steve Haake, editors, *The Engineering of Sport 6*, pages 413–418. Springer New York, 2006.

[Pop00] Stephen B. Pope. *Turbulent Flows*. Cambridge University Press, UK, 2000.

[Rei10] B. A. Pettersson Reif. Mek4330 - turbulence theory and modeling. personal lecture notes, 2010.

[Rey90] W. Reynolds. The potential and limitations of direct and large eddy simulations. In J. Lumley, editor, *Whither Turbulence, Turbulence at the Crossroads*, volume 357 of *Lecture Notes in Physics*, pages 313–343. Springer Berlin / Heidelberg, 1990.

[Sch07] François G. Schmitt. About boussinesq's turbulent viscosity hypothesis: historical remarks and a direct evaluation of its validity. *Comptes Rendus Mécanique*, 335(9-10):617 – 627, 2007. Joseph Boussinesq, a Scientist of bygone days and present times.

[SM04] L. K. Su and M. G. Mungal. Simultaneous measurements of scalar and velocity field evolution in turbulent crossflowing jets. *Journal of fluid mechanics*, 513:1–45, 2004.

[SMM$^+$06] Eric Sprigings, Peter McNair, Grant Mawston, David Summer, and Mark Boocock. A method for personalising the blade size for competitors in flatwater kayaking. *Sports Engineering*, 9:147–153, 2006.

[SRS$^+$02] M. Sacchi, R. Rodanol, R. Squadrone, A. Veicsteinas, G. Merati, and A. Marzegan. Evaluation of kinematic left-right asymmetries in elite, intermediate and novice kayakists. *Medicine & Science in Sports & Exercise*, 34, 2002.

[SSBH03] D. Sumner, E. Sprigings, J. Bugg, and J. Heseltine. Fluid forces on kayak paddle blades of different design. *Sports Engineering*, 6:11–19, 2003. 10.1007/BF02844156.

[SV94] S. G. Saddoughi and V. S. Veeravalli. Local isotropy in turbulent boundary layers at high reynolds number. *J. Fluid Mech*, 268:333–372, 1994.

[TH03] Michael S. Triantafyllou and Franz S. Hover. *Maneuvering and Control of Marine Vehicles*. Department of Ocean Engineering, Massachusetts Institute of Technology, Cambridge, Massachusetts USA, 2003.

[TL08] Ernie Tuck and Leo Lazauskas. Drag on a ship and michell's integral. In *XXII ICTAM*, Adelaide, Australia, 25–29 August 2008.

[Tuc98] E. O. Tuck. The wave resistance formular of j.h. michelle (1898) and its significance to recent research in ship hydrodynamics. *Journal Australian Mathematical Society*, B(30):365–377, 1998.

[VS05] Valerio Viti and Joseph Schetz. Comparison of first and second order turbulence models for a jet/3d ramp combination in supersonic flow. *43rd AIAA Aerospace Sciences Meeting and Exhibit*, 1100, 2005.

[Whi06] Frank M. White. *Viscous Fluid Flow*. McGra-Hill, USA, third edition, 2006.

# Bibliography for Online-Links

[CFD11] CFD Online Wiki. SSTk-omega model. `http://www.cfd-online.com/Wiki/SST_k-omega_model`, 2011. [Online; accessed 6-December-2011].

[Flu11] DG Flugzeugbau. Technical data of the DG-1000/1001. `http://www.dg-flugzeugbau.de/technische-daten-1000-e.html`, 2011. [Online; accessed 11-November-2011].

[ITT11] ITTC. International towing tank conference. `http://ittc.sname.org/`, 2011. [Online; accessed 2-November-2011].

[Wik11a] Wikipedia. Drag — Wikipedia, the free encyclopedia. `http://en.wikipedia.org/wiki/Drag_(physics)`, 2011. [Online; accessed 1-November-2011].

[Wik11b] Wikipedia. Kanurennsport — Wikipedia, the free encyclopedia. `http://de.wikipedia.org/wiki/Kanurennsport`, 2011. [Online; accessed 30-October-2011].

[Wik11c] Wikipedia. Rotorschiff — Wikipedia, the free encyclopedia. `http://de.wikipedia.org/wiki/Rotorschiff`, 2011. [Online; accessed 1-November-2011].

[Wik11d] Wikipedia. Strouhal number — Wikipedia, the free encyclopedia. `http://en.wikipedia.org/wiki/Strouhal_number`, 2011. [Online; accessed 22-December-2011].

[Wik11e] Wikipedia. Wingtip divice — Wikipedia, the free encyclopedia. `http://en.wikipedia.org/wiki/Wingtip_device`, 2011. [Online; accessed 14-December-2011].